AD NUMBER
ADC020797
CLASSIFICATION CHANGES
TO: unclassified
FROM: confidential
LIMITATION CHANGES
TO: Approved for public release, distribution unlimited
FROM: Controlling DoD Organization. Naval Ocean Systems Center, San Diego, CA 92152.
AUTHORITY
ONR ltr, 31 Jan 2006; ONR ltr, 31 Jan 2006

CONFIDENTIAL

NOSC

LEVEL II

NOSC TR 466

NOSC TR 466

Technical Report 466

BEARING STAKE ACOUSTIC ASSESSMENT (U)

AL Anderson, Report Coordinator
RR Gardner, Project Technical Director

Research and Development: January — May 1977

28 September 1979

Classified by: OPNAVINST S5513.5-03
Review on: 8 October 1994

"NATIONAL SECURITY INFORMATION"

"Unauthorized Disclosure Subject to Criminal Sanctions"

NAVAL OCEAN SYSTEMS CENTER
SAN DIEGO, CALIFORNIA 92152

CONFIDENTIAL

NAVAL OCEAN SYSTEMS CENTER, SAN DIEGO, CA 92152

AN ACTIVITY OF THE NAVAL MATERIAL COMMAND

SL GUILLE, CAPT, USN
Commander

HL BLOOD
Technical Director

ADMINISTRATIVE INFORMATION (U)

(U) The work in this report was sponsored by the Naval Electronic Systems Command (PME-124) under X0755104.

(U) Technical reviewers were E. B. Tunstall and R. R. Gardner. Work was performed from January through May 1977.

Released by
N. O. BOOTH, HEAD
Environmental Acoustics
Division

Under authority of
J. D. Hightower, Head
Environmental Sciences
Department

CONFIDENTIAL

SECURITY CLASSIFICATION OF THIS PAGE *(When Data Entered)*

REPORT DOCUMENTATION PAGE

READ INSTRUCTIONS BEFORE COMPLETING FORM

1. REPORT NUMBER: NOSC Technical Report 466 (TR 466)

2. GOVT ACCESSION NO.:

3. RECIPIENT'S CATALOG NUMBER:

4. TITLE *(and Subtitle)*: BEARING STAKE ACOUSTIC ASSESSMENT (U)

5. TYPE OF REPORT & PERIOD COVERED: R&D: Jan–May 1977

6. PERFORMING ORG. REPORT NUMBER:

7. AUTHOR(s): A.L. Anderson et al

8. CONTRACT OR GRANT NUMBER(s): Research and development Jan - May 17

9. PERFORMING ORGANIZATION NAME AND ADDRESS: Naval Ocean Systems Center, San Diego, California 92152

10. PROGRAM ELEMENT, PROJECT, TASK AREA & WORK UNIT NUMBERS: 16 X0755104 17 X0755104

11. CONTROLLING OFFICE NAME AND ADDRESS: Naval Electronic Systems Command, Washington, D. C. 20360

12. REPORT DATE: 28 September 1979 (12 275)

13. NUMBER OF PAGES: 280

14. MONITORING AGENCY NAME & ADDRESS *(if different from Controlling Office)*: 14 NOSC/TR-466

15. SECURITY CLASS. *(of this report)*: CONFIDENTIAL

15a. DECLASSIFICATION/DOWNGRADING SCHEDULE: Review on: 8 October 1994

16. DISTRIBUTION STATEMENT *(of this Report)*: 10 Aubrey L. /Anderson; Don F. /Fenner; William J. /Cronin, Jr.; S. K. /Mitchell

17. DISTRIBUTION STATEMENT *(of the abstract entered in Block 20, if different from Report)*: R. R. /Gardner

18. SUPPLEMENTARY NOTES:

19. KEY WORDS *(Continue on reverse side if necessary and identify by block number)*:
Acoustic surveillance
Ambient noise
Propagation
Reflectivity

20. ABSTRACT *(Continue on reverse side if necessary and identify by block number)*:
(C) Presents findings and conclusions based on the at-sea exercise BEARING STAKE and the extensive analysis of the data base which has been generated. The BEARING STAKE exercise was conducted by NOSC at five sites in the Northwest Indian Ocean between January and May 1977.

DD FORM 1 JAN 73 1473 EDITION OF 1 NOV 65 IS OBSOLETE
S/N 0102-LF-014-6601

CONFIDENTIAL

SECURITY CLASSIFICATION OF THIS PAGE *(When Data Entered)*

393159

JOB

BEARING STAKE ACOUSTIC ASSESSMENT (U)

Report Coordinator: Aubrey L. Anderson
Naval Ocean Research and Development Activity

Project Technical Director: R. R. Gardner
Naval Ocean Systems Center

with contributions from:

Don F. Fenner and William J. Cronin, Jr.
Naval Ocean Research and Development Activity

S. K. Mitchell and K. C. Focke
Applied Research Laboratories/University of Texas,

and

Edwin L. Hamilton and Richard T. Bachman
Melvin A. Pederson
R. A. Wagstaff and J. W. Aitkenhead
J. A. Neubert
Naval Ocean Systems Center

FOREWORD (U)

(C) The BEARING STAKE exercise was conducted in the Northwest Indian Ocean from January to May 1977 with preliminary bathymetric surveys being conducted from October through December 1976. The objectives of the exercise were to conduct acoustic measurements of the area utilizing near-surface, mid-water, and bottom-mounted receivers to determine the following acoustic parameters:

(1) Propagation loss versus frequency, depth, range;

(2) Omnidirectional ambient noise;

(3) Ambient noise directionality;

(4) Wavefront coherence;

(5) Vertical arrival structure;

(6) Bottom interaction; and

(7) Bottom reflectivity.

(C) The exercise was sponsored by NOP-095 through the Undersea Surveillance Project (PME-124). Commander of the exercise was CINCPACFLT. Operations were administered by COMSEVENTHFLT (including air operations through the Officer in Tactical Command CTF 73). MSCLANT and MSCPAC provided logistic support for all U.S. ships involved.

(U) The participants represented a Navy laboratory-wide effort and various contractors. Dr. E.B. Tunstall (NOSC) was the Associate Technical Director and was responsible for the overall operation at sea during the second half of the exercise on board the USNS MYER. Scientists-in-charge aboard the ships were A.E. Fadness (TRW) and B. Steinberg (NADC), USNS WILKES; J.W. Reese (NOSC) and W. Toy (WECo), USNS MIZAR; T.H. Steen (WECo) and R. Hoepple (WECo), USNS KINGSPORT; W. Redden (WECo) and E. Dawley (WECo), USNS MYER. Serving aboard the HMAS DIAMANTINA was Dr. A. Fabula (NOSC) with G. Myers of WRE, Australia, the engineer-in-charge. ACODAC Operations on the USNS MIZAR were under the direction of Dr. E.E. Hays (WHOI). Principal investigators for the analysis were: Dr. S.K. Mitchell (ARL/UT) for Bottom Interaction; Dr. D.F. Fenner (NORDA) for Oceanographic Data; Dr. L.P. Solomon (PSI) for Surface Shipping Surveillance; Dr. E.L. Hamilton (NOSC) for Bottom Geoacoustic Models; Dr. R.A. Wagstaff (NOSC) for Ambient Noise; Mr. Ron Scudder (WECo) for BMA Data Analysis; Dr. J.A. Neubert (NOSC) for Coherence Data Analysis; Mr. M.A. Pedersen (NOSC) for Acoustic Propagation Analysis; Dr. A.L. Anderson (NORDA) for Acoustic Assessment. The enthusiasm, dedication, and hard work of all these individuals and the others in their organizations are gratefully acknowledged.

(C) This acoustic area assessment presents findings and conclusions based on the at-sea exercise and the extensive analysis of the data base which has been generated. In addition, each measurement system has a data report and each major environmental and acoustic subject has an analysis report which are

referenced herein. The data base for this ocean area is now well established and is available for further studies as appropriate.

(U) Special appreciation and thanks are due RADM D.M. Jackson for continued support during the exercise as the Surveillance Project Manager.

R. R. Gardner
BEARING STAKE
Technical Director

BEARING STAKE ACOUSTIC ASSESSMENT (U)

CONTENTS (U)

SUMMARY (U)

GENERAL (U)

(C) The BEARING STAKE exercise has produced data allowing a description of several acoustic environments in the Northwest Indian Ocean. Specifically, on the basis of data acquired during the period from January through May 1977, the following parameters can be described for the Oman Basin, Arabian Basin, and Somali Basin:

Sound speed profile

Bottom bathymetry and geophysical parameters

Bottom loss from 25 to 400 Hz

Propagation loss from 20 to 290 Hz for source depths from 18 to 245 m and receiver depths from a few hundred m to the seafloor

Omnidirectional ambient noise from below 20 to 200 Hz for receiver depths from a few hundred m to the seafloor (with data available up to 800 Hz for receivers on the seafloor)

Directional ambient noise from 20 to 40 Hz for shallow depth (200 to 300 m) and for bottom horizontal arrays

Phase coherence from 22 to 290 Hz for a bottom horizontal array and from 22 to 25 Hz for a shallow (200 to 300 m) towed array

Array signal gain at 25 Hz for a horizontal bottom array and for shallow (200 to 300m) towed arrays

SOUND CHANNEL (U)

(C) Sound speed profiles from the Northwest Indian Ocean characteristically exhibit high sound speeds at the ocean surface and wide sound channels with large axis depths (frequently on the order of 1800 m). Some sound speed variability is exhibited, especially between depths of 100 and 1000 m. The sound channel is bottom limited at all times throughout the region with the exception of the northern Somali Basin, which exhibits some small and seasonally dependent depth excess (during BEARING STAKE, depth excess ranged from 0 to 121 m).

SEAFLOOR (U)

(C) In addition to coastal shelves and slopes, the seafloor in this region consists of bare rock or partially sediment covered ridges plus sediment filled basins with relatively flat, featureless floors. Sediment fill in these basins is among the thickest known, with several hundred metres of unconsolidated sediment overlying additional hundreds or even thousands of metres of sedimentary rock for a total sediment section over basement basalt of up to 9 km.

BOTTOM INTERACTION (U)

(C) Waterborne acoustic energy impinging on the thick unconsolidated sediment sections of the basin floors apparently penetrates into the sediment, is refracted upward by the sediment sound speed profile, and returns to the water column with low loss. When low frequency bottom interaction data are analyzed and interpreted in terms of bottom reflectivity, the resulting bottom losses are quite low. Such bottom loss measurements in the basins of the Northwest Indian Ocean indicate lowest loss (e.g., about 0.1 dB per bounce for low angles at 25 Hz) in the southern Arabian Basin, with increasing, but still low, bottom losses observed in the northern Arabian Basin, Oman Basin, and Somali Basin, respectively. Higher losses are inferred for the coastal features and partially sediment covered ridges surrounding the basins with highest bottom losses inferred for the topographically rugged, bare basaltic ridges such as the Carlsberg Ridge.

PROPAGATION LOSS (U)

(C) Signal propagation, as expressed by propagation loss, is highly variable over short range intervals (fluctuates relatively rapidly), with no evidence of convergence zone structure (except for higher-frequency data in the Somali Basin). Average propagation loss over the sediment filled basins is generally quite low. For example, over the Oman Basin, 50-km-range-averaged data at 200-km range showed propagation losses of 84 to 87 dB at 25 Hz, 85 to 91 dB at 140 Hz, and 82 to 94 dB at 290 Hz. In general, propagation loss throughout the region is usually equal to or better than the familiar Eleuthera reference curve. Highest losses are exhibited for receivers blocked by bathymetric features or mounted on the higher bottom loss ridges or topographic highs of the region; or for source-to-receiver tracks traversing some of the higher loss, rough bottom regions. Throughout the bottom limited region average propagation loss is virtually independent of depth for sources or receivers more than a few wavelengths away from the surface or bottom. The usual surface image interference effects are shown for sources near the ocean surface. A related interference effect, producing a source-depth and frequency-dependent near bottom propagation loss maximum ("notch"), is theoretically indicated and partially supported by data. If confirmed, such a propagation loss depth dependence could be used to optimize signal-to-noise ratio by height-off-the-bottom selection for near-bottom sensors. In the Somali Basin, convergence zone structure is exhibited with frequency-dependent (and probably sound-speed-profile – i.e., seasonally – dependent) convergence zone strength. For frequencies above 50 Hz, in this basin, optimum propagation (minimum average loss) is exhibited for receivers near the conjugate depth of shallow sources. For lower frequencies, average propagation loss exhibits a complex dependence on receiver depth and frequency.

AMBIENT NOISE (U)

(C) As is true for range averaged transmission loss, for receivers over the bottom-limited basins the omnidirectional ambient noise is essentially independent of depth for receivers removed from the ocean surface or bottom by more than a few (perhaps two) wavelengths. The low transmission loss, together with high shipping densities, produces high noise levels throughout the region. Highest omnidirectional noise levels (90 to 95 dB from 10 to 50 Hz) are observed in the Oman Basin, with only 5 – 10-dB lower levels observed

in the Arabian and Somali Basins. Noise levels for frequencies above 50 Hz are also high but with less dependence on the basin (and probable stronger dependence on wind speed/wave height). Persistent anisotropy of at least 10 dB is shown by the horizontal directional ambient noise data at low frequencies (23 and 36 Hz). The directions of noise peaks are well correlated with maxima of the shipping density.

COHERENCE (U)

(C) Phase coherence for horizontal arrays is variable but generally high for signals propagating over the sediment filled basins (coherence does decrease with increasing frequency). Somewhat higher coherence fluctuations are exhibited for an array at 300 m than for a shallower (200 m) or deeper (bottom) array. Decreased array coherence is shown for signals propagating over bottom topographic features (e.g., seamounts or hills). For the towed arrays (but not for the bottom array), signal coherence is reduced when sources pass over the sloping near-coastal bottom.

CHAPTER I

INTRODUCTION (U)

by

Aubrey L. Anderson

Numerical Modeling Division, Code 320

Naval Ocean Research and Development Activity

NSTL Station, Mississippi 39529

CHAPTER I. INTRODUCTION (U)

CONTENTS (U)

CHAPTER I. INTRODUCTION (U)

I.1 (U) GENERAL

(C) The BEARING STAKE exercise was a major acoustic survey program conducted in the Northwest Indian Ocean from January through May 1977. The program was sponsored by the Naval Electronic Systems Command (PME-124) and was designed to collect acoustic data to describe several acoustic environments in the region, to provide inputs to system performance models, and to provide acoustic data for assessing surveillance system options in selected areas of the Indian Ocean.

(U) The survey utilized near-surface, midwater, and near-bottom receivers (omnidirectional hydrophones and/or arrays) to collect data at several sites for description of the following ocean acoustic parameters:

Propagation loss

Ambient noise

Bottom interaction (bottom loss)

Spatial coherence

Appropriate sensors were used to provide data for a description of the environment during the acoustic measurements — specifically, the sound speed versus depth profiles, bathymetry, and bottom physical properties (geoacoustic models). During some of the ambient noise measurements, aerial surveillance of surface ships was conducted.

I.2 (U) REPORT OUTLINE

(C) This report serves two purposes. First it provides, in chapters II through VII, summary presentations of the major observations and conclusions resulting from analysis of the BEARING STAKE results by several principal investigators. Second it provides, in chapter VIII, another degree of summarization by combining the key observations of these principal investigators into an acoustic assessment of the Northwest Indian Ocean (a statement of the major features of the nature of this ocean region as an acoustic medium as revealed by the BEARING STAKE measurements).

(U) Chapters II through VII are condensed statements of material presented elsewhere in greater detail by the principal investigators (Fenner and Cronin, 1973; Hamilton and Bachman, 1979; Mitchell et al., 1979; Pedersen and Yee, 1979; Wagstaff and Aitkenhead, 1979; Neubert, 1978a,b,c,d; and Fabula and Neubert, 1978). The material prepared for these chapters by the principal investigators was edited to bring some degree of conformity to the style of presentation (to assist the reader), but the sections were allowed to retain a great deal of their individuality. Because of this editorial approach, a small degree of repetition has occurred, especially in the beginning section of a few of the chapters. Because each chapter author had his own points to make, the small additional bulk to this already sizable report seemed acceptable.

(U) Figures and tables are numbered sequentially in each chapter by Arabic numerals prefixed by a Roman numeral indicating the chapter (e.g., table 2 of chapter IV is designated on the table as: table IV-2). In any chapter, references to figures or tables within that same chapter omit the prefixed Roman numeral for the chapter. References to tables or figures in other chapters retain the prefixed Roman numeral.

(C) A glossary at the back of the report defines several of the terms and acronyms used herein. However, one diversity of the geographical references in the various chapters must be noted. As indicated in several of the chapters (III, IV, and VIII), the region of interest in this report, the Northwest Indian Ocean, contains a large central basin wherein the detritus from the Indus River has formed a very large deep sea fan or cone (underwater delta) on the seafloor. Because this physiographic feature was built by the Indus River outflow and because it occurs in the Arabian Sea, it is denoted by various authors as either the Indus Basin, Indus Cone, Arabian Fan, or Arabian Cone. In this report, the term Arabian Basin is also used to denote the central basin of the Arabian Sea which contains the Arabian Fan (see, for example, figure IV-1 or figure VIII-2).

I.3 (U) EXERCISE OUTLINE

(C) Although, ideally, one would like to develop a description of the nature of a given ocean region as an acoustic medium (an acoustic assessment) without reference to measurement systems or procedures (a stand-alone reference handbook), some reference to data acquisition and analysis procedures as well as theoretical extrapolations or interpolations are usually required. Large scale, low-frequency ocean measurements are by their nature difficult and expensive; thus, the few areas surveyed are usually sparsely sampled in both space and time. The description of regional acoustic features will be constrained to those features revealed by available measurements and such extrapolations with acoustic theory as can be made with confidence. This present assessment report is based on the results of analysis of data from a large scale measurement program, the BEARING STAKE exercise, carried out in the Northwest Indian Ocean as briefly described in section I.1 above. Because many of the observations of this report are heavily weighted by (and, as always, sometimes constrained by) the format of the measurement systems, methods, and successes versus failures, it is important to have at least an outline of the exercise available. Thus, such an outline is presented below. It is purposely restricted in scope and detail because the central focus of this report is a description of the regional acoustics rather than the survey itself. Much more detailed BEARING STAKE survey descriptions are available in some of the principal investigators' reports cited above and in other references to be cited below.

(C) During the time period from 13 January to 4 May 1977, the BEARING STAKE exercise was conducted in the Northwest Indian Ocean in four cruises. Five sites (fig 1) were selected for placement of various fixed receiving systems, and measurements were conducted by towing continuous-wave (CW) acoustic sources and deploying explosive (SUS) charges on ship (or aircraft) tracks centered on, and designed to sample the regions around, these fixed sites. Site 1 was occupied twice, and these occupations are kept separate by designating one as Site 1A, the other as Site 1B.

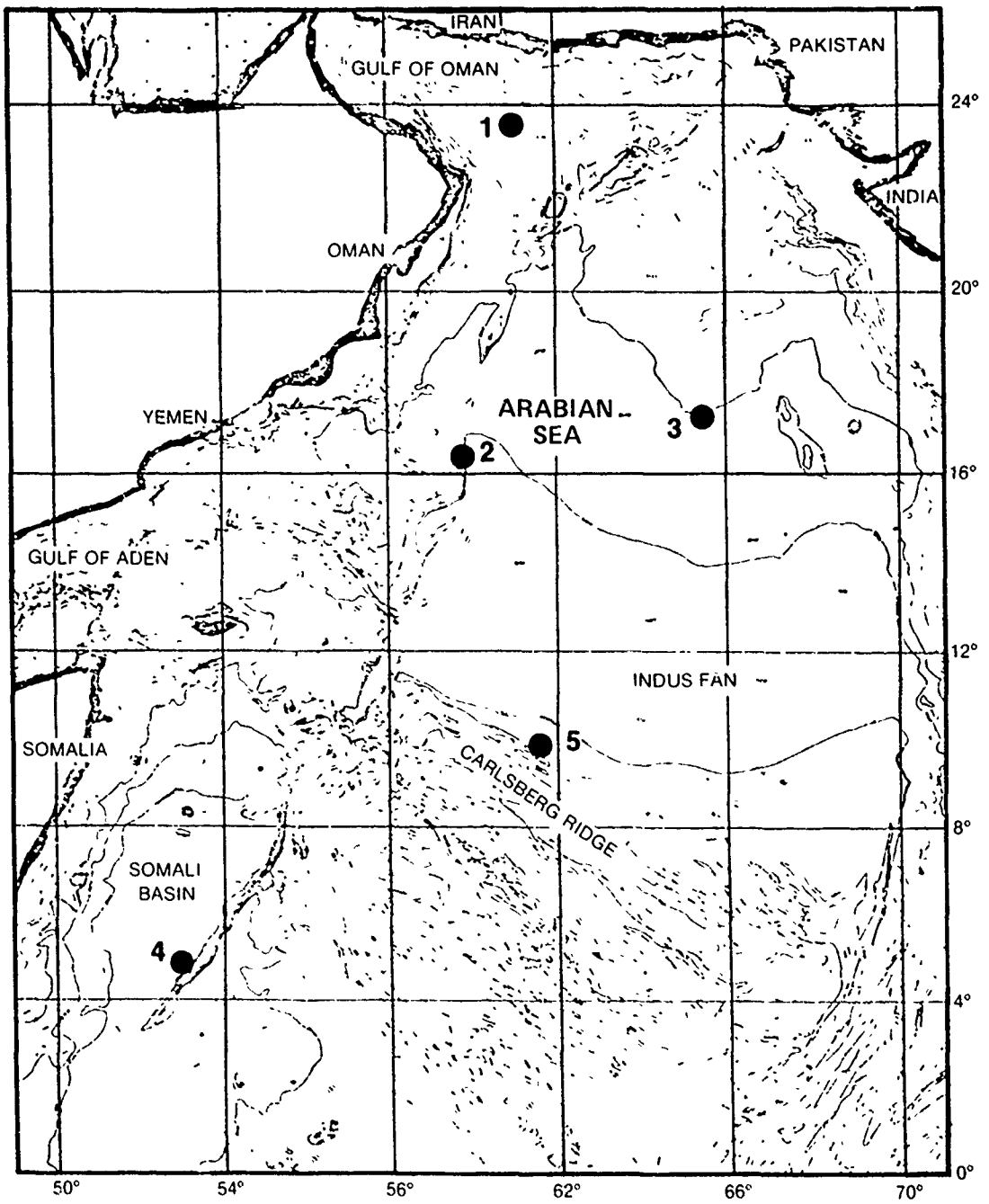

Figure I-1. (C) Geographic locations of the five principal BEARING STAKE sites. (C)

(C) Times (in 1977) of and sites occupied during the four cruises are:

Cruise	Dates	Site(s) Occupied
1	13 Jan - 26 Jan	1A
2	30 Jan - 26 Feb	3 and 1B
3	5 Mar - 30 Mar	4
4	4 Apr - 4 May	5 and 2

(C) The acoustic measurement system which was actually located at each of the designated sites for each occupation is a Bottom-Mounted Array (BMA) of hydrophones. This was the only acoustic receiving system deployed at all sites. Others, of a variety of receiving systems, were deployed near the BMA during source tows around the five sites. The acoustic receiving system suite from which results are used for this report included:

Bottom-Mounted Array (BMA) from PME-124/WECo

Vertical ACODAC (VAC) from WHOI

Ocean Acoustic Measurement System (OAMS) from PME-124/NOSC.

Long Acoustic Towed Array (LATA) from WRE, Australia

(C) These acoustic receivers were deployed at or near the sites in figure 1 as indicated below:

	Site Numbers					
Receiver	1A	3	1B	4	5	2
BMA	X	X	X	X	X	X
VAC		X	X	X		
OAMS		X	X	X	X	X
LATA		X	X	X	X	X

(C) The Bottom-Mounted Array (BMA), which was deployed for all six site occupations, is an array of eight hydrophones intended for placement on the ocean floor. At Sites 1B and 3, the array was deployed flat and horizontal with all hydrophones on the bottom. At Sites 1A and 5, deployment was similar except that two hydrophones (Nos. 1 and 2) were buoyed up off the bottom. At Site 4, all hydrophones were on the bottom but the array was placed along the sloping side of the Somali Basin with hydrophone no. 1 at about 4700 m depth and the remaining hydrophones at successively shallower depths up the slope until no. 8 (the shallowest) at about 3800 m depth. At Site 2, all hydrophones were on the bottom but the array was draped across a local topographic high such that hydrophones 1 through 7 were at successively shallower depths (no. 1 deepest) up a slope facing the Arabian Basin while hydrophone 8 was partially shielded from the basin behind ("over the top of") the local feature. Details of the deployments including hydrophone spacing and array orientation are given in other BEARING STAKE Reports (e.g., Yee et al., 1977).

(C) The Vertical ACODAC (VAC) System, deployed near the BMA location at Sites 1B, 3 and 4, consisted of 13 hydrophones deployed (in three closely spaced groups plus a single phone) at four depths in the water column. Hydrophones 1 through 4 were in the shallowest group deployed in the upper part of the sound channel at a depth of a few hundred metres. Hydrophones 5 through 8 were deployed in a midwater group near the sound channel axis depth. Hydrophones 9 through 12 were deployed as a group at a depth about 30 m above the seafloor. Hydrophone 13 was on the seafloor.

(C) The Ocean Acoustic Measurement System (OAMS) is a horizontal towed array of 32 directional hydrophone groups spaced over an acoustic aperture of 925 m. By design this array is highly directional and was constrained to acquiring data for beams within a few degrees of broadside (Neubert, 1978d). The OAMS array was operated for Sites 3, 1B and 4 in the vicinity of the BMA, while for Sites 5 and 2 the OAMS array operated more than 400 km from the BMA. At each site, the OAMS array was deployed to a cable scope of between 300 and 350 m. Speed of the towing ship was adjusted to maintain a nominal array tow depth of 200 m. Ship speed varied between 2 and 3 knots. Ship maneuvers at each site consisted of polygon tows (to assess ambient noise horizontal directionality) and straight line tows which were oriented in a manner such that the acoustic paths from operating sources were generally within $\pm 15^{0}$ of broadside to the array. Data for determination of coherence, propagation loss and beam noise temporal statistics were collected during the straight tows.

(C) The Long Acoustic Towed Array (LATA) is a horizontal towed array of 64 omnidirectional hydrophone groups uniformly spaced 19 m apart ($\lambda/2$ at about 40 Hz) over an acoustic aperture of 1200 m. The LATA was operated for Sites 3, 1B and 4 in the vicinity of the BMA, while for Sites 5 and 2 it was operated more than 700 km from the BMA. For reasons described elsewhere (Neubert, 1978d), LATA data were processed for coherence estimates only for Sites 4, 5, and 2. The array was towed at a nominal depth of 305 m at a speed of 2 to 3 knots. Coherence measurements were made on straight line tows oriented so that the array would be nearly broadside or nearly endfire to the projector.

(C) Both narrowband (CW) projectors and broadband, explosive (SUS) sources were used. The SUS charges were deployed along preselected tracks from ships or aircraft at fixed spacings along the track. They were operated by depth (pressure) sensitive fuses and were preset to explode at one of four depths: 18, 91, 245, or 455 m. The two CW sources operated at frequencies between 22 and 290 Hz. The high-frequency source, operating at 140 and 290 Hz, was towed at 18-m nominal depth while the low-frequency source, operating at frequencies of 22, 25, 36, 39, and 42 Hz, was towed either at 91 m or between 78 and 84 m.

(C) Tracks for source tows (CW) and explosive (SUS) deployments are shown in figures in subsequent sections (see especially chapter II). On these figures and in references to the source tracks (or "events" in chapter V), a fixed nomenclature is used for identification. Each track is identified by an alphanumeric sequence of either three or four characters. The first character is a number used to designate the BEARING STAKE measurement site at which the BMA receiver was deployed for reception of signals from the source track (for Sites 1A and 1B this requires two characters). The second character (third for 1A and 1B events) is one of the three letters: P, S and A. These are used to designate, respectively: CW source tows, ship tracks for explosive

(SUS) deployment, and aircraft tracks for SUS deployment. The third (or fourth) character numbers the different types of source events for each site in sequence. Thus, the track for the third CW source tow at Site 4 is designated 4P3 while the first ship track for SUS deployment at Site 1B is designated 1BS1.

(C) Ships used during BEARING STAKE were the following:

- USNS KINGSPORT conducted all long range projector tows, launched all ship dropped SUS, collected 3.5 kHz sub-bottom profile data, and also collected sound velocity/salinity-temperature-depth (SV/STD) and expendable bathythermograph (XBT) data.
- USNS MYER was responsible for all BMA operations.
- USNS MIZAR launched and retrieved the VAC (and other systems) and served as the tow ship for the OAMS array.
- USNS WILKES collected environmental data, including bottom profiles, SV/STD, and Wide-Angle Bottom Reflection (WABR) data, and took bottom core samples. She was also engaged in work with other systems not used for the present assessment.
- HMAS DIAMANTINA towed and operated the LATA in conjunction with MIZAR tow runs, and also collected supporting environmental/oceanographic data.

REFERENCES (U)

Fabula, A.G. and J.A. Neubert (1978). "BEARING STAKE Data Analysis: LATA (U)," Naval Ocean Systems Center, San Diego, California, NOSC TN 589, November. (CONFIDENTIAL)

Fenner, D.F. and W.J. Cronin, Jr. (1978). "BEARING STAKE Exercise: Sound Speed and Other Environmental Variability (U)," Naval Ocean Research and Development Activity, NSTL Station, Mississippi, NORDA Report 18, September. (CONFIDENTIAL)

Hamilton, E.H. and R.T. Bachman (1979). "Geoacoustic Models of the Sea Floor: Gulf of Oman, Arabian Sea, and Somali Basin (U)," Naval Ocean Systems Center, San Diego, California, NOSC TR 347. (CONFIDENTIAL)

Mitchell, S.K., K.C. Focke, J.J. Lemmon and M.M. McSwain (1979). "Analysis of Acoustic Bottom Interaction in BEARING STAKE (U)," Applied Research Laboratories, The University of Texas at Austin, Texas, ARL-TR-79-24, February. (CONFIDENTIAL)

Neubert, J.A. (1978a). "BEARING STAKE Coherence Data Analysis: Part I. The OAMS Array (U)," Naval Ocean Systems Center, San Diego, California, NOSC TN 380, February. (CONFIDENTIAL)

Neubert, J.A. (1978b). "BEARING STAKE Coherence Data Analysis: Bottom Mounted Array (U)," Naval Ocean Systems Center, San Diego, California, NOSC TN 452, May. (CONFIDENTIAL)

Neubert, J.A. (1978c). "BEARING STAKE Array Signal Gain Data Analysis (U)," Naval Ocean Systems Center, San Diego, California, NOSC TN 642, December. (CONFIDENTIAL)

Neubert, J.A. (1978d). "BEARING STAKE Coherence and Array Gain Area Assessment Report (U)," Naval Ocean Systems Center, San Diego, California, NOSC TR 383, December. (CONFIDENTIAL)

Pedersen, M.A. and G.S. Yee (1979). "BEARING STAKE Propagation Loss (U)" (approximate Title; Report in Preparation), Naval Ocean Systems Center, San Diego, California. (CONFIDENTIAL)

Wagstaff, R.A. and J.W. Aitkenhead (1979). "BEARING STAKE Ambient Noise (U)" (Approximate Title; Report in Preparation), Naval Ocean Systems Center, San Diego, California. (CONFIDENTIAL)

Yee, G.S., et al. (1977). "BEARING STAKE Exercise Preliminary Results (U)," Naval Ocean Systems Center, San Diego, California, NOSC TR 169, October. (CONFIDENTIAL)

CHAPTER II

OCEANOGRAPHIC ENVIRONMENTAL DESCRIPTION (U)

by

Don Fenner and William J. Cronin, Jr.

Ocean Acoustics Division, Code 340

Naval Ocean Research and Development Activity

NSTL Station, Mississippi 39529

CHAPTER II. OCEANOGRAPHIC ENVIRONMENTAL DESCRIPTION (U)

CONTENTS (U)

CHAPTER II. OCEANOGRAPHIC ENVIRONMENTAL DESCRIPTION (U)

II.1 (U) GENERAL DISCUSSION OF ENVIRONMENTAL DATA

(C) During the BEARING STAKE exercise, participating vessels routinely collected oceanographic, meteorological, bathymetric, and other environmental data throughout the Northwest Indian Ocean. Table 1 summarizes oceanographic and meteorological data collected at each major acoustic site (fig 1). Oceanographic data consisted of expendable bathythermograph (XBT) observations and sound velocity/salinity-temperature-depth (SV/STD) stations. Meteorological data included observations of wind speed, wind direction, sea height, and swell height. In addition to those data listed in table 1, sea surface temperature observations were collected continuously by WILKES at Sites 1A, 1B, 3 and 4. Bathymetric data were collected by KINGSPORT, WILKES, and MIZAR throughout the exercise.

(C) Three types of XBTs were deployed during the exercise: Sippican Model T-5 probes (maximum depth of 1830 m) by KINGSPORT, MYER, WILKES, and MIZAR; Model T-7 probes (maximum depth of 760 m) by MIZAR and DIAMANTINA; and Model T-4 probes (maximum depth of 450 m) by DIAMANTINA. The great majority of MIZAR XBTs were T-7 probes; the great majority of the DIAMANTINA XBTs were T-4 probes. All XBT traces were machine digitized and converted to speed through the equation of Wilson (1960). Salinities necessary for sound speed calculation were individually assigned to each XBT trace, and were based on a salinity field derived from exercise SV/STD data and historical northeast monsoon Nansen cast data. All three XBT models measure temperature to $\pm 0.2^{\circ}C$, which results in a calculated sound speed accuracy of about ± 0.8 m/s assuming that there are no errors in Wilson's equation. The SV/STD systems used by KINGSPORT, WILKES, and MIZAR measure sound speeds with a precision of about +0.3 m/s and yield Wilson equation sound speeds accurate to about ± 0.1 m/sec. Generally, BEARING STAKE sound speeds calculated from XBT temperatures were up to 1.0 m/s higher than those measured directly and up to 0.5 m/s higher than those calculated from SV/STD temperatures and salinities. Most of this error is attributable to XBT inaccuracies compounded by inaccuracies in Wilson's equation (Carnvale et al., 1968; Mackenzie, 1971). Despite these inaccuracies, the total exercise sound speed data base is adequate for propagation loss calculations since measured and calculated sound speed gradients were nearly identical throughout the upper 2000-2500 m of the water column. Below 3000 m, sound speeds measured during the exercise were used in all analyses so as not to bias propagation loss calculations.

(U) As previously reported (Naval Ocean Systems Center, 1977), a substantial percentage of data from BEARING STAKE XBTs initially appeared too warm below a depth of 600-1000 m when compared to exercise SV/STD data. Preliminary evaluation of the XBT traces indicated that these erroneously warm temperatures were caused mainly by an alteration in the sink rate of the XBT probes due to entanglement with towed projectors, wire rubbing, etc. However, during later analysis of the traces, XBT recorder malfunctions (caused by a slow recorder servo-motor response) were uncovered that could lead to indications of warmer temperatures in that region of the water column where temperature becomes basically isothermal (i.e., below about 1000 m). These errors were compensated for during machine digitization of the traces, with the

TABLE II-1. (C) SUMMARY OF BEARING STAKE OCEANOGRAPHIC DATA. (U)

SHIP	100-600 m	600-1500 m	1500 m	SV/STDs	WEATHER OBS.
KINGSPORT	4	Site 1A	24	4	132
MYER	4	9	9	0	240
WILKES	1	4	1	5	0
Total	9	13	34	9	336
KINGSPORT	10	Site 1B	1	12	84
MYER	0	4	8	0	158
WILKES	3	4	13	5	0
MIZAR	7	6	5	2	96
DIAMANTINA	20	0	0	0	13
Total	40	15	28	19	351
Site 1 Total	49	28	62	28	687
		Site 3			
KINGSPORT	4	7	21	12	168
MYER	3	2	13	0	321
WILKES	9	12	36	6	0
MIZAR	20	10	2	5	96
DIAMANTINA	12	0	0	0	13
Total	48	31	72	23	598
		Site 4			
KINGSPORT	2	25	25	13	288
MYER	0	4	14	0	332
WILKES	13	20	36	4	0
MIZAR	6	18	4	3	264
DIAMANTINA	32	8	0	0	44
Total	53	75	79	20	928
		Site 5			
KINGSPORT	2	16	4	4	132
MYER	2	11	3	0	253
MIZAR	2	4	0	3	156
DIAMANTINA	21	4	0	0	29
Total	27	45	7	7	570
		Site 2			
KINGSPORT	1	10	0	1	108
MYER	1	3	9	0	192
MIZAR	9	10	1	1	156
DIAMANTINA	0	0	0	0	25
Total	11	23	10	2	481
Grand Total	188	202	230	80	3264

result that most XBT temperatures below about 1000 m agreed to 0.1° -0.2°C with those measured with SV/STDs. This agreement lies well within the accuracy of the XBT system. Nevertheless, approximately 45% of the T-5 probes deployed failed at depths less than 1500 m because of wire entanglement, wire rubbing, and actual wire breakage. Fortunately, it was possible to determine deep sound channel (DSC) statistics throughout the exercise area from exercise SV/STD data and those T-5 XBTs that reached their maximum depth.

II.2 (U) GENERAL OCEANOGRAPHIC SETTING

(C) Figure 1 shows the location of the five BEARING STAKE acoustic sites and four ancillary sites occupied by MIZAR and DIAMANTINA. These sites are shown superimposed on Indian Ocean sound speed provinces (after Colborn, 1976). The sound speed structure of the Northwest Indian Ocean has been extensively discussed by Fenner and Bucca (1972a and b). These previous works document the effects of various intrusive water masses on Indian Ocean sound speed structures, and are used as the primary basis for oceanographic interpretations contained in the following paragraphs. Sound speed profiles and temperature-salinity diagrams representative of each of the exercise sites during the northeast monsoon or the transitional periods between the northeast and southwest monsoons are presented in figure 2.

(C) Sites 1A and 1B, occupied approximately one month apart both were under the influence of high-salinity Persian Gulf Intermediate Water that emanates from the Persian Gulf through the Straits of Hormuz. This water mass exhibits a temperature and salinity maximum at 200-250 m which frequently causes perturbations in sound speed at the base of the permanent thermocline. At both Sites 1A and 1B, near-surface temperatures and sound speeds were somewhat lower than at other exercise sites. This anomaly was caused by the northeast monsoon upwelling along the northern edge of the Arabian Sea. Between about 200 and 1200 m, sound speeds at Site 1B were several m/s lower than those observed at Site 1A (also see fig 28). A maximum sound speed difference of about 4 m/s occurred at a depth of 400 m and corresponds to a temperature decrease of 1.1°C. This phenomenon probably was caused by increased upwelling after the Site 1A occupation.

(C) Site 2 was under the influence of both Persian Gulf Intermediate Water and high-salinity Red Sea Intermediate Water. The latter water mass exhibits a temperature and salinity maximum below 600 m. It emanates from the Red Sea into the Gulf of Aden and then into the Arabian Sea. Unfortunately, no exercise SV/STD data were available at site 2. However, sound speed microstructure above 1000 m on the Site 2 representative profile (fig 2) apparently was caused by the sinking and mixing of Red Sea and Persian Gulf Intermediate Waters. The presence of these two water masses also caused higher sound speeds (above 1200 m depth) than at any other exercise site. In contrast, at Site 3 water mass effects were minimal, and the representative sound speed profile generally was smooth and regular except at about 500-600 m, where Red Sea Intermediate Water caused a small amount of sound speed microstructure.

(C) Site 4 lay directly astride a primary flow of Red Sea Intermediate Water (600-900 m) that extends south along the entire east African coast. Site 4 also was under the influence of low-salinity Subtropical Subsurface Water that flows north along the east African coast at about 400 m. Intermixing and sinking of these two water masses and cold, low-salinity Antarctic

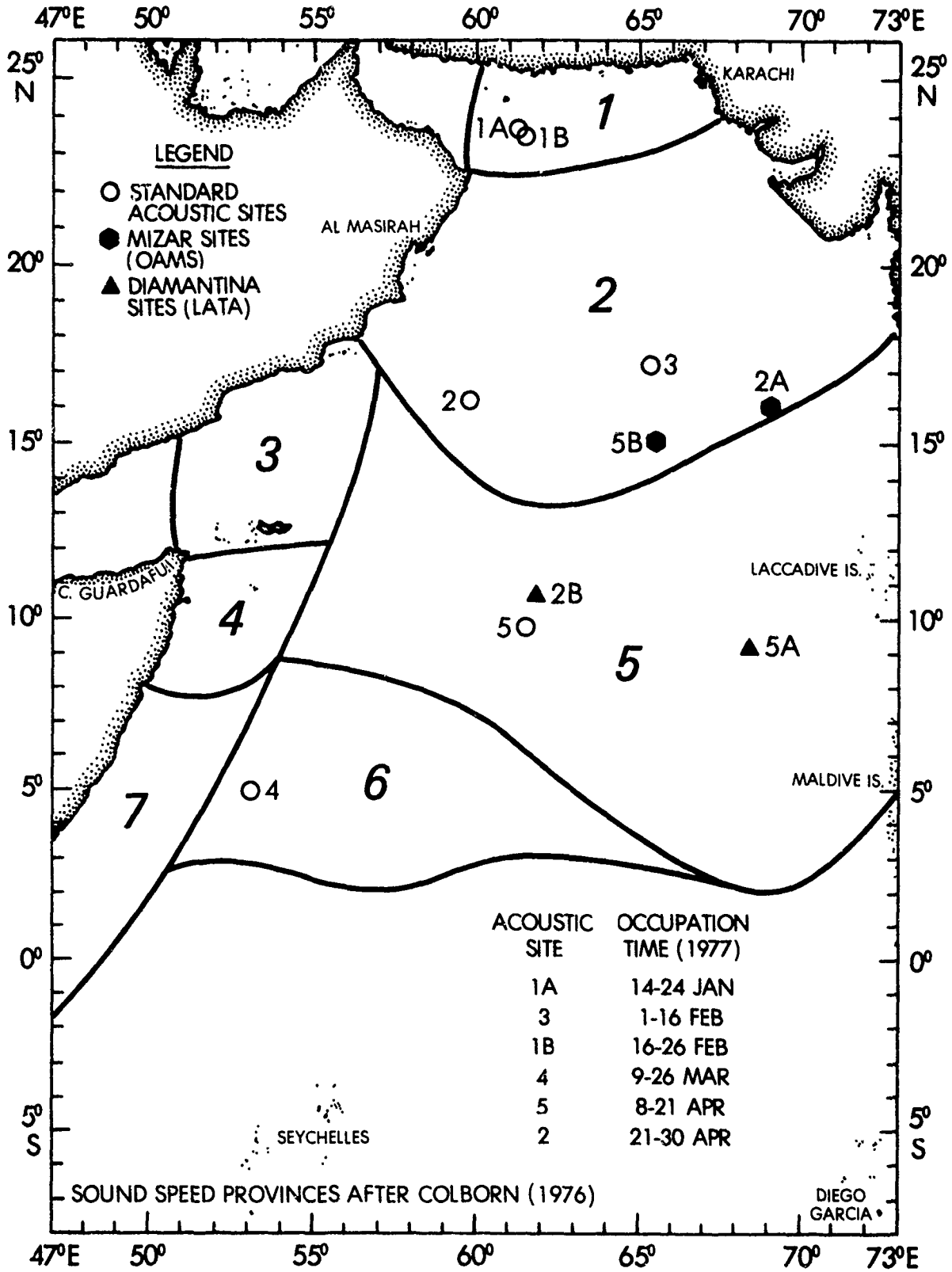

Figure II-1. (C) Location of exercise sites and Indian Ocean sound speed profiles. (U)

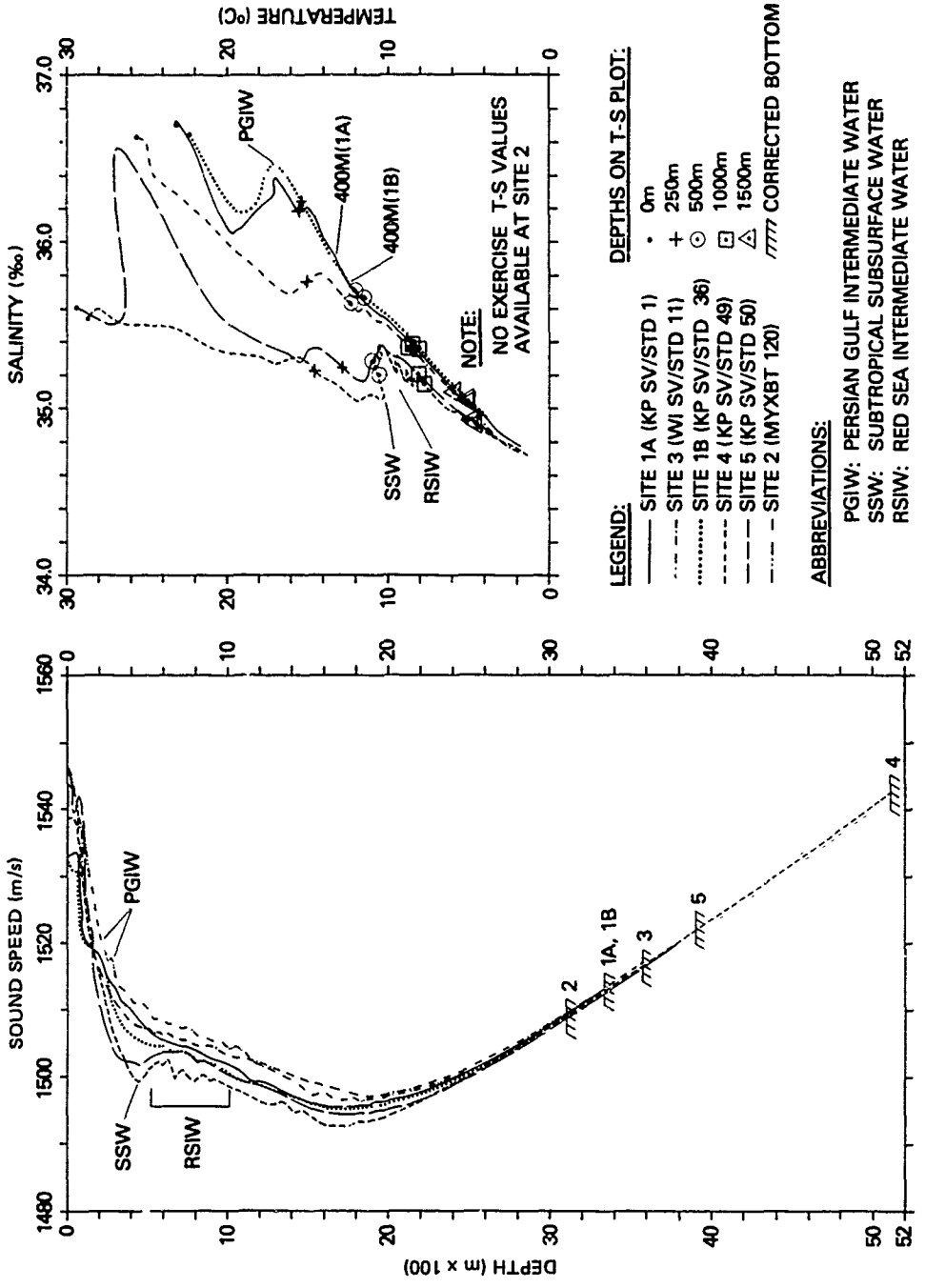

Figure II-2. (C) Representative sound speed and temperature-salinity profiles at each exercise site. (U)

and Banda Intermediate Waters (below 700 m) caused extremely complex temperature-salinity and sound speed structures at Site 4. Profiles exhibited rapidly varying microstructure to a depth of at least 1600 m. Primarily because of the effects of Antarctic Intermediate Water, representative sound speeds at Site 4 (fig 2) were lower than those observed at any other exercise site. Since Site 4 was occupied near the end of the northeast monsoon, it was not influenced by the strong Somali Current that flows north along the east African coast during summer. Generally, the monsoon reversal does not take place until late April or early May, well after the Site 4 occupation.

(C) Site 5 lay astride a strong flow of Red Sea Intermediate Water (at about 600 m) and also was influenced by Subtropical Subsurface Water. However, the oceanography at Site 5 was much less complex than that at Site 4. Because of its location north of the Carlsberg Ridge, the representative sound speed profile at Site 5 (fig 2) closely resembled that for Site 3 below 700 m. However, above 700 m, the profile at Site 5 exhibited a bichannel structure similar to that for Site 4. Sound speed profiles in the vicinity of Site 4 frequently displayed perturbations at depths above 100 m that were caused by a temperature-salinity inversion at the bottom of the mixed layer. This inversion also is evident in much of the March-April data collected in the vicinity of Site 5 by the International Indian Ocean Expedition.

II.3 (U) ENVIRONMENTAL VARIABILITY AT EXERCISE SITES

(C) In the following sections, each major BEARING STAKE acoustic site (Sites 1A, 1B, 2, 3, 4, and 5) will be discussed separately in terms of sound speed and meteorological variability. Each section is introduced by a location chart that shows the positions of various acoustic receivers, and the KINGSPORT SUS and CW tows and lists the total elapsed time for each acoustic event. The location chart is followed by a time-series plot of sound speed profiles keyed to a time-series plot of wind speed, wind direction, sea height, and swell height. For the time series, daily sound speed profiles were chosen from data within 20 nmi (37 km) of the site. Wind speed, sea height, and swell height are presented every 4 hours, wind direction every 12 hours, based mainly on MYER data. Finally, each section contains one or more sound speed cross sections corresponding to KINGSPORT acoustic events. The bathymetric and sound speed data contained in each cross section are identical with those used to compute propagation losses along various acoustic tracks (discussed in chapter V). Table 2 lists all acoustic runs for which analyzed sound speed and bathymetric data are available.

(C) The temporal and spatial sound speed presentations in the following sections are annotated with the depth of the sonic layer (near-surface sound speed maximum) and the depth of the DSC axis (absolute sound speed minimum). Critical depth and 90 m conjugate depth are annotated only on Site 4 analytical figures (fig 16-19). At all other sites, propagation was bottom limited for both the near-surface (18-25 m) and subsurface (91-102 m) source. Critical depth is defined as that depth at which the maximum sound speed at the surface or in the near-surface layer recurs, and as such delimits the bottom of the DSC. Similarly, 90 m conjugate depth is defined as that depth at which the sound speed at 90 m recurs, and delineates the minimum depth necessary for refraction of downward rays from a 90 m source. Each time-series plot and cross section includes a sound speed profile overplot to a maximum depth of 3000 m which defines the total sound speed variability of each presentation.

TABLE II-2. (C) KINGSPORT ACOUSTIC TRACKS WITH ANALYZED SOUND SPEED AND BATHYMETRIC PROFILES. (U)

SITE	ACOUSTIC TRACK						
1A	P2	P7	S1	1A1			
1B	S1	P1	P5				
2	P1	S1	P3a	P3			
3	S1	S2	P2	P3	P4	3A2	
4	P1	S1	P2	P3	P4	P5	4A1
5	S1	P1	P5				

LEGEND: P = CW projector
S = SUS
A = Aircraft SUS
__ = Sound speed cross section contained herein

II.3.1 (U) SITE 1A VARIABILITY

(C) Figure 3 shows the location of Site 1A and the seven KINGSPORT acoustic tracks occupied there. In addition, this figure shows the location of KINGSPORT track 1A1 that was planned to correspond with an aircraft SUS track flown between 220914Z and 221103Z Jan 1977. Unfortunately, the actual aircraft track lay about 43 nmi (80 km) east of the KINGSPORT track. Site 1A was located east of the Gulf of Oman within the Oman Basin. As previously mentioned, this site is strongly influenced by warm, high-salinity Persian Gulf Intermediate Water with a core at 200-250 m. Figure 4 presents the Site 1A environmental summary. Sound speed perturbations above about 600 m shown in this figure reflect the effects of Persian Gulf Intermediate Water that apparently was sinking at Site 1A. A sonic layer 50-70 m deep was present at the site throughout most of the occupation. The exception was between 17 and 20 January when surface insolation masked the layer. During the 19-day occupation, the depth of the DSC oscillated between about 1600 and 1850 m with a sound speed variation at the axis of about 2.5 m/s. The greatest sound speed variability in the water column (about 10 m/s) occurred at 100 m, the approximate depth of the low-frequency CW source. Meteorological conditions were relatively stable at Site 1A, with wind speeds generally less than 10 m/s, sea heights less than 2 m, and swell heights less than 3 m. Two KINGSPORT tracks are presented as sound speed cross sections, event S1 (fig 5) and event 1A1 (fig 6). Both tracks had a sonic layer at about 50 m, and a DSC between about 1750 and 1950 m. Along the S1 track (fig 5), the Site 1A profile (KINGSPORT XBT 38) had substantially lower sound speeds than those farther to the northwest within the Gulf of Oman (because of the effects of Persian Gulf Intermediate Water). Sound speed variability along the 1A1 track (fig 6) was considerably greater than that along the S1 track, primarily because of mixing between Persian Gulf and Red Sea Intermediate Waters south of about 18°N.

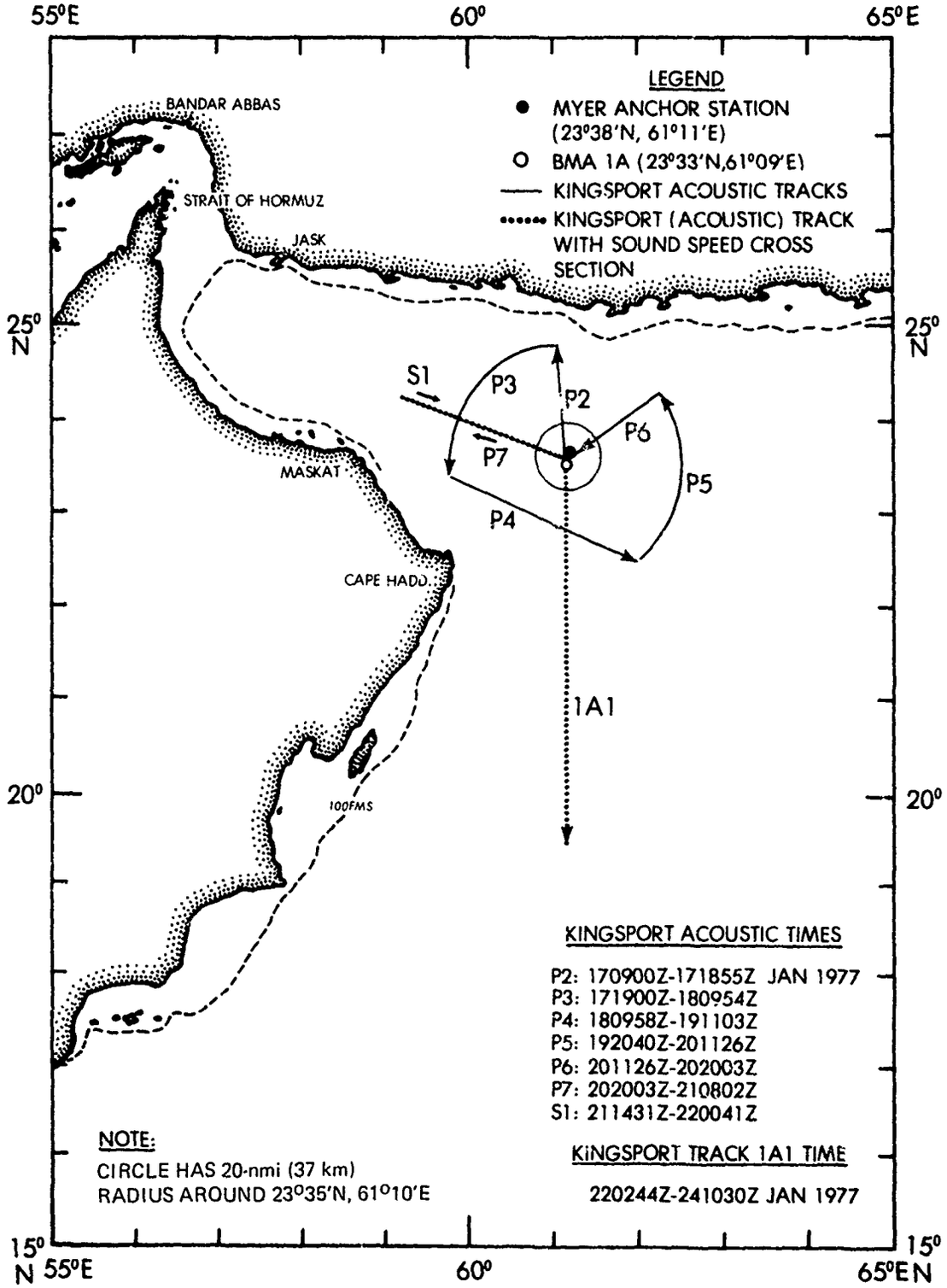

Figure II-3. (C) Site 1A location chart. (U)

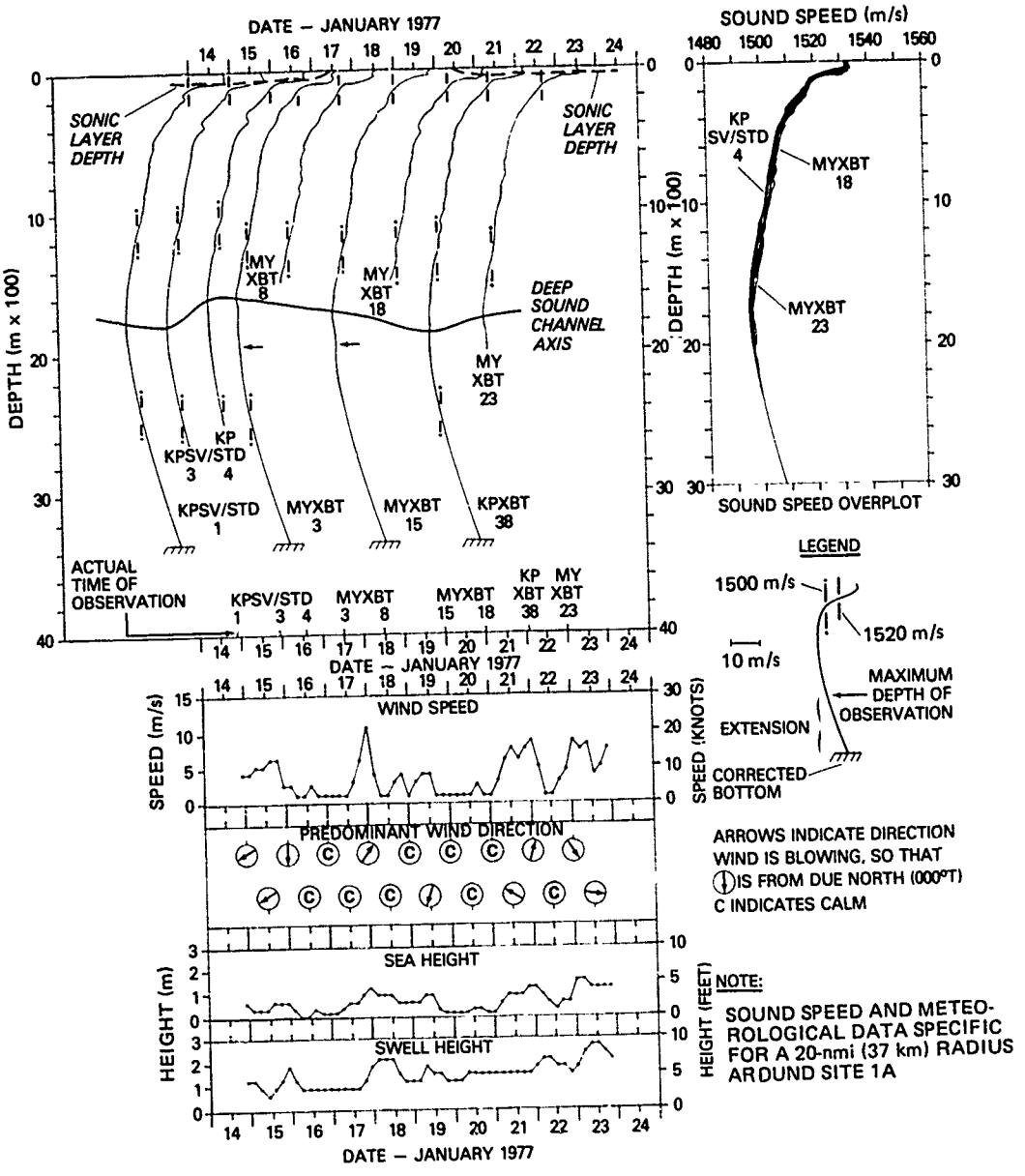

Figure II-4. (C) Environmental summary at Site 1A (14-24 January 1977. (U)

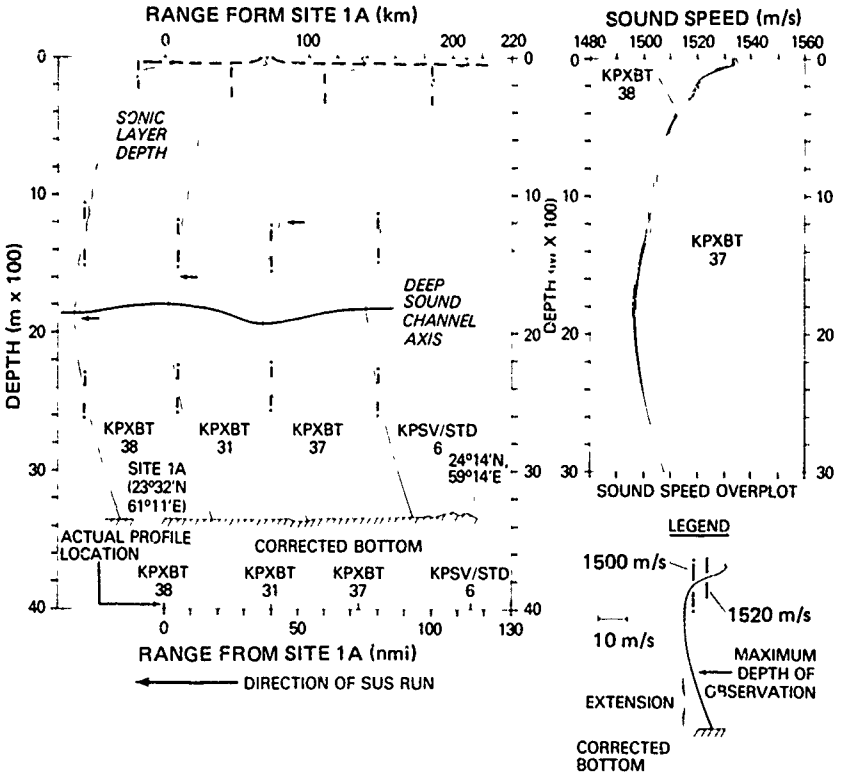

Figure II-5. (C) Sound speed structure along KINGSPORT S1 Track at Site 1A. (U)

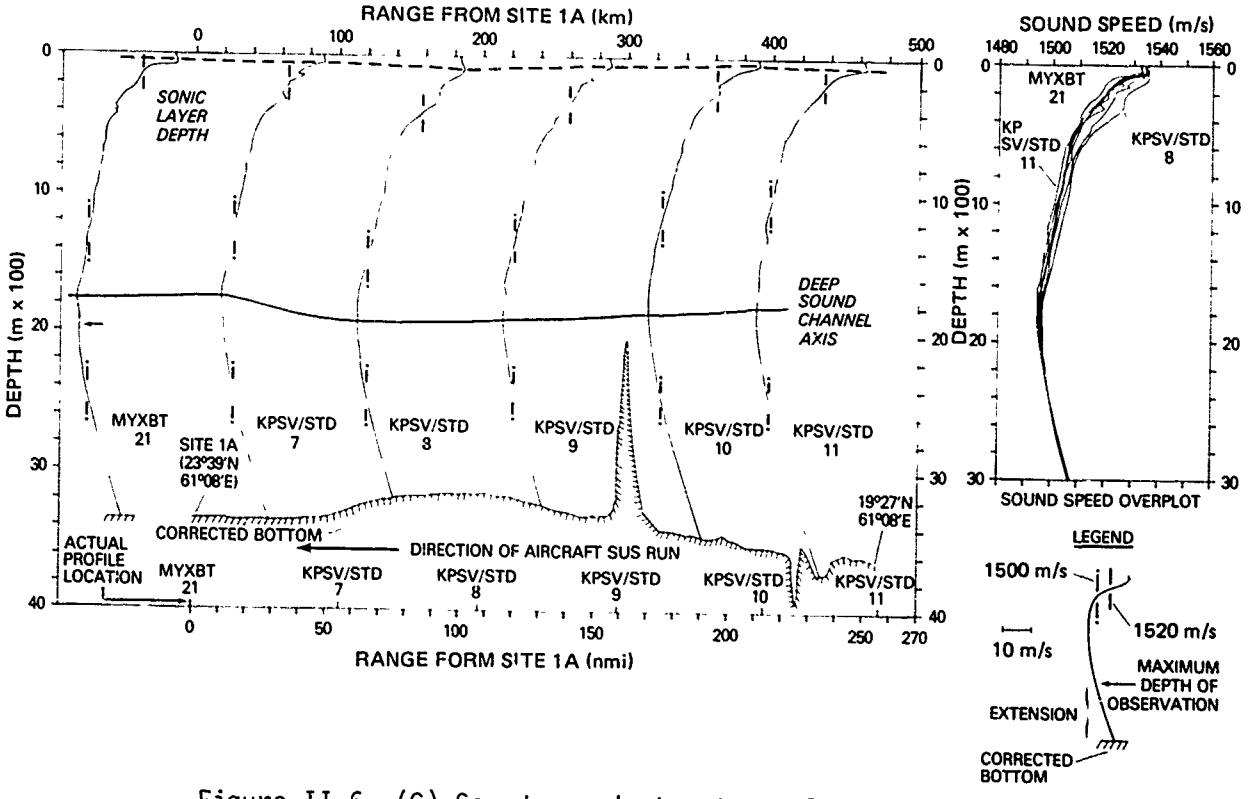

Figure II-6. (C) Sound speed structure along KINGSPORT 1A1 Track at Site 1A. (U)

II.3.2 (U) SITE 1B VARIABILITY

(C) Figure 7 shows the location of Site 1B and the six acoustic tracks occupied by KINGSPORT at this site. The BMA (Bottom-Mounted Array) at Site 1B was within 5 nmi (9 km) of that at Site 1A, but was implanted nearly one month later. The environmental summary for Site 1B is given in figure 8. Although Persian Gulf Intermediate Water was present at Site 1B, it did not cause sound speed perturbations in the upper water column. A sonic layer was absent during most of the Site 1B occupation, apparently because of surface insolation. The depth of the DSC varied between about 1580 and 1820 m over nine days with a sound speed change of less than 2 m/s. The greatest temporal variability (about 10 m/s) again occurred at 100 m, the approximate depth of the low-frequency source. Wind speed, sea height, and swell height gradually decreased during the occupation, but were moderate throughout. At depths less than 1800 m, the envelope of sound speed variability at Site 1B lay at lower sound speeds than that for site 1A (fig 4), with a maximum difference of about 5 m/s at 400 m depth. This probably was caused by increased upwelling during early February. Wind speeds and directions between 16 and 20 February were conducive to upwelling, and were far more persistent than those encountered at Site 1A (fig 4).

(C) Figure 9 shows a sound speed cross section along the KINGSPORT S1 track at Site 1B. This track was a replicate of the S1 track at Site 1A (fig 5), but extended approximately 40 nmi (75 km) further into the Gulf of Oman. On the last sound speed profile (KINGSPORT SV/STD 27), Persian Gulf Intermediate Water caused a distinct upper channel between 100 and 200 m. The profile at Site 1B (KINGSPORT SV/STD 26) had anomalously low speeds when compared to other profiles along the track, and was the lowest sound speed profile encountered at the site (fig 8). Largely because of this anomalous profile, sound speed at 400 m varied by 10.5 m/s along the S1 track. Most of this variation occurred in the first 57 nmi (105 km), and may have had some effect on acoustic propagation, even for a bottom-limited situation.

II.3.3 (U) SITE 3 VARIABILITY

(C) Figure 10 shows the location of Site 3 and the six KINGSPORT acoustic tracks run at this site. Also shown in figure 10 is the location of KINGSPORT track 3A2 that corresponds to an aircraft SUS event flown between 080850Z and 081021Z February 1977. Site 3 was located in the central Arabian Sea and was not influenced markedly by intrusive water masses. Persian Gulf Intermediate Water had no noticeable effects on sound speed at this site, and Red Sea Intermediate Water caused only minor perturbations between about 400 and 600 m. Subtropical Subsurface Water apparently was not present at Site 3. The environmental summary is presented as figure 11. A sonic layer was present during the first five days, but later was masked by surface insolation. The depth of the DSC remained quite constant (1720-1850 m) and the axis showed a sound speed variation of less than 2 m/s. The maximum variation in the water column occurred at about 100 m, and was only about 5 m/s. Overall, sound

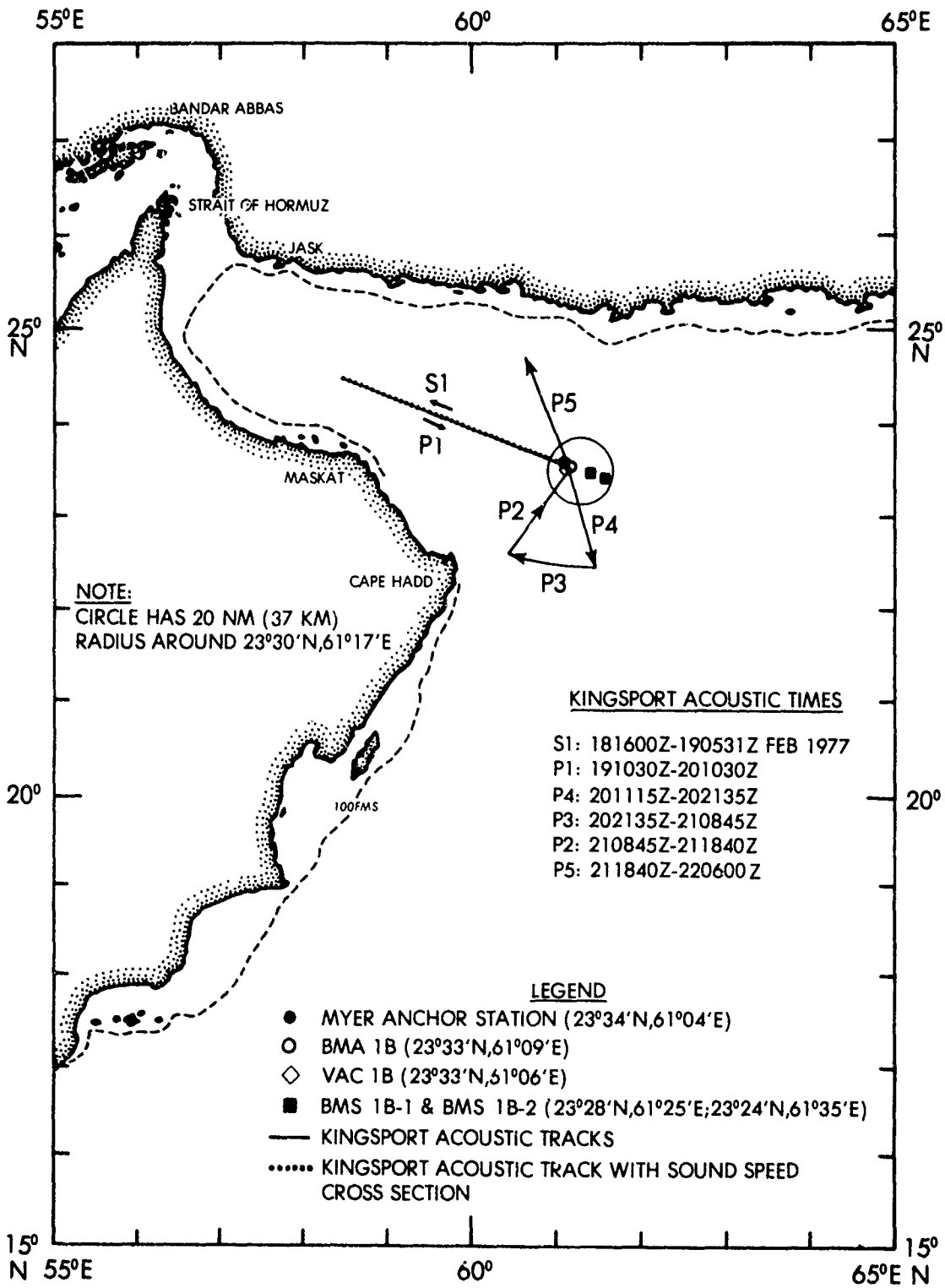

Figure II-7. (C) Site 1B location chart. (U)

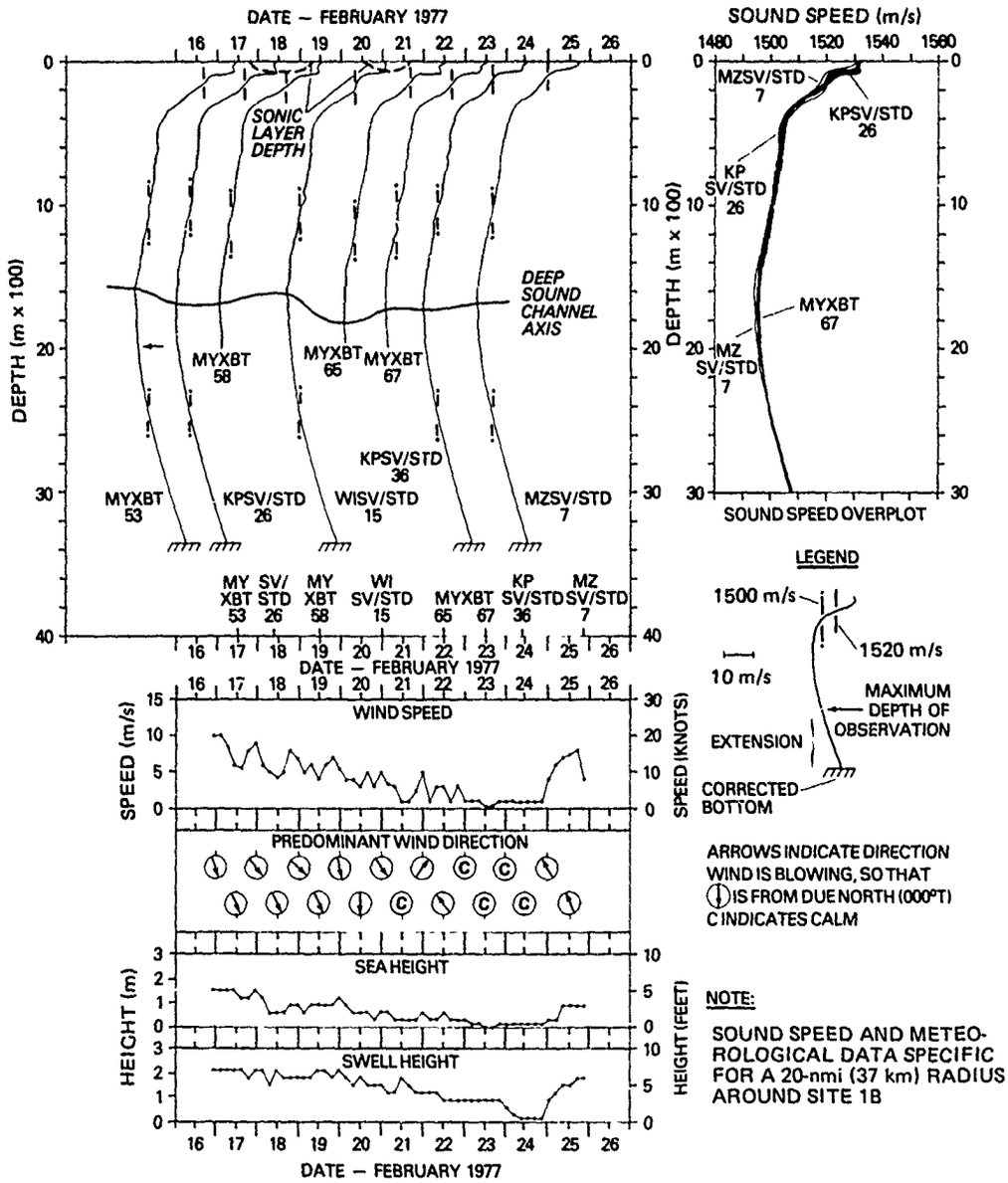

Figure II-8. (C) Environmental summary at Site 1B (1-16 February 1977). (U)

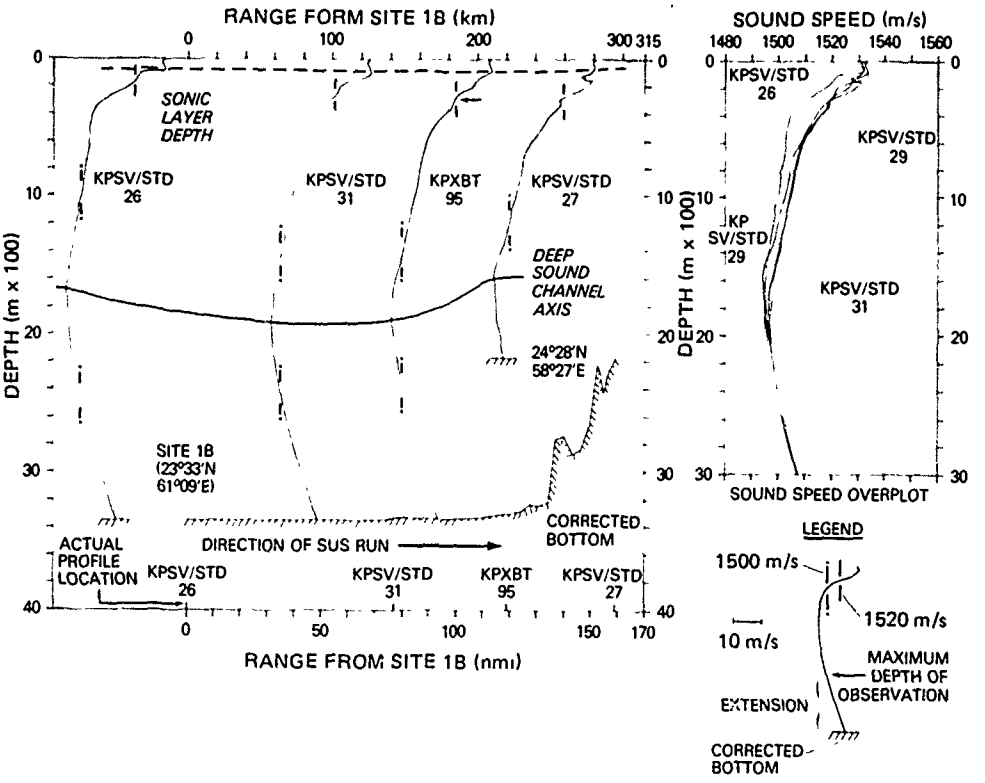

Figure II-9. (C) Sound speed structure along KINGSPORT S1 track at Site 1B. (U)

speed variability at Site 3 was less than at any other exercise site. Meteorological conditions were also very constant at Site 3. Wind speeds averaged about 5 m/s and were associated with sea and swell heights of less than 2 m. Three KINGSPORT tracks are presented as sound speed cross sections: Event P2 (fig 12), Event P4 (fig 13), and Event 3A2 (fig 14). A sonic layer generally was present along the P2 and 3A2 tracks but was absent along most of the P4 track. Overall, sound speed variability was the least along the P2 track and the greatest along the 3A2 track. Along all three tracks, variability was greatest at about 100 m, the approximate depth of the low-frequency CW source.

II.3.4 (U) SITE 4 VARIABILITY

(C) Figure 15 shows the location of Site 4 and the seven acoustic runs made there by KINGSPORT. The figure also shows the location of the KINGSPORT 4A1 track that corresponds to an aircraft SUS flight made between 200611Z and 200756Z March 1977. Site 4 was located on the edge of the Chain Ridge, with acoustic runs oriented across the Somali Basin. The oceanography at Site 4 was the most complex encountered during BEARING STAKE because of the mixing of several intrusive water masses. The water masses and their approximate core depths were as follows:

Cool, low salinity Subtropical Subsurface Water, 400-500 m

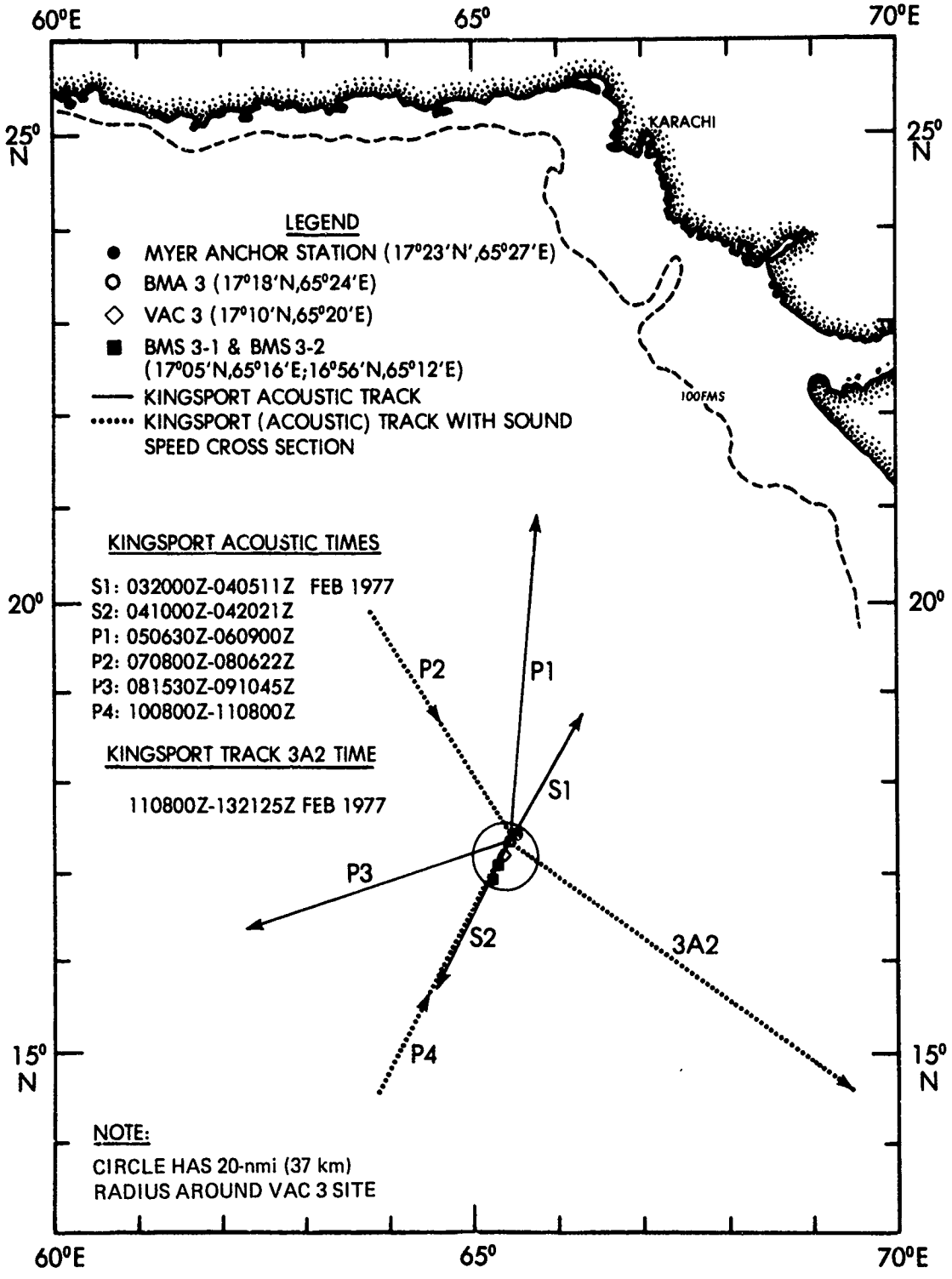

Figure II-10. (C) Site 3 location chart. (U)

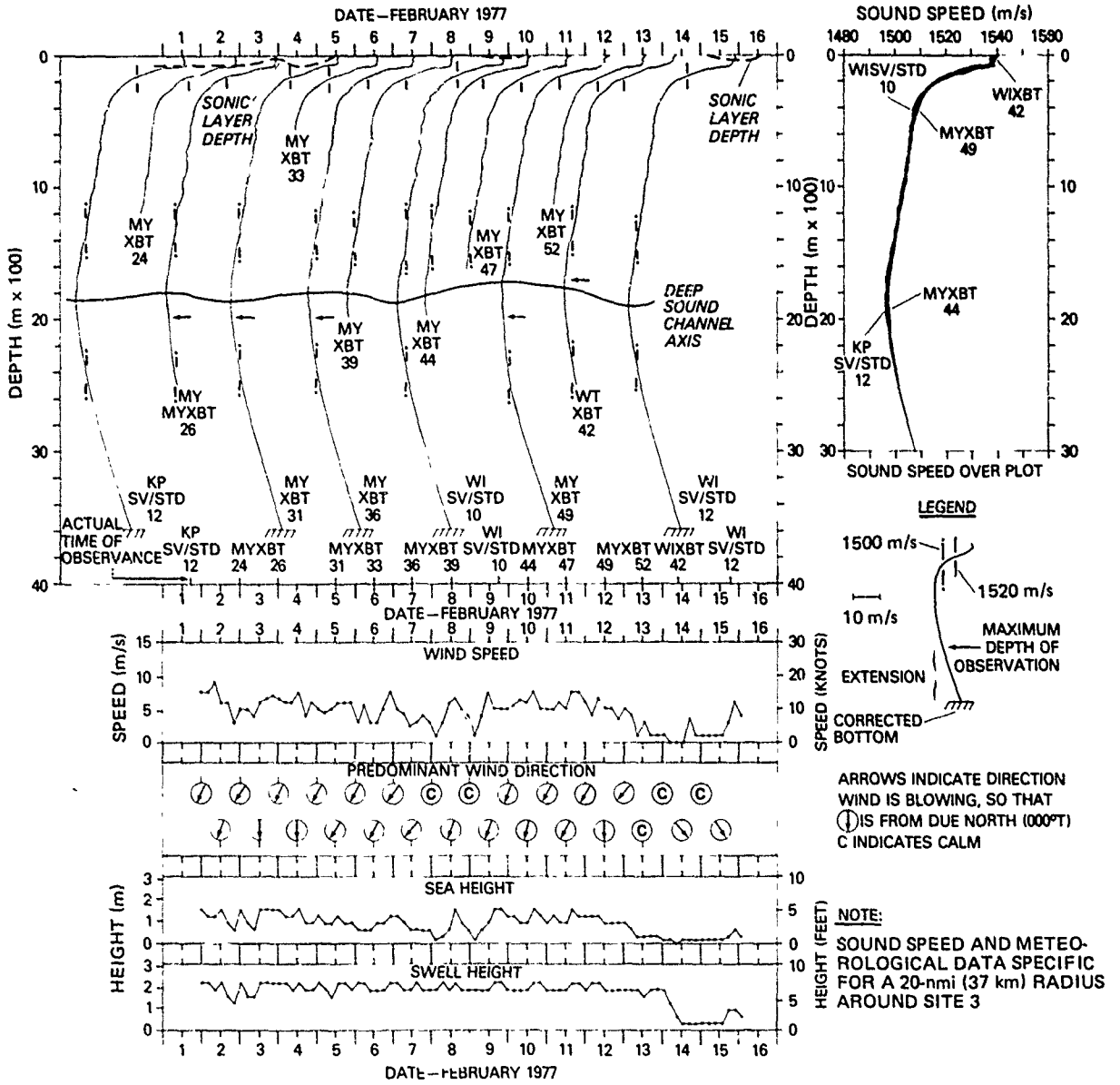

Figure II-11. (C) Environmental summary at Site 3 (1-16 February 1977). (U)

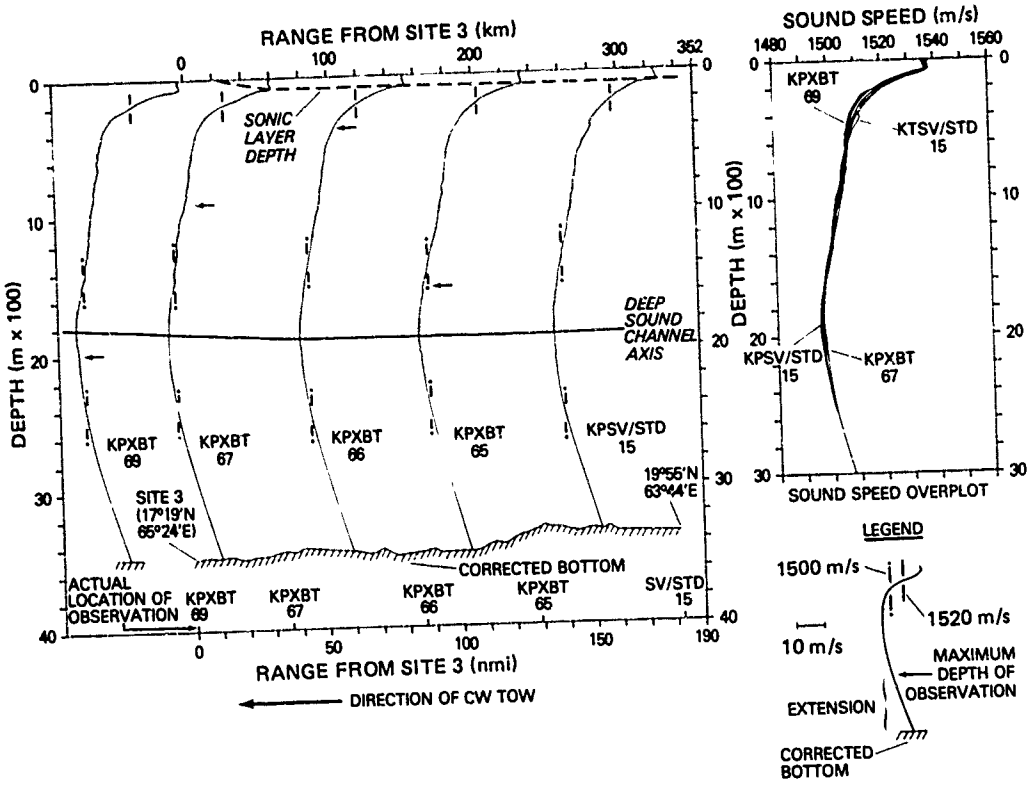

Figure II-12. (C) Sound speed structure along KINGSPORT P2 track at Site 3. (U)

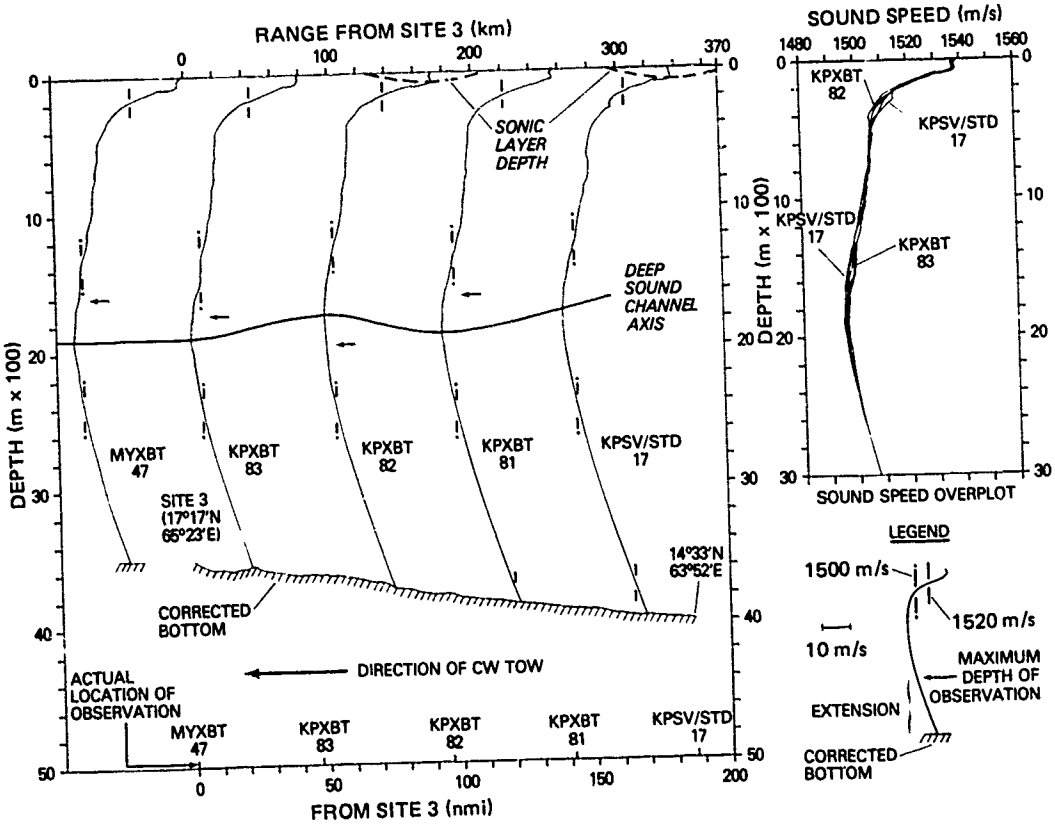

Figure II-13. (C) Sound speed structure along GSPORT P4 track at Site 3. (U)

Cool, low salinity Subtropical Subsurface Water, 400-500 m

Warm, high salinity Red Sea Intermediate Water, 600-900 m

Cold, low salinity Antarctic Intermediate Water, 700-800 m

Cold, low salinity Banda Intermediate Water, 900-1000 m.

Details on the distribution and characteristics of each water mass are given by Fenner and Bucca (1972b).

(C) The environmental summary for site 4 is given in figure 16. Throughout the occupation, sound speed profiles displayed extremely variable microstructure between about 300 and 1800 m. As previously mentioned, this microstructure was caused by intermixing of the four intrusive water masses listed above and by sinking of Red Sea Intermediate Water as a result of this intermixing. A sporadic layer frequently was present but was not a permanent feature at Site 4. Over 16 days, the depth of the DSC lay between 1600 and 1850 m, with a sound speed variability of 3-4 m/s. At 100 m, the approximate depth of the low-frequency CW source, sound speed varied by more than 17 m/s, the greatest variability encountered at any exercise site. Even though the corrected bottom depth at Site 4 was 5109 m, the site was effectively bottom limited throughout the occupation. Before March, 90 m conjugate depth was less than 200 m shallower than the bottom. However, between 17 and 21 March, 90 m conjugate depth shoaled to a level about 700 m above the bottom. This should have provided enough depth excess to assure some refraction of downward rays from the low-frequency source. The rapid change in 90 m conjugate depth was caused by a cooling of the main thermocline that also resulted in a change of shape of the sound speed profile above a depth of about 200 m. Wind speeds at Site 4 averaged 5 m/s, accompanied by approximately 1 m seas and 2 m swells.

(C) Sound speed cross sections along three KINGSPORT tracks are given in figure 17 (P1 track), figure 18 (P5 track), and figure 19 (4A1 track). Sound speed profiles along all three tracks were extremely irregular because of the persistent presence of Red Sea Intermediate Water. The bottom depth along all three tracks was a minimum of 200 m deeper than 90 m conjugate depth, allowing for some refraction of downward rays from the low-frequency source. However, all three tracks were basically bottom limited in respect to the high- and medium-frequency sources (nominal depth of 18 m). Generally, the greatest sound speed variability along the P1, P5, and A1 tracks (17-19 m/s) occurred at about 150 m, below the nominal depth of the low frequency source. A sonic layer occurred only along the 4A1 track (fig 19), but was relatively shallow (20-30 m) and ill defined. Along the 4A1 track, sound speed profiles were even more complex than at Site 4 itself, particularly at the northern end of the track, where Red Sea Intermediate Water was being rapidly diluted by

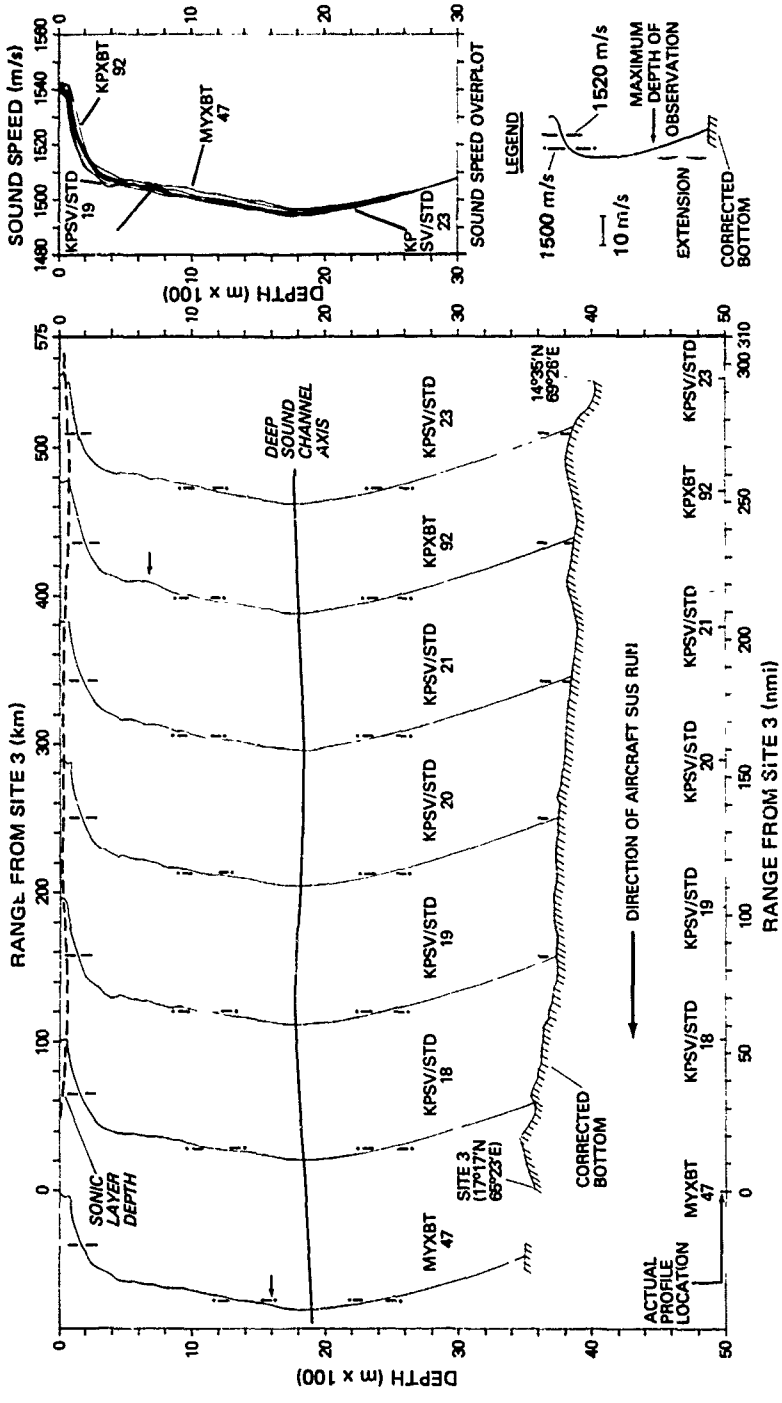

Figure II-14. (C) Sound speed structure along KINGSPORT 3A2 track at Site 3. (U)

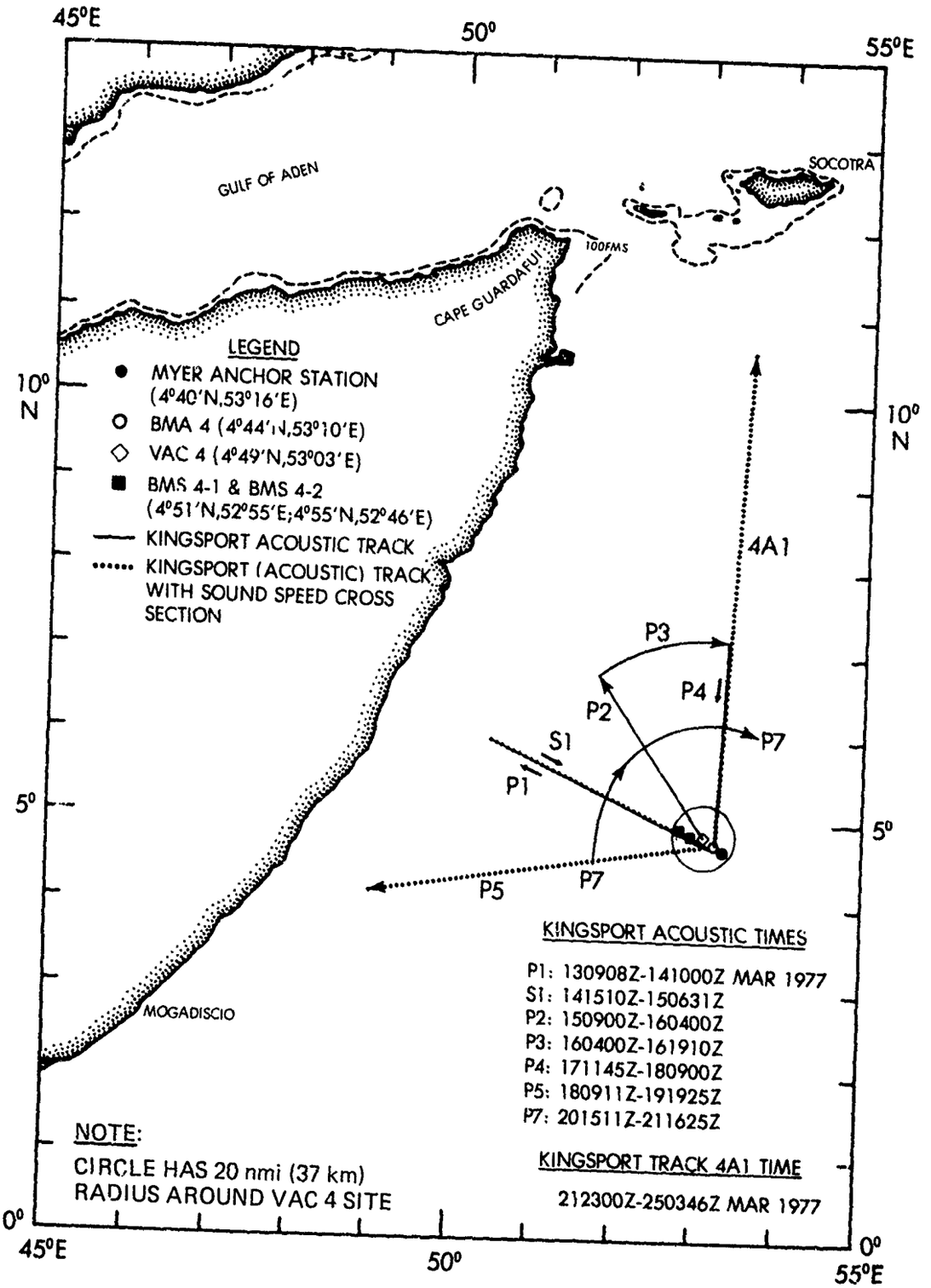

Figure II-15. (C) Site 4 location chart. (U)

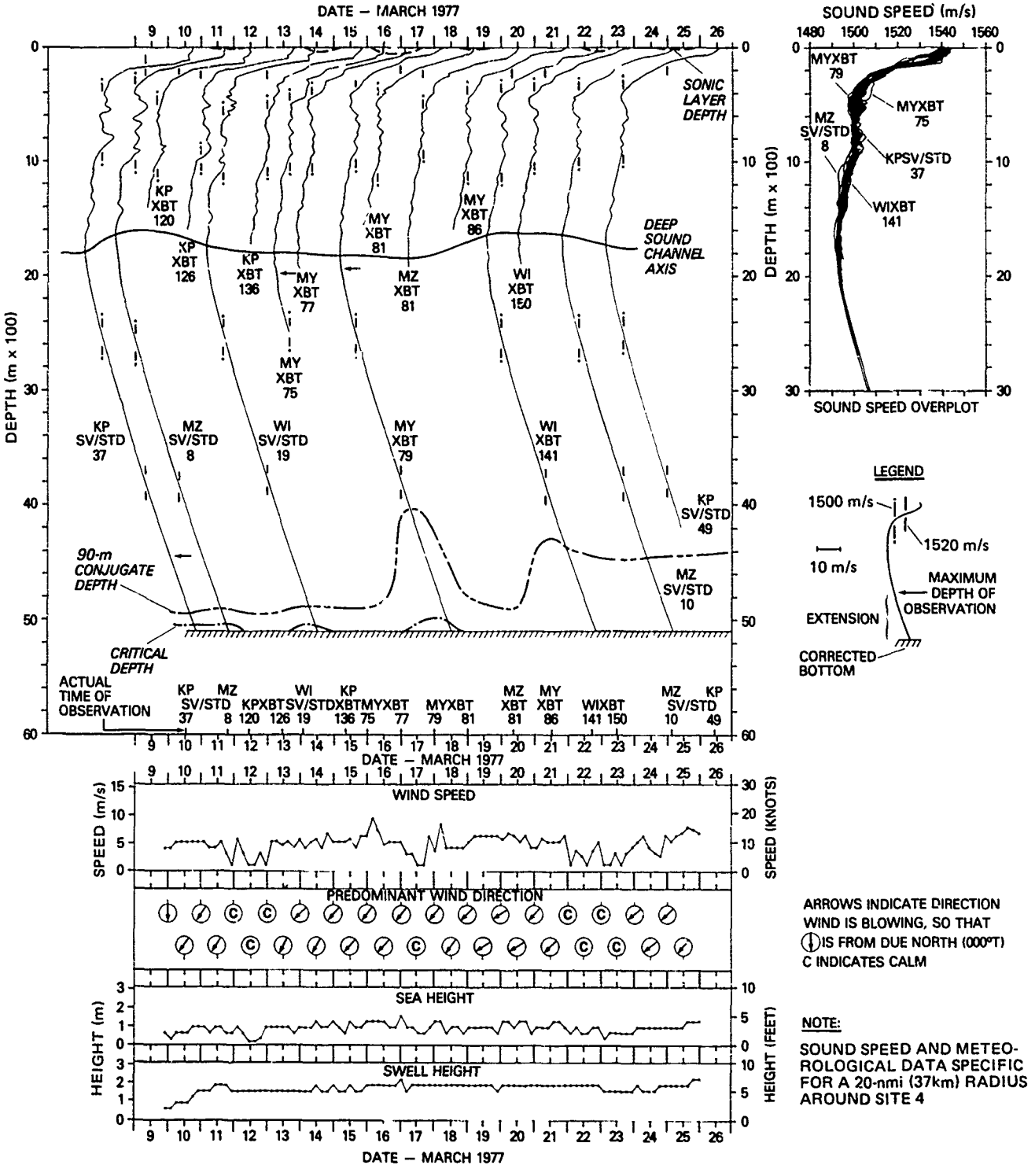

ARROWS INDICATE DIRECTION WIND IS BLOWING, SO THAT ⊕ IS FROM DUE NORTH (000°T)
C INDICATES CALM

NOTE:
SOUND SPEED AND METEOROLOGICAL DATA SPECIFIC FOR A 20-nmi (37km) RADIUS AROUND SITE 4

Figure II-16. (C) Environmental summary at Site 4 (9-26 March 1977). (U)

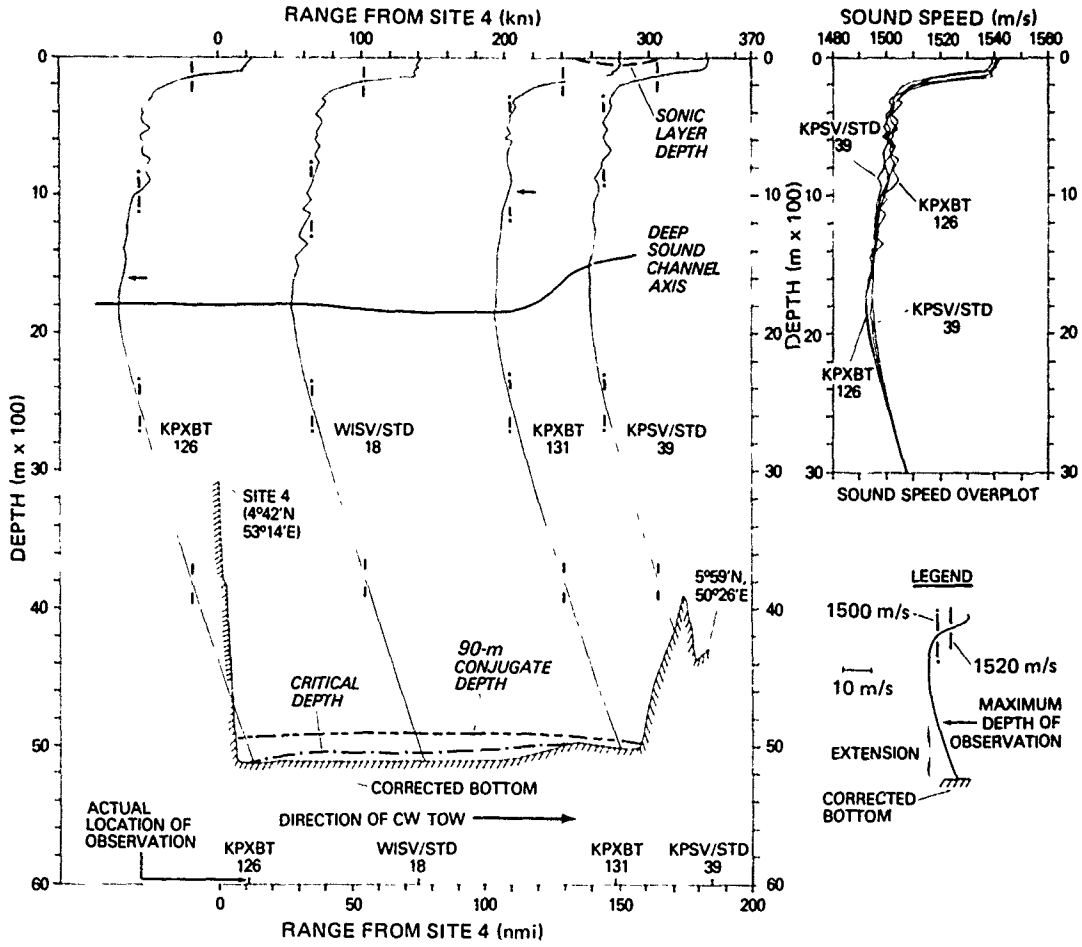

Figure II-17. (C) Sound speed structure along KINGSPORT P1 track at Site 4. (U)

mixing with other intrusive water masses. DSC structure along the 4A1 track was more variable than that at the site or that along the P1 and P5 tracks.

II.3.5 (U) SITE 5 VARIABILITY

(C) Figure 20 shows the location of Site 5, the five KINGSPORT acoustic tracks run there, and generalized operational areas for DIAMANTINA (Site 5A) and MIZAR (Site 5B). Site 5 lay at the southern edge of the Arabian Basin on the flanks of the Carlsberg Ridge, and, as previously mentioned, was under the influence of a strong, preferential flow of Red Sea Intermediate Water. The environmental summary for Site 5 is presented in figure 21. Unfortunately, only one good SV/STD was available at Site 5, and the majority of XBTs dropped within 20 nmi (37 km) of the site failed at depths shallower than the DSC. All sound speed profiles shown in figure 21 displayed a sound speed minimum at about 400-m depth associated with Subtropical Subsurface Water. Two of the profiles (KINGSPORT SV/STD 50 and MYER XBT 100) showed a significant sound speed perturbation at the top of the permanent thermocline (30-100 m). A

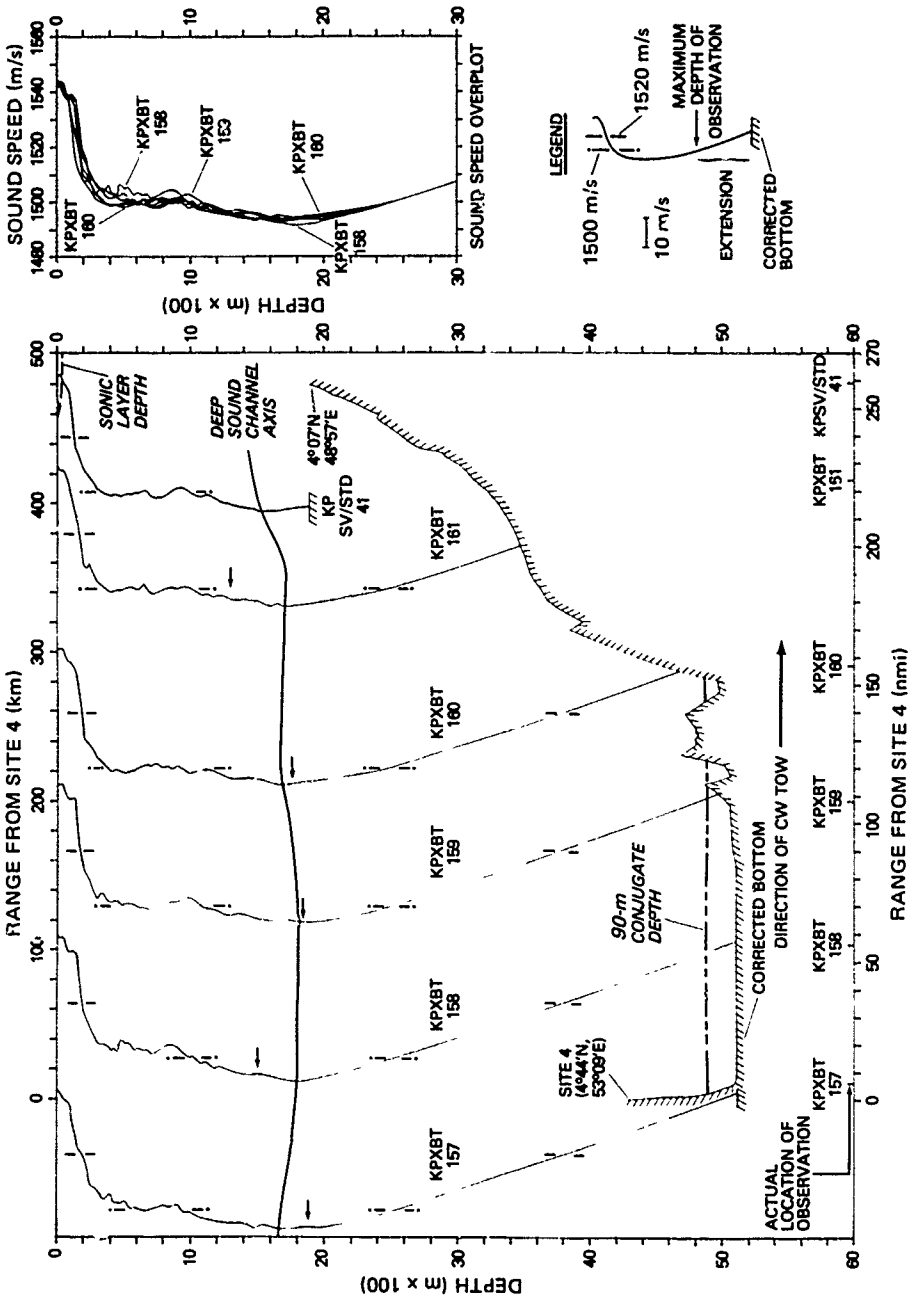

Figure II-18. (C) Sound speed structure along KINGSPORT P5 track at Site 4. (U)

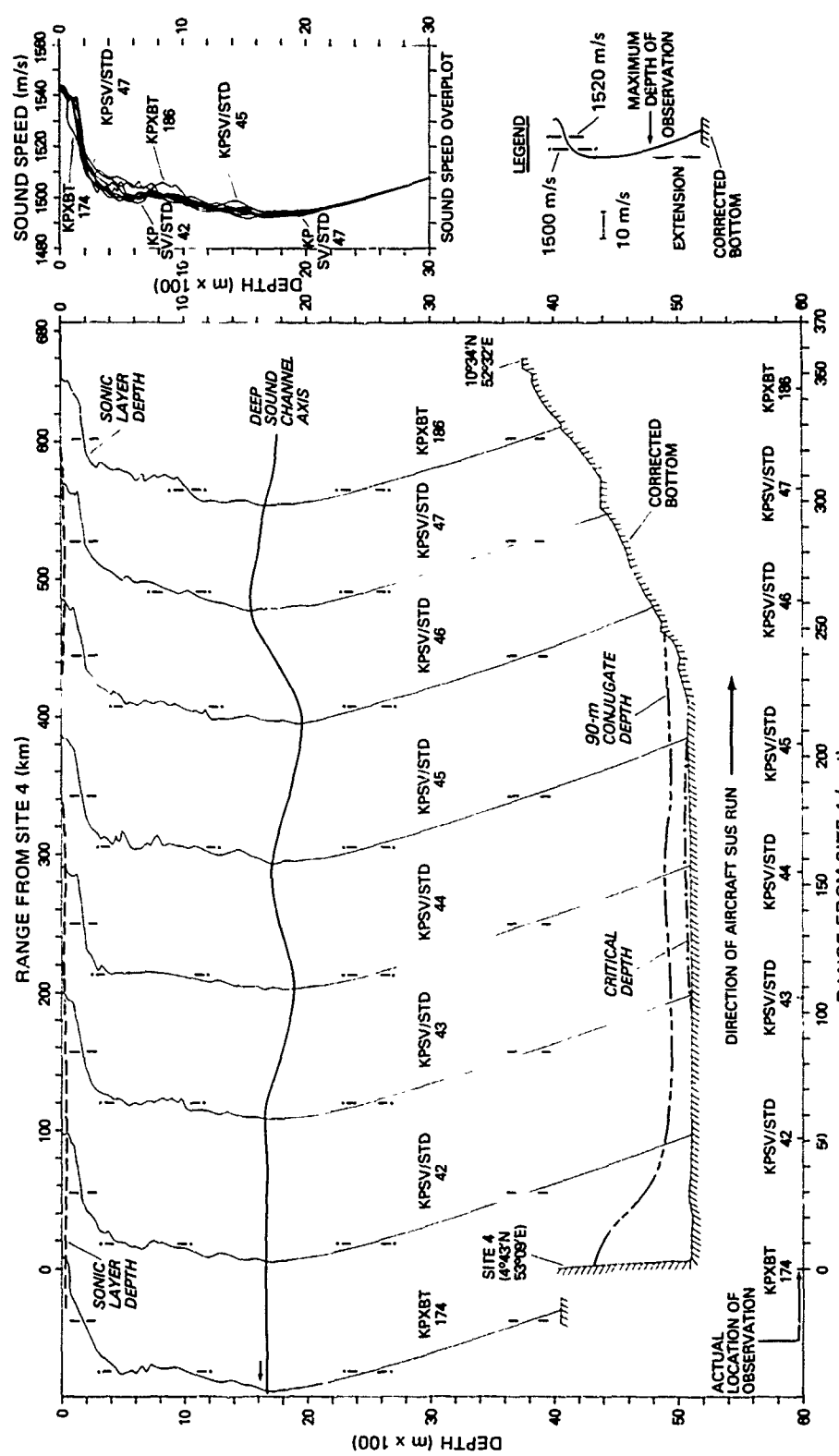

Figure II-19. (C) Sound speed structure along KINGSPORT 4A1 track at Site 4. (U)

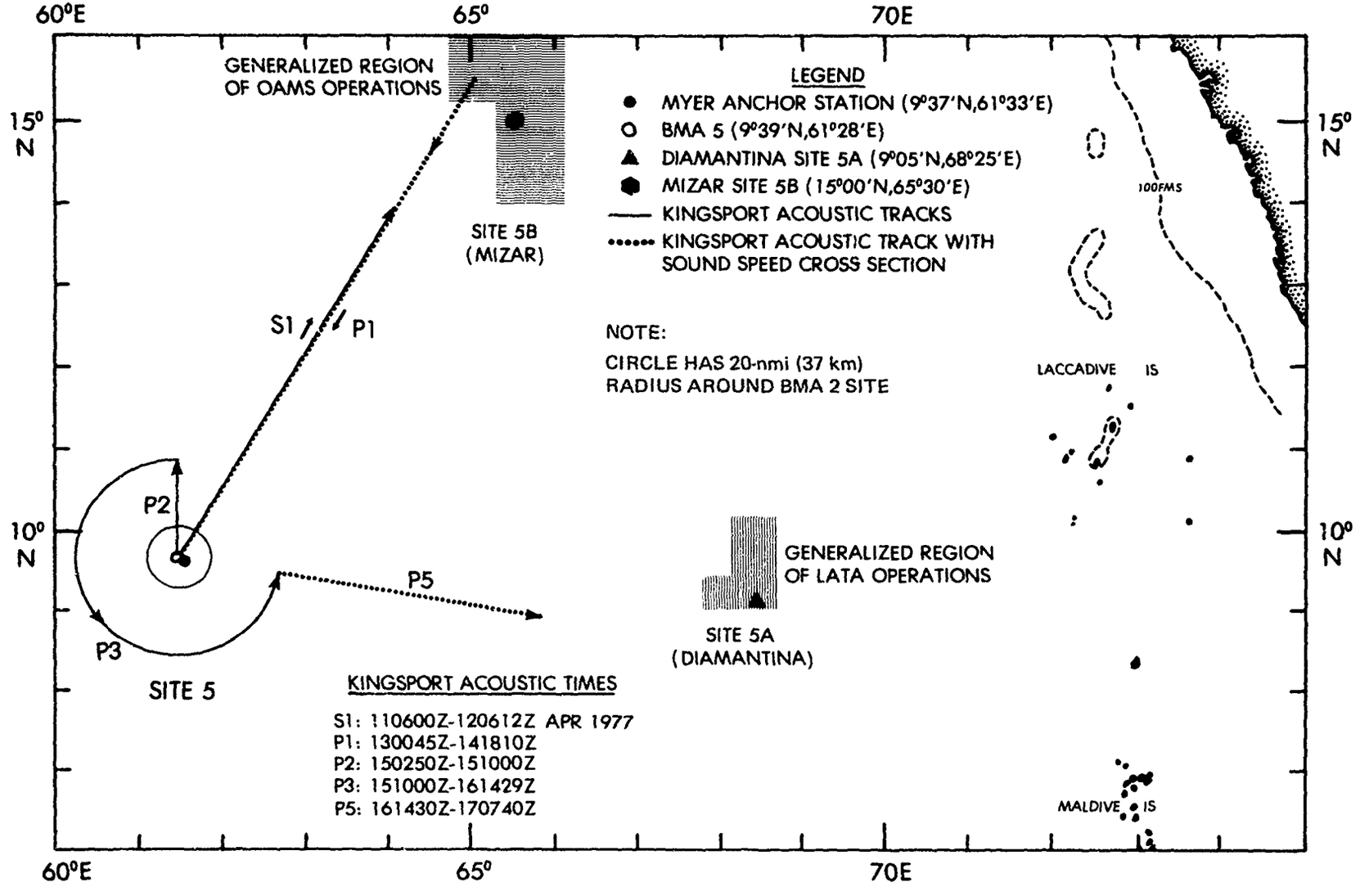

Figure II-20. (C) Site 5 location chart. (U)

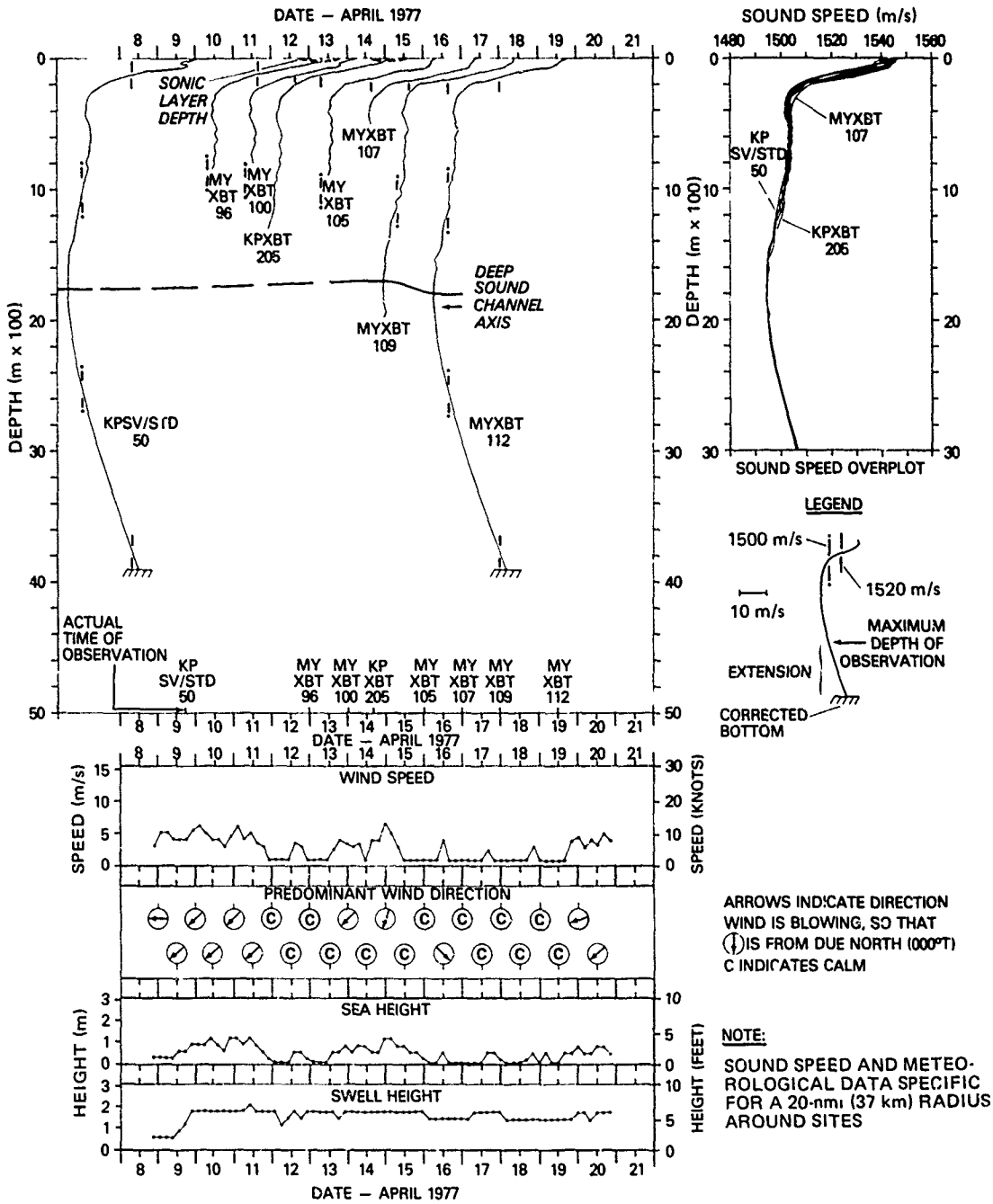

Figure II-21. (C) Environmental summary at Site 5 (8-21 April 1977). (U)

similar structure was encountered sporadically along most Site 5 acoustic tracks (e.g., fig 22 and 23). A sonic layer was not persistently present at Site 5, and the greatest sound speed variability in the water column (about 15 m/s) occurred at about 150 m, below the depth of the low-frequency source. Meteorological conditions were moderate throughout the 12-day occupation of Site 5, with wind speeds less than 6 m/s, sea heights generally less than 1 m, and swell heights averaging less than 2 m. Sound speed variability was considerably greater along the P1 track (fig 22) because of its orientation to the northeast across preferential flows of Red Sea Intermediate and Subtropical Subsurface Waters. Along this track, sound speed varied by a maximum of about 13 m/s at a depth of 150 m. A shallow sonic layer was present along much of the P1 track but was generally absent along the P5 track (fig 23). DSC structure along both tracks is speculative, since most of the XBTs failed at depths shallower than 1500 m.

II.3.6 (U) SITE 2 VARIABILITY

(C) Figure 24 shows the location of Site 2, the five KINGSPORT acoustic tracks occupied there, and generalized operational areas for MIZAR (Site 2A) and DIAMANTINA (Site 2B). Site 2 lay on the Owen Ridge in direct line with the mouth of the Gulf of Aden. This site was influenced by warm, high salinity Persian Gulf and Red Sea Intermediate Waters. However, neither water mass caused meaningful sound channels at Site 2, only microstructure. The environmental summary for this site is presented in figure 25. Unfortunately, no reliable SV/STD data were collected during the Site 2 occupation. Based on MYER XBT data, sound speed variability at site 2 was less than that at other exercise sites (except Site 3). A maximum variation of about 5 m/s occurred between 100 and 150 m, below the depth of the low-frequency source. A sonic layer was absent at Site 2 throughout the 9-day occupation. The DSC lay between 1720 and 1900 m and displayed a variability of less than 2 m/s. Winds were generally calm at Site 2, resulting in wave heights less than 1 m superimposed on about 2 m swells. Sound speed cross sections along the P1 and P3 tracks are presented in figures 26 and 27, respectively. A persistent sonic layer occurred along the P1 track but was absent along the P3 track. Far more sound speed variability occurred along the P3, track where a maximum variation of about 10 m/s was found at about 300 m. Due to XBT failures, data spacing along the P3 track was far from adequate and the DSC along both tracks is speculative.

II.4 (U) COMPARISON OF REPRESENTATIVE EXERCISE AND HISTORICAL SOUND SPEED DATA

(C) Representative BEARING STAKE sound speed profiles and their associated temperature-salinity diagrams have been illustrated previously in figure 2. The representative profiles were derived from the time-series plots of sound speed presented in the environmental summaries for each site and

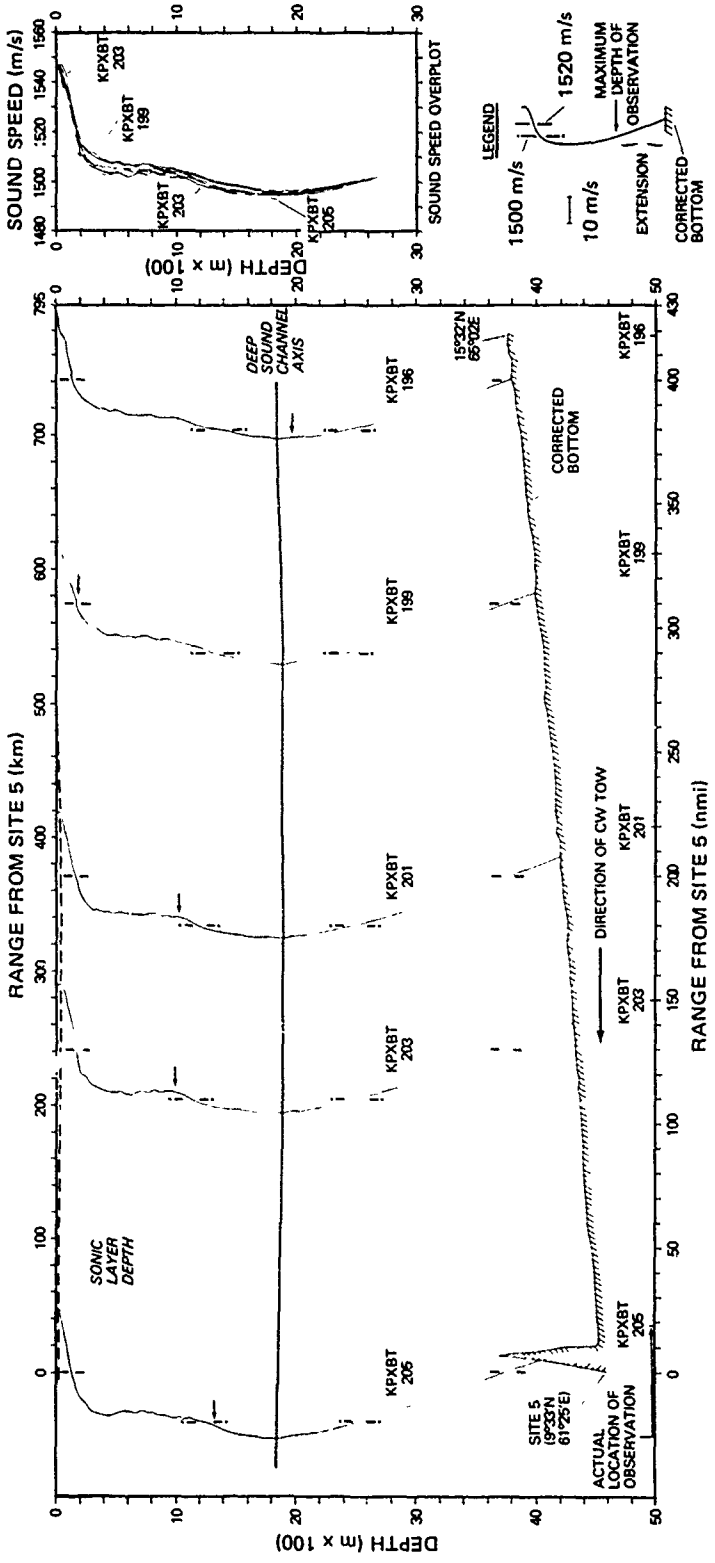

Figure II-22. (C) Sound speed structure along KINGSPORT P1 track at Site 5. (U)

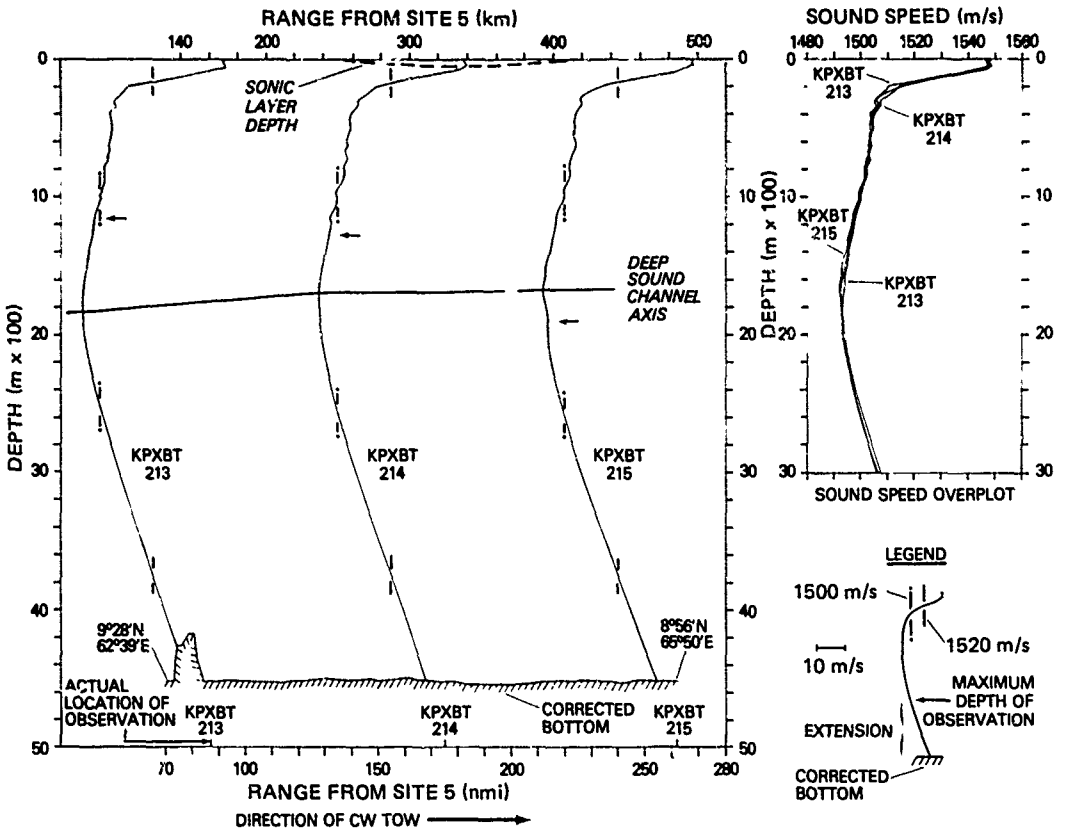

Figure II-23. (C) Sound speed structure along KINGSPORT P5 track at Site 5. (U)

generally are near-modal profiles. For all sites except Site 2, the representative sound speed profiles are based upon SV/STD data so as not to incorporate XBT inaccuracies. In the following sections, the profiles are compared with typical December-February or March-May profiles from the Indian Ocean sound speed provinces shown in figure 1 (after Colborn, 1976) and representative southwest monsoon profiles derived by the authors from historical International Indian Ocean Expedition data. Colborn's typical sound speed province profiles and the representative profiles for the southwest monsoon both are based on Nansen cast data and therefore do not show the same degree of microstructure found in exercise SV/STD data.

II.4.1 (C) NORTHEAST MONSOON

(C) Figure 28 compares representative BEARING STAKE and typical historical sound speed profiles for the same time period at each exercise site. According to Colborn's analyses, the northeast monsoon extends from December through February and is followed by a transitional season (March - May) prior to the southwest monsoon. Therefore, sites 1A, 1B, and 3 are compared with a typical northeast monsoon profile; sites 4, 5, and 2 with typical transitional season profiles. The site 1A and 1B exercise profiles varied significantly from

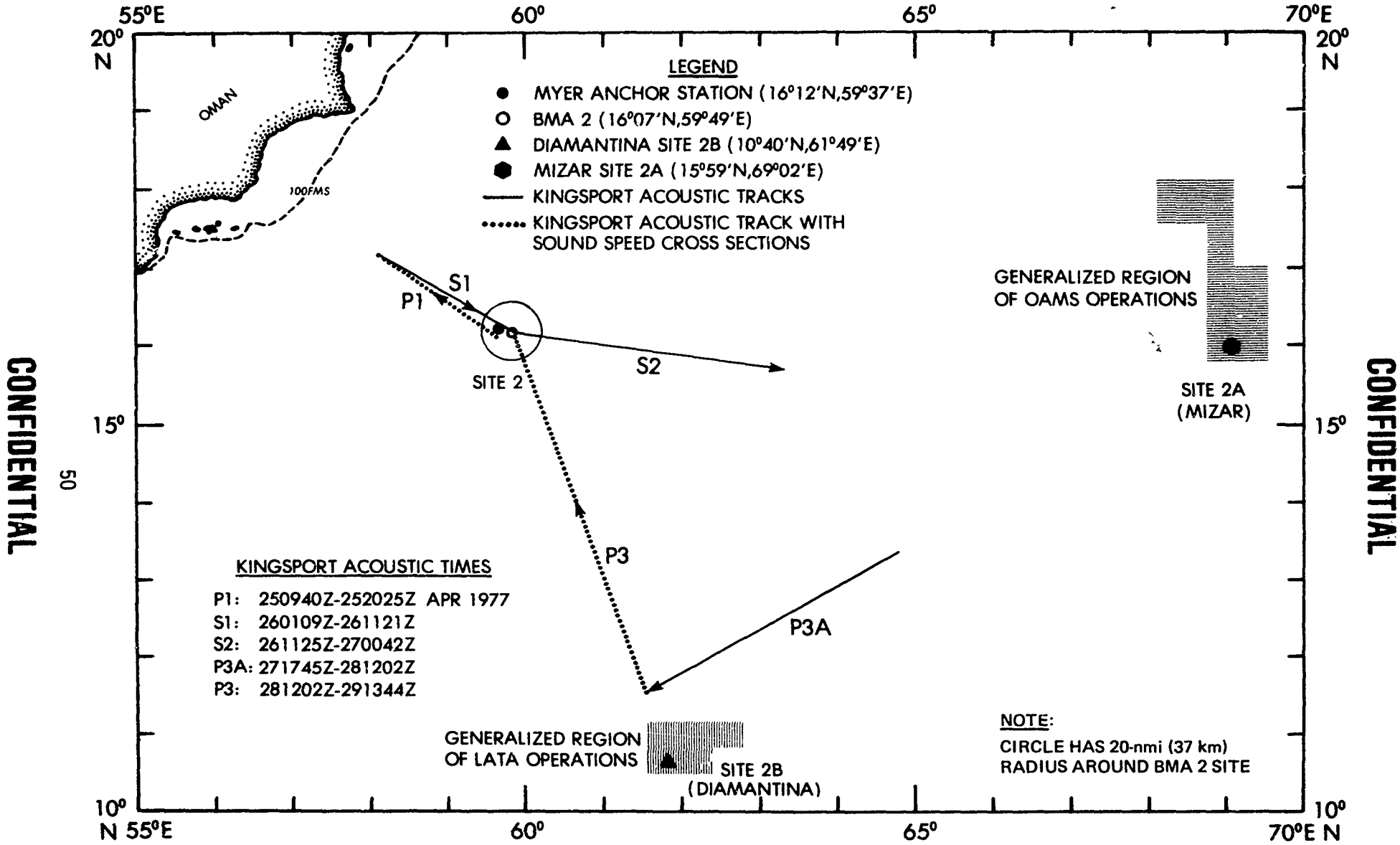

Figure II-24. (C) Site 2 location chart. (U)

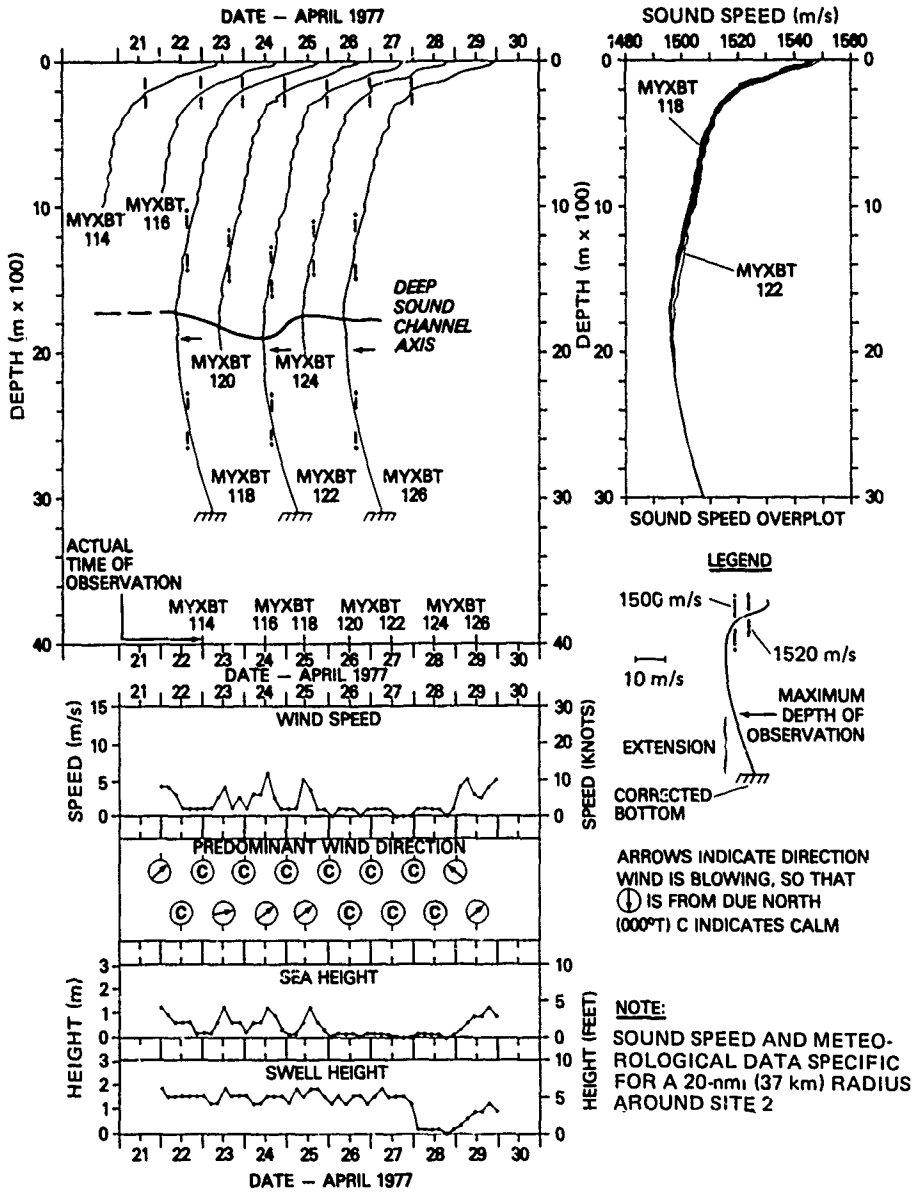

Figure II-25. (C) Environmental summary at Site 2 (21-30 April 1977). (U)

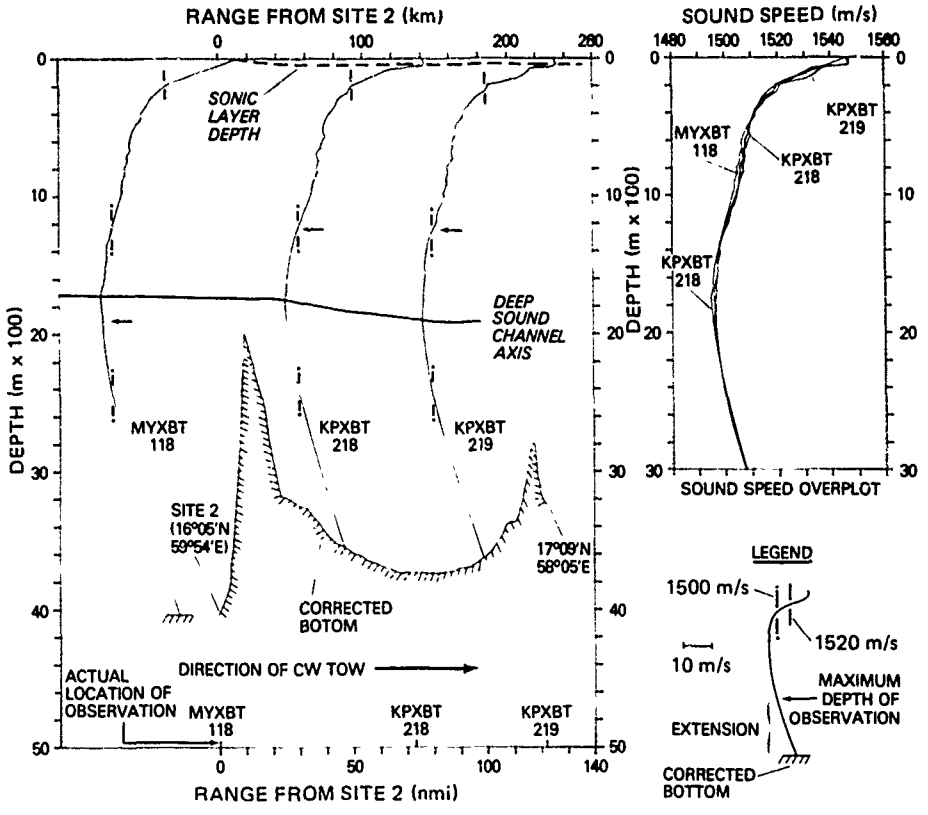

Figure II-26. (C) Sound speed structure along KINGSPORT P1 track at Site 2. (U)

Colburn's typical northeast monsoon profiles at depths above about 1400 m. For both sites, the representative profiles lay at lower sound speeds than those shown by Colborn, with maximum differences of about 7 m/s at the surface and about 4 m/s at 400 m. At Site 3, the representative exercise profile was similar to Colborn's typical profile in the near-surface layer, up to 5 m/s higher than Colborn's data between 200 and 800 m, and slightly lower than the typical northeast monsoon profile between 800 and 2600 m. However, below 800 m, sound speed gradients for historical and exercise profiles were nearly identical. At Site 4, the historical profile lacked the marked microstructure evident in exercise data, and generally represented a lesser concentration of Red Sea Intermediate Water (i.e., lesser sound speeds) between about 500 and 1600 m. Above about 200 m, however, the two profiles were practically identical. At Site 5, Colborn's profile for the transitional season lacked both the sound speed perturbation in the near-surface layer and the upper sound channel (sound speed minimum at 500 m, maximum at 700 m). At Site 2, Colburn's data were quite similar to the representative exercise profile except above 100 m, where exercise sound speeds were a maximum of 9 m/s lower than historical values.

(C) Since the exercise area was basically bottom limited, moderate variations between representative and typical Colborn sound speed profiles should

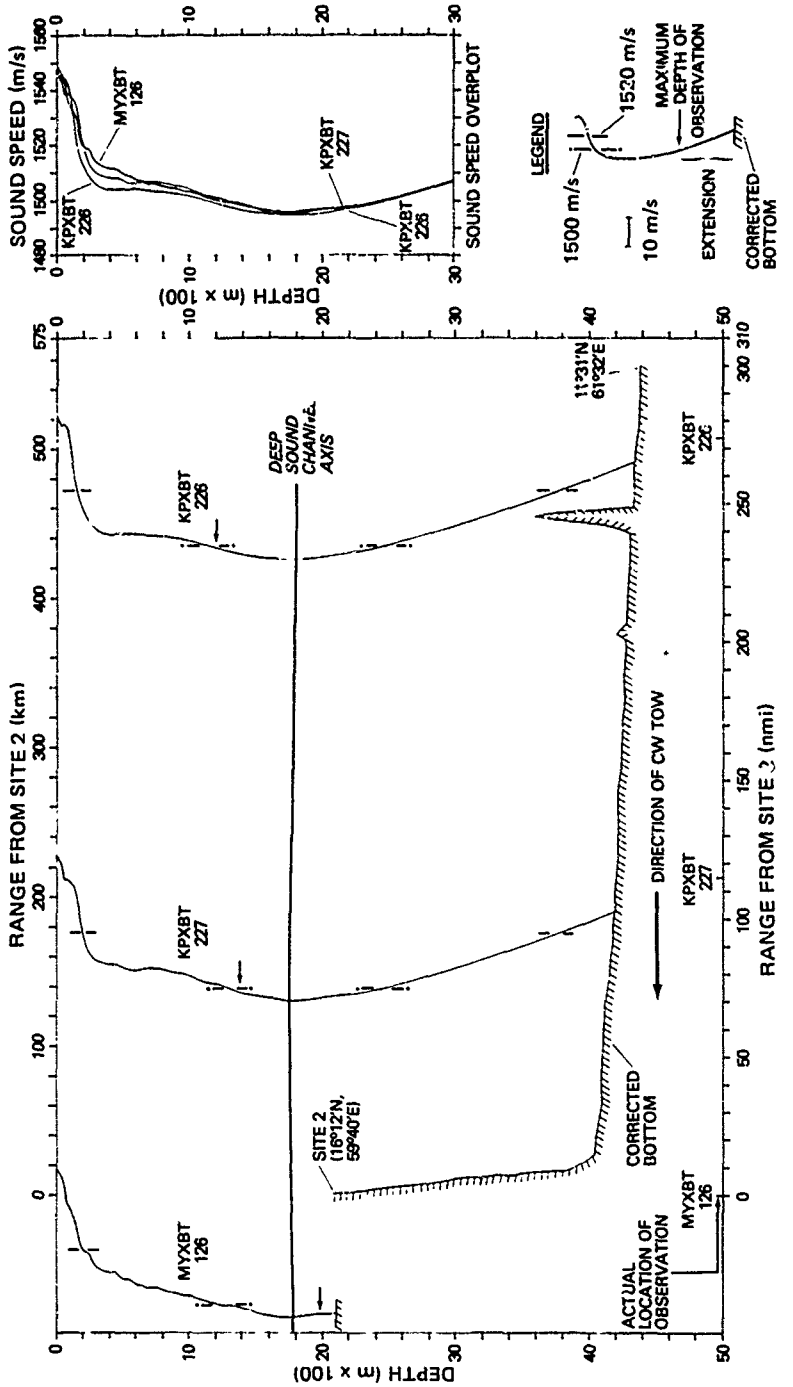

Figure II-27. (C) Sound speed structure along KINGSPORT P3 track at Site 2. (U)

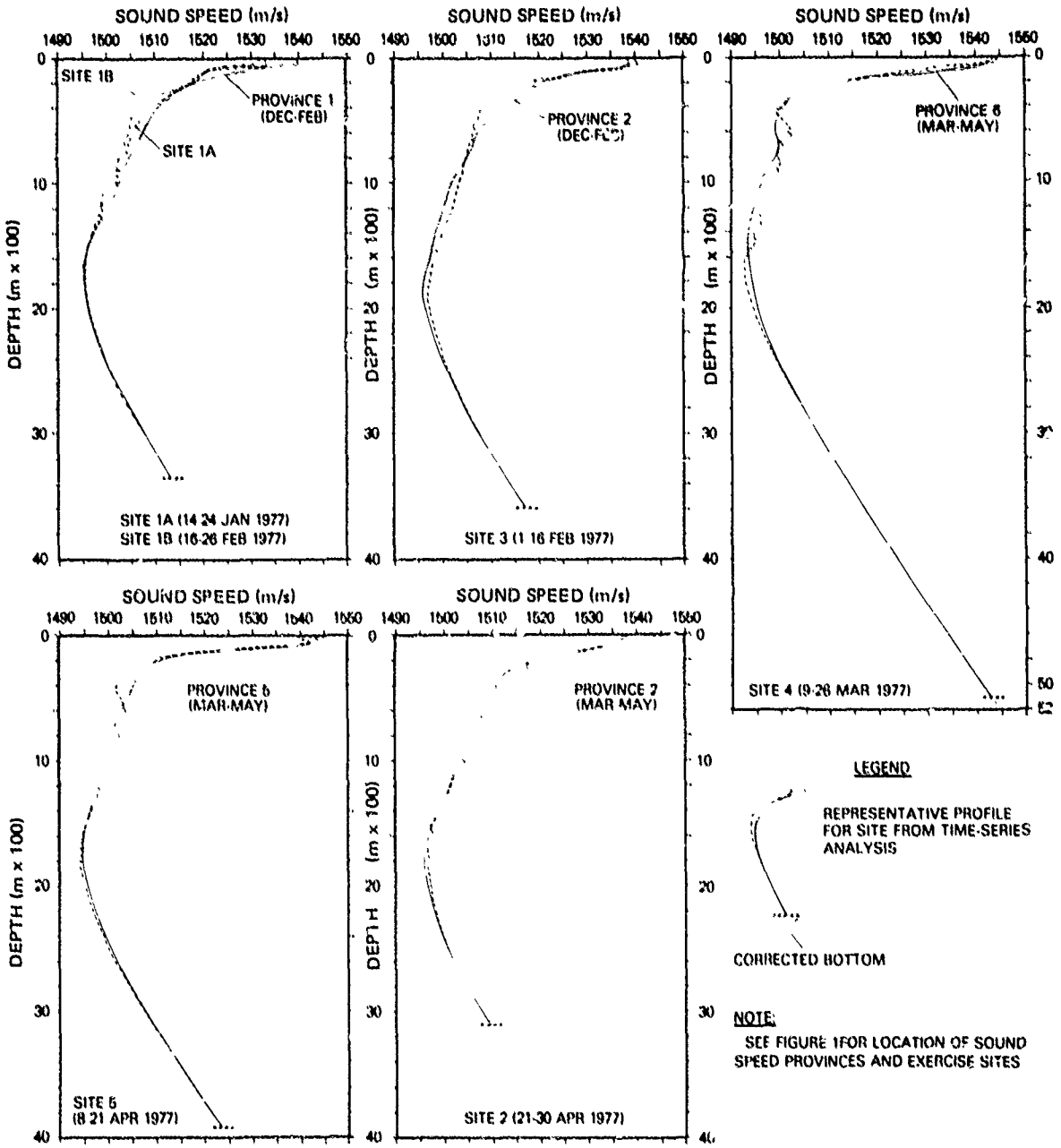

Figure II-28. (C) Comparison of representative exercise and typical historical sound speed profiles at each site. (U)

not cause extreme changes in propagation loss unless the sound speed variability occurs at or above the depth of the source. Variability in the near-surface layers was most pronounced at Sites 1A/1B, 2, and 5. In all three cases, exercise sound speeds were less than historical sound speeds, and at Site 5 the sound speed perturbation between 50 and 100 m was totally absent in the typical profile for March-May. However, at Site 4, the considerable microstructure exhibited by the representative exercise profile should have had some effects on propagation loss, particularly for the low frequency source.

II.4.2 (C) SOUTHWEST MONSOON

(C) Figure 29 compares representative exercise sound speed profiles at each site with representative profiles from the southwest monsoon (June-September). Profiles presented in figure 29 are listed in table 3 (Sites 1A and 1B), table 4 (Sites 3 and 4), and table 5 (Sites 5 and 2). The representative southwest monsoon profiles were chosen from nistorical data positioned as close to each site as possible and therefore are not typical for any specific oceanic province. At Sites 1A/1B, the representative profiles for both monsoons were quite similar except at the surface, where the southwest monsoon profile sound speed was nearly 10 m/s higher than that found during the exercise. At Site 3, the northeast and southwest monsoon profiles were nearly identical except in the near-surface layer, where sound speeds were about 5 m/s higher during the summer. At Site 4, the southwest monsoon profile had considerably lower sound speeds above about 400 m. The maximum difference (17 m/s) occurred at the surface and apparently was caused by southwest monsoon upwelling off the Somali coast. At site 5, the southwest monsoon profile had sound speeds up to 15 m/s higher than the exercise profile at depths above 400 m, but lower sound speeds below 400 m. In addition, the upper sound speed minimum was far better developed during the exercise, probably because of the presence of more Red Sea Intermediate Water. At Site 2, the entire southwest monsoon profile had sound speeds less than those found during the exercise because of the effects of southwest monsoon upwelling off the Oman and Muscat coasts. As expected, representative profiles from the southwest monsoon generally were quite similar to those for the northeast monsoon except above 400-500 m and in regions where upwelling is expected during summer, in keeping with the findings of Fenner and Bucca (1972b). In any case, the southwest monsoon profiles shown in figure 29 are adequately representative for acoustic modeling during the southwest monsoon.

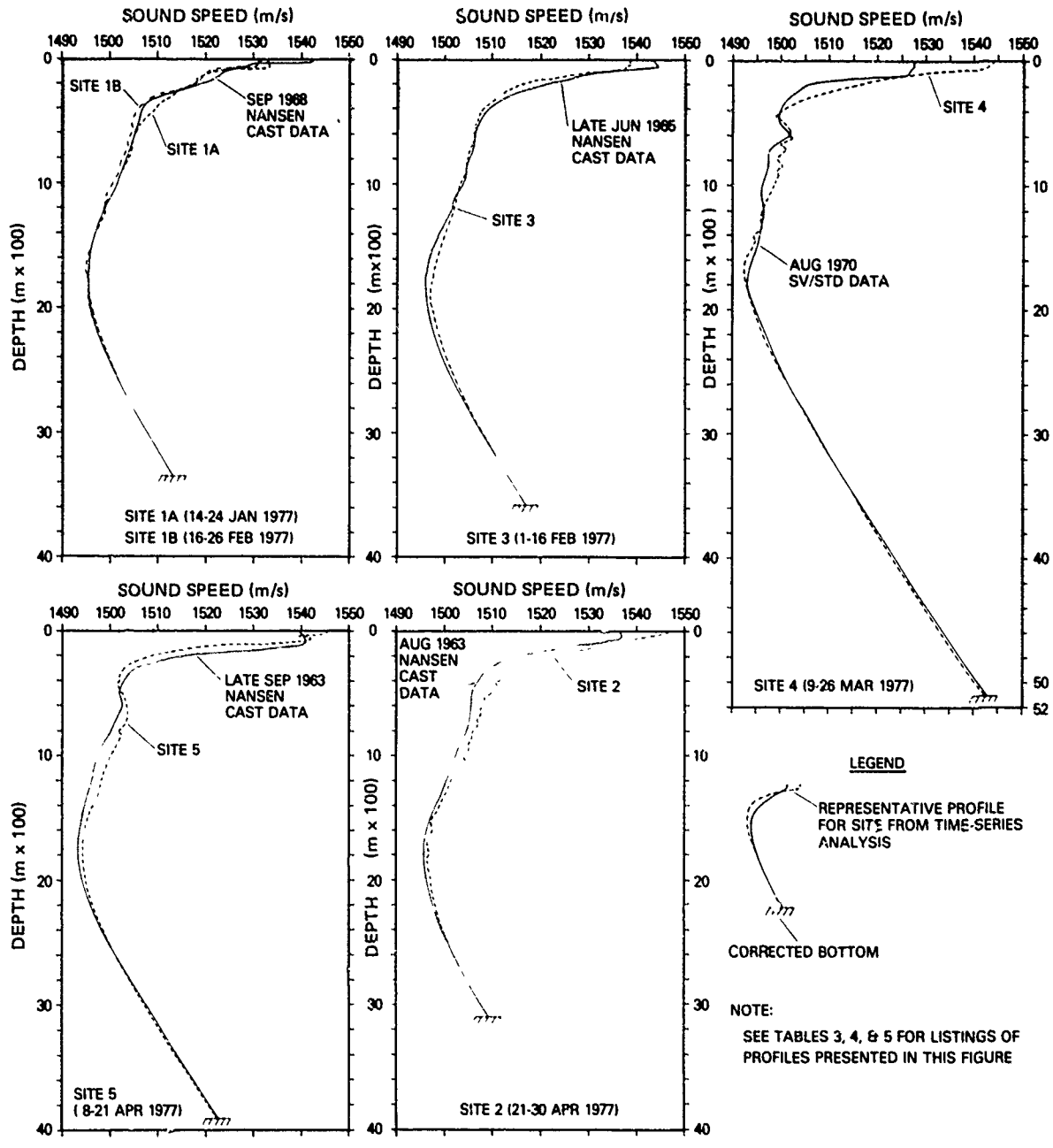

Figure II-29. (C) Comparison of representative exercise and southwest monsoon sound speed profiles at each site. (U)

TABLE II-3. (C) REPRESENTATIVE EXERCISE AND SOUTHWEST MONSOON SOUND SPEED PROFILES FOR SITES 1A AND 1B. (C)

EXERCISE (Site 1A)		EXERCISE (Site 1B)		S.W. MONSOON	
Depth (m)	SS (m/s)	Depth (m)	SS (m/s)	Depth (m)	SS (m/s)
0	1533.0	0	1531.9	0	1542.5 SLD
25	1533.1	10	1532.0 SLD	10	1542.3
65	1533.3 SLD	25	1530.9	20	1542.3
100	1521.1	50	1530.8	30	1530.6
125	1519.8	75	1522.4	50	1528.6
150	1518.7	100	1520.4	75	1526.5
165	1517.9	150	1519.1	100	1523.6
185	1518.5	200	1517.7	125	1523.0
200	1517.6	250	1514.0	150	1522.0
250	1514.4	300	1509.5	200	1519.8
300	1513.2	350	1507.4	250	1515.0
350	1510.9	400	1506.0	300	1511.0
400	1509.7	500	1504.8	400	1506.6
501	1506.7	550	1504.5	500	1506.1
600	1505.4	575	1504.6	600	1505.0
700	1504.6	625	1504.0	700	1504.5
800	1503.9	675	1503.6	800	1503.6
900	1502.6	700	1503.7	900	1502.6
1000	1501.7	800	1502.6	1000	1501.6
1100	1500.3	900	1501.9	1100	1500.3
1150	1499.2	1000	1500.5	1200	1499.1
1200	1499.1	1100	1499.1	1300	1497.8
1300	1498.3	1200	1498.6	1400	1496.9
1400	1497.1	1300	1497.7	1500	1496.1
1500	1496.3	1400	1496.8	1750	1495.6 DSC
1600	1495.6	1500	1495.9	2000	1496.0
1750	1495.4 DSC	1600	1495.3	2500	1500.6
1825	1495.6	1725	1495.0 DSC	3000	1507.8
1900	1495.8	1800	1495.3	3350	1513.3 CBD
2000	1496.3	1901	1495.2		
2200	1497.8	2000	1495.7		
2500	1500.7	2200	1497.2		
3000	1507.7	2500	1500.3		
3350	1513.3 CBD	3000	1507.7		
		3350	1513.5 CBD		

ABBREVIATIONS:

SLD = Sonic Layer Depth
DSC = Deep Sound Channel
CBD = Corrected Bottom Depth

TABLE II-4. (C) REPRESENTATIVE EXERCISE AND SOUTHWEST MONSOON SOUND SPEED PROFILES FOR SITES 3 AND 4. (C)

SITE 3				SITE 4			
EXERCISE		S. W. MONSOON		EXERCISE		S. W. MONSOON	
Depth (m)	SS (m/s)	Depth (m)	SS (m/s)	Depth (m)	SS (m/s)	Depth (m)	SS (m/s)
0	1538.5	0	1543.6	0	1543.9 SLD	0	1528.1 SLD
35	1538.9 SLD	10	1543.8	25	1543.0	10	1527.6
50	1537.8	20	1544.0	50	1541.0	20	1527.6
75	1537.2	30	1544.1	75	1532.9	30	1527.6
100	1529.5	50	1544.5 SLD	100	1528.2	50	1527.3
150	1521.7	75	1536.0	160	1518.2	75	1526.5
200	1515.9	100	1532.5	201	1514.3	100	1526.3
250	1512.7	125	1529.1	250	1509.4	125	1522.1
300	1511.1	200	1519.6	300	1505.1	150	1511.1
350	1509.3	250	1516.3	400	1499.8	200	1505.0
400	1507.9	300	1512.1	450	1498.9	250	1503.5
480	1506.9	400	1509.0	500	1500.5	300	1501.5
500	1507.0	500	1507.3	575	1501.9	400	1499.5
540	1506.4	600	1506.6	600	1501.4	500	1499.3
560	1506.7	700	1506.0	625	1502.4	600	1501.8
600	1506.2	800	1505.1	675	1499.6	700	1497.6
630	1506.4	900	1504.5	726	1500.7	800	1497.1
701	1505.5	1000	1504.0	799	1498.9	900	1496.8
800	1504.8	1100	1502.1	849	1500.1	1000	1496.1
900	1504.3	1200	1501.3	874	1499.1	1100	1495.3
1000	1503.1	1300	1500.0	925	1499.3	1200	1496.3
1100	1502.6	1400	1498.8	999	1498.4	1300	1496.0
1200	1501.9	1500	1497.8	1098	1497.2	1400	1495.3
1300	1500.9	1750	1495.8 DSC	1197	1496.1	1500	1494.8
1400	1500.0	2000	1496.2	1297	1495.6	1750	1493.0 DSC
1500	1499.2	2500	1500.6	1346	1495.9	2000	1494.6
1600	1498.3	3000	1507.7	1421	1494.2	2500	1500.3
1700	1497.8	3580	1516.9 CBD	1470	1494.6	3000	1507.5
1801	1497.1			1595	1492.4	4000	1523.6
1890	1496.9 DSC			1743	1492.3 DSC	5106	1542.8 CBD
2001	1497.2			1892	1493.2		
2200	1498.5			1991	1494.1		
2500	1501.3			2189	1495.8		
3001	1507.6			2511	1500.1		
3580	1516.8 CBD			3004	1507.3		
				3498	1515.2		
				4012	1523.5		
				4501	1531.4		
				5106	1542.5 CBD		

ABBREVIATIONS:

Same as previous table

TABLE II-5. (C) REPRESENTATIVE EXERCISE AND SOUTHWEST MONSOON SOUND SPEED PROFILES FOR SITES 5 AND 2. (C)

SITE 5

EXERCISE Depth (m)	SS (m/s)		S. W. MONSOON Depth (m)	SS (m/s)	
0	1545.5	SLD	0	1540.3	
30	1539.5		10	1540.5	
50	1542.1		20	1540.6	
75	1540.0		30	1540.8	
100	1526.3		50	1541.1	
150	1514.6		75	1541.3	SLD
200	1509.3		100	1540.6	
250	1504.9		125	1535.8	
301	1502.7		150	1529.5	
350	1501.9		200	1513.5	
400	1501.8		250	1508.0	
450	1501.6		300	1504.5	
500	1502.7		400	1503.0	
550	1503.2		500	1502.1	
649	1503.6		600	1502.5	
699	1503.4		700	1501.3	
800	1501.9		800	1500.1	
824	1502.2		900	1498.8	
900	1501.4		1000	1497.6	
1000	1500.0		1100	1496.8	
1098	1499.1		1200	1496.1	
1198	1498.1		1300	1495.5	
1296	1497.5		1400	1494.6	
1396	1496.4		1500	1494.1	
1495	1495.2		1750	1493.3	DSC
1594	1494.7		2000	1494.1	
1693	1494.4		2500	1499.8	
1768	1494.3	DSC	3000	1507.5	
1893	1494.6		3909	1522.5	CBD
1991	1495.1				
2189	1496.3				
2511	1499.9				
3003	1506.9				
3495	1515.1				
3909	1522.5	CBD			

SITE 2

EXERCISE Depth (m)	SS (m/s)		S. W. MONSOON Depth (m)	SS (m/s)	
0	1546.7	SLD	0	1536.8	
25	1544.4		10	1537.0	
50	1540.0		20	1537.0	
75	1537.4		30	1537.1	SLD
100	1534.6		50	1536.6	
150	1526.7		75	1534.1	
200	1520.3		100	1530.6	
250	1517.1		125	1526.3	
270	1517.3		150	1522.1	
300	1513.6		200	1515.3	
350	1512.6		250	1511.8	
410	1510.7		300	1509.1	
440	1510.9		400	1506.8	
480	1510.2		500	1505.6	
530	1508.2		600	1505.5	
560	1508.4		700	1505.1	
620	1507.6		800	1504.6	
660	1507.6		900	1503.5	
710	1506.8		1000	1502.5	
750	1507.0		1100	1501.5	
800	1505.8		1200	1500.5	
850	1505.6		1300	1499.5	
900	1505.0		1400	1498.1	
950	1504.9		1500	1497.1	
1010	1503.9		1750	1495.6	DSC
1040	1504.2		2000	1496.1	
1100	1502.7		2500	1500.5	
1200	1501.4		3100	1509.0	CBD
1300	1500.3				
1400	1499.2				
1540	1497.1				
1600	1497.4				
1720	1496.3				
1780	1496.6				
1820	1496.2	DSC			
1900	1496.6				
1980	1497.1				
2200	1498.0				
2500	1500.3				
3100	1509.1	CBD			

ABBREVIATIONS:

Same as previous table

II.5 (U) CONCLUSIONS

1. (U) The total exercise sound speed data base is adequate for propagation loss calculations.

2. (C) Except for Site 4, propagation at all exercise sites was bottom limited in respect to both the high/medium frequency (18-25 m) and low-frequency (91-102 m) source depths.

3. (C) Site 4 exhibited small but finite depth excess in respect to the high/medium frequency source (nominal depth of 18 m). However, for the low-frequency source (nominal depth of 91 m), at least 200 m of depth excess was found both at the site and along most acoustic tracks.

4. (C) At all sites, the maximum sound speed variation in the water column occurred between 100 and 150 m, at or just below the tow depth of the low-frequency source.

5. (C) Overall, sound speed variability was least at Sites 2 and 3, intermediate at Sites 1A/1B and 5, and greatest at Site 4.

6. (C) At Site 4, intermixing of four intrusive water masses and sinking of Red Sea Intermediate Water caused extremely complex and variable sound speed profiles. The intense variability could have some effects on acoustic propagation, particularly for the 91 m source.

7. (C) Sound speed profiles at Site 1B were up to 5 m/s lower than those at Site 1A (occupied nearly one month earlier). This anomaly probably was caused by increased northeast monsoon upwelling after the Site 1A occupation.

8. (C) Oceanographically, representative sound speed profiles from the exercise varied substantially from typical historical profiles for the same time period presented by Colburn (1976), particularly at Sites 1A/1B, 4, and 5.

9. (C) From the standpoint of propagation loss calculations, variations between representative exercise and Colburn sound speed profiles should be significant only at Sites 1A/1B, 2, and 5 (due to near-surface differences) and Site 4 (due to extensive sound speed microstructure).

10. (C) Representative exercise and southwest monsoon sound speed profiles generally were quite similar except above a depth of 400-500 m (effects of monsoonal reversal) and in regions where summer upwelling is expected (Sites 2 and 4).

11. (C) The entire exercise took place either during the northeast monsoon or at the beginning of the transitional season between the northeast and southwest monsoons.

12. (C) Wind speeds, sea heights, and swell heights were moderate to low at all exercise sites and should not have marked effects on ambient noise levels.

REFERENCES (U)

Carnvale, A., P. Bowen, M. Basileo, and J. Sprenke (1968). Absolute Sound Velocity Measurement in Distilled Water. J. Acoust. Soc. Am., v. 44, n. 4, April, p. 1098-1102.

Colborn, J. G. (1976). Sound-Speed Distribution in the Western Indian Ocean. Naval Undersea Center, San Diego, Calif., February, 168 p. (NUC TP 502).

Fenner, D. F. and P. J. Bucca (1972a). Sound Velocity Structure of the Northwest Indian Ocean. J. Mar. Biolog. Assoc. India, v. 14, n. 1, January, p. 61-83.

Fenner, D. F. and P. J. Bucca (1972b). The Sound Velocity Structure of the North Indian Ocean. Naval Oceanographic Office, Washington, D. C., December, 98 p. (NAVOCEANO TR-231).

Mackenzie, K. V. (1971). A Decade of Experience with Velocimeters. J. Acoust. Soc. Am., v. 50, n, 5, May, p. 1321-1332.

Naval Ocean Systems Center (1977). BEARING STAKE Exercise: Preliminary Results (U). San Diego, Calif., October, 136 o. (NOSC Tech. Rep. 169). (CONFIDENTIAL)

Wilson, W. D. (1960). Equation for the Speed of Sound in Sea Water. J. Acoust. Soc. Am., v. 32, n. 10, October, p. 1357-1358.

CHAPTER III

GEOACOUSTIC MODELS OF THE SEAFLOOR (U)

by

Edwin L. Hamilton and Richard T. Bachman

Environmental Acoustics Division, Code 531

Naval Ocean Systems Center

San Diego, California 92152

CHAPTER III: GEOACOUSTIC MODELS OF THE SEAFLOOR (U)

CONTENTS (U)

CHAPTER III. GEOACOUSTIC MODELS OF THE SEAFLOOR (U)

III.1 (U) INTRODUCTION

(C) This report is concerned with geoacoustic models of the seafloor in three general areas of the Northwest Indian Ocean (fig 1) wherein measurements were made of energy losses ("bottom losses") when sound interacted with the seafloor during the BEARING STAKE expedition (January to April 1977). Ten such models were developed for various locations along the tracks of the expedition's ships. Eight of these models were along specific ship's tracks involved in bottom loss measurements. Nine additional geoacoustic models were developed for extrapolation of bottom loss measurements over geomorphic provinces of the seafloor or for use with acoustic theory to compute and thus predict bottom losses. Examples of the primary (ten) geoacoustic models are in appendix A. Each model in appendix A is in the form of two tables with footnotes. The first, or main, table, with the footnotes, presents sediment and rock layer thicknesses and the variations with depth in the seafloor of compressional wave (sound) velocity, shear wave velocity, the attenuation of compressional and shear waves, and density. The second table lists properties of the bottom water (depth, temperature, salinity, pressure, sound speed, density, and impedance).

(U) All the finished geoacoustic models were forwarded to the Applied Research Laboratories (University of Texas) in January-February 1978, where they were used in studies of measurements of energy losses when sound interacted with the seafloor, and in extrapolation of these measurements to adjacent areas. Results are reported in chapter IV.

(U) At higher sound frequencies, the acoustician may be interested in only the first few metres, or tens of metres, of sediments. At lower frequencies, information must be provided on the whole sediment column and on properties of the underlying rock. This information should be provided in the form of geoacoustic models of the seafloor.

(U) A "geoacoustic model" is defined as a model of the real seafloor with emphasis on measured, extrapolated, and predicted values of those properties important in underwater acoustics and those aspects of geophysics involving sound transmission. In general, a geoacoustic model details the true thicknesses and properties of the sediment and rock layers of the seafloor.

(U) Geoacoustic models are important to the acoustician studying sound interactions with the seafloor in several critical aspects: to guide theoretical studies, to reconcile experiments at sea with theory, and to be able to predict the effects of the seafloor on sound propagation.

(U) The information required for a complete geoacoustic model should include the following for each layer (in some cases, the state of the art allows only rough estimates, in others, information may be nonexistent):

- Properties of the overlaying water mass from Nansen cast and velocimeter lowerings.
- Sediment information (from cores, drilling, or geologic extrapolation); sediment types, grain-size distributions, densities,

porosities, compressional and shear wave velocities and attenuations, and other elastic properties. Gradients of these properties with depth; for example, velocity gradients and interval velocities from sonobuoy measurements.

- o Thicknesses of sediment layers (in time) determined at various frequencies by continuous reflection profiling.
- o Locations, thicknesses, and properties of reflectors within the sediment body as seen at various frequencies.
- o Properties of rock layers. Those at or near the seafloor are of special importance to the underwater acoustician.
- o Details of bottom topography, roughness, relief, and slope; for example, as seen by underwater cameras and deep-towed equipment.

(U) Among the above properties and information, the basic, minimum information required for most current work in sound propagation is

(1) Thicknesses of layers

(2) Compressional wave (sound) velocity in each layer

(3) Sound velocity gradient through the layers

(4) Sound attenuation in each layer

(5) Density in each layer

(U) Newer and more sophisticated mathematical computer models involving sound interaction with the seafloor require (in addition to the above):

(6) The gradient of sound attenuation through the layers

(7) The density gradient through the layers

(8) Shear wave velocity and attenuation, and gradients (from which, with density and compressional wave velocity, other elastic properties can be derived).

III.2 (U) GEOLOGIC SETTING

(C) This section will include very brief discussions of the geology of the three general areas included in this report: the Gulf of Oman, the Arabian Sea (including the Arabian Fan and adjacent areas), and the Somali Basin. Locations and bathymetry of these areas are indicated in figure 1 (printed on a foldout page at the end of the chapter for ready reference). Detailed accounts of the geology of two of these are in recent reports of the Deep Sea Drilling Project (DSDP) (Arabian Fan, Leg 23: Whitmarsh et al., 1974; Somali Basin, Leg 24: Fisher et al., 1974). The Oman Basin was discussed by White and Klitgord (1976). The deep structure and plate tectonics of these areas are in these reports, and will not be included below. Figures 2 to 6,

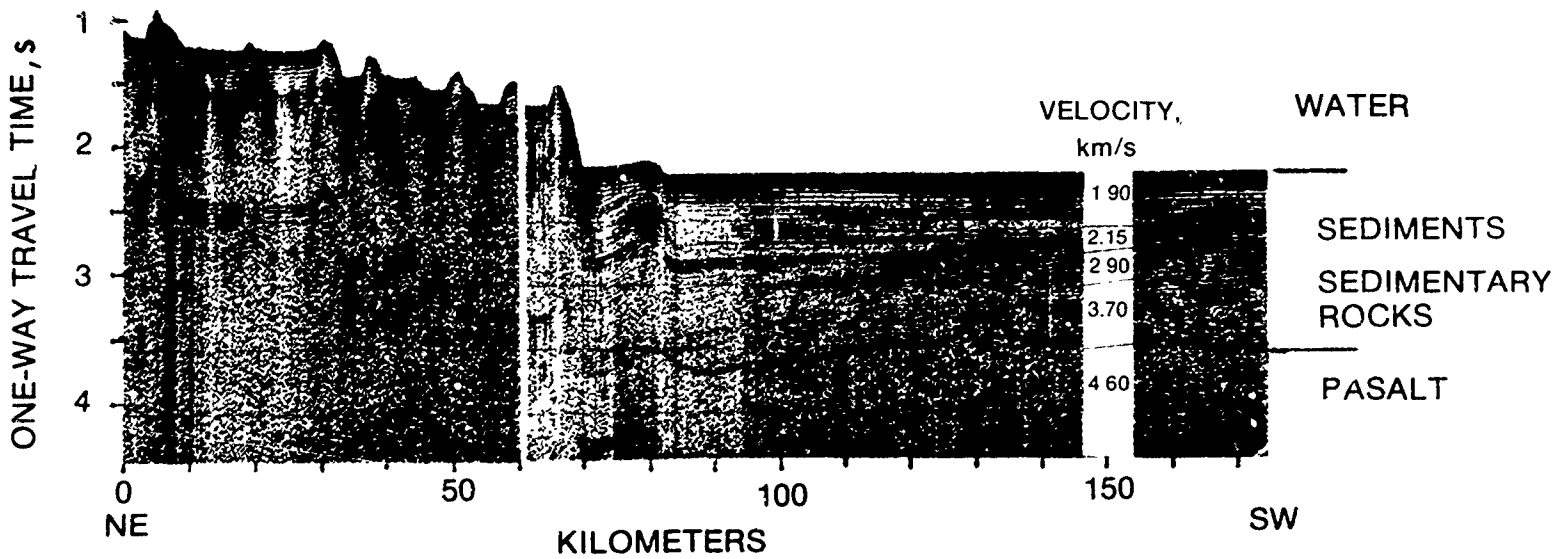

Figure III-2. (C) Acoustic reflection profile from the Gulf of Oman (from White and Klitgord, 1976, Figure 2). Right side (SW) is at 23°25'N, 61°35'E; left side (NE) is at 24°45'N, 62°31'E. The velocity data are from sonobuoy measurements by White and Klitgord. (C)

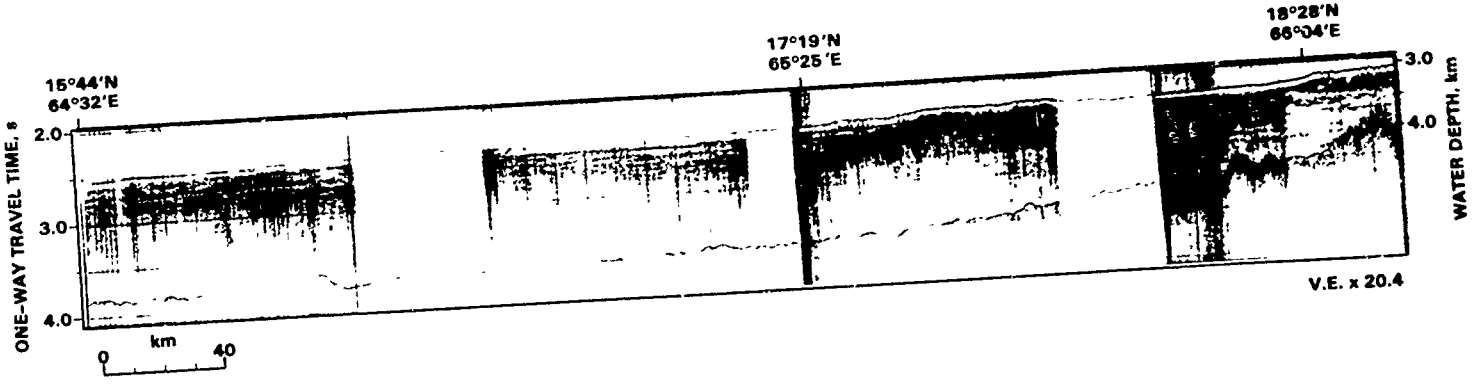

Figure III-3. (C) Acoustic reflection profile in Area 3, north central Arabian Fan (fig 1). The three positions noted above the top border are the positions (left to right) of Geoacoustic Models 3a, 3b, and 3c (3a is southwest and 3c northeast). On the left side, sediments and sedimentary rocks overlie basalt and are more than 3500 m thick; in the center they are about 3300 m thick; and over the basement ridge on the right side they are about 1000 m thick. (C)

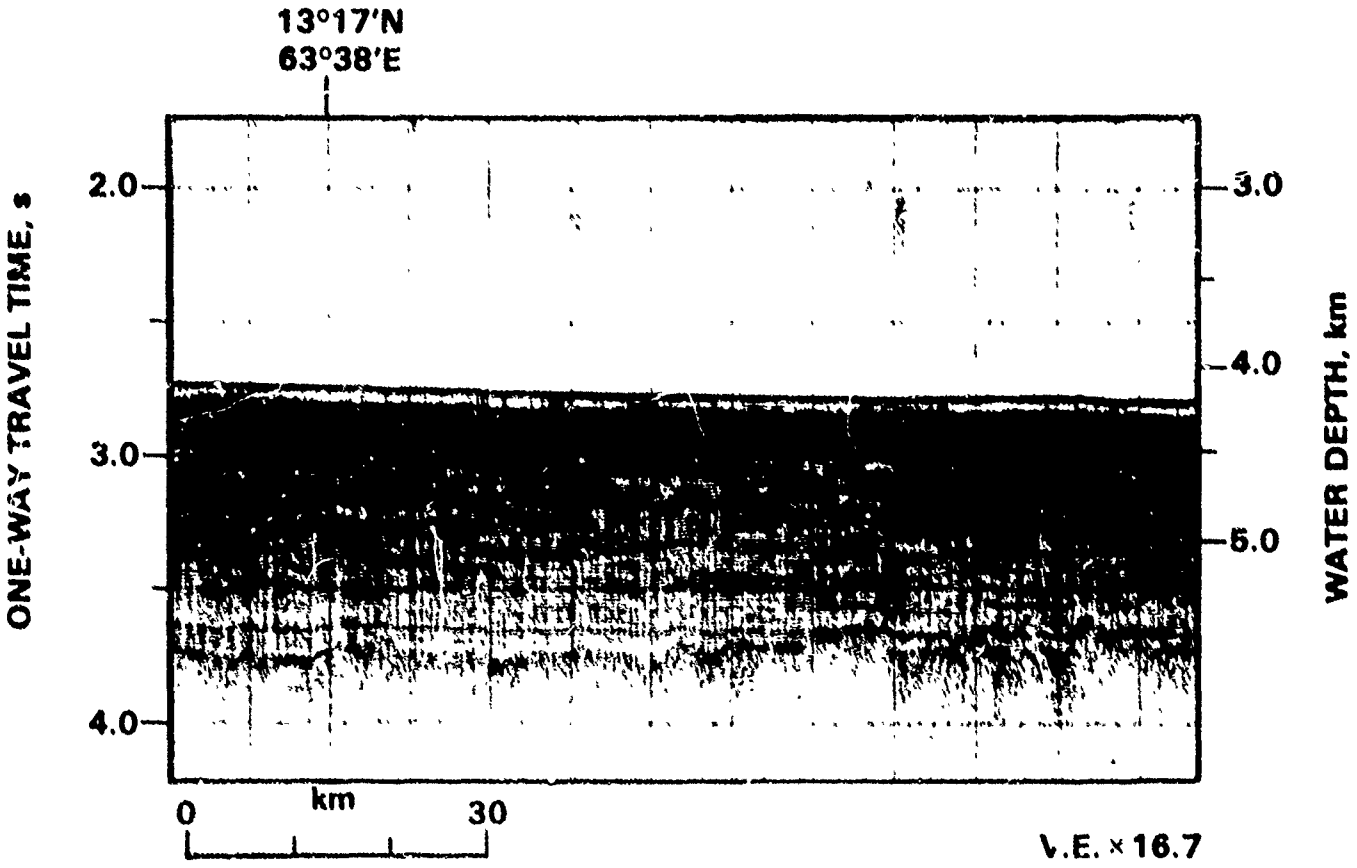

Figure III-4. (C) Acoustic reflection profile, west central Arabian Fan, at the location of Geoacoustic Model A2 (fig 1). The record shows about 2400 m of sediments and sedimentary rocks overlying basalt. (C)

inclusive, are selected parts of the acoustic reflection records which illustrate relief of the seafloor, reflectors, sub-bottom relief, and sediment and rock thicknesses (in seconds of sound travel time) over acoustic basement in the three areas. In the following discussions a great deal of detailed information not pertinent to the geoacoustic modeling is excluded.

III.2.1 (C) OMAN BASIN

(C) The Gulf of Oman (Area 1), containing the Oman Basin (fig 1), is bounded on the north by the coasts of Iran and Pakistan, on the southeast by Murray Ridge, and on the southwest by the Arabian Peninsula. White and Klitgord have published an excellent survey of the area. The material below is mostly from their report.

(C) The continental margin in the Gulf of Oman is formed by a sequence of east-west trending folds of sediment and sedimentary rock which are parallel to the coast. The folds form a series of ridges and troughs typically about 3 to 4 kilometres wide and with ridges up to about 800 metres high (fig 2). Sediments from the coast have partly covered those ridges and troughs nearest the coast, but these sediments are prevented from reaching the flat abyssal plain to the south.

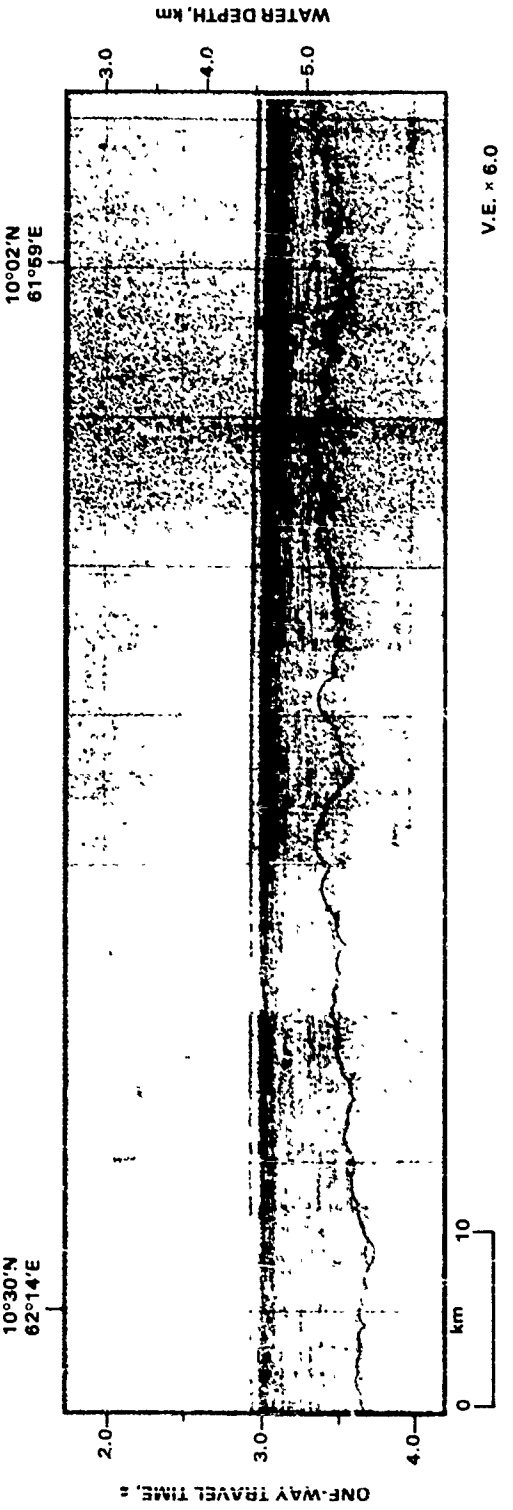

Figure III-5. (C) Acoustic reflection profile near the southern end of the Arabian Fan (fig 1). Geoacoustic model A3a, near the right side, or south end of the profile, has about 1000 m of sediments and sedimentary rocks overlying basalt. (C)

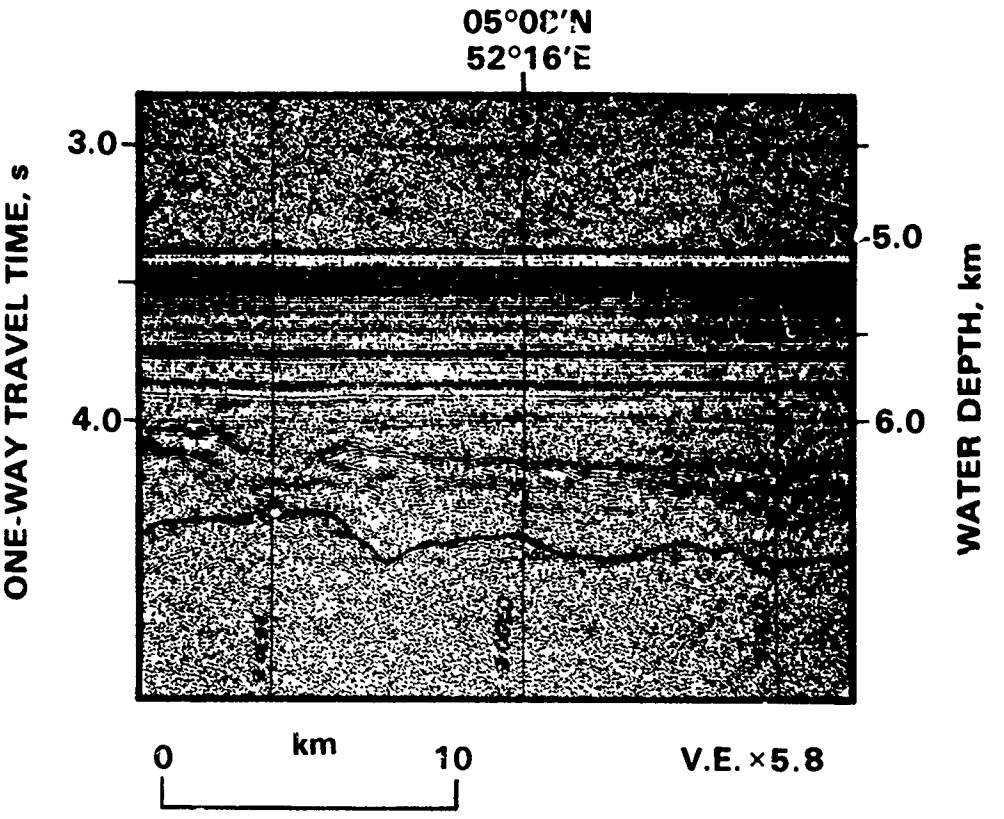

Figure III-6. (C) Acoustic reflection profile near the center of Somali Basin at the site of Geoacoustic Model 4a (fig 1). The record shows a first layer of sediments and sedimentary rocks (about 1600 m thick) and a second layer of sedimentary rock (about 900 m thick) overlying the acoustic basement of basalt. (C)

(C) The major portion of the basin is filled with flat-lying turbidites which form an abyssal plain. These turbidites overlie several layers of sediments and sedimentary rocks which dip to the north at about 0.8^{0} (fig 2). The underlying rock with a velocity greater than 4.5 km/s is probably volcanic. Measurements from the acoustic reflection records taken on the BEARING STAKE expedition and computations of thicknesses indicate that in the center of the basin at the location of Geoacoustic Model 1a, the first layer of sediment and sedimentary rock is about 1250 m thick and layers 2 and 3 (sedimentary rock) are about 985 and 100 m thick, respectively. As discussed in the next section (Arabian Fan), there should be a transition from soft (unlithified) sediment to rock (mudstone) at depths in the first layer between 500 and 700 m.

(C) The sediments forming the abyssal plain are typical turbidites. The cores in the area indicate that, typically, the thicker layers are silty clay and clayey silt (about 50 to 120 cm thick), with intercalated, thinner (about 20 cm) layers of silt. There should be hundreds of layers of this type in the 1250-metre-thick first layer. These sediments entered the plain from the Persian Gulf to the west and from the Pakistan coast to the east. No channels were seen on the echo-sounder records.

III.2.2 (C) ARABIAN FAN

(C) Of the various names used on charts and in reports, the writers prefer the name Arabian Fan ("Indus Cone" and "Arabian Abyssal Plain" are also used) to include the sediments which occupy the area bounded by Murray and Owen Ridges to the north and west, by Carlsberg Ridge to the south, and on the east by the Laccadive-Chagos Ridge (not shown in fig 1) and the subcontinent of India (fig 1).

(C) The Arabian Fan (Area 3) has been formed mostly by mineral detritus eroded from the Himalaya Mountains, transported down the Indus River, and through the Indus Canyon (incised into the continental terrace off northwest India), and deposited over an originally rough basaltic seafloor. The fan, consequently, slopes to the south-southwest (fig 1). The sediments are very thick (over 9 km) in the northernmost part of the fan near the Indus Canyon (Naini and Talwani, 1977), and thin to about 400 to 500 m in the southernmost end of the fan before finally pinching out against the northern edge of the Carlsberg Ridge. From the Indus Canyon in the north the mineral particles were mostly transported by turbidity currents through great leveed channels. In the northwest part of the fan, levee heights above the channels are up to about 50 m, with the western levee the higher. When these turbidity currents topped the levees and left the channels, the sediments (turbidites) were deposited in the interchannel areas. This is the same mode of deposition seen in the Bengal Fan on the east side of India, in the Gulf of Alaska, and in other areas.

(C) Figure 3 illustrates the very thick sediment layer over probable basalt in the north central part of the fan. In figure 1 this profile is between Geoacoustic Models 3a-3c. At the site of 3a ($15^{o}44'N$, $64^{o}32'E$) the sediment and sedimentary rock layer is over 3500 m thick; it thins to about 1975 m at the site of model 3c. Figure 4 (Model A2 in fig 1) illustrates a 2450 m layer of sediments and sedimentary rocks. Figure 5 illustrates thicknesses near the southern end of the fan. At the site of A3a ($10^{o}00'N$, $61^{o}58'E$) the sediments are still thick: about 985 m. Volume 23 of the Initial Reports of the Deep Sea Drilling Project (DSDP) contains many more illustrations of acoustic reflection records.

(C) At Site 222 of the DSDP ($20^{o}05'N$, 61o31'E), in the northwest part of the fan, more than 1300 m of sediments and sedimentary rocks (mudstone) was drilled. Most of the sediment was a greenish gray silty clay or clayey silt with relatively few layers of silt; there were some carbonate sediments in the top of the section. Except in the channels (where coarser sediments might be expected) these are probably typical of sediments in the Arabian Fan.

(C) In thick terrigenous sediment sections, as above, there is usually a transitional section through which the sediment gradually lithifies (hardens) and below which the material is a rock, usually a mudstone. This transition at Site 222 occurs at about 600 m (Bachman and Hamilton, 1976). Consequently, in the various geoacoustic models with very thick first layers, the material is named as "sediment and sedimentary rock." This nomenclature implies a gradual transition from sediments to sedimentary rock at about 500 to 700 m.

(C) Reflectors in most of the Arabian Fan are probably formed by layers of silt in the interchannel areas and by silts and sands, and mixtures of the

two, in the channels. In the thick sediment sections considered in the geoacoustic models there are many hundreds of these reflectors on the order of about three metres apart. Most of them are sub-parallel to the sediment surface in areas away from the leveed channels.

III.2.3 (C) OWEN RIDGE

(C) The western margin of the Arabian Fan is controlled by the Owen Fracture Zone (not shown) and by Owen Ridge, just west of the Fracture Zone. Owen Ridge is formed by an uplifted sediment and rock section which dips to the west and is bounded on the east by a steep fault scarp. The DSDP drilled at Site 224 on Owen Ridge at 16°33'N, 59°42'E. Volume 23 of the Initial Reports of the DSDP contains acoustic reflection records and much other information about the ridge.

(C) Geoacoustic Model 2a is on top of Owen Ridge. Data from expedition coring and reflection records, plus information from DSDP Site 224, were used to predict the model. This model shows a first layer of sediment (calcareous clayey silt) 100 m thick, over a second layer (claystone, siltstone) 175 m thick , in turn over a third layer (chalk and claystone) 520 m thick. The acoustic basement is basalt.

III.2.4 (C) CARLSBERG RIDGE

(C) Carlsberg Ridge forms the southern boundary of the Arabian Fan (fig 1). This ridge is a major feature in the Northwest Indian Ocean. It is roughly defined by the 4000 m contour on each side (to the north and south) and has many peaks and ridges at top depths between 1500 and 2000 m.

(C) The ridge is formed by basaltic lavas in the form of blocks, pillows, linear ridges, and mountains. The center of the ridge is almost bare of sediments, with small, thin patches of calcareous sediments in depressions and hollows. Steep escarpments, gaps, and fissures are common: slopes range from low to vertical, or even overhanging. It is an extremely rugged area of the seafloor.

III.2.5 (C) SOMALI BASIN

(C) The Somali Basin (Area 4) is bounded on the north by ridges essentially connecting the African continent to Socotra Island to Carlsberg Ridge (fig 1). The basin is bounded on the west and northwest by the African continent and on the east by Chain Ridge.

(C) Figure 6 illustrates the acoustic stratigraphy in the center of the basin at Geoacoustic Model 4a. There are three distinct layers: (1) a thick turbidite layer (sediment and sedimentary rock) about 1580 m thick, forming an abyssal plain, (2) an underlying layer of sedimentary rock about 940 m thick, and (3) the acoustic basement of basalt. The basin floor is very flat with no channels indicated on echo-sounder records.

(C) Drilling at DSDP Site 234 (Fisher et al., 1974) and cores in the area indicate that the top of the first layer is calcareous ooze and clay. From cores and 3.5-kHz records, reflectors appear to be silt or silty sand and about 3 m apart.

(U) On the west side of the basin (at Model 4c), the second layer rises toward the surface and the upper layer thins to about 970 m.

(C) Chain Ridge on the east side of the Somali Basin is a continuous, basaltic ridge with a series of summit peaks. Minimum water depths along the ridge vary between about 1780 and 3000 m. The base of the ridge is defined by the 5000-m contour. Therefore, the ridge varies in height between about 2000 and 3200 m. Acoustic reflection records in Bunce et al. (1966) indicate about 0.13 s (one-way sound travel time) of pelagic sediment on the west side and near the top of the ridge. Computations of sediment thicknesses indicate a little more than 200 m of sediments which are probably calcareous ooze and calcareous silty clay.

III.3 (U) GEOACOUSTIC MODELS AND EXTRAPOLATION

(C) The ten principal BEARING STAKE geoacoustic models of the seafloor were developed for three areas in the Northwest Indian Ocean wherein bottom loss measurements were made during the BEARING STAKE expedition (January to April 1977). The three areas (fig 1) are in the Gulf of Oman (Area 1B), in the Arabian Sea (Area 3), and in the Somali Basin (Area 4) off northeast Africa. Most of the necessary environmental data were collected from the USNS WILKES (T-AGS-33). Additional bathymetric data were taken by USNS KINGSPORT (T-AG-164) and USNS MIZAR (T-AGOR-11). The environmental data concerning the seafloor were furnished the writers by NAVOCEANO (Codes 3408 and 3432) and NORDA (Code 341). These data, plus information from the scientific literature, were used to formulate the models. Examples of the actual models in the form of tables with footnotes are in appendix A.

(U) Nine additional models were developed to extrapolate the geophysical and geological data within adjacent geomorphic provinces. All models are presented by Hamilton and Bachman (1979) and should be used in extrapolating data and models.

(U) All the extrapolated models are generalized and approximate, and are intended as estimates which allow a rationale for an acoustician to extrapolate or predict bottom losses or reflection coefficients in these general areas. The methods used to derive the values listed in the table for all the models are discussed by Hamilton and Bachman (1979).

(C) The three general areas discussed here are distinctive geomorphic provinces. They are the Oman Basin, the Arabian Fan and adjacent areas in the Arabian Basin, and the Somali Basin. The geology of these areas was discussed under Geologic Setting in section III.2 and the bathymetry is illustrated in figure 1. Examples of acoustic reflection records are in figures 2 through 6.

OMAN BASIN (C)

(C) Oman Basin (fig 1 and 2) is occupied by a very flat abyssal plain surrounded by hills to the north and northwest, by the continental terrace to the east, by Murray Ridge to the southeast, and by the Arabian Peninsula to the southwest.

(C) In the Oman Basin, Geoacoustic Model 1a (appendix A) can be extrapolated within the flat, abyssal plain in the center of the basin. It is

recommended that this model be used within (deeper than) the 3000 m water depth contour.

(C) Geoacoustic Model 1b (Hamilton and Bachman, 1979) is intended for use in the folded sedimentary ridges of the continental slope northeast, north and northwest of the abyssal plain in the Gulf of Oman. These ridges are probably formed by squeezing and compression of former abyssal plain sediments with a thin layer of pelagic sediments on their tops. This model represents the ridge tops. The upper layer is based on coring data, but the lower layers are tenuous asumptions.

ARABIAN FAN (C)

(C) Geoacoustic Models 3a, 3b, and 3c (fig 1, appendix A) were along a line in the north central fan where bottom loss measurements were made during the BEARING STAKE expedition. Additional Models A1-A5, inclusive (Hamilton and Bachman, 1979), were composed to allow extrapolation of data to most of the remainder of the fan. Model 2b (Hamilton and Bachman, 1979) is along an expedition line in Area 2, but no bottom loss measurements are currently available along this line. Model 2b can be used as an additional model for extrapolation.

(C) The additional models (A1-A5) were placed to give reasonable areal coverage over the fan, and where additional information was available on sediment and sedimentary rock thicknesses. These models were placed as follows (see fig 1; and lat. and long. in appropriate tables in Hamilton and Bachman, 1979).

(1) Geoacoustic Model A1 was placed in the southeast fan near an acoustic reflection line between Deep Sea Drilling Project Sites 221 and 222.

(2) Geoacoustic Model A2 was along a USNS WILKES acoustic reflection line in the south central fan.

(3) Geoacoustic Model A3a in the south central fan was placed on a WILKES track. Models A3b and A3c were placed in the southeast and southwest fan on the 1000 m sediment thickness (isopach) line of Naini and Talwani (personal communication, 1977).

(4) Geoacoustic Models A4a and A4b were near the southern end of the fan and on the 500 m sediment thickness contour lines of Naini and Talwani.

(5) Geoacoustic Model A5 was placed to obtain a real coverage in the northwest fan. It is on the 3400 m water depth contour. The sediment thickness from Naini and Talwani is 2300 m.

(C) All the models for the Arabian Fan are essentially the same except for surface ("Sfc") properties, which depend on water depth. This is because a common velocity-sediment depth curve was averaged from sonobuoy measurements and used over the whole fan; and because generalized data for the upper three meters of sediments were determined from averages in eight cores in Area 3 and used for the whole fan.

OWEN RIDGE (C)

(C) Owen Ridge forms the western boundary of the Arabian Fan (fig 1). It is an uplifted block of sediments and rocks which is tilted to form a low slope to the west. The eastern boundary of Owen Ridge is a relatively steep fault scarp.

(C) Geoacoustic Model 2a (Hamilton and Bachman, 1979) is on top of Owen Ridge in BEARING STAKE Area 2. DSDP Site 224 was drilled to the north of Model 2a (at 16°33'N, 59°42'E) and the DSDP report furnished much useful data which helped to formulate the model.

(C) Although on top of a ridge, there is a thick section for this environment (795 m of sediments and sedimentary rocks over basalt). There are no models farther west, but Model 2a can be used to compute bottom losses into the basin to the west; for example, along KINGSPORT track 2P1 (fig 1). For some acoustic modeling purposes, special attention should be accorded the asymmetric nature of Owen Ridge. The fault scarp on the east side of the ridge (in the vicinity of Area 2) has a slope of about 17°. On the west side of the ridge the relatively low slope is about 2.5°.

CARLSBERG RIDGE (C)

(C) Carlsberg Ridge which forms the southern boundary of the Arabian Fan was described in the section Geologic Setting. This basaltic ridge, as noted, is rough, with steep escarpments, gaps, fissures, isolated ridges and seamounts. Near and along the top of this feature there are only thin patches of sediments in depressions.

(C) The rugged topography would control bottom losses, and it would be impossible to model the area as a generality. Small areas could be modeled, given a very detailed bathymetric chart. Geoacoustic Model A6 (Hamilton and Bachman, 1979), placed on the crest of the Carlsberg Ridge, indicates a small area wherein basaltic lavas are at the seafloor with no sediment cover. The velocity data are from a seismic refraction survey line measured by the Soviets through 5°00'N, 62°30'E.

SOMALI BASIN (C)

(C) Geoacoustic Models 4a, 4b, and 4c (4a in appendix A) can be used to extrapolate data in the Somali Basin and adjacent areas. Model 4a, in the center of the plain, can be used within the 4800 m contour (fig 1). Model 4b can be used for the slopes and top of Chain Ridge on the east side of the basin. Geoacoustic Model 4c can be used to represent the African continental rise, west of the basin, from the 4800 m contour to about the 4000 m contour.

APPENDIX III-A: (U) GEOACOUSTIC MODELS

INTRODUCTION (U)

(U) The following examples of the ten BEARING STAKE geoacoustic models of the seafloor are along the tracks of the USNS KINGSPORT during the expedition (fig 1). These ten models are intended primarily for use in reconciling experimental bottom loss measurements with theory, and secondarily for use with other models in Hamilton and Bachman (1979) for extrapolating measurements and predictions to other, adjacent, areas.

(U) In the following tables, in most cases, the listed numerical values of properties are not rounded off but are shown as computed (to better indicate trends and gradients). There is no intent to indicate accuracy or probable errors. All values must be considered as generalizations and estimates especially when one model is extrapolated over a general area or along an insonified line along the seafloor.

(C) LIST OF GEOACOUSTIC MODELS (U)

(C) Geoacoustic Model: 1a Area: Gulf of Oman (Area 1A and 1B) (C)

Location: 23°33'N Lat.: 61°09'E Long.

Water Depth: Echo-Sounder: 1826 fm; 3340 m; set at 1500 m/s
Corrected: 1831 fm; 3348 m (from station data)

Province and Description of the seafloor: Abyssal Plain Province. The seafloor is composed of a first layer of flat-lying turbidites overlying two other sedimentary rock layers which dip to the north. The acoustic basement is probably basalt.

Layer No.	Material	Thickness, s	Thickness, m	Depth, m	Velocity, m/s V_p (1)	V_s (2)	Attenuation, k_p (3)		k_s (4)	Density, g/cm^3 (5)
	Btm Water				1514.5					1.04306
	Seafloor									
1	Sediment and Sedimentary Rock	0.62	1250	Sfc	1515	120	0/05	0.10	0.20	15.0	1.58
				100	1638	377	0.07	0.11	0.19	16.5	1.67
				200	1750	442	0.10	0.12	0.17	18.0	1.80
				300	1851	499	0.12	0.13	0.16	19.5	1.91
				400	1943	558		0.14		21.0	2.02
				500	2026	619		0.14		21.0	2.10
				600	2101	679		0.12		18.0	2.13
				700	2168	730		0.11		16.5	2.15
				800	2230	780		0.10		15.0	2.18
				900	2286	820		0.08		12.0	2.20
				1000	2337	860		0.07		10.5	2.22
				1100	2385	900		0.06		9.0	2.24
				1200	2429	935		0.0.5		7.5	2.25
				1250-	2450	950		0.05		7.5	2.26
				1250+	2565	1040		0.05		7.5	2.30
2	Sedimentary Rock	0.34	980	1743	2900	1300		0.03		4.5	2.40
				2236-	3235	1560		0.02		3.0	2.49
				2236+	3400	1700		0.02		3.0	2.52
3	Sedimentary Rock	0.30	1104	2788	3685	1843		0.02		3.0	2.57
				3340-	3975	1988		0.02		3.0	2.61
4	Basalt (?)			3340+	4600	2270		0.02		0.07	2.50

(cont.)

(C) Model 1a (cont) (U)

Notes (for further derivation of values and discussions see Hamilton and Bachman, 1979) (U)

1. (U) V_p (Compressional Wave (Sound) Velocity).

   a. (U) First layer

   $$Vp = 1.515 + 1.292D - 0.611D^2 + 0.141D^3$$

   where V_p is in km/s, and depth in the seafloor, D is in km

   b. (U) Lower layers: V_ps from literature.

2. (U) V_s (Shear Wave Velocity). From unpublished study by Hamilton of V_p/V_s ratios in marine sediments and rocks. Basalt V_s from Christensen and Salisbury (1975).

3. (U) k_p (Constant in: attenuation of compressional waves, α_p, in dB/m = $k_p f$; where f is frequency in kHz). The three listed values to 300 m are: probable minimum, recommended for first trial in bottom loss modeling, and probable maximum. From Hamilton (1972, 1974, 1976a).

4. (U) k_s (Constant in: attenuation of shear waves, α_s, in dB/m = $k_s f$; where f is frequency in kHz. Based on Hamilton (1976c) at surface; proportional to k_p at depth.

5. (U) Density (Saturated bulk density, in situ). Surface density computed from core data. Density at depth from Hamilton (1978, 1976b). Basalt density from Christensen and Salisbury (1975).

6. (U) General

   a. (U) "Thickness, s" (in seconds of one-way sound travel time) from reflection records. "Thickness, m" from one-way travel time and layer mean velocity.

   b. (U) In the above model, the "Sfc" (surface) values are a composite of the 0-1 depth interval. For a detailed model of this interval see the diagram and notes below.

(cont)

Detail of First Meter

Layer No.	Material	Thickness s	Thickness m	Depth, m	Velocity, m/s V_p (1)	V_s (2)	Attenuation, k_p (3)		k_s (4)		Density g/cm^3 (5)
	Btm Water				1514.5						1.04306
1a	Silt clay		0.8	Sfc	1485	115	0.05	0.10	0.20	15.0	1.53
				0.8-	1486	119		0.10		15.0	1.53
1b	Silt		0.2	0.8+	1620	130	0.45	0.60	0.85	13.0	1.80

Notes (U)

1. (U) The geoacoustic models (such as in the main table) showing thick sediment and sedimentary rock sections over "acoustic basement" (such as basalt) are generalized and do not account for the multiple reflectors as seen (usually at high frequencies), for example, in the 3.5-kHz records, or in cores.

2. (U) If a detailed, multireflector model is desired, the above sequence of a thicker silt-clay layer and a thinner silt (or other) layer can be alternated to any desired depth. If so, the property values can be corrected for depth as follows.

   a. (U) For the silt-clay layer.

      (1) (U) For V_p: increase V_p using gradients computed from the V_p vs depth equation.

      (2) (U) Other properties: vary the value of the property with depth using the appropriate gradient from the values listed in the main table.

   b. (U) For the silt (or other layer).

      (1) (U) For V_p: increase V_p as above for silt-clay.

      (2) (U) For k_p: vary k_p along line "B" and "C" (Figure 7).

(3) (U) Other properties: as above for silt-clay.

3. (U) It should be noted that in areas where turbidites form abyssal plains or fans (such as in the Oman Basin, Arabian Fan, and Somali Basin), the reflectors usually represent coarser sediments spilling discontinuously from leveed channels. These reflectors cannot usually, be followed over very great distances, nor correlated from area to area. Any detail, as above, is a gross generalization of widely varying layers (in thickness and properties).

4. (U) The values listed in the main, general table for "Sfc" (surface) are composite, proportional values for the first one meter of sediment (illustrated above). Other properties in three cores for 0-1 m depth are as follows (silt-clay porosity was salt corrected from Core 4 in center of basin; silt porosity from velocity-porosity relations of other data).

Property	Silt-clay	Silt
Velocity ratio	0.98	1.07
	Composite: 1.00	
Porosity,%	71	55
	Composite: 68	
Mean grain size,	8.39	6.09
(No. in sample)	(46)	(6)
Grain density, g/cm^3	Average of all samples: 2.73	
(no. in sample)		(56)

5. (U) Although the generalized illustration, above, indicates a sharp top boundary between the silt-clay and silt layers, it is more apt to be gradational in all properties.

TABLE 1A-1. (U) IN SITU PROPERTIES OF BOTTOM WATER. (U)

True Depth	T, °C	S, ppt	P, kg/cm^2	Sound speed, m/sec	Density, g/cm^3	Impedance, $g/cm^2 sec \times 10^5$
3348	1.83	34.74	346.7	1514.5	1.04306	1.57971

END of Model 1a

(C) Geoacoustic Model: 3a Area: Arabian Sea, Central Arabian Fan (C)

Location: $15^{o}44'N$ Lat.: $64^{o}32'E$ Long.

Water Depth: Echo-Sounder: 2081fm; 3805 m; set at 1500 m/s
Corrected: 2089 fm; 3820 m (Matthew's Tables)

Province and Description of the seafloor: Abyssal Plain (abyssal Deep-Sea Fan) Province. The Arabian Fan (or "Cone") was formed by very thick accumulations of turbidity current deposits overlying basalt. The sediments are transported through natural, leveed channels from sources in northern India and Pakistan, and deposited on the fan.

Layer No.	Material	Thickness s	Thickness m	Depth, m	Velocity, m/s V_p (1)	V_s (2)	Attenuation, k_p (3)		k_s (4)		Density, g/cm^3 (5)
	Btm Water				1521.5						1.04514
	Seafloor										
	Sediment			Sfc	1506	125	0.05	0.10	0.20	15.0	1.57
				100	1624	361	0.07	0.11	0.19	16.5	1.65
				200	1736	435	0.10	0.12	0.17	18.0	1.78
				300	1844	494	0.12	0.13	0.16	19.5	1.90
	and			400	1948	562		0.14		21.0	2.02
				500	2047	635		0.14		21.0	2.10
				600	2142	714		0.12		18.0	2.14
				700	2234	780		0.11		16.5	2.17
	Sedimentary	1.30	3540	800	2321	850		0.10		15.0	2.21
1				900	2406	915		0.08		12.0	2.24
	Rock			1000	2487	975		0.07		10.5	2.27
				1500	2852	1260		0.04		6.0	2.38
				2000	3166	1505		0.02		3.0	2.47
				2500	3456	1728		0.02		3.0	2.53
				3000	3747	1874		0.02		3.0	2.58
				3500	4065	2033		0.02		3.0	2.62
				3530-	4085	2043		0.02		3.0	2.62
2	Basalt			3530+	5400	2744		0.02		0.07	2.72

TABLE 3A-1. (C) IN SITU PROPERTIES OF BOTTOM WATER. (U)

True Depth, m	T, ^{o}C	S, ppt	P, kg/cm^2	Sound speed, m/s	Density, g/cm^3	Impedance, g/cm^2s $x10^5$
3820	1.73	34.72	395.9	1521.5	1.04514	1.59018

(cont)

(C) Model 3a (cont) (U)

Notes (for further derivation of values and discussions see Hamilton and Sachman, 1979) (U)

1. (U) V_p (Compressional Wave (Sound) Velocity).

   a. (U) First layer.

   $$V_p = 1.506 + 1.20D - 0.253D^2 + 0.034D^3$$

   where V_p is in km/s, and depth in the seafloor, D, is in km

   b. (U) Lower Layers: V_ps from literature.

2. (U) V_s (Shear Wave Velocity). From unpublished study by Hamilton of V_p/V_s ratios in marine sediments and rocks. Basalt V_s from Christensen and Salisbury (1975).

3. (U) k_p (Constant in: attenuation of compressional waves, α_p, in dB/m = $k_p f$; where f is frequency in kHz). The three listed values to 300 m are: probable minimum, recommended for first trial in bottom loss modeling, and probable maximum. From Hamilton (1972, 1974, 1976a).

4. (U) ks (Constant in: attenuation of shear waves, α_s, in dB/m = $k_s f$; where f is frequency in kHz. Based on Hamilton (1976c) at surface; proportional to k_p at depth.

5. (U) Density (Saturated bulk density, in situ). Surface density computed from core data. Density at depth from Hamilton (1978, 1976b). Basalt density from Christensen and Salisbury (1975).

6. (U) General

   a. (U) "Thickness, s" (in seconds of one-way sound travel time) from reflection records. "Thickness, m" from one-way travel time and layer mean velocity.

   b. (U) In the above model, the "Sfc" values are a composite of the 0-3 m depth interval. For a detailed model of this interval see the diagram and notes below.

7. (U) The relationships between Geoacoustic Model 3a and the other models in Area 3 (3b, 3c) are indicated in the accompanying diagram, which also illustrates water depths and sediment thicknesses (see also figure 3 for reflection records along this track).

(cont)

Detail of First Three Meters

Layer No.	Material	Thickness, s	Thickness, m	Depth, m	Velocity, m/s V_p (1)	V_s (2)	Attenuation, k_p (3)		k_s (4)		Density, g/cm^3 (5)
Btm					1521.5						1.04514
Seafloor											
1a	Silt clay		2.8	Sfc	1491	115	0.05	0.10	0.20	15.0	1.55
				2.8-	1494	128		0.10		15.0	1.55
1b	Sand-silt-clay		0.2	2.8+	1610	175		0.60		13.0	1.80
				3.0-							

Notes (U)

1. (U) The geoacoustic models (such as in the main table) showing thick sediment and sedimentary rock sections over "acoustic basement" (such as basalt) are generalized and do not account for the multiple reflectors as seen (usually at high frequencies), for example, in the 3.5-kHz records, or in cores.

2. (U) If a detailed, multireflector model is desired, the above sequence of a thicker silt-clay layer and a thinner silt (or other) layer can be alternated to any desired depth. If so, the property values can be corrected for depth as follows:

   a. (U) For the silt-clay layer.

      (1) (U) For V_p: increase V_p using gradients computed from the V_p vs. depth equation.

      (2) (U) Other properties: vary the value of the property with depth using the appropriate gradient from the values listed in the main table.

   b. (U) For the silt (or other layer).

      (1) (U) For V_p: increase V_p as above for silt-clay.

      (2) (U) For k_p: vary k_p along line "B" and "C" (fig 7).

      (3) (U) Other properties: as above for silt-clay.

(cont.)

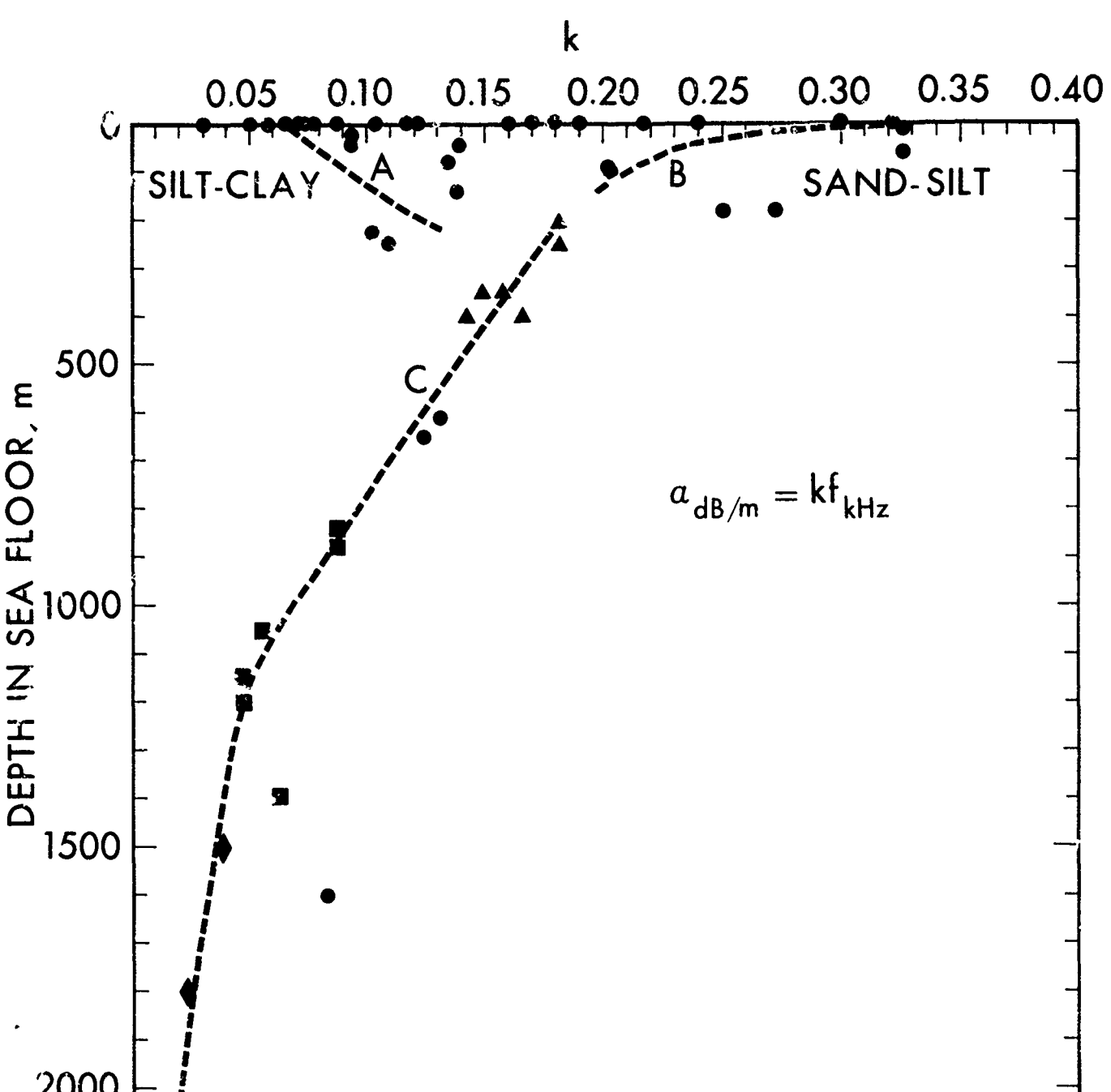

Figure III-7. (U) Attenuation of compressional waves (expressed as the constant k, in attenuation in dB/m, $a_p = kf_{kHz}$) versus depth in the sea floor (from Hamilton, 1976a). Symbols: circles, measurements from the literature; triangles, squares, and diamonds represent the first, second, and third layers, respectively, in the sea floor in seven areas (from Neprochnov, 1971). See Hamilton (1976a) for additional information. (U)

3. (U) It should be noted that in areas where turbidites form abyssal plains or fans (such as in the Oman Basin, Arabian Fan, and Somali Basin), the reflectors usually represent coarser sediments spilling discontinuously from leveed channels. These reflectors cannot, usually, be followed over very great distances, nor correlated from area to area. Any detail, as above, is a gross generalization of widely varying layers (in thickness and properties).

4. (U) The values listed in the main, general table for "Sfc" (surface) are composite values for the 0-3 m depth interval (illustrated above). Some averaged properties in eight cores for this interval, other than those listed above, are as follows (silt-clay porosity is based on salt-corrected value in the first two samples in each core; sandsilt-clay porosity based on velocity-porosity relations from other data).

Property	Silt-clay	Sand-silt-clay
Velocity ratio	0.98 Composite: 0.99	1.06
Porosity, %	70 Composite: 69	55
Mean grain size, (No. in sample)	8.55 (466)	6.86 (2)
Grain density, g/cm^3	Avg. all samples: 2.74	
(No. in sample)		(457)

5. (U) Although the generalized illustration, above, indicates a sharp top boundary between the silt-clay and sand-silt-clay layers, it is more apt to be gradational in all properties.

END of Model 3a

GEOACOUSTIC MODELS 3A, 3B, AND 3C
(NOT TO SCALE)

GEOACOUSTIC MODEL 3A

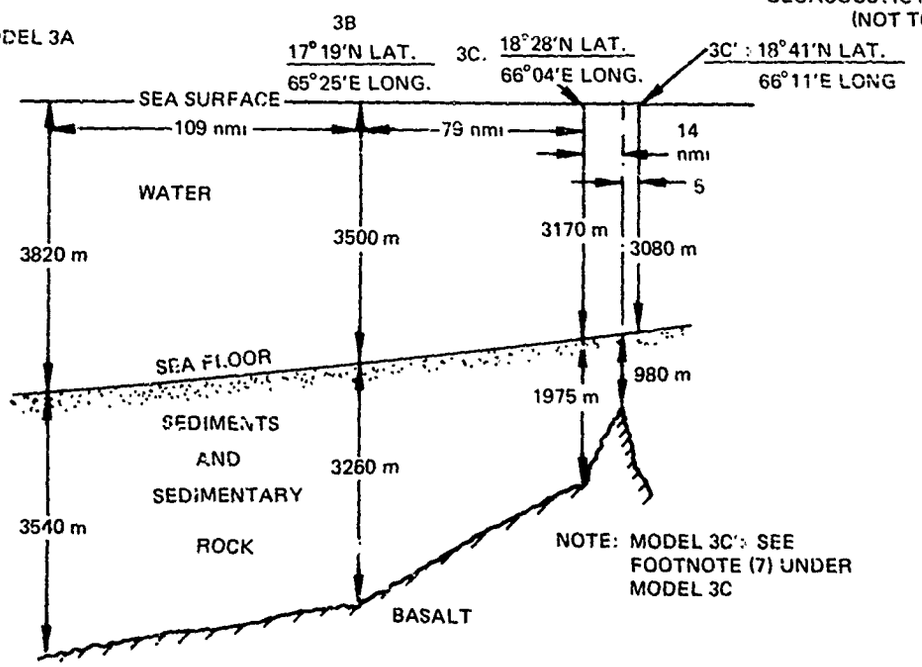

(C) Geoacoustic Model: 3b Area: Arabian Sea, Central Arabian Fan (C)

Location: $17^{o}19'N$ Lat.: $65^{o}25'E$ Long.

Water Depth: Echo-Sounder: 1908 fm: 3489 m: set at 1500 m/s
Corrected: 1914 fm: 3500 m (Matthews' Tables)

Province and Description of the seafloor: Abyssal Plain (Abyssal Deep-Sea Fan) Province. The Arabian Fan (or "Cone") was formed by very thick accumulations of turbidity current deposits overlying basalt. The sediments are transported through natural, leveed channels from sources in northern India and Pakistan, and deposited on the fan.

Layer No.	material	Thickness s	Thickness m	Depth, m	Velocity, m/s V_p (1)	V_s (2)	Attenuation k_p (3)		k_s (4)		Density, g/cm^3 (5)
	Btm Water				1516.5						1.04373
	Seafloor										
1	Sediment and Sedimentary Rock	1.23	3260	Sfc	11501	125	0.05	0.10	0.20	15.0	1.57
				100	1619	356	0.07	0.11	0.19	16.05	1.65
				200	1731	433	0.10	0.12	0.17	18.01	1.77
				300	1839	491	0.12	0.13	0.16	19.5	1.90
				400	1943	558		0.14		21.00	2.02
				500	2042	631		014		21.0	2.10
				600	2137	710		0.12		18.0	2.14
				700	2229	780		0.11		16.5	2.17
				800	2316	845		0.10		15.0	2.21
				900	2401	910		0.08		12.0	2.24
				1000	2482	975		0.07		10.5	2.24
				1500	2847	1255		0.04		6.0	2.38
				2000	3161	1500		0.02		3.0	2.47
				2500	3451	1726		0.02		3.0	2.53
				3000	3742	1871		0.02		3.0	2.58
				3260-	3902	1951		0.02		3.0	2.60
2	Basalt			3260+	5400	2744		0.02		0.7	2.72

TABLE 3B-1. (C) IN SITU PROPERTIES OF BOTTOM WATER. (U)

True Depth m	t, ^{o}C	S, ppt	P, kg/cm^2	Sound speed, m/sec	Density, g/cm^3	Impedance, g/cm^{2}sec x10^5
3500	1.74	34.73	362/5	1516.5	1.04373	1.58282

(cont)

(C) Model 3b (cont) (U)

Notes (for further derivation of values and discussion see Hamilton and Bachman, 1979) (U)

1. (U) V_p (Compressional Wave (Sound) Velocity),

   a. First layer

   $$V_p = 1.501 + 1.20D - 0.253D^2 + 0.034D^3$$

   where V_p is in km/s, and depth in the seafloor, D, is in km

   b. (U) Lower layers: V_ps from literature.

2. (U) V_s (Shear Wave Velocity). From unpublished study by Hamilton of V_p/V_s ratios in marine sediments and rocks. Basalt V_s from Christensen and Salisbury (1975).

3. (U) k_p (Constant in: attenuation of compressional waves, α_p, in dB/m = $k_p f$; where f is frequency in kHz). The three listed values to 300 m are: probable minimum, recommended for first trial in bottom loss modeling, and probable maximum. From Hamilton (1972, 1974, 1976a).

4. (U) k_s (Constant in: attenuation of shear waves, α_s, in dB/m = $k_s f$; where f is frequency in kHz. Based on Hamilton (1976c) at surface; proportional to k_p at depth.

5. (U) Density (Saturated bulk density, in situ). Surface density computed from core data. Density at depth from Hamilton (1978, 1976b). Basalt density from Christensen and Salisbury (1975).

6. (U) General

   a. (U) "Thickness, s" (in seconds of one-way sound travel time) from reflection records. "Thickness, m" from one-way travel time and layer mean velocity.

   b. (U) In the above model, the "Sfc" (surface) values are a composite for the 0-3 m depth interval. If a detailed model of this interval is desired: use detailed model as in 3a except change silt-clay V_ps to 1486 (Sfc, V_p ratio of 0.98) and 1489 at 2.8 m.

7. (U) The relationships between Geoacoustic Model 3b and the other models in Area 3 (3a, 3c) are indicated in the diagram in model 3a.

END of Model 3b

(C) Geoacoustic Model: 3c Area: Arabian Sea, Central Arabian Fan (C)

Location: $18^{o}28'N$ Lat. $66^{o}04'E$ Long.

Water Depth: Echo-Sounder: 1730 fm; 3164 m; set at 1500 m/s
Corrected: 1733 fm; 3170 m (Matthews' Tables)

Province and Description of the seafloor: Abyssal Plain (Abyssal Deep-Sea Fan) Province. The Arabian Fan (or "Cone") was formed by very thick accumulations of turbidity current deposits overlying basalt. The sediments are transported through natural, leveed channels from sources in northern India and Pakistan, and deposited on the fan.

Layer No.	Material	Thickness s	Thickness m	Depth, m	Velocity, m/s V_p (1)	V_s (2)	Attenuation, k_p (3)		k_p (4)		Density, g/cm^3 (5)
	Btm Water				1510.9						1.04227
	Seafloor										
	Sediment and			Sfc	1495	125	0.05		0.10	0.20	15.0	1.57
				100	1613	349	0.07		0.11	0.19	16.5	1.64
				200	1725	430	0.10		0.12	0.17	18.0	1.77
				300	1833	488	0.12		0.13	0.16	19.5	1.89
				500	2036	626			0.14		21.0	2.10
1	Sedimentary			600	2131	705			0.12		18.0	2.14
	Rock			700	2223	775			0.11		16.5	2.18
				800	2310	840			0.10		15.0	2.21
				900	2395	905			0.08		12.0	2.24
				1000	2476	970			0.07		10.5	2.20
				1500	2841	1250			0.04		6.0	2.39
				1975-	3140	1485			0.02		3.0	2.46
2	Basalt			1975+	5400	2744			0.02		0.07	2.72

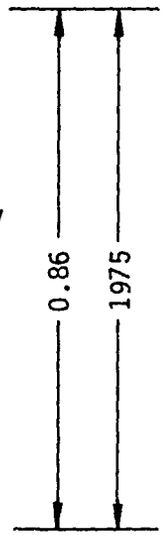

TABLE 3C-1. (C) IN SITU PROPERTIES OF BOTTOM WATER. (U)

True Depth, m	T, ^{o}C	S, ppt	P, kg/cm^2	Sound speed, m/s	Density, g/cm^3	Impedance, g/cm^2s $x10^5$
3170	1.80	34.74	328.2	1510.9	1.04227	1.57477

(cont)

(C) Model 3c (cont) (U)

Notes (for further derivation of values and discussions see Hamilton and Bachman, 1979) (U)

1. (U) V_p (Compressional Wave (Sound) Velocity)
   a. (U) First layer
      $V_p = 1.495 + 1.20D - 0.253D^2 + 0.034D^3$
      where V_p is in km/s, and depth in the sea floor, D, is in km
   b. (U) Lower layers: V_ps from literature.

2. (U) V_s (Shear Wave Velocity). From unpublished study by Hamilton of V_p/V_s ratios is marine sediments and rocks. Basalt V_s from Christensen and Salisbury (1975).

3. (U) k_p (Constant in: attenuation of compressional waves, α_p, in dB/m = $k_p f$; where f is frequency in kHz). The three listed values to 300 m are: probable minimum, recommended for first trial in bottom loss modeling, and probable maximum. From Hamilton (1972, 1974, 1976a).

4. (U) K_s (Constant in: attenuation of shear waves, α_s, in dB/m = $k_s f$; where f is frequency in kHz. Based on Hamilton (1976c) at surface; proportional to k_p at depth.

5. (U) Density (Saturated bulk density, in situ). Surface density computed from core data. Density at depth from Hamilton (1978, 1976b). Basalt density from Christensen and Salisbury (1975).

6. (U) General
   a. (U) "Thickness, s" (in seconds of one-way sound travel time) from reflection records. "Thickness, m" from one-way travel time and layer mean velocity.
   b. (U) In the above model, the "Sfc" values are a composite for the 0-3 m depth interval. For a detailed model of this interval: use the detailed model as in 3a except change silt-clay V_p to 1480 (Sfc, V_p ratio of 0.98) and 1483 at 2.8 m.

7. (U) Near the end of run S1 the acoustic basement rises into a ridge as indicated in the diagram in model 3a. This ridge, now covered by about 980 m of sediments, is verified as an elongate NW-SE trending ridge by Naini (personal communication, 1977). For a geoacoustic model over the ridge (3c'), use all information listed under model 3c to a depth of 980 m.

END of Model 3c

(C) Geoacoustic Model: 4a Area: Somali Basin, off northeast Africa (C)

Location: 05°08'N Lat. 52°16'E Long.

Water Depth: Echo-Sounder: 2769 fm; 5064 m; set at 1500 m/s
Corrected: 2789 fm; 5100 m (from station data)

Province and Description of the seafloor: Abyssal Plain Province. The northern Somali Basin, between the east African continental rise and Chain Ridge, is composed of a thick layer of flat-lying turbidite sediments and sedimentary rocks overlying basalt.

Layer No.	Material	Thickness s	Thickness m	Depth, m	Velocity, m/s V_p (1)	V_s (2)	Attenuation k_p (3)	k_s (4)		Density g/cm^3 (5)
	Btm Water				1543.8					1.05065
	Seafloor									
	Sediment and Sedimentary Rock	0.76	1580	Sfc	1528	125	0.04	0.08	0.18	15.0	1.42
				100	1649	390	0.06	0.09	0.17	19.3	1.68
				200	1760	448	0.09	0.11	0.16	23.5	1.81
				300	1864	507	0.11	0.12	0.15	25.7	1.93
				400	1960	570		0.14		30.0	2.03
				500	2048	636		0.14		30.0	2.11
				600	2128	702		0.12		25.7	2.14
				700	2202	755		0.11		23.5	2.17
				800	2269	810		0.10		21.4	2.19
				900	2330	855		0.08		17.1	2.22
				1000	2385	900		0.07		15.0	2.24
				1500	2582	1050		0.04		8.6	2.30
				1595-	2607	1070		0.03		6.4	2.31
				1595+	3500	1750		0.03		3.0	2.54
2	Sedimentary Rock	0.25	940	2065	3750	1875		0.02		3.0	2.58
				2535-	4000	2000		0.02		3.0	2.61
3	Basalt			2535+	5300	2680		0.02		0.07	2.70

TABLE 4A-1. (C) IN SITU PROPERTIES OF BOTTOM WATER. (U)

True Depth, m	T, °C	S, ppt	P, kg/cm^2	Sound speed m/s	Density g/cm^3	Impedance, g/cm^{2}s
5100	1.38	34.69	529.6	1543.8	1.05065	1.62199

(cont)

(C) Model 4a (cont) (U)

Notes (for further derivation of values and discussions see Hamilton and Bachman, 1979) (U)

1. (U) V_p (Compressional Wave (Sound) Velocity)

   a. (U) First layer

   $$V_p = 1.528 + 1.25D - 0.45D^2 + 0.0568D^3$$

   where V_p is in km/s, and depth in the seafloor, D, is in km

   b. (U) Lower layers: V_ps from literature.

2. (U) V_s (Shear Wave Velocity). From unpublished study by Hamilton of V_p/V_s ratios in marine sediments and rocks. Basalt V_s from Christensen and Salisbury (1975).

3. (U) k_p (Constant in: attenuation of compressional waves, α_p, in dB/m = $k_p f$; where f is frequency in kHz). The three listed values to 300 m are: probable minimum, recommended for first trial in bottom loss modeling, and probable maximum. From Hamilton (1972, 1974, 1976a).

4. (U) k_s (Constant in: attenuation of shear waves, α_s, in dB/m = $k_s f$; where f is frequency in kHz. Based on Hamilton (1976c) at surface; proportional to k_p at depth.

5. (U) Density (Saturated bulk density, in situ). Surface density computed from core data. Density at depth from Hamilton (1978, 1976b). Basalt density from Christensen and Salisbury (1975).

6. (U) General

   a. (U) "Thickness, s" (in seconds of one-way sound travel time) from reflection records. "Thickness, m" from one-way travel time and layer mean velocity.

   b. (U) In the above model, the "Sfc" (surface) values are a composite for the 0-3 m depth interval. For a detailed model of this interval see the diagrams and notes below.

(cont)

Detail of First Three Meters

Layer No.	Material	Thickness s	Thickness m	Depth m	Velocity, m/s V_p (1)	V_s (2)	Attenuation, k_p (3)		k_s (4)		Density, g/cm^3 (5)
	Btm Water			1543.8							1.05065
	Sea Floor										
				sfc	1513	115	0.03	0.07	0.17	15.0	1.39
1a	Silt-clay		2.8	2.8-	1517	128	0.03	0.07	0.17	15.0	1.39
				2.8+							
1b	Sand-silt-clay		0.2	3.0-	1635	175	0.04	0.06	0.08	13.0	1.78

Notes (U)

1. (U) The geoacoustic models (such as in the main table) showing thick sediment and sedimentary rock sections over "acoustic basement" (such as basalt) are generalized and do not account for the multiple reflectors as seen (usually at high frequencies), for example, in the 3.5 kHz records, or in cores.

2. (U) If a detailed, multireflector model is desired, the above sequence of a thicker silt-clay layer and a thinner silt (or other) layer can be alternated to any desired depth. If so, the property values can be corrected for depth as follows:

   a. (U) For the silt-clay layer.

      (1) (U) For V_p: increase V_p using gradients computed from the V_p vs. depth equation.

      (2) (U) Other properties: vary the value of the property with depth using the appropriate gradient from the values listed in the main table.

   b. (U) For the silt (or other layer).

      (1) (U) For V_p: increase V_p as above for silt-clay.

      (2) (U) For k_p: vary k_p along lines "B" and "C" (fig 7).

      (3) (U) Other properties: as above for silt-clay.

(cont)

3. (U) It should be noted that in areas where turbidites form abyssal plains or fans (such as in the Oman Basin, Arabian Fan, and Somali Basin), the reflectors usually represent coarser sediments spilling discontinuously from leveed channels. These reflectors cannot, usually, be followed over very great distances, nor correlated from area to area. Any detail, as above, is a gross generalization of widely varying layers (in thickness and properties).

4. (U) The values listed in the main, general table for "Sfc" (surface) are composite values for the 0-3 m depth interval (illustrated above). Some averaged properties in four cores for this interval, other than those listed above, are as follows (porosity in silt-clay (0-100 cm) is salt corrected; porosity in sand-silt-clay based on velocity porosity relations from other data).

Property	Silt-clay	Sand-silt-clay
Velocity ratio	0.98	1.06
	Composite: 0.99	
Porosity, %	79	55
	Composite: 77	
Mean grain size, Φ	8.95	5.48
(No. in sample)	(182)	(2)
Grain density, g/cm^3	Avg. all samples: 2.66	
(No. in sample)		(179)

5. (U) Although the generalized illustration, above, indicates a sharp top boundary between the silt-clay and sand-silt-clay layers, it is more apt to be gradational in all properties.

END of Model 4a

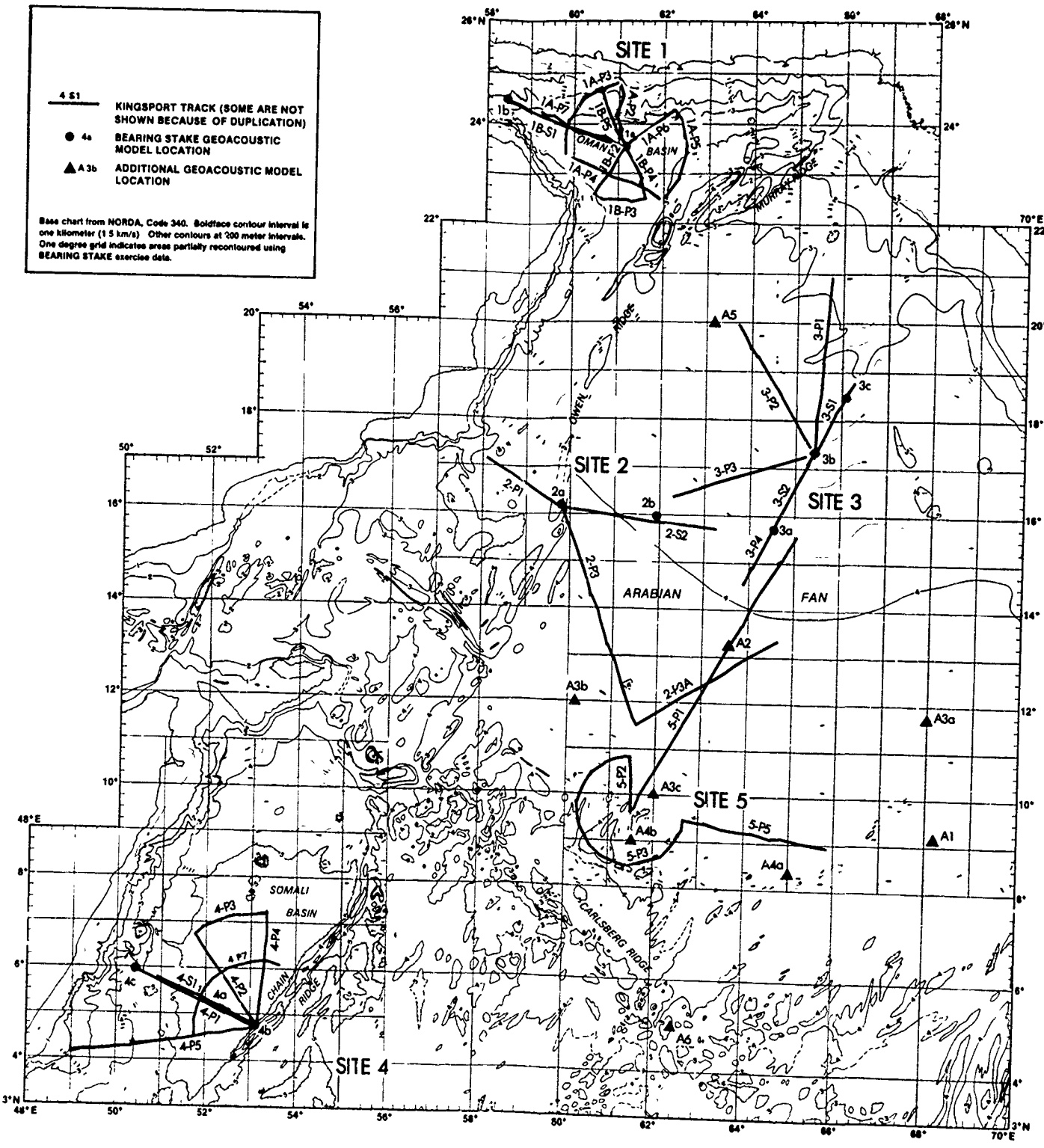

Figure III-1. (C) Location chart of the expedition, Northwest Indian Ocean. (C)

REFERENCES (U)

Bachman, R.T., and Hamilton, E.L. (1976). Density, porosity, and grain density of sample from Deep Sea Drilling Project Site 222 (leg 23) in the Arabian Sea, Jour. Sedimentary Petrology, v. 46, p. 654-658.

Bunce, E.T., Bowin, C.O., and Chase, R.L. (1966). Preliminary results of the 1964 cruise of R.V. Chain to the Indian Ocean, Phil. Trans. Roy. Soc. London, A, v. 259, p. 218-226.

Christensen, N.I., and Salisbury, M.H. (1975). Structure and constitution of the lower oceanic crust, Reviews of Geophysics and Space Physics, v. 13, p. 57-86.

Fisher, R.L., et al. (1974). Initial Reports of the Deep Sea Drilling Project, v. 24, U.S. Government Printing Office, Washington, D.C.

Hamilton, E.L. (1972). Compressional wave attenuation in marine sediments, Geophysics, v. 37, p. 620-646.

Hamilton, E.L. (1974). Geoacoustic models of the sea floor, in Physics of Sound in Marine Sediments, edited by L. Hampton, p. 181-221, Plenum Press, N.Y., 567 pp.

Hamilton, E.L. (1976a). Sound attenuation as a function of depth in the sea floor, Jour. Acoust. Soc. Am., v. 59, p. 528-535.

Hamilton, E.L. (1976b). Variations of density and porosity with depth in deep sea sediments, Jour. Sedimentary Petrology, v. 46, p. 280-300.

Hamilton, E.L. (1976c). Attenuation of shear waves in marine sediments, Jour. Acoust. Soc. Am., v. 60, p. 334-338.

Hamilton, E.L. (1976d). Shear-wave velocity versus depth in marine sediments: a review, Geophysics, v. 41, p. 985-996.

Hamilton, E.L. (1978). Sound velocity-density relations in sea-floor sediments and rocks, Jour. Acoust. Soc. Am., v. 63, p. 366-377.

Hamilton, E.L. and Bachman, R.T. (1979). "Geoacoustic Models of the Sea Floor: Gulf of Oman, Arabian Sea, and Somali Basin (U)," Naval Ocean Systems Center, San Diego, California. CONFIDENTIAL.

Houtz, R.E. (1974). Preliminary study of global sediment sound velocities from sonobuoy data, in Physics of Sound in Marine Sediments, edited by L. Hampton, p. 519-535, Plenum Press, N.Y.

Naini, B., and Talwani, M. (1977). Sediment distribution and structures in the Indus Cone and the western continental margin of India (Arabian Sea), Trans. Am. Geophys. Union, v. 58, p. 405 (abstract).

Neprochnov, Yu. P. (1971). Seismic studies of the crystal structure beneath the sea and oceans, Oceanology (English translation), v. 11, p. 709-715.

White, R.S., and Klitgord, K. (1976). Sediment deformation and plate tectonics in the Gulf of Oman, Earth Planet. Sci. Lett., v. 32, p. 199-209.

Whitmarsh, R.B., et al. (1974). Initial Reports of the Deep Sea Drilling Project, v. 23, U.S. Government Printing Office, Washington, D.C.

CHAPTER IV

BOTTOM INTERACTION (U)

by

S. K. Mitchell and K. C. Focke

Environmental Sciences Division

Applied Research Laboratories

The University of Texas at Austin

Austin, Texas 78712

CHAPTER IV. BOTTOM INTERACTION (U)

CONTENTS (U)

CHAPTER IV. BOTTOM INTERACTION (U)

IV.1 (U) INTRODUCTION

(U) The primary data recording system devoted to analysis of bottom interaction in BEARING STAKE was the vertical ACODAC (VAC) recorder. The VAC data were analyzed at ARL:UT during FY77 (Mitchell et al., 1978); these bottom loss results form the bulk of the data used in this section. In addition, the BMA recordings from Sites 5 and 1A included portions which were analyzed for bottom interaction (Focke, 1978); some of these results are presented here. To obtain estimates of geophysical parameters, wide-angle profiling records were obtained at Sites 4 and 5 (Naval Ocean Systems Center, 1977). These data contributed to the geophysical models presented in chapter III of this report; in turn, those results contributed to the bottom interaction modeling presented in section IV.3 of this chapter.

(U) Bottom interaction analysis work has included the interpretation of BEARING STAKE bottom interaction data in terms of geoacoustic models and the determination from the data of the values of geophysical parameters. Results from the initial phases of this study are used here; methods and results are described in detail by Mitchell et al. (1979).

(U) Locations of sites from which data are available are given in figure 1. Site particulars are given in table 1. The shading of figure 1 delineates the different geophysical provinces on the basis of material supplied by Hamilton (1978).

(C) This chapter provides estimates of bottom loss versus grazing angle and frequency for the different areas of the Northwest Indian Ocean. To the extent possible, these are supported by data available from BEARING STAKE itself. In addition, it is shown that, in the major basin areas, calculated bottom loss curves agree very well at all frequencies with the measured data. These calculations are based upon the basic geoacoustic models of chapter III, with values of some acoustic parameters modified by using the actual acoustic data. These parameters are presented in section IV.3.

(C) In general, it was found that the bottom loss in the Northwest Indian Ocean basin areas was low; actual values are given in the following section. An important result of the current analysis is that these bottom loss values can best be explained by assuming that attenuations at depths in these ocean sediments were considerably lower than predicted (only 15% to 40% of predicted values).

IV.2 (U) BOTTOM LOSS DATA

(U) Bottom loss measurements from the BEARING STAKE exercise are presented in figures 2 through 5. Data recording, processing, and data quality are described by Mitchell et al. (1978). The data in figures 2 and 3 (Sites 1B and 4) are averages over many samples from three source depths, two receiver depths, and the indicated numbers of reflections. The data from Site 3 (fig 4) are estimated from multipath propagation loss to near-bottom receivers; problems with the VAC (which are discussed by Mitchell et al. 1978) prevented direct measurement of bottom loss at Site 3. The data from Site 5 are averages over three source depths (Focke, 1978) with a single receiver depth being used.

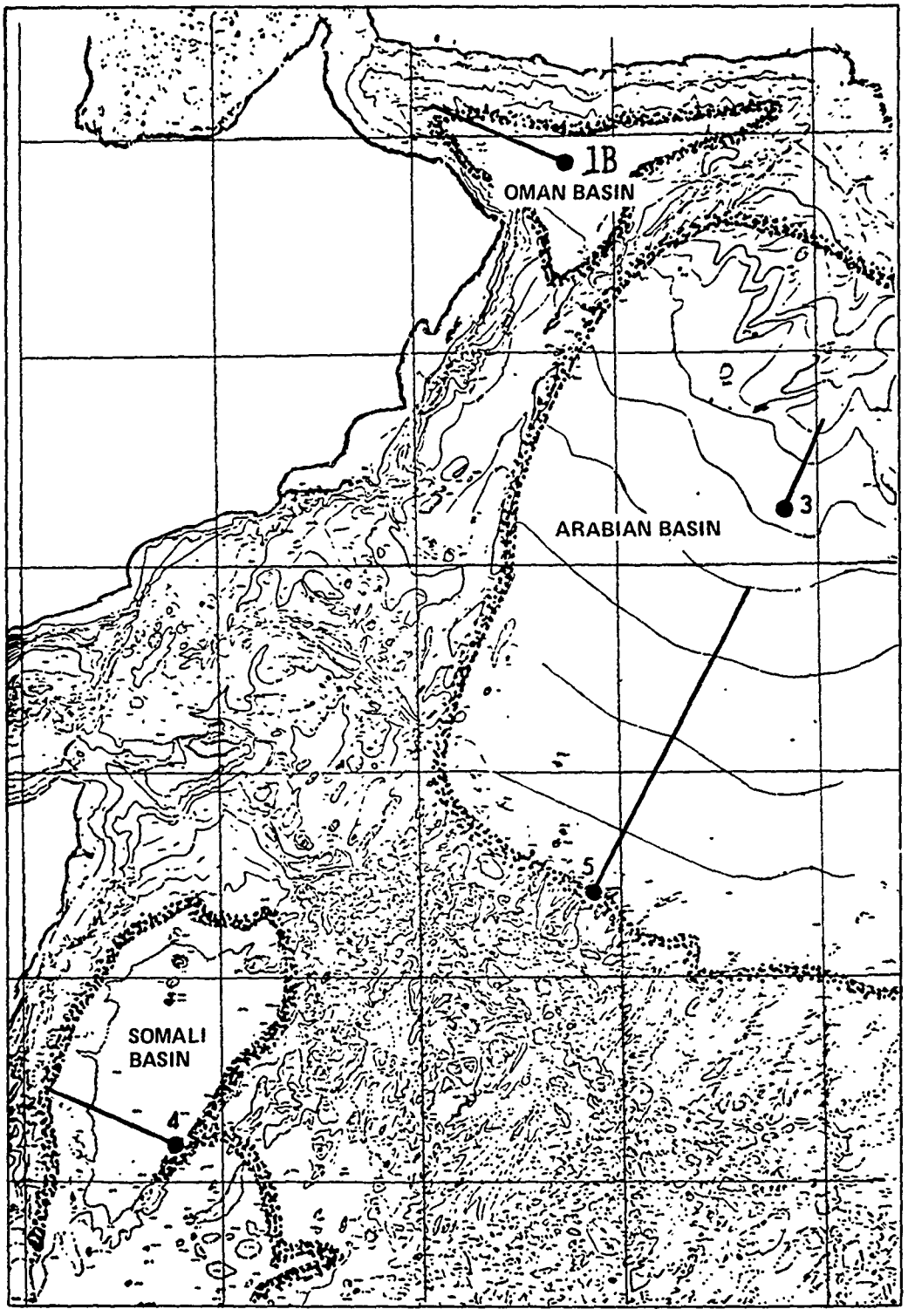

Figure IV-1. (C) BEARING STAKE bottom interaction data locations and source tracks. (U)

TABLE IV-1. (C) SUMMARY OF AVAILABLE BOTTOM LOSS DATA (U)

Site	Location	Frequency Range (Hz)	Comments
1	Oman Basin	20-500	Bottom limited — measurement difficulties below 10-deg grazing angle.*
3	Arabian Basin	20-500	Estimates only because of VAC failure.*
5	Arabian Basin	20-1200	Bottom limited — measurement difficulties below 10-deg grazing angle.**
4	Somali Basin	20-500	*

*Mitchell et al., 1978.
**Focke, 1978.

(C) The extent of the ocean bottom covered by the bottom loss averages for each site is shown by the source tracks on figure 1. These tracks cross a large part of the basins, so the bottom loss samples for each site are from a large area. However, at each site, uniform results are obtained from along the entire track. This indicates uniform bottom reflectivity within each basin area. This result is consistent with the geophysical descriptions which show uniform sediment types in each basin.

(C) The bottom loss data shown for the Arabian Basin, particularly for Site 5 (fig 5), show very little loss. This is demonstrated by figure 6, which shows the envelope of the signal from a shot at long range received at Site 5. The presence of the reflected-arrival pulses after many reflections is another indication of the very low bottom loss in the area.

IV.3 (U) MODELING

(C) The BEARING STAKE acoustic assessment requires accurate estimates of bottom loss for a major portion of this region. Bottom loss values are needed for frequencies ranging from 25 Hz up to 1 kHz. During the exercise itself, bottom loss measurements were taken at selected sites for frequencies that generally were 500 Hz or less (Mitchell, 1978). Bottom loss estimates are being extended to other regions and other frequencies through the use of numerical models of the bottom loss.

(U) Modeling of bottom loss requires parameters from a geoacoustic model. Table 2 presents the parameters needed to model the bottom loss at Site 1B. Of necessity, many of the parameters defining a geoacoustic model are extrapolated or predicted values, since these parameters are difficult to measure in situ. These estimates are based on data reported in the literature and on laboratory measurements of physical properties of sediment samples (Hamilton,

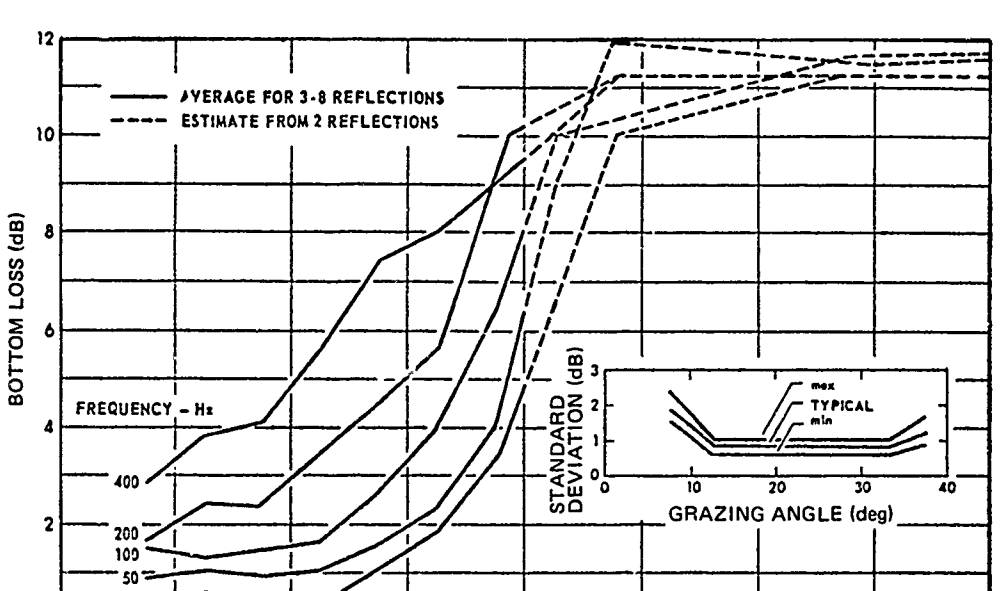

Figure IV-2. (C) Measured bottom loss at Site 1B. See figure 1 for source track. (U)

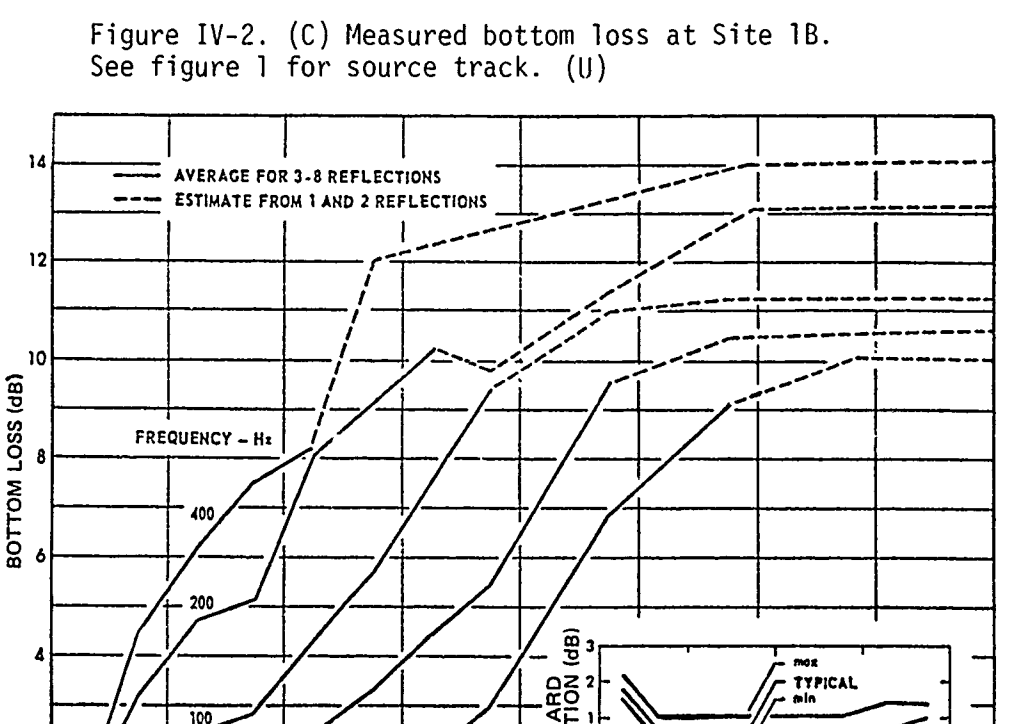

Figure IV-3. (C) Measured bottom loss at Site 4. (U)

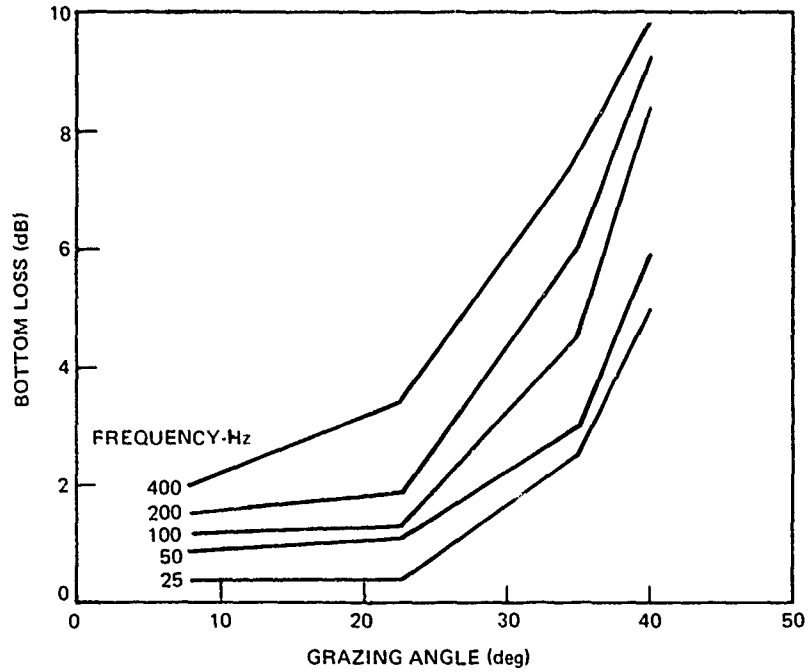

Figure IV-4 (C) Estimated bottom loss at Site 3. See figure 1 for source track. (U)

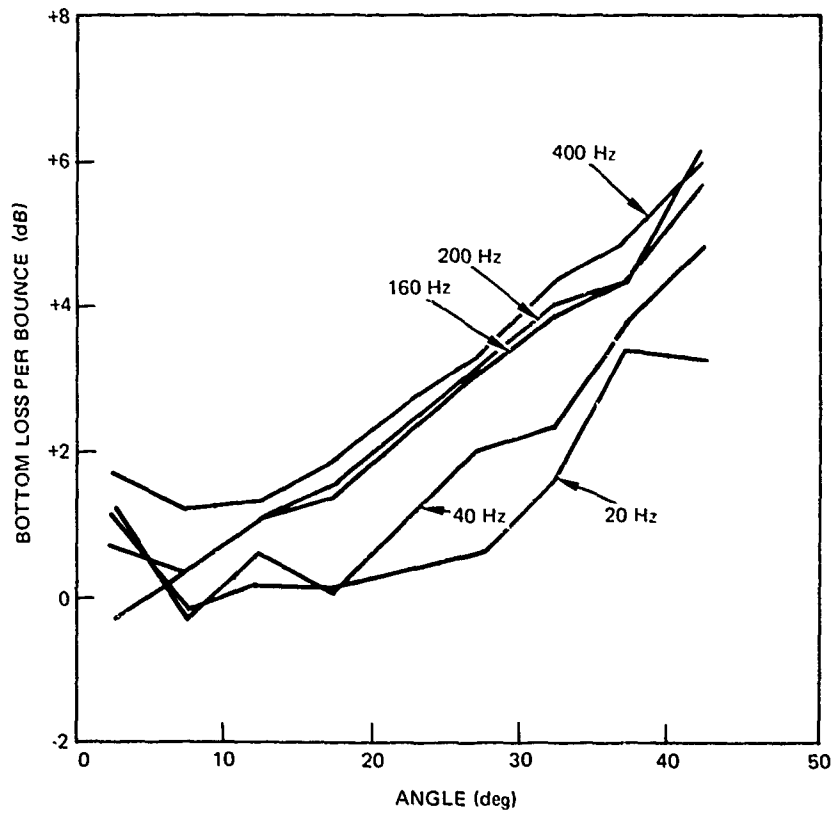

Figure IV-5. (C) Measured bottom loss at Site 5. See figure 1 for source track. (U)

TABLE IV-2. (C) INITIAL GEOACOUSTIC INPUTS FOR BOTTOM LOSS CALCULATIONS IN THE OMAN BASIN (FROM REF 4). (U)

Layer Material	Depth(m)	Velocity(m/s)	Attenuation-k_p (dB/m - kHz)	Density (g/cm^3)
Bottom Water		1514.5		1.04306
Sediment	0.	1515.	.10	1.59
	100.	1638.	.11	1.67
	200.	1750.	.12	1.80
	300.	1851.	.13	1.91
	400.	1943.	.14	2.02
	500.	2026.	.14	2.10
	600.	2101.	.12	2.13
	700.	2168.	.11	2.15
	800.	2230.	.10	2.18
	900.	2286.	.08	2.20
	1000.	2337.	.07	2.22
	1100.	2385.	.06	2.24
	1200.	2429.	.05	2.25
	1231.	2443	.05	2.26
Sedimentary Rock	1231.	2565.	.05	2.30

Substrate shear wave velocity 1040 m/s
Substrate shear wave attenuation 7.5 dB/m - kHz

1974). Therefore, the geoacoustic parameter estimates for a particular area generally can be improved by using actual acoustic data prior to their use as parameter inputs for prediction of bottom loss.

(U) Modifications to the geoacoustic parameters which are given here were based on comparisons between measured and calculated bottom loss. The estimates from Hamilton (1978) of the geoacoustic parameters, such as those in table 2, were used as inputs for the first comparison. Those parameters which have large uncertainties and which have a major effect on the predicted loss were then varied to improve the comparison between the calculated and the measured values of bottom loss.

(U) An understanding of how the various geoacoustic parameters affect the bottom loss calculations can aid in making modifications to these parameters.

(U) A simple picture of energy interacting with the ocean bottom would combine energy reflected from the water/sediment interface and energy penetrating into the sediment and then being reflected or refracted back into the water (fig 7). The energy reflected at the sediment surface can be determined by calculating a reflection coefficient. The amount of energy reflected or refracted through the sediment can be determined by tracing rays through an attenuating medium.

(U) The reflection due to impedance mismatch at the water/sediment interface can be determined by matching the boundary conditions at the interface. By following Brekhovskikh (1960), the Rayleigh reflection coefficient is found to be

$$V = \frac{m \sin\theta - (n^2 - \cos^2\theta)^{1/2}}{m \sin\theta + (n^2 - \cos^2\theta)^{1/2}} \quad , \qquad (1)$$

$$m = \rho_s/\rho_w \quad ,$$

$$n = c_w/c_s \quad ,$$

where θ is grazing angle in the water, ρ is density, c is sound speed, and the subscripts denote either the sediment (s) or the water (w).

As the grazing angle increases, V rapidly converges to the high-angle limit

$$V = \frac{\rho_s \, c_s - \rho_w \, c_w}{\rho_s \, c_s + \rho_w \, c_w} \quad , \qquad (2)$$

obtained by setting the grazing angle to 90^o. Since c_s and c_w generally differ by less than 2%, this high angle limit is determined primarily by the density contrast of the interface.

(U) Energy transmitted through the bottom will be influenced by the structure of the bottom. An increase in path length, $L(\theta)$, will tend to increase the loss for the penetrating ray. As an example, if the bottom has a constant attenuation with depth, α, the loss in decibels incurred along a ray path through the bottom will be

$$\text{Loss} = \alpha L(\theta) \qquad (3)$$

As the grazing angle increases, the path length and thus the loss increase until a reflecting layer at some depth is reached (Hawker et al., 1979). The sound speed gradient and the interface sound speed ratio also affect the path length. Doubling the sound speed gradient will decrease $L(\theta)$ by one-half. When n, the sound speed ratio, is near 1, a 1% variation in this ratio can vary the path length from 0 to over 500 m for small grazing angles. If this ratio is greater than 1, angles below the critical angle will have zero path length.

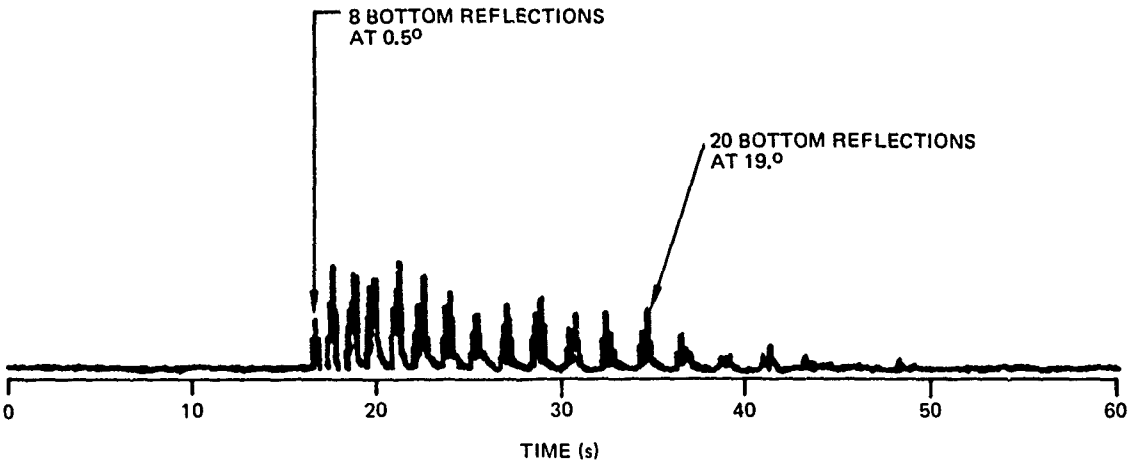

Figure IV-6, (C) Envelope of 91-m SUS arrival at Site 5 from 465-km range. The long duration indicates very low bottom loss in the Arabian Basin. (C)

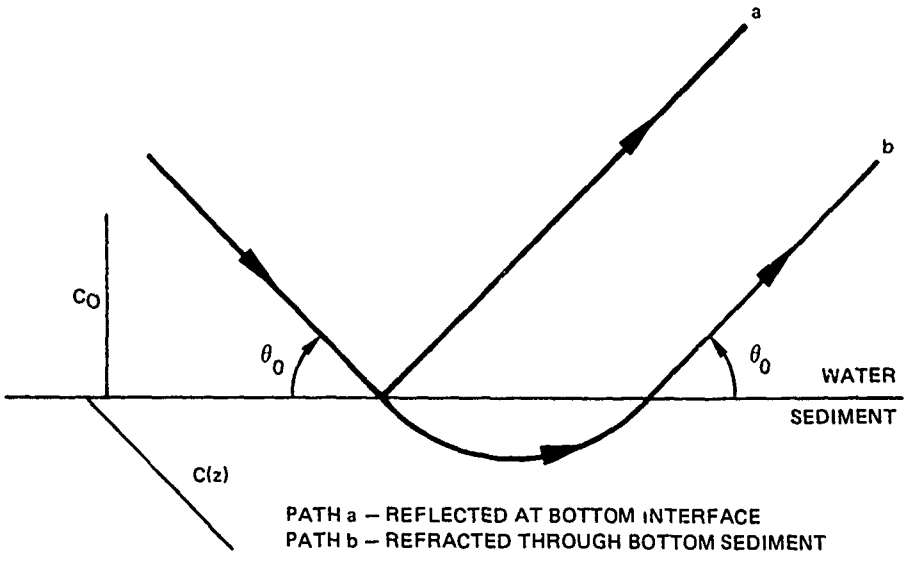

Figure IV-7. (U) Ray path presentation of bottom interacting energy. (U)

(U) Figure 8 presents a comparison between a computed (Hawker et al., 1979) bottom loss and eq 2 and 3. The geoacoustic inputs used in these calculations are those presented in table 2 and figure 9. The calculations were made at a frequency of 100 Hz. In this example at grazing angles greater than 40^{0} the bottom loss is dominated by the Rayleigh reflection and can be approximated by eq 2. Below 35^{0} the bottom loss fluctuates about the curve defined by the losses incurred along the ray paths (eq 3). The fluctuations result from phase interferences between the Rayleigh reflection and the bottom penetrating contributions. These fluctuations tend to disappear when the bottom loss calculations are averaged over a one-third octave band, as will be done for the remaining calculated curves.

(U) Variations in the geoacoustic parameters will change the relationship between curves a and b in figure 8. For example, changes in the interface density contrast will shift curve a up or down. Changes in the interface sound speed contrast will shift the lower portion of curve b left or right. Changes in the sound speed gradient or the attenuation will shift the upper portion of curve b left or right as well as changing the slope of curve b.

(U) All modifications to the geoacoustic parameters have been simple for the work reported here. For example, if the attenuation was to be decreased, it was decreased by the same factor at all depths. Modifications of a more complex nature will be done as part of ongoing work.

(U) Modifications to the geoacoustic parameters are based on comparisons between calculated bottom loss runs and measured data. The measured bottom loss values were computed in one-third octave bands. The measurements presented in this report were then averaged over 2^{0} angular bins. The theoretical bottom losses shown here were also calculated over one-third octave bands, but they have been plotted every degree without averaging over angle.

(U) The initial bottom loss model computations were made for the Oman Basin at frequencies of 25 and 200 Hz (fig 10 and 11). The geoacoustic model has been presented in figure 9. These initial computed values showed that modifications to the geoacoustic model were needed in order to substantially decrease the bottom loss for angles below 40^{0}. Based on the discussion above, modifications to the sound speed gradient or the attenuation would affect the losses at these lower angles. Separate analysis of the VAC data indicates that the gradient is approximately correct, so the attenuation values have been varied.

(U) The attenuation values were first decreased by a factor of two. The resulting comparisons at 25 Hz are presented in figure 12. Below 40^{0} the agreement between calculation and measurement is within 1 dB. Figure 13 shows that, at 200 Hz, however, there were still large discrepancies (8 dB or more) between the two curves. When the attenuation at all depths was decreased to one-seventh that of figure 9, the resulting calculations at 200 Hz were within 1 dB of the measured values, as shown by figure 14. Calculations at 25 Hz, shown in figure 15, were within 1 dB of the measurements for grazing angles less than 35^{0}. Above 35^{0} the 25-Hz measured data show a rapid increase in loss out to 45^{0} while the calculations increase slowly out to 53^{0} and then increase rapidly.

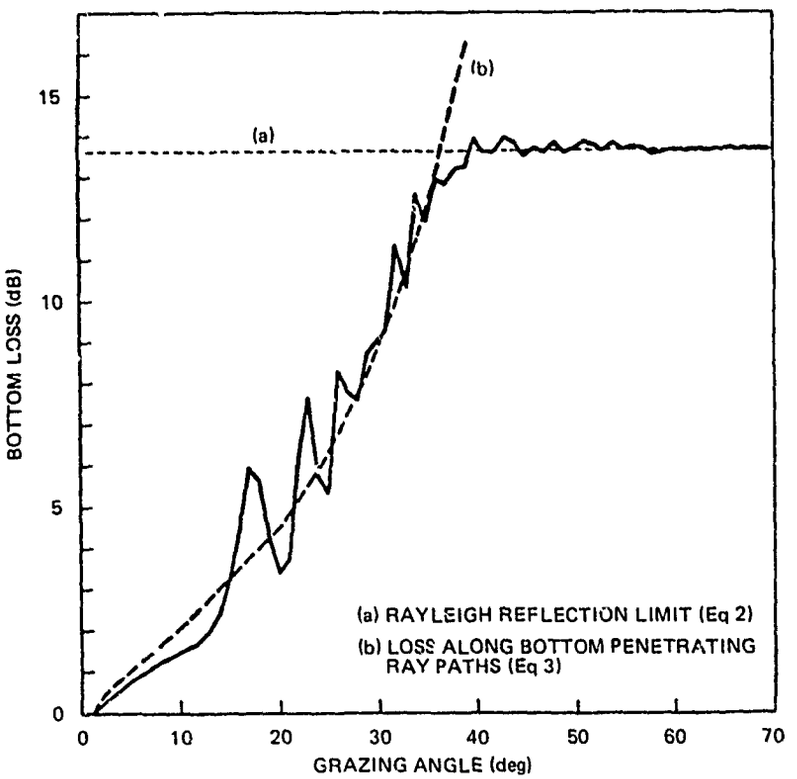

Figure IV-8. (U) Comparison between bottom loss calculations and simple ray path approximations. (U)

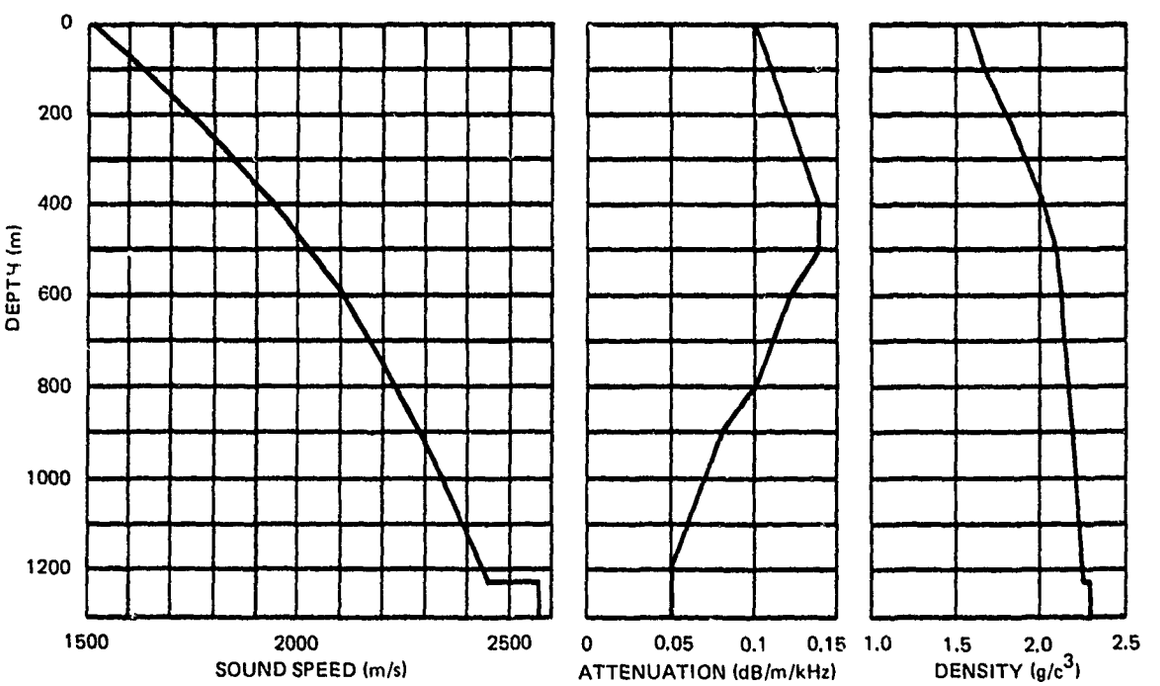

Figure IV-9. (C) Initial set of geoacoustic parameters for Site 1B. (U)

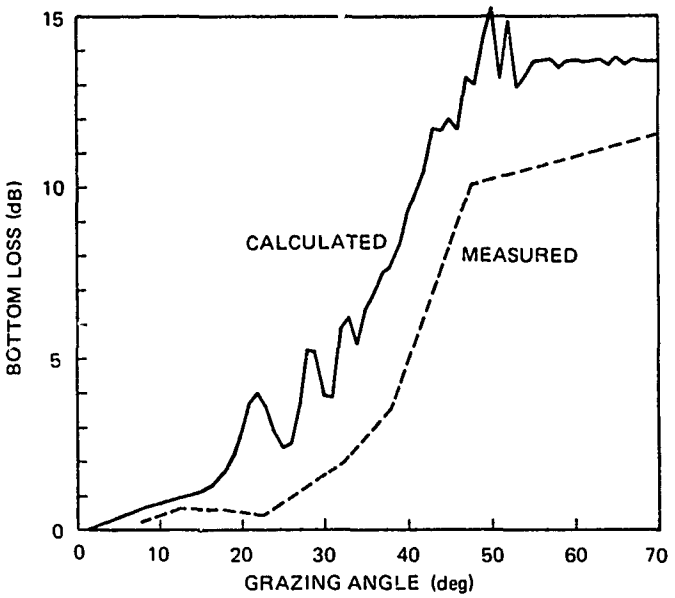

Figure IV-10. (C) Comparison between measured bottom loss and bottom loss calculations at 25 Hz. (Unmodified geoacoustic input parameters.) (C)

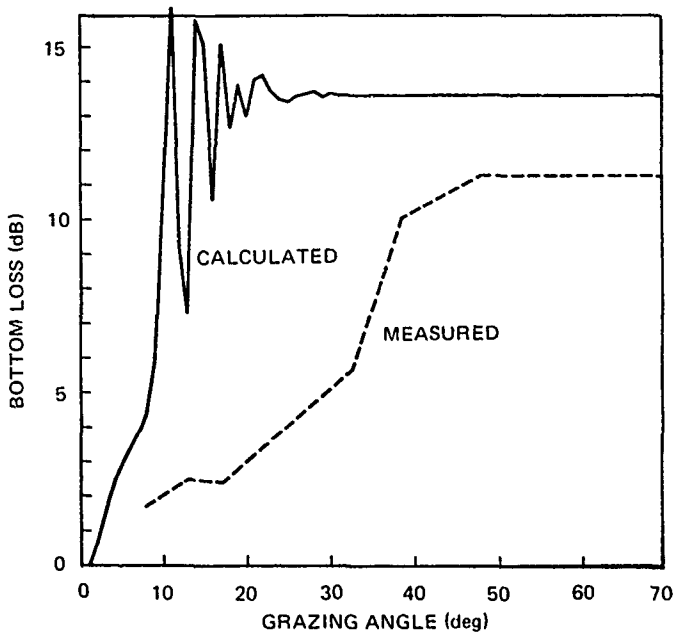

Figure IV-11. (C) Comparison between measured bottom loss and bottom loss calculations at 200 Hz. (Unmodified geoacoustic input parameters. (C)

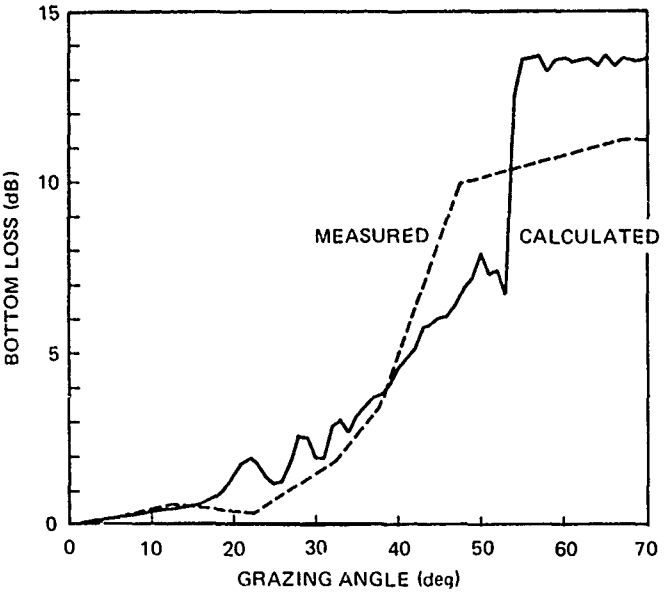

Figure IV-12. (C) Comparison between measured bottom loss and bottom loss calculations at 25 Hz. (Attenuations decreased to one-half the original values.) (C)

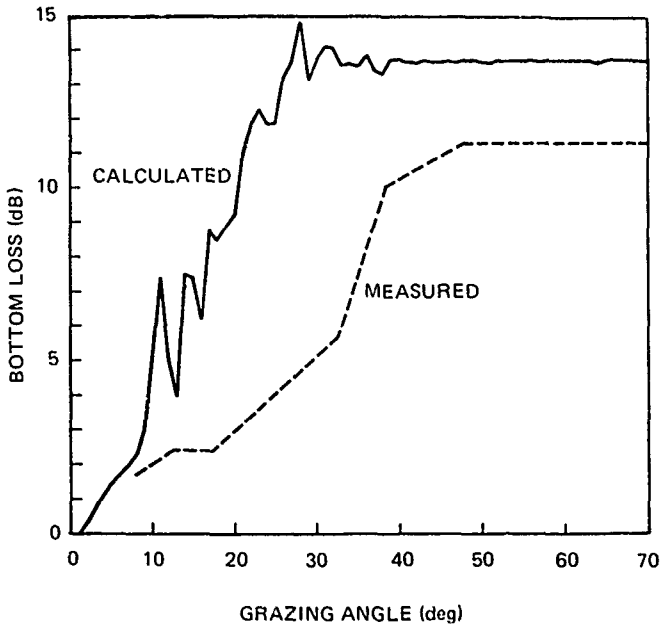

Figure IV-13. (C) Comparison between measured bottom loss and bottom loss calculations at 200 Hz. (Attenuations decreased to one-half the original values.) (C)

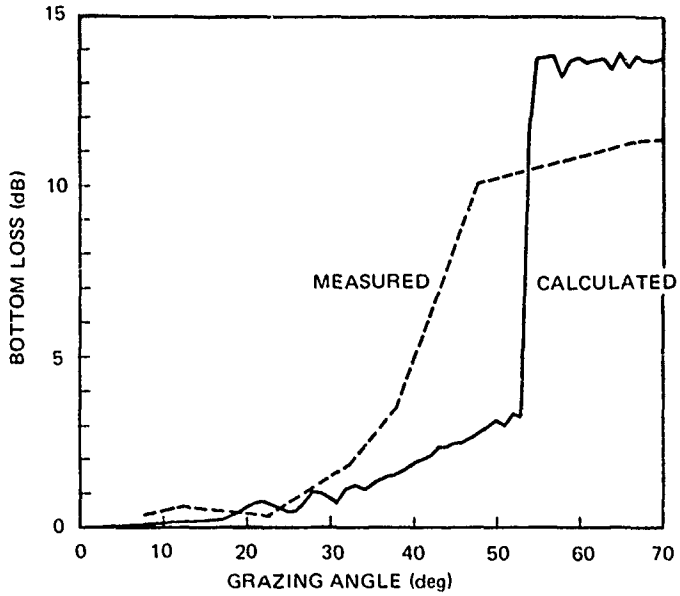

Figure IV-14. (C) Comparison between measured bottom loss and bottom loss calculations at 25 Hz. (Attenuations decreased to one-seventh the original values.) (C)

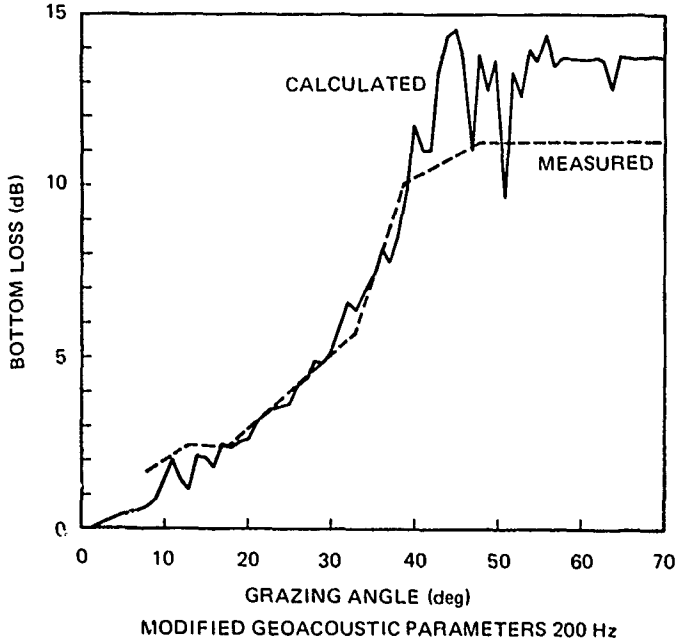

Figure IV-15. (C) Comparison between measured bottom loss and bottom loss calculations at 200 Hz. (Attenuations decreased to one-seventh the original values.) (C)

(U) In long range acoustic propagation the low-angle, low-loss region of the bottom loss curves dominates the influence of the bottom (Spofford, 1978). The calculated bottom loss curves in figures 14 and 15 are within 0.5 dB of the measured values in the low-angle, low-loss region. They will lead to reasonable predictions of long range acoustic propagation. The modified geoacoustic model for the Oman Basin has one-seventh the attenuation of the initial model (fig 16).

(U) Future modifications to this geoacoustic model will deal with the factors influencing bottom loss at the higher angles and frequencies below 100 Hz. Increased attenuation at depth will result in increased losses at the low frequencies. Because the higher frequencies are dominated by the Rayleigh reflection at these angles, the high-frequency loss should be unaffected by such modifications.

(C) Table 3 presents the adjusted geoacoustic parameter values which were used to compute bottom loss for the Oman Basin. Bottom loss measurements from the Somali Basin (fig 3) and the Arabian Basin (fig 4) during the BEARING STAKE exercise have also been used to modify the geoacoustic parameters for these regions. Modifications were derived in the manner described above for the Oman Basin. In the Somali Basin the attenuation values at all depths were reduced to 0.4 of the initial values. The resultant geoacoustic parameters used for bottom loss calculations are presented in table 4. In the Arabian Basin, as was the case in the Oman Basin, the attenuations were reduced by a factor of seven. The Arabian Basin data also required an increase of the sound speed ratio at the water/sediment interface from 0.99 to 1.00. Table 5 presents the geoacoustic parameters used in computing bottom loss for the Arabian Basin.

(C) Bottom loss calculations using the geoacoustic parameters of tables III-V have been computed for each of the areas at frequencies of 25, 50, 100, 200, 400, and 1000 Hz. Figures 17, 18, and 19 present these calculations for the Oman Basin, Arabian Basin, and Somali Basin, respectively. At the lower frequencies (25 and 50 Hz) the bottom loss for figures 17 and 18 is noticeably lower than the measured values (fig 2 and 4) between approximately 20° and 50°. This is because, as discussed, the attenuation at depths from 100 to 500 m should be greater than that shown in tables 3 and 5.

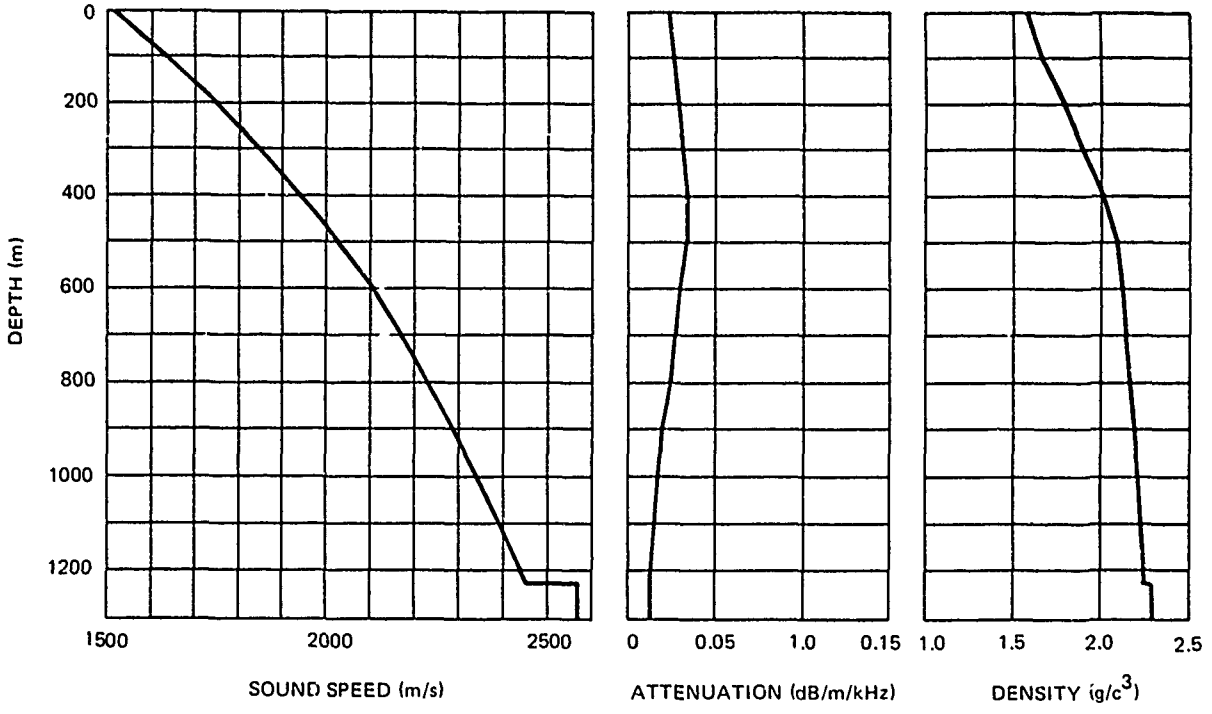

Figure IV-16. (C) Modified geoacoustic model for the Oman Basin. (C)

TABLE IV-3. (C) MODIFIED GEOACOUSTIC INPUTS FOR BOTTOM LOSS CALCULATIONS IN THE OMAN BASIN. (C)

Layer Material	Depth(m)	Velocity(m/s)	Attenuation-k_p (dB/m - kHz)	Density (g/cm^3)
Bottom Water		1514.5		1.04306
Sediment	0.	1515.	.014	1.59
	100.	1638.	.016	1.67
	200.	1750.	.017	1.80
	300.	1851.	.019	1.91
	400.	1943.	.020	2.02
	500.	2026.	.020	2.10
	600.	2101.	.017	2.13
	700.	2168.	.016	2.15
	800.	2230.	.014	2.18
	900.	2286.	.011	2.20
	1000.	2337.	.010	2.22
	1100.	2385.	.009	2.24
	1200.	2429.	.007	2.25
	1231.	2443.	.007	2.26
Sedimentary Rock	1231.	2565.	.050	2.30

Substrate shear wave velocity 1040 m/s
Substrate shear wave attenuation 7.5 dB/m - kHz

TABLE IV-4. (C) MODIFIED INPUTS FOR BOTTOM LOSS CALCULATIONS IN THE SOMALI BASIN. (C)

Layer Material	Depth(m)	Velocity(m/sec)	Attenuation-k_p (dB/m - kHz)	Density (g/cm^3)
Bottom Water		1543.8		1.05
	000.	1528.	.028	1.41
	100.	1649.	.036	1.68
	200.	1760.	.044	1.81
	300.	1864.	.048	1.93
	400.	1960.	.056	2.03
	500.	2048.	.056	2.11
Sediment	600.	2128.	.048	2.14
	700.	2202.	.044	2.17
	800.	2269.	.04	2.19
	900.	2330.	.032	2.22
	1000.	2385.	.028	2.24
	1500.	2582.	.016	2.30
	1580.	2604.	.012	2.31
Sedimentary Rock	1580.	3500.	.03	2.54

Substrate shear wave velocity 1750 m/s
Substrate shear wave attenuation 3.0 dB/m - kHz

TABLE IV-5. (C) MODIFIED INPUTS FOR BOTTOM LOSS CALCULATION IN THE ARABIAN BASIN. (C)

Layer Material	Depth(m)	Velocity(m/s)	Attenuation-k_p (dB/m-kHz)	Density (g/cm^3)
Bottom Water		1516.5		1.04373
	0.	1517.	.014	1.56
	100.	1635.	.016	1.65
	200.	1747.	.017	1.77
	300.	1855.	.019	1.90
	400.	1959.	.020	2.02
	500.	2058.	.020	2.10
	600.	2153.	.017	2.14
	700.	2245.	.016	2.17
Sediment	800.	2332.	.014	2.21
	900.	2417.	.011	2.24
	1000.	2498.	.010	2.27
	1500.	2863.	.006	2.38
	2000.	3177.	.003	2.47
	2500.	3467.	.003	2.53
	3000.	3758.	.003	2.58
	3260.	3918.	.003	2.60
Basalt	3260.	5400.	.020	2.72

Substrate shear wave velocity 2744. m/s
Substrate shear wave attenuation .070 dB/m - kHz

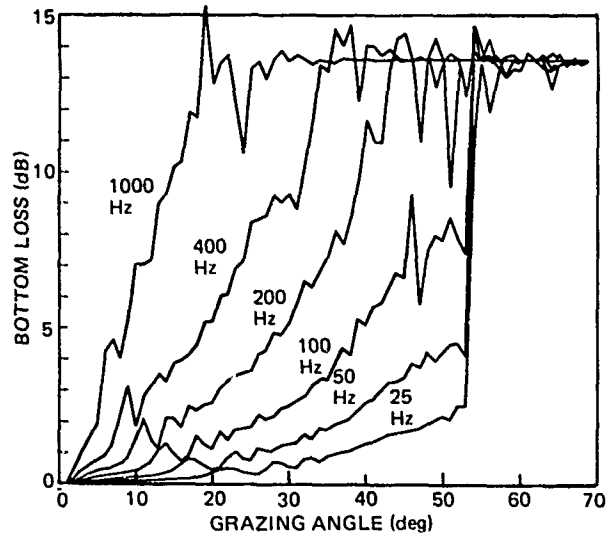

Figure IV-17. (C) Calculated bottom loss curves for the Oman Basin. (C)

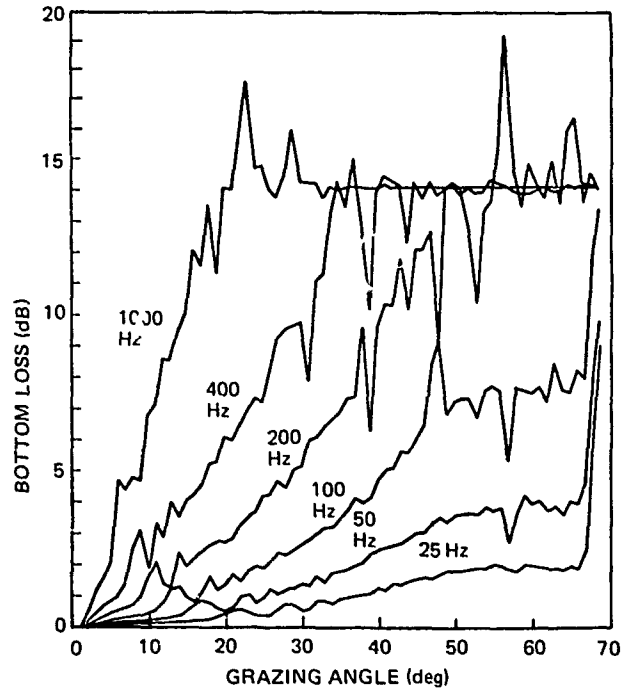

Figure IV-18. (C) Calculated bottom loss curves for the Arabian Basin at frequencies of 25, 50, 100, 200, 400, and 1000 Hz. (C)

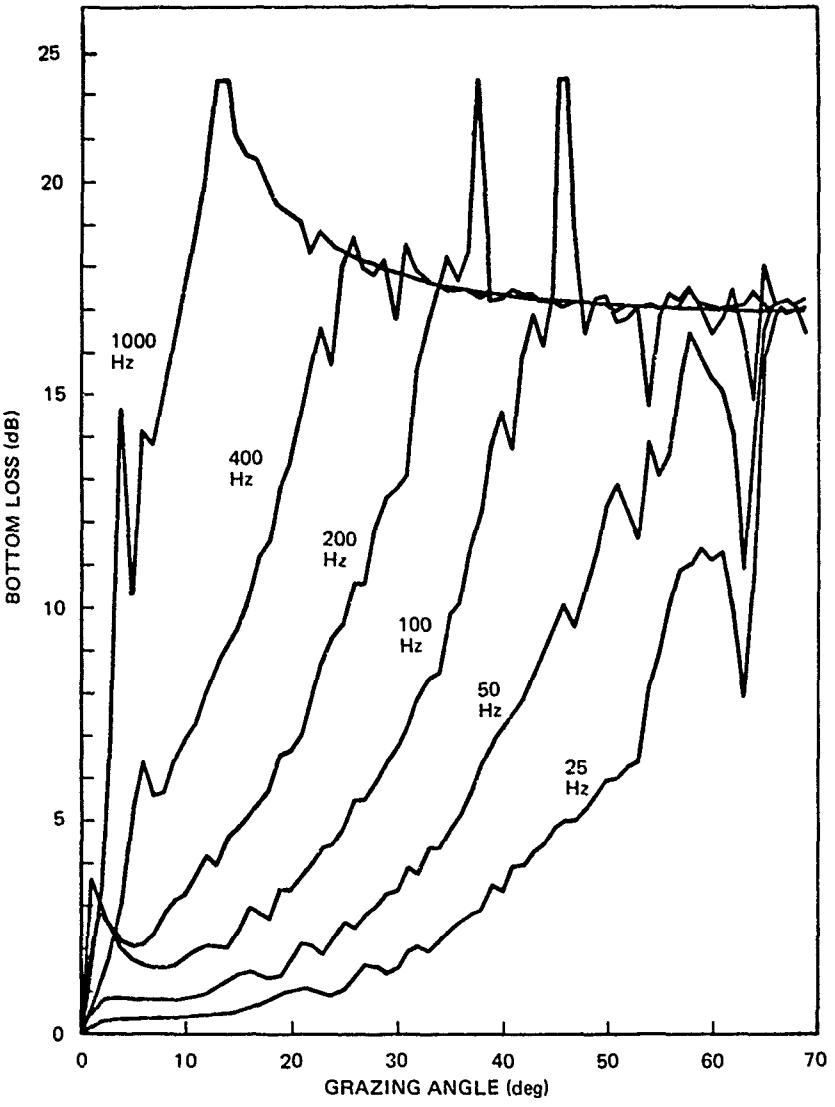

Figure IV-19. (C) Calculated bottom loss curves for the Somali Basin at frequencies of 25, 50, 100, 200, 400, and 1000 Hz. (C)

REFERENCES (U)

Brekhovskikh, L.M. (1960). Waves in Layered Media, Academic Press.

Focke, K.C. (1978). ARL Letter to M.A. Pederson, NOSC. Subject: Bottom Interaction at Site 5.

Hamilton, E.L. (1974). "Geoacoustic Models of the Sea Floor," Physics of Sound in Marine Sediments, edited by Loyd Hampton, Plenum Press.

Hamilton, E.L. (1978). Letters from NOSC to S.K. Mitchell and K.C. Focke, ARL:UT.

Hawker, K.E., W.E. Williams, and T.L. Foreman (1979). "A Study of the Acoustical Effects of Sub-bottom Absorption Profiles," to be published in The Journal of the Acoustical Society of America.

Mitchell, S.K., et al. (1978). "BEARING STAKE Vertical ACODAC Acoustic Measurements Data Report (U)," Mitchell, et al, Applied Research Laboratories Technical Report No. 78-8 (ARL-TR-78-8), Applied Research Laboratories, The University of Texas at Austin. (CONFIDENTIAL)

Mitchell, S.K., K.C. Focke, J.J. Lemmon, and M.M. McSwain (1979). "Analysis of Acoustic Bottom Interaction in BEARING STAKE (U)," Applied Research Laboratories Technical Report No. 79-24 (ARL-TR-79-24), Applied Research Laboratories, The University of Texas at Austin. (CONFIDENTIAL)

Naval Ocean Systems Center (1977). "BEARING STAKE: Preliminary Report (U)," NOSC/TR 169, Naval Ocean Systems Center, San Diego, CA., October. (CONFIDENTIAL)

Spofford, C.W. (1978). "The Sensitivity of Long-Range Propagation-Loss to Bottom-Loss," Science Applications, Inc. Report (SAI-78-548-WA).

CHAPTER V

PROPAGATION LOSS (U)

by

Melvin A. Pedersen

Systems Concepts and Analysis Division, Code 724

Naval Ocean Systems Center

San Diego, California 92152

CHAPTER V. PROPAGATION LOSS (U)

CONTENTS (U)

CHAPTER V. PROPAGATION LOSS (U)

V.1 (U) INTRODUCTION

V.1.1 (U) General

(U) This chapter contains those topics judged of most importance in the assessment of propagation for the BEARING STAKE exercise. Within length constraints, data and analyses are provided to support conclusions. The principal investigators' report (Pedersen and Yee, 1979) provides more data, a more detailed discussion of the analyses, and a number of additional topics of relatively minor importance. The second major section of this chapter treats the various BEARING STAKE sites on an individual basis while the last section makes assessments based on all the sites. Conclusions and recommendations are not provided in separate sections but are integrated into those for the acoustic assessment. The remainder of this section discusses the general nature of the propagation data and how they were smoothed for analysis.

V.1.2 (U) Data Smoothing Procedures

(C) The first impression obtained of the BEARING STAKE data is the extreme variability. Figure 1 presents unaveraged data at 25 Hz taken in event P1 at Site 1B in the Oman Basin. The crosses and dots, respectively, represent data for the WECo BMA receiver and ACODAC receiver 13, both mounted on the basin floor. Figure 1 shows a jumbled and ragged band about 15 dB wide, typical of most of the CW data appearing in the WECo report (Osborne, 1978). With the exception of some convergence zone data at higher frequencies at Site 4 in the Somali Basin, the variability between successive observations dominated (or at least obscured) trends in the data.

(U) In an endeavor to explain this variability, the multilayered normal mode program (Gordon, 1979a) was used to make propagation loss calculations for Site 1B. The sound speed input to this model was based on the Fenner representative profile for Site 1B (see chapter II). The sub-bottom input to the model was based on the structure derived by Hamilton (chapter III) and modified by Mitchell (chapter IV). Figure 2 compares theoretical results with the ACODAC experimental data (fig 1) over the range interval 25–75 km. We see that the experimental variability is not excessive and is to be expected. This may be regarded as typical of bottom-limited propagation involving a large number of multipaths in a low-bottom-loss situation.

(U) The study of Gordon and Floyd (1979) examines the effect of rapid increases in propagation loss (fades) on the beamforming of linear arrays. Such fades can decrease the array signal gain by several dB and can also cause bearing errors. Figure 2 indicates that the BEARING STAKE acoustic environment is characterized by a large number of fades.

(C) Gordon (1979b) describes the propagation by counting the number of fades in some range interval and then dividing the interval by the number of fades to produce an average distance between fades, or a fade interval. Based on normal mode results similar to those of figure 2, Gordon prepared the summary of fade intervals shown in table 1. The first six columns of this table represent Site 1B. The salient features include a slight increase in fade

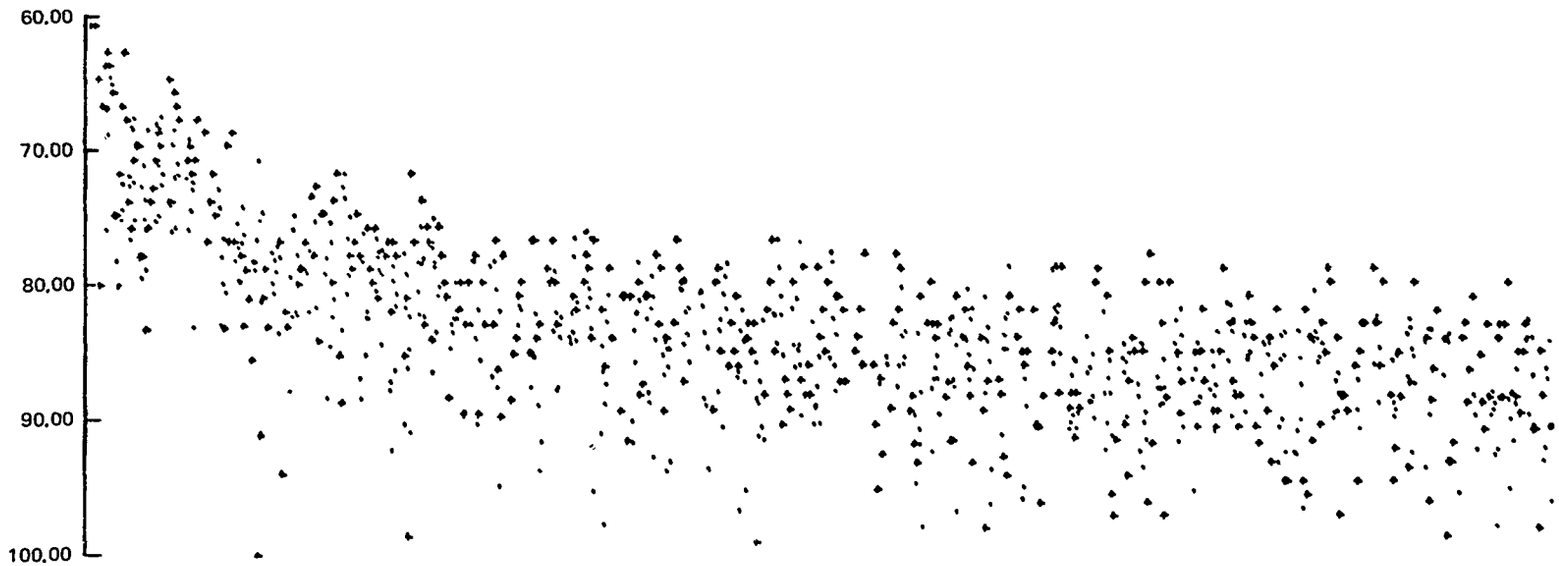

Figure V-1. (C) Unaveraged CW propagation loss data at 25 Hz, event P1 at Site 1B. (C)

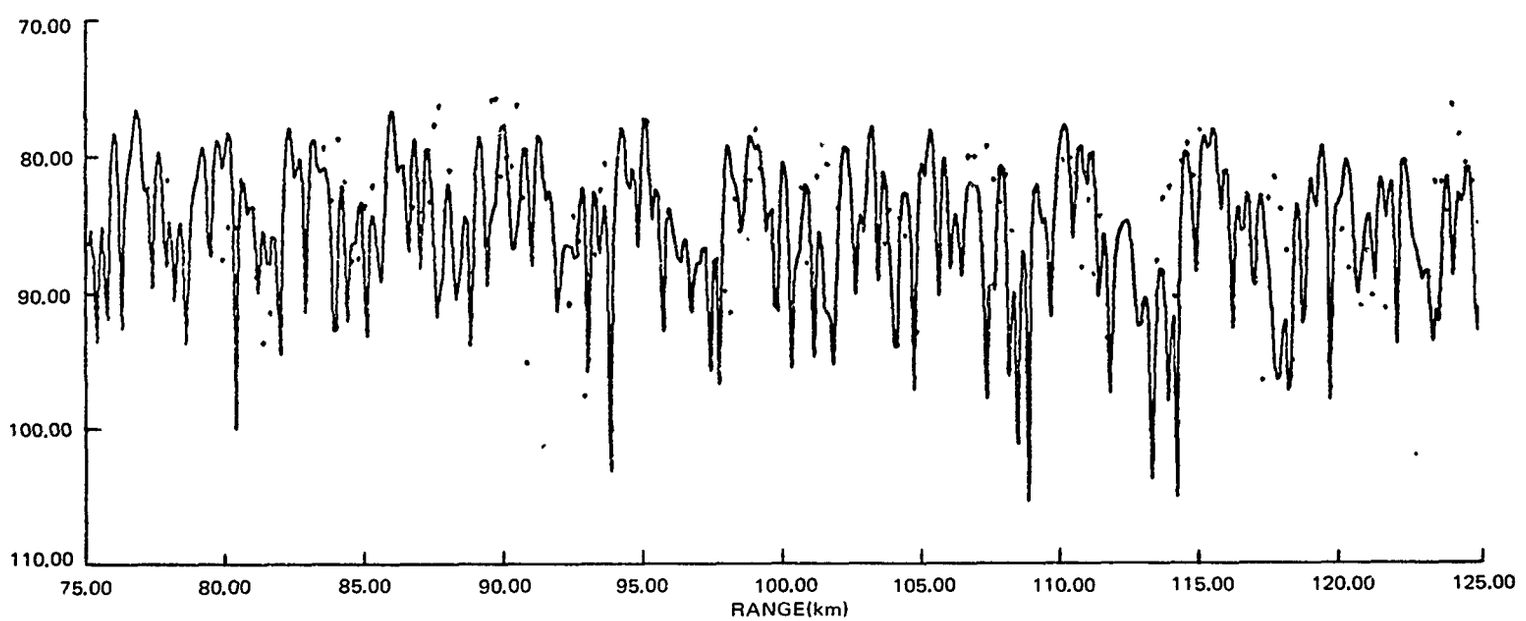

Figure V-2. (C) Comparison of the propagation losses of normal mode theory with unaveraged data. (U)

interval with range. This can be attributed to the stripping off of arrival paths at longer ranges due to bottom loss. There is also a consistent decrease in the fade interval at higher frequency. For the range interval 463–556 km (250–300 nmi) data are also presented for the spread of values obtained by Gordon for convergence zone conditions in the Atlantic and Pacific oceans. Ten-dB fades in propagation loss appear to occur at least three times as often for bottom-limited conditions in the Indian Ocean as they do for convergence zone propagation in the Atlantic or Pacific. Thus, beamforming problems may be more severe in the Indian Ocean than in other areas.

	RANGE INTERVAL (km)						
	25-75	75-125	125-175	175-225	225-275	463-556	
AREA	1B	1B	1B	1B	1B	1B	OTHER OCEANS
25 Hz, 5 dB	0.9	0.8	0.9	0.9	1.1	1.7	5.4 TO 10.3
25 Hz, 10 dB	1.4	1.8	1.9	2.0	2.0	8.6	10.3 TO 20.6
50 Hz, 5 dB	0.4	0.5	0.5	0.6	0.7	1.4	3.2 TO 20.6
50 Hz, 10 dB	0.8	1.0	1.0	1.3	1.3	2.7	6.9 TO 30.8

TABLE V-1. (C) DISTANCE BETWEEN 5- AND 10-DB FADES AT 25 AND 50 HZ OVER VARIOUS RANGE INTERVALS FOR SITE 1B AND FOR OTHER OCEANS OVER THE RANGE INTERVAL FROM 463-556 KM. (C)

(U) In order to analyze the experimental data, it was necessary to use smoothing techniques. The principal smoothing method was to average the CW and shot data in 50-km range bins or 30^{0} bearing bins. In the case of radial events the data were averaged in 50-km range bins centered at integral multiples of 50 km. Thus, the 50-km bin covers the interval from 25 to 75 km, the 100-km bin covers the interval from 75 to 125 km, etc. The squared pressure corresponding to each propagation loss observation in the bin was summed, divided by the number of observations, and then converted to dB to obtain an average propagation loss for the bin. This choice of mean squared pressure is based on fundamental physical principles of conservation of energy and is commensurate with theoretical propagation loss models such as ASTRAL and RAY WAVE, which incoherently add the squared pressures of multipath contributions. Examples will be presented later.

(U) In the case of arc events (circular runs made at constant range) the data were averaged in 30^{0} bearing bins centered at integral multiples of 30^{0} in azimuth. This bin size was chosen so that the number of observations per bin (about 70) was comparable to that for the 50-km range bins.

(U) A second method of smoothing was to average the CW data in 2-km range bins. This method was useful at Site 4 to illustrate the convergence zones, as discussed later, but was of limited value at other sites.

V.2 (U) ASSESSMENT OF INDIVIDUAL SITES

(U) This section presents the important characteristics of each BEARING STAKE site. The discussion follows a general format. First, the dependence on receiver depth is presented. Second, the differences between various events are presented, which assesses the propagation in different directions from the receiver location. Third, the dependence on range and frequency is presented for the receiver depth and event with smallest propagation loss.

V.2.1 (C) Site 1, Oman Basin

(U) The same geographical location was surveyed twice at times about 1 month apart. The tracks for the source events for these two surveys (1A and 1B) are shown in figures II-3, II-7, and III-1.

(C) Table 2 presents the dependence of propagation loss on receiver depth at Site 1A. Propagation loss data for BMA receiver 1, suspended 496 m above the ocean floor, and for BMA receiver 2, suspended 100 m above the ocean floor, were compared with the average for BMA receivers 3, 5, and 8 which were mounted on the ocean floor. The experimental data at 25 Hz are based on events P7 and P5 while those at 50 Hz are based on event S1. The experimental propagation losses for BMA receivers 1 and 2 are in all cases greater than those at the ocean floor. The last three columns of table 2 present the corresponding theoretical results, based on normal mode theory. Agreement between theory and experiment is excellent.

(C) Table 3 presents the dependence on receiver depth at Site 1B. In this case the propagation losses for ACODAC receivers 2, 6, and 10 (which are suspended in the water column) are compared to those for ACODAC receiver 13 (which is mounted on the ocean floor). The experimental data are based on events P1 through P5. The experimental results are similar for 25 and 140 Hz. The propagation losses for receivers 2 and 6, which are well up in the water column, are between 2 and 3 dB greater than the loss at the bottom. The propagation loss for receiver 10, which is 30 m off the bottom, is slightly less than that at the bottom. There is substantial agreement between the results of mode theory and the experimental result at 25 Hz. The experimental results at 290 Hz appear to differ significantly from those at 25 and 140 Hz. We should note, however, that the 290-Hz data are suspect for reasons discussed elsewhere in this report. These experimental data need to be thoroughly investigated and verified by theory before we would accept the depth dependence indicated for 290 Hz.

		EXPERIMENT SOURCE DEPTH			NORMAL MODE THEORY SOURCE DEPTH		
RECEIVER	RECEIVER DEPTH	91 m	91 m	243 m	91 m	91 m	243 m
BMA	(m)	25 Hz	50 Hz	50 Hz	25 Hz	50 Hz	50 Hz
1	2855	2.2	2.5	2.0	2.0	2.6	1.9
2	3251	--	1.0	1.5	2.	1.5	0.6
3, 5, 8	3351	0	0	0	0	0	0

TABLE V-2. (C) PROPAGATION LOSS DIFFERENCES BETWEEN OTHER RECEIVERS AND A BOTTOMED RECEIVER FOR SITE 1A. (U)

RECEIVER	RECEIVER DEPTH	EXPERIMENT FREQUENCY			NORMAL MODE FREQUENCY	
ACODAC	(m)	25 Hz	140 Hz	290 Hz	25 Hz	50 Hz
2	496	2.3	2.3	-0.3	1.6	2.3
6	1685	2.1	2.9	1.0	2.0	2.7
10	3321	-0.2	-0.4	0.1	-0.2	0.9
13	3351	0	0	0	0	0

TABLE V-3. (C) PROPAGATION LOSS DIFFERENCE BETWEEN OTHER RECEIVERS AND A BOTTOMED RECEIVER FOR SITE 1B. (U)

(C) The good agreement between theory and experiment justifies the use of theoretical results to assess the receiver depth dependence for the entire water column (rather than only for the six depths at which experimental data are available). Figures 3 and 4 present the theoretical propagation loss versus receiver depth for respective source depths of 18 and 91 m, a frequency of 25 Hz, and ranges of 50, 100, 200, 500, and 1000 km. In these computations the modes are added in random phase at the given fixed range. This procedure averages out the detailed structure of the phased acoustic field and produces a good representation of the depth structure. There is a scale break at 500 m and another at 2920 m. The region between 500 and 2900 m shows very little change and has not been plotted in detail. However, the maximum value of propagation loss in the interval is indicated between the scale breaks.

(C) The salient features near the ocean surface are very similar to those in convergence zone propagation (Pedersen, Gordon, and White, 1975). For the shallow source of figure 3 there is a minimum in propagation loss at the surface decoupling depth, which is defined as the depth of the first (shallowest) antinode of the mode depth structure (Pedersen, Gordon, and White, 1975). This depth is about 30 m at 50-km range and increases to about 55 m at 1000-km range. This increase in depth with increasing range occurs because the steeper angle arrivals dominate at shorter ranges and steeper angles have smaller decoupling depth. These steeper angle arrivals are

stripped off by bottom loss at the longer ranges. In convergence zone propagation the surface decoupling depth is nearly independent of range because the dominant arrivals are nearly independent of range. For source depths below the surface decoupling depth, as in figure 4, there is a minimum in propagation loss at a receiver depth equal to the source depth. This same condition occurs for convergence zone propagation (Pedersen, Gordon, and White, 1975).

(C) In contrast, the conditions near the ocean bottom are drastically different for figures 3 and 4 than under convergence zone conditions in which the near-bottom propagation loss at long range increases rapidly with increasing receiver depth (Gordon, 1977). One important feature of figures 3 and 4 is the notch (relative maximum in propagation loss) which occurs somewhat off the ocean bottom. As will be discussed later, this notch would be important in suppressing shipping noise. In figure 3 the notch occurs about 30 m off the bottom at 50-km range and shallows to about 50 m off the bottom at 1000-km range. In figure 4, the corresponding depths of the notch are 85 to 95 m off the bottom. This notch is caused by destructive interference between the downgoing and upgoing (after bottom reflection) arrivals at the receiver. Another significant feature is the relative minimum in propagation loss at the bottom in figure 3 and slightly above the bottom in figure 4. This is caused by constructive interference between the upgoing and downgoing acoustic arrivals.

(C) A number of plots similar to figures 3 and 4 have been examined. These include source depths of 6, 18, 91, 102, and 243 m and frequencies of 20, 25, and 50 Hz. Except for the near-surface region the total variation of loss with receiver depth was small, with most of the values falling within an envelope 3 or 4 dB wide. For example in figure 3 at a range of 1000 km the total spread in propagation loss for receivers deeper than about 22 m is 4 dB. Thus, if differences of a few dB in propagation loss are of little concern, then any receiver depth which avoids the near-surface (decoupling) region would be suitable.

(C) If optimal receiver depths are desired, there are several choices. The minimum propagation loss often occurs at the source depth. This is not a practical choice for a fixed installation and moreover it requires knowledge of the source depth. The propagation loss at the ocean floor is, in most cases, within 1 dB of the minimum propagation loss, so from a practical standpoint this would appear to be a good choice. However, from the standpoint of signal-to-noise ratio there is an even better choice. The noise generated by distant shipping may be reduced by positioning the receiver depth in the propagation loss notch for shallow sources. Computations for a 6-m source depth show the notches to be in the identical locations as those shown in figure 3 for an 18-m source. Thus, as long as the source is in the surface decoupling region, the depth of the notch is independent of source depth. The reason for this property is that the dominant arrival angles do not change with source depth as long as the source is in the surface decoupling depth region. In contrast, for sources below the surface decoupling region, the location of the notch shifts with source depth. Thus, a notch in the noise field should occur at the same depth from surface vessels of various drafts; and as long as the target submarine is deeper than the decoupling depth, its notch will appear at a different depth.

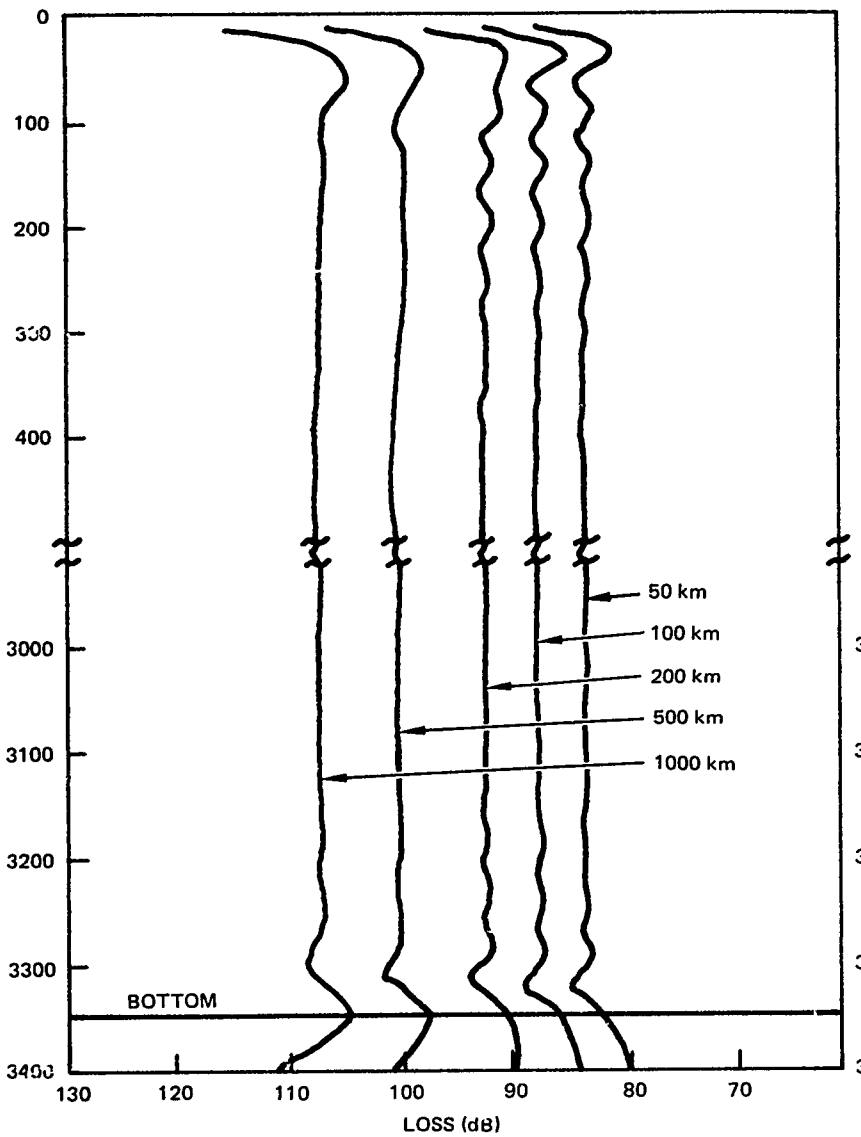

Figure V-3. (C) Theoretical propagation loss versus depth for an 18-m source depth at 25 Hz. (C)

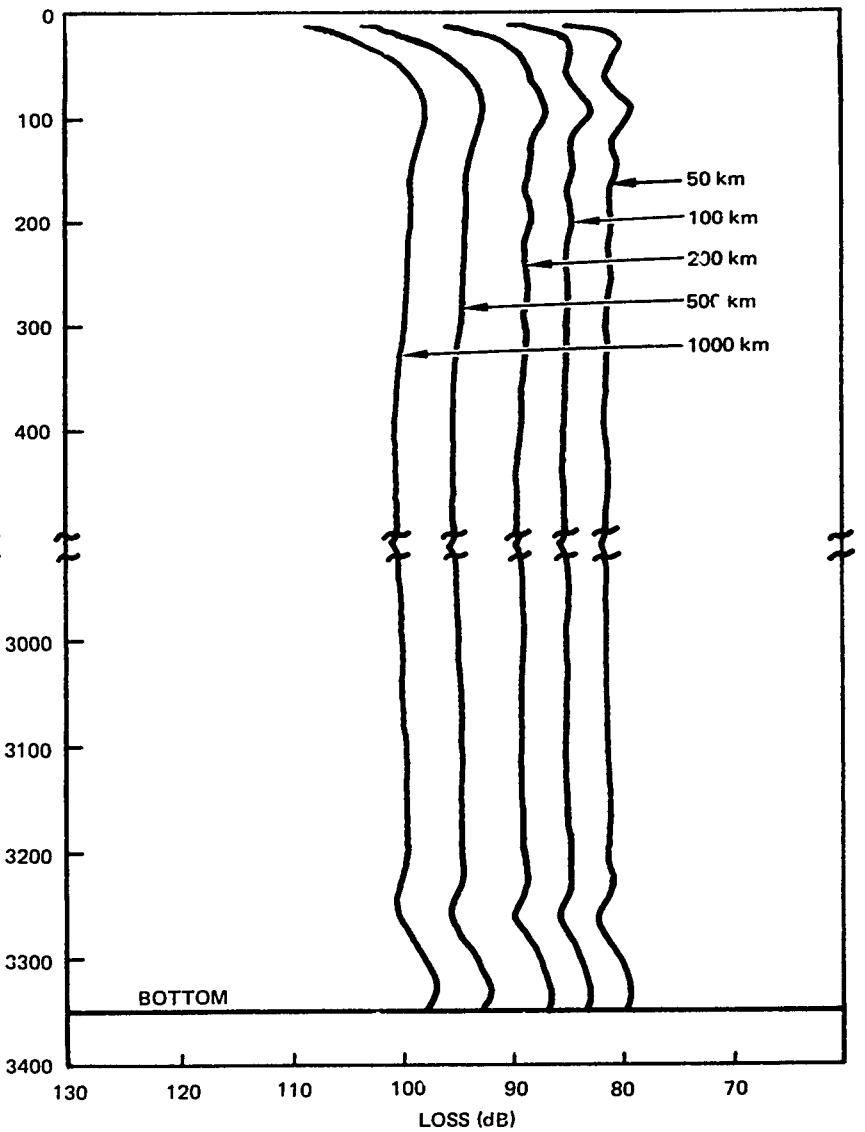

Figure V-4. (C) Theoretical propagation loss versus receiver depth for a 91-m source depth at 25 Hz. (C)

(C) This concept is illustrated in figure 5, which presents the propagation loss difference between a source (noise) at 6-m depth and a source (target) at 91-m depth for a frequency of 25 Hz. The target is assumed to be at a fixed range of 200 km. The difference in propagation loss is shown as a function of receiver height off the ocean bottom. Each curve represents a different range for the noise source starting at 50-km range and progressing in steps of 50 km to a maximum range of 1000 km. Consider now a receiver depth 30 m off the ocean bottom. This is near optimum for noise generated at about 100-km range. For the noise ranges of figure 5 this receiver represents a 2.5–3-dB improvement in the signal-to-noise ratio from that of a receiver on the ocean bottom. One drawback to this scheme is that the optimum depth varies somewhat with frequency. For example, at a frequency of 20 Hz the notch is about 35 m off the ocean bottom for a 100-km noise source. The corresponding value for 50 Hz is 18 m off the ocean bottom.

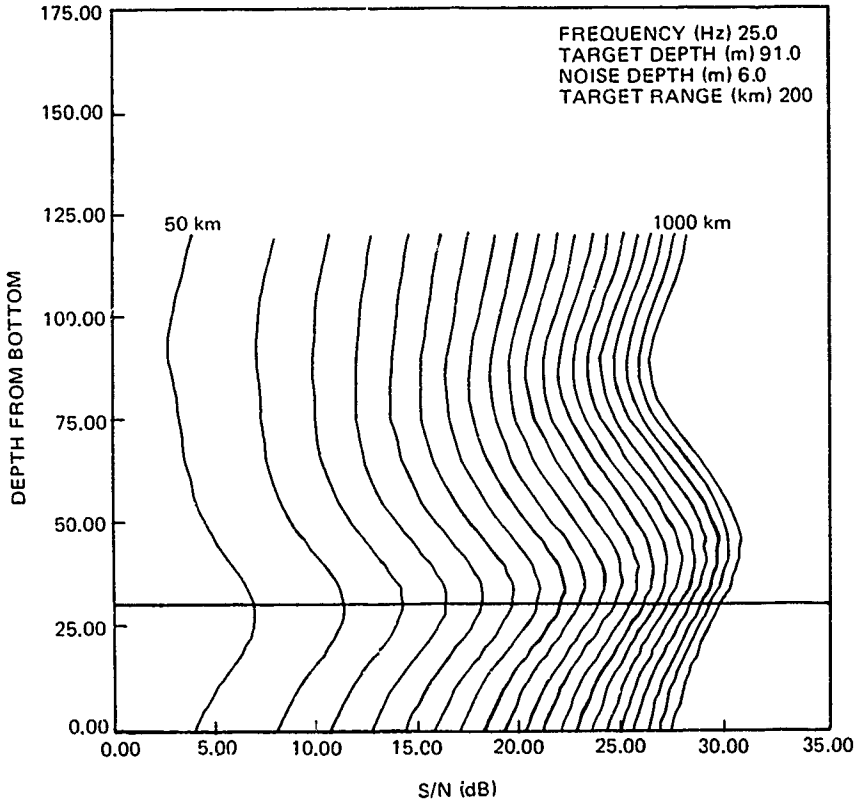

Figure V-5. (C) Propagation loss difference between a source (noise) at 6-m depth and a source (target) at 91-m depth for a frequency of 25 Hz shown as a function of height of the receiver off the ocean bottom. (C)

(U) Figures 6A to 6C present propagation loss data for the receivers with lowest propagation loss for all events at Site 1A and 1B. For this site these are the BMA receivers on the bottom. When multiple bottomed receivers were processed, an average value was calculated, based on all available data.

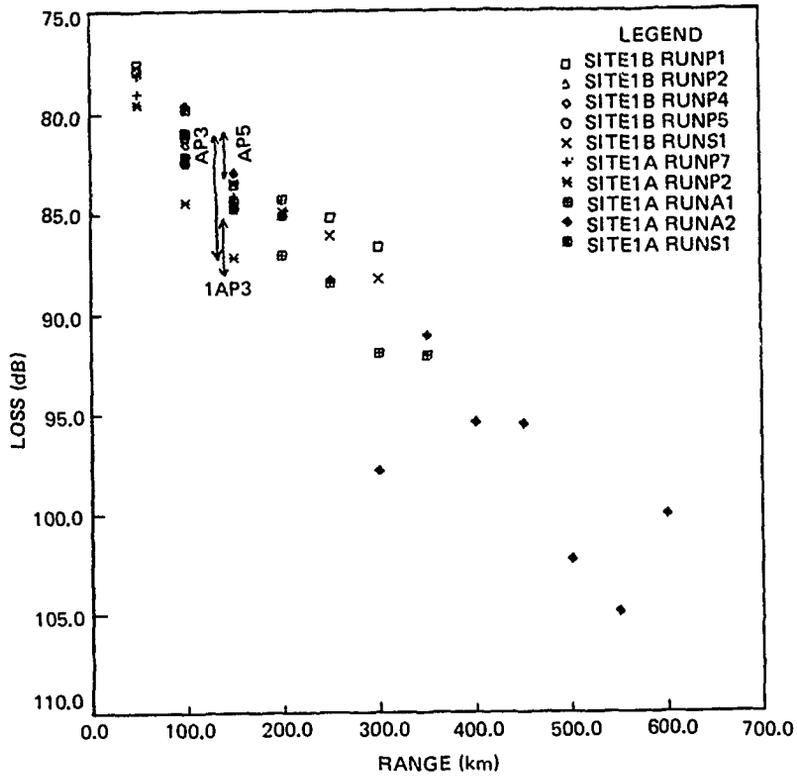

Figure V-6A. (C) Propagation loss versus range for all events at Site 1A and 1B: low frequency. (C)

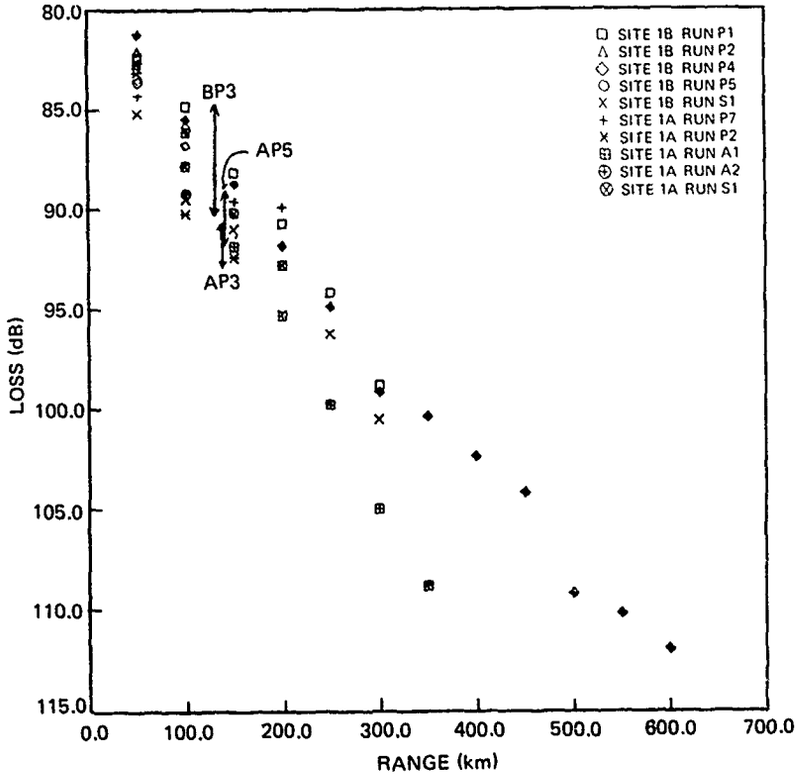

Figure V-6B. (C) Propagation loss versus range for all events at Site 1A and 1B: 140 Hz. (C)

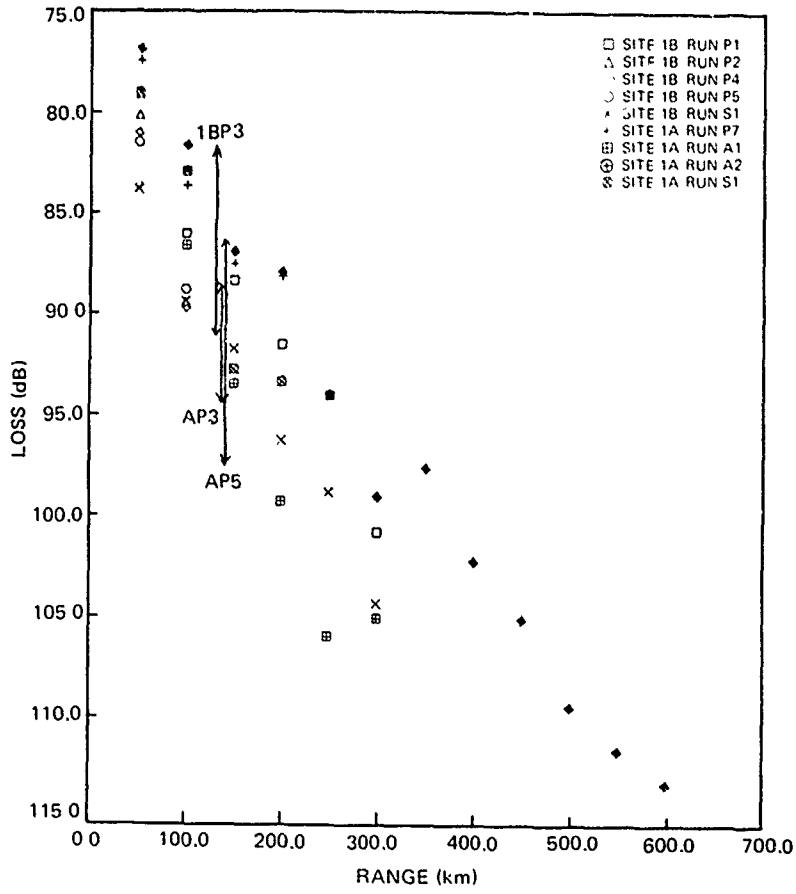

Figure V-6C. (C) Propagation loss versus range for all events at Site 1A and 1B: 290 Hz. (C)

The spread of values for the arc events 1AP3, 1AP5 and 1BP3 is plotted at the nominal range of these events. In the case of shot events the 91-m values were used. This same depth shot was also used for all other sites in similar figures to be presented later. Table 4 ranks the events according to increasing propagation loss for each frequency. Since data points beyond 150 km represent propagation over a ridge, these data were not used in the ranking of event 1AA1.

(C) In figure 6A and in table 4 the term low frequency is used. This is a term which will be used throughout this chapter to indicate a mix of low frequencies. Although the standard frequency for CW events was 25 Hz, there were some CW events at other frequencies. For example, event 1AP3 was at 39 Hz. The range of CW low frequencies used during BEARING STAKE is 22 to 42 Hz. The low frequency processed by WECo for all shot events was 20 Hz.

(C) There are some complications which make a rigorous comparison difficult. First we note that, other things being equal, the shot data for any site have somewhat higher loss than the corresponding CW data. A complication peculiar to this site is that the CW events for Site 1B low frequency were at 102-m depth rather than the standard 91-m depth. Finally at Site 1A, the CW sources at 140 and 290 Hz were operated at 24-m depth rather than the 18-m depth used at all other sites. These complications make it difficult to

compare Site 1A with 1B. There are fours events which ran over essentially the same bathymetry – events 1AP7, 1AS1, 1BP1, and 1BS1. However, the ranking of these events does not make much sense. For example, at low frequency 1BP1 and 1BS1 rank high whereas 1AP7 and 1AS1 rank low. At 140 Hz 1BP1 and 1AS1 rank high whereas 1AP7 and 1BS1 rank low. At 290 Hz AP7, 1BP1, and 1AS1 all rank high, but 1BS1 ranks low. However, if we ignore these anomalies and pick the best of these four events for the overall ranking and ignore the remaining three of these events, we see a definite pattern in table 4.

(C) We proceed in obtaining one overall ranking of events by combining the data in Table 4 for all three frequencies. The best event appears to be event 1BP1 followed closely by 1AA2. Both these events proceed up the center of the major axis of the Oman Basin (see fig II-16). The next best events are 1AA1, 1BP2, and 1BP4. These events head in a southerly direction from the basin center (fig II-11 and II-16). Finally, the events with largest loss are 1BP5 and 1AP2. These events head in a northerly direction from the basin center and proceed up the continental shelf (figs II-11 and II-16). The arc events support the same picture. Highest losses for event 1AP3, in figures 6A to 6C, occur for the bearing bin, almost due north of the receiver location, where the bottom shallows to almost 1000 m. Similarly the highest losses for event 1AP5 occur for the northernmost sector of the event, although exceptionally high losses only occur at 290 Hz. The losses for event 1BP3 appear to be comparable to the radial run data, with higher losses along the arc sector which connects to event 1BP4.

	FREQUENCY (Hz)		
RANK	LOW*	140	290
1	1BP1	1BP1	1AA2
2	1AA2	1AA2	1AP7
3	1AA1	1BP2	1BP1
4	1BS1	1AA1	1AS1
5	1BP2	1AS1	1AA1
6	1BP6	1BP4	1BP2
7	1BP5	1BP5	1BP4
8	1AP1	1AP7	1BP5
9	1AS1	1AP2	1BS1
10	1AP2	1BS1	

*See text

TABLE V-4. (C) RANKING OF EVENTS AT SITE 1A AND 1B. (U)

(C) The propagation losses for events 1BP1 and 1AP7 are compared to the Eleuthera reference in figure 7. The slope at low frequency is less than that of the reference, with losses at maximum range as much as 12 dB less than those of the reference. The slope at 140 Hz is slightly less than the reference, with loss values for Site 1B from 0 to 4 dB less than those of the reference. The slope at 290 Hz is comparable to that of the reference with loss values for Site 1A within 1 dB of those of the reference. Loss values for Site 1B are larger than those of the reference by 1 to 2.5 dB.

(C) The remainder of the discussion for Sites 1A and 1B is concerned with a comparison between the experimental and theoretical dependence of propagation loss on range and on source depth. Figure 8 compares propagation loss versus range for various theoretical and experimental data for event P1 at Site 1B. The BMA data are based on averages for three bottomed receivers. The normal mode model for Site 1B was used to make coherent calculations of propagation loss (at range intervals of 100 m) such as shown in figure 2. These data were then p^2 averaged in 50-km range bins, converted to propagation loss, and plotted in figure 8. The normal mode theory was also used to calculate reflection coefficients at the ocean bottom. Using the bottom loss derived from these theoretical coefficients and the Fenner representative profile for Site 1B (chapter II), propagation losses were computed by using the RAY WAVE model at 2-km range intervals. These data were also p^2 averaged in 50-km range bins and plotted in figure 8.

(C) Statistical analysis shows that the differences between experiment and model results in figure 8 are not significantly range dependent. The average experimental losses for the five range bins are 2.6 dB and 1.3 dB smaller than mode theory for the BMA and ACODAC data, respectively. Corresponding standard errors of the mean are 0.5 and 0.4 dB.

(C) There are a number of subjects of concern in figure 8. First, consider the difference between the ACODAC and BMA data. Analysis of the data from events P1, P2, P4, and P5 at Site 1B yields bottomed-ACODAC propagation losses which are 1.5, 2.6, and 4.6 dB higher than the BMA propagation losses for frequencies of 25, 140, and 290 Hz. These values are statistically significant. The reason for these differences is not known, but they should be investigated further. The normal model results suggest that the ACODAC values at 25 Hz could be the more nearly correct. As will be discussed later, the BMA results are extremely consistent, but they could be subject to a consistent bias.

(C) The next subject is the difference between the two theoretical results based on models with identical sound speed profiles and bottom losses. In this case, the RAY WAVE model produces propagation losses which are 1.0 to 1.6 dB higher than the normal mode values. This has been ascribed to the fact that RAY WAVE is a model which incoherently combines various arrivals. However, figure 4 indicates that the upgoing and downgoing arrivals at the ocean bottom are more nearly in phase, as illustrated by the enhancement at or near the bottom. The depth structure in figure 4 for receiver depths from 3000 to 3200 might represent losses more like incoherent addition of ray arrivals. We see in figure 4 that the losses over this interval are some 1 to 2 dB greater than the loss at the bottom, which is in general agreement with the results of figure 8.

(C) The last subject of concern in figure 8 is the general disagreement between the low-frequency propagation loss results of BEARING STAKE and theory. These discrepancies are thought to be due to a small error in the low-frequency source levels and possibly to a systematic bias in the data processing techniques. However, both these factors require further investigation.

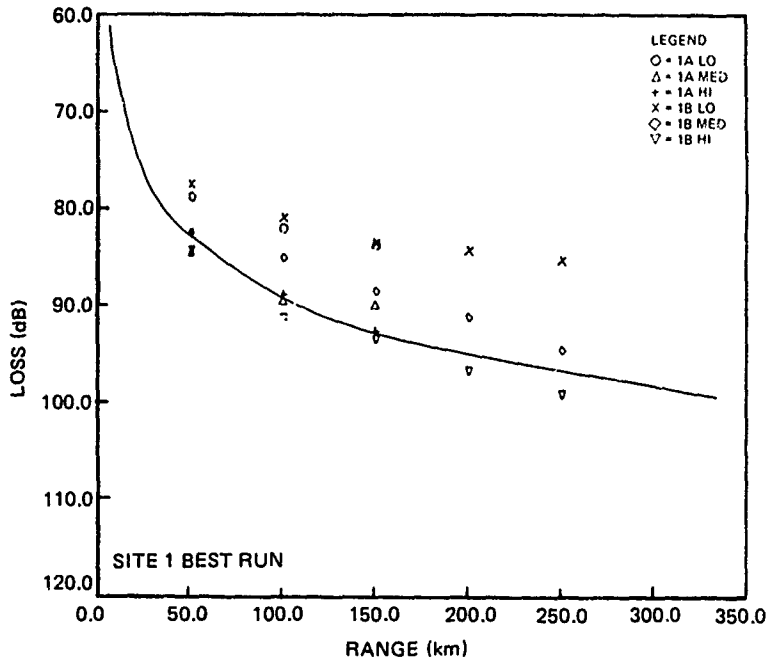

Figure V-7. (C) Comparison of the lowest-propagation-loss events at Sites 1A and 1B with the Eleuthera reference. (U)

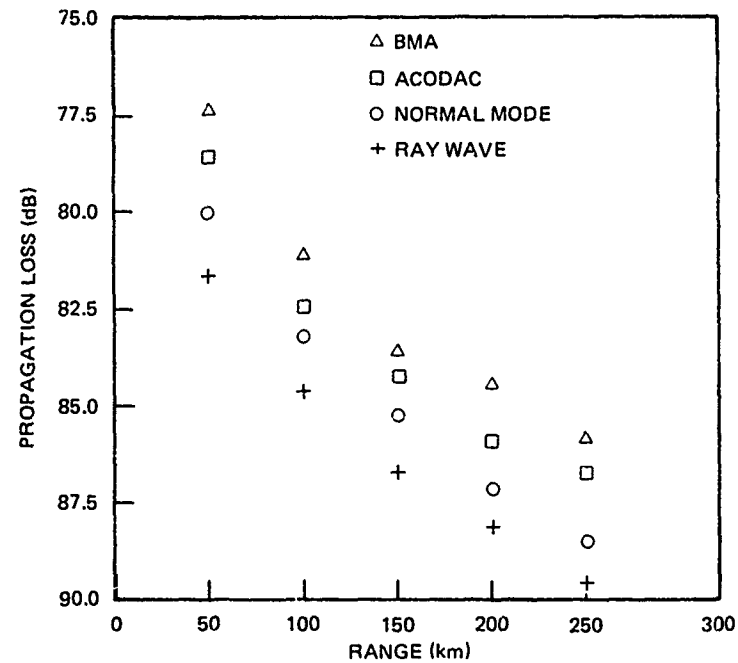

Figure V-8. (C) Comparison of the BMA and ACODAC CW experimental propagation losses at 25 Hz for event P1 at Site 1B with the results of normal mode theory and of the RAY WAVE model. (C)

(C) Figure 9A compares the experimental shot data at 20 Hz from Station 1A and 1B with the propagation losses for the normal mode model for Station 1B with modes added in random phase. Values for the standard shot depths of 18, 91, and 243 m are presented. All data are for bottomed BMA receivers. In comparing experiment to theory, the shot data for event 1AA2 beyond 200 km were not included in the analysis because this event track crosses a small seamount which affected the longer range loss values. Similarly the shot data for event 1AA1 beyond 150 km were not included because the event crossed a prominent ridge. Figure 9B is the counterpart of figure 9A for 50 Hz. The differences between theory and experiment were investigated. There appeared to be no significant trends with range and no appreciable dependence on event. The data for all range bins and all events were lumped to produce an average difference between them and the theoretical results for each source depth and each frequency.

(C) The results of this analysis are presented in table 5. The average values represent range-independent offsets between theory and experiment. The relatively small value of the standard error of the mean indicates that the offsets are statistically significant. At each frequency the 18-m and 91-m values are based on independent data from 16 range bins while the 243-m values are based on 10 range bins. The negative values for 50 Hz are evident in figure 9B, where almost all the experimental data lie below the theoretical curves. These data suggest that the source levels used to convert the 50 Hz shot data to propagation loss may be from 1.6 to 2.8 dB too high, depending on source depth.

(C) The behavior at 20 Hz is somewhat more complicated. Here the source levels for the 18-m shots appear to be 1.8 dB too high, whereas those for 91 and 243 m appear to be, respectively, 1.4 and 4.3 dB too low. The differences in table 5 may not necessarily all be due to source level errors. Other effects which produce a systematic bias can also contribute. However, table 5 indicates that systematic biases do occur, and we are suggesting that shot source levels are subject to further examination.

Frequency (Hz)	20Hz	50 Hz				
Shot Depth (m)	18	91	243	18	91	243
Average	-1.8	1.4	4.3	-2.8	-2.3	-1.6
Standard Error	0.2	0.2	0.4	0.3	0.3	0.1

TABLE V-5. (C) THE AVERAGE DIFFERENCE BETWEEN THEORETICAL AND EXPERIMENTAL PROPAGATION LOSSES FOR SHOT EVENTS AT SITES 1A AND 1B. STANDARD ERRORS OF THE MEAN ARE ALSO GIVEN. (U)

(C) Note in figures 9A and 9B that the theoretical propagation loss for the 91-m source is less than that for the 243-m source. This conflicts with the expectation that the 243-m source depth would have the smaller loss because a deeper source would have rays with lower grazing angles at the bottom and hence lower losses. This theoretical result is explained in part

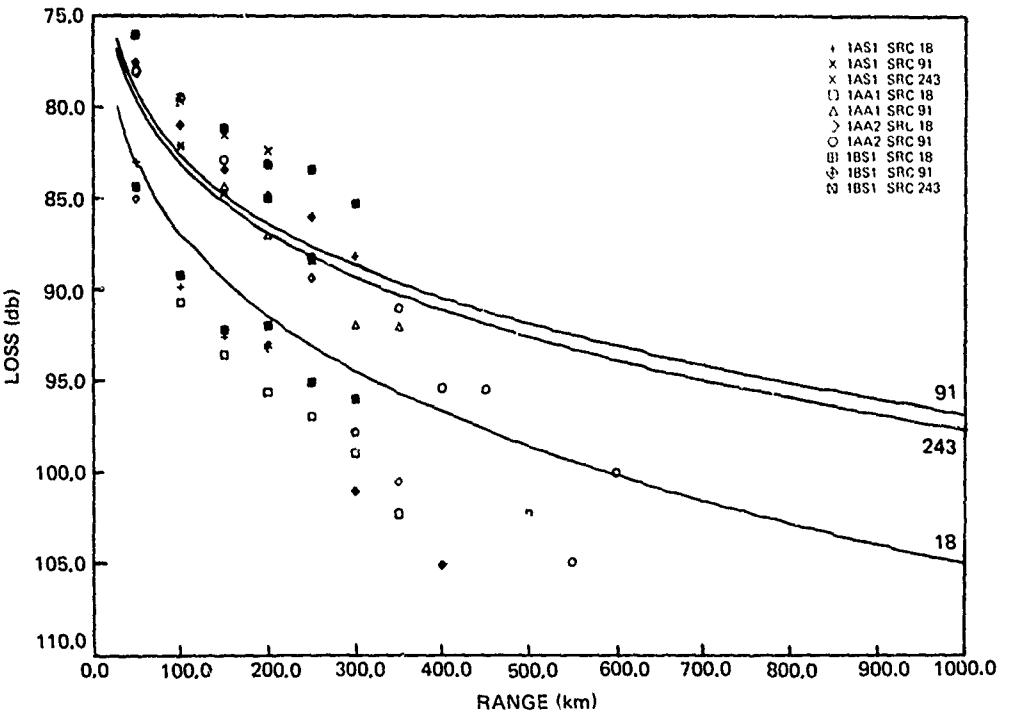

Figure V-9A. (C) Comparison of shot experimental propagation losses at Sites 1A and 1B with normal mode theory: 20 Hz. (C)

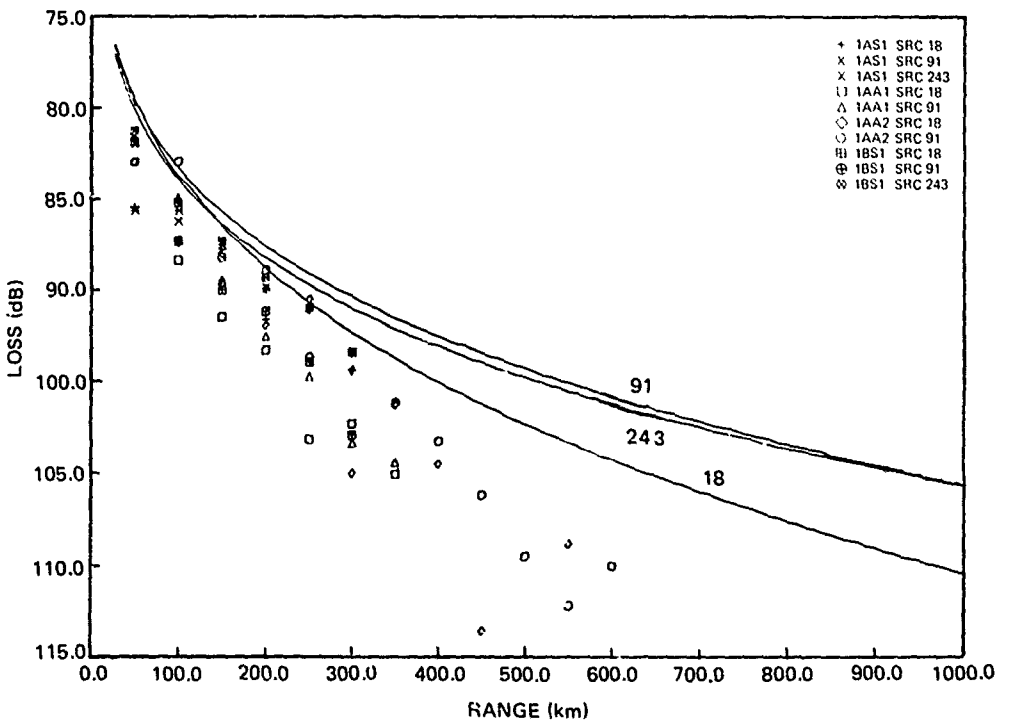

Figure V-9B. (C) Comparison of shot experimental propagation losses at Sites 1A and 1B with normal mode theory: 50 Hz. (C)

by figure 10, which is the counterpart of figure 3 or 4 for a fixed receiver depth. This figure presents propagation loss versus source depth for a receiver on the ocean bottom. In all cases the source depth with smallest propagation loss also occurs on the ocean bottom. Thus, this property obeys our previous rule of thumb that the lowest propagation loss generally occurs when source and receiver are at the same depth. A somewhat more surprising result is that the optimum source depth above the axis occurs at the surface decoupling depth; ie, at the depth of the first (shallowest) antinode for the dominant arrivals. This optimum depth takes advantage of the reinforcement of arrivals which occurs when they are in phase somewhat below the ocean surface. The-25 Hz frequency of figure 10 lies between the 20- and 50-Hz cases of figures 9A and 9B. Nonetheless, figure 10 indicates that the 91-m shots are closer to the decoupling depth and hence have lower propagation loss than the 243-m shots. Indeed a source depth of about 45 m would be optimal for ranges of 50 to 200 km in figure 10.

(C) The depth of the low-frequency CW source varied from site to site and to some extent during events. The spread of values was between 77 and 102 m. Figure 10 shows that this is not critical. For example, at 500 km range the source depth can vary between 40 and 250 m with a spread of average propagation loss of less than 1 dB.

(C) We have shown good agreement between experiment and theory in tables 2 and 3 for the dependence on receiver depth. We have compared the experimental and theoretical dependence on range and source depth and found agreement subject to possible change in source level. Our remaining task is to examine the experimental evidence for the "notch" of high propagation loss which appears somewhat off the bottom in figures 3 and 4. This notch represents a critical interaction between source depth, receiver depth, and frequency. There are only two receiver depths which might provide data — the BMA receiver 2, at Site 1A, which is 100 m off the bottom, and ACODAC receiver 10, at Site 1B, which is 30 m off the bottom. The BMA receiver is close to the notch of figure 4 for 25 Hz, at 91-m source depth. Unfortunately, WECo only processed this receiver for shots at 50 Hz. However, the ACODAC receiver is ideally situated in the notch for figure 3 for 25 Hz at 18-m source depth. Unfortunately, there were problems with the experimental data set. The bottomed ACODAC was not designed to be processed for shots and the shots available from the other ACODAC receivers were very sparse because of overloads. (The overloads were caused by the first and second bottom bounce arrivals. Bottom losses were determined by ARL by processing higher-order bottom bounce arrivals which were not overloaded).

(C) Figures 11A to 11C for 20, 25, and 50 Hz, respectively, present the difference in ACODAC propagation loss between 18- and 91-m shots as a function of range. The curves represent the normal mode results for the three ACODAC receivers. The experimental data were obtained by p^2 averaging, in 50-km bins, the data which were not overloaded for each source depth and then plotting the difference between the 18- and 91-m averages. Since the theoretical values were so close for ACODAC receiver 2 at 496-m depth and ACODAC receiver 6 at 1685-m depth, the experimental data were lumped and plotted as circles in figures 11A to 11C. Whereas the quality of the data leaves something to be desired, a definite pattern emerges when further differences are considered which take into account the offsets in the data.

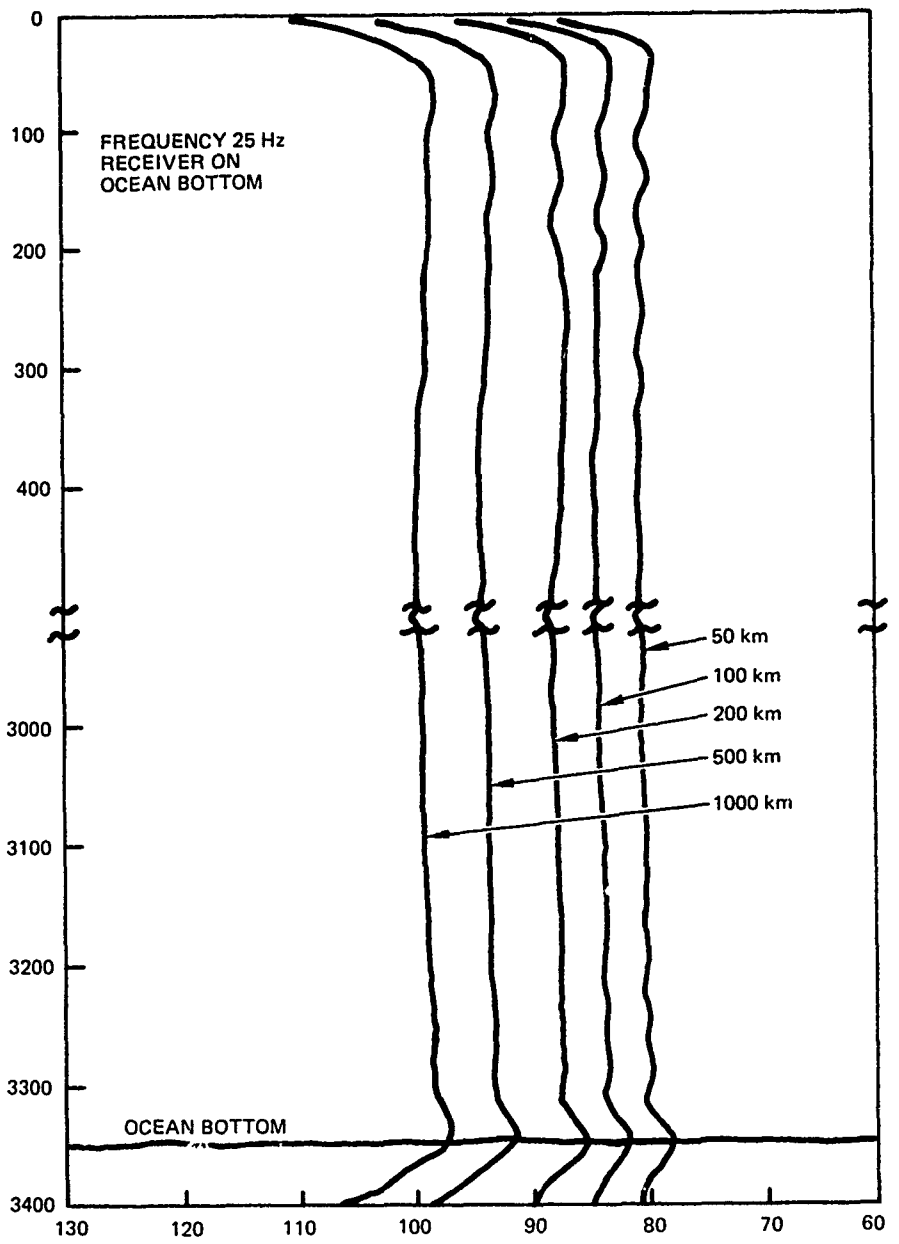

Figure V-10. (C) Theoretical propagation loss versus source depth for a bottom receiver at 25 Hz. (C)

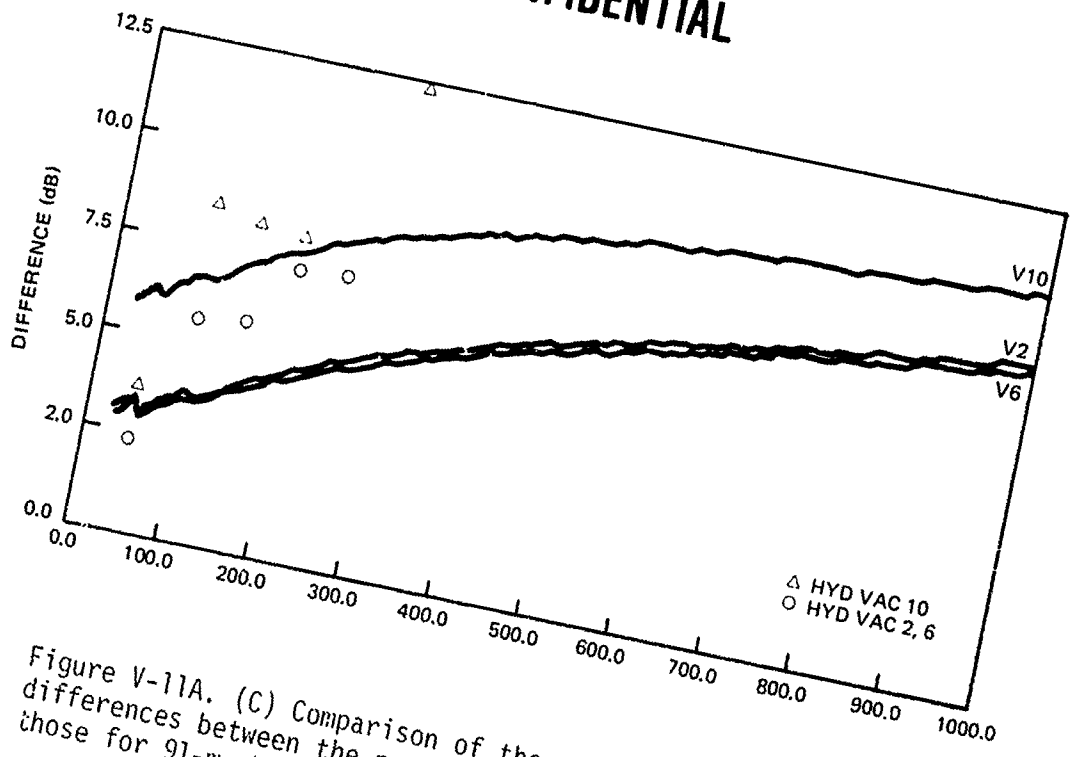

Figure V-11A. (C) Comparison of the experimental and theoretical differences between the propagation loss for 18-m shots and those for 91-m shots: 20 Hz. (C)

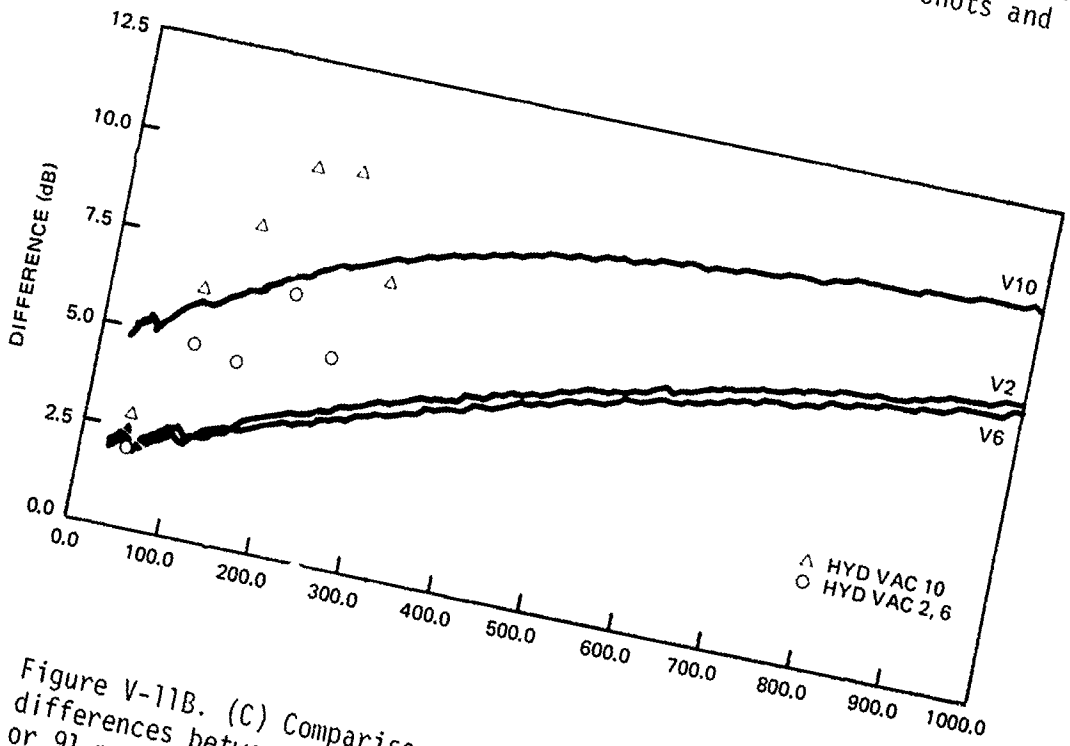

Figure V-11B. (C) Comparison of the experimental and theoretical differences between the propagation loss for 18-m shots and those or 91-m shots: 25 Hz. (C)

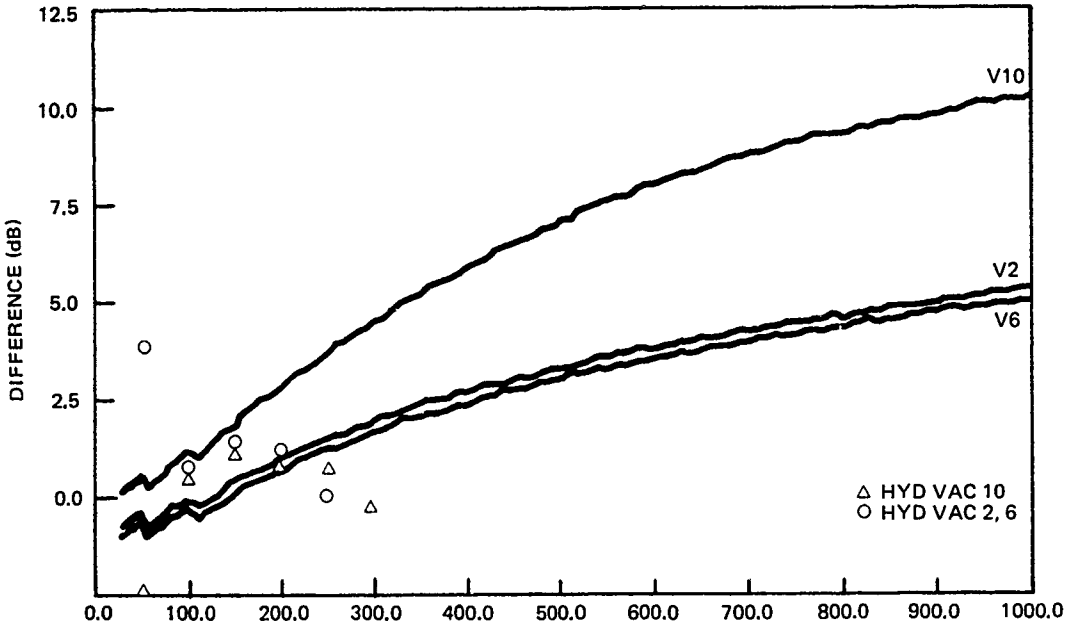

Figure V-11C. (C) Comparison of the experimental and theoretical differences between the propagation loss for 18-m shots and those for 91-m shots: 50 Hz. (C)

(C) These differences are summarized in table 6. The second column represents the average difference between the normal mode results of ACODAC 10 and the average of ACODAC 2 and 6 for ranges out to 250 km. Values of the standard error of this mean are also given as the second row of data for each frequency. The third column of table 6 is the experimental counterpart of the second column. In calculating these differences the data points at 250 km in figure 11A and at 50 km in figure 11C were rejected as being too far out of line with the remaining data. Comparison between theory and experiment is fair at 20 and 25 Hz and poor at 50 Hz. The experimental data show that the differences in propagation loss for the two source depths are indeed larger for receiver 10.

	THEORY	EXPERIMENT
20 Hz	3.0	2.0
	0.1	0.9
25 Hz	3.5	2.7
	0.3	1.6
50 Hz	1.8	0.2
	0.3	0.2

TABLE V-6. (C) AVERAGE DIFFERENCE BETWEEN THE VALUES OF FIGURES 11A TO 11C FOR RECEIVER 10 AND THE AVERAGE OF RECEIVERS 2 AND 6 (U).

(C) The absolute values of the experimental data do not agree well with the theory. This is most likely due to relative errors in shot source levels. If the shot levels were adjusted according to table 5, the experimental values of figure 11A and 11C would be reduced by 3.2 dB and 0.5 dB, respectively. This adjustment does not markedly improve the agreement between theory and experiment. The necessity for rejecting overloaded data subjects the remaining data to a bias which is difficult to assess.

(C) The data of figures 11A and B, while not definitive, are certainly encouraging enough to support a recommendation that the "notch" phenomenon be investigated further theoretically and that experiments be designed to specifically test it.

(C) Further evidence of the "notch" phenomenon was sought by comparing the ambient noise levels for ACODAC receivers 10 and 13. Figure 2.2.1 of Pedersen and Yee (1979) indicates that these noise levels were within 0.5 dB of each other over the frequency range from about 15 to 100 Hz. We attribute this negative result to the high density of shipping at Site 1B, where onboard personnel reported that shipping was within view throughout most of the exercise. The noise from nearby shipping cannot be reduced by the "notch" phenomenon. For this noise reduction concept to work, the receiver should be located in an area which is free of nearby shipping.

(C) This completes the discussion of Sites 1A and 1B, which is much longer than that for the remaining sites. Although it remains to be verified, we believe that the extensive results presented for Sites 1A and 1B are representative of any location which is severely bottom limited with low bottom loss.

V.2.2 (C) Site, 2, Owen Ridge

(C) The events for Site 2 are shown in figures II-24 and III-1. The receivers were draped over the Owen Ridge, which bounds the western edge of the Indus Fan. The close range bathymetric profiles differ considerably for the various events because the aspect the the ridge changes. Figure 12A presents the close range bathymetric profile for event S2, which runs out over the Indus Fan in an almost easterly direction. This event runs almost perpendicular to the ridge. The eastern edge of the ridge is a steep scarp which intersects the fan at a depth of 4000 m. The separation between BMA receivers 1 and 8 is about 13.5 km. Depths of these receivers are given in table 7A.

(C) Figures 12B and 12C are the counterparts of figure 12A for events P1 (or S1) and P3, respectively. Event P1 runs in a northwesterly direction. In figure 12B we see a relatively gentle slope to the northwest. The deepest point along event P1 is 3700 m (not shown in fig 12B), with the bathymetry rising again as the Arabian Peninsula is approached. Event P3 runs over the Fan in a south by southeasterly direction. The near-range profiles change for each receiver because the event is almost normal to the line of receivers. The near-range bathymetry for event A1 over the Fan is similar to that of event S2. That of event A3 to the southwest is similar to that of event P1. That of event A2 is almost too complicated to describe or to be of value because the event parallels the ridge and each bathymetric cut changes drastically with range along the event. For other events the near-range bathymetry holds for all but the closest ranges.

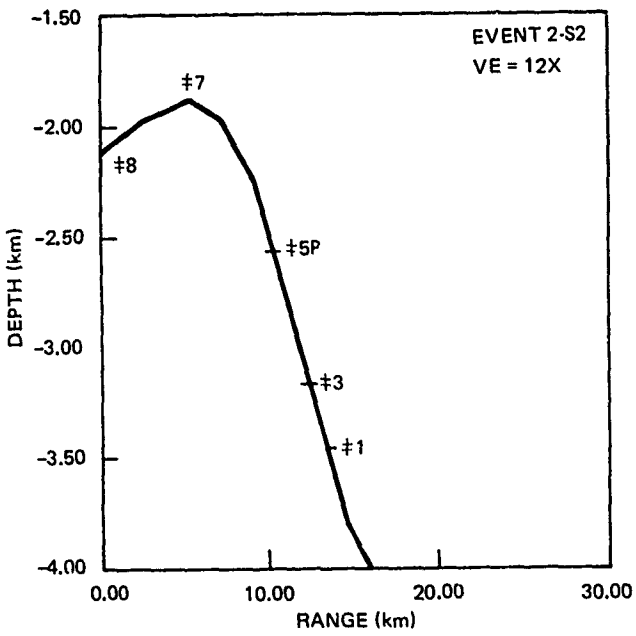

Figure V-12A. (C) Short range bathymetry at Site 2: Event S2. (U)

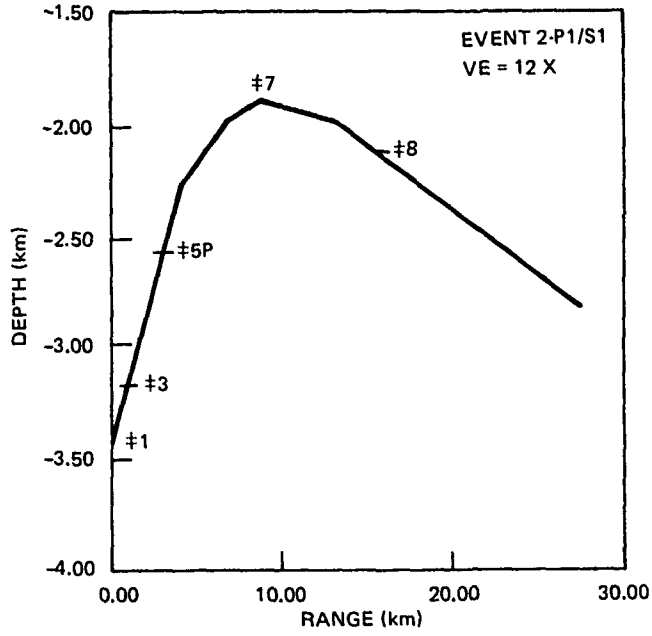

Figure V-12B. (C) Short range bathymetry at Site 2: Event P1. (U)

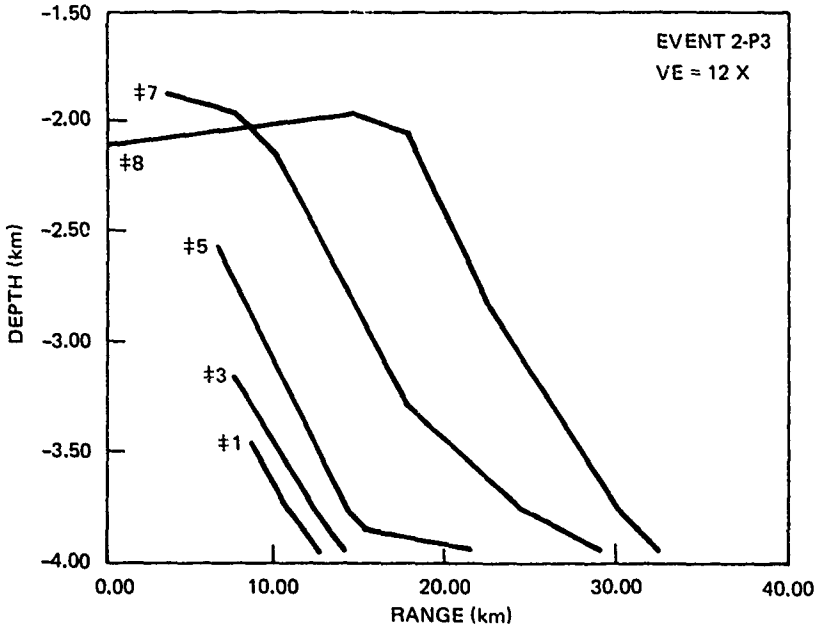

Figure V-12C. (C) Short range bathymetry at Site 2: Event P3. (U)

Receiver	Receiver Depth	Event P1		Event P3	
BMA	(m)	25 Hz	140 Hz	25 Hz	140 Hz
1	3454	5.0		0.8	
3	3162	7.6	5.8	0	0
6	2563	1.4		0.5	
7	1880	1.1	0	1.2	7.2
8	2112	0		1.5	

TABLE V-7A. (C) PROPAGATION LOSS DIFFERENCES BETWEEN OTHER RECEIVERS AND THE RECEIVER WITH LOWEST PROPAGATION LOSS FOR SITE 2 CW EVENTS. (U)

(C) The receiver depth dependence for the CW events is given in table 7. The results at 25 Hz for event P1 appear reasonable for propagation from the west. The lowest loss is for receiver 8 in figure 12B, and the loss generally increases for propagation over the ridge and down the steep scarp. However, it is not obvious why the loss should be higher for receiver 3 than for receiver 1, as receiver 1 is further down the scarp. The loss for receiver 7 on top of the ridge is less than that for receiver 3, which is well down on the scarp, for events P1, S1, and A3 of table 7. Again this is to be expected for propagation from the west of the ridge.

(C) The results at 25 Hz for event P3 appear reasonable. The losses are in general larger for those receivers in figure 12C which require longer traverses up the slope. However, it is not obvious why receivers 3 and 6 should have lower loss than receiver 1. Results at 140 Hz for event P3 are as expected.

(C) The results for S2 and A1 are generally as expected for propagation up the scarp of figure 12A. The losses for receiver 3 are less than for receiver 7 for eleven out of fifteen possible cases. However, it is not clear why the differences at 140 Hz for event A1 are so much smaller than those for event S2 when the bathymetric profiles are so similar.

(C) The results for event A2 in table 7 are mixed, with apparently little difference between receivers 3 and 7. This is probably related to the fact that the event parallels the ridge and the traverses do not favor one receiver over the other.

(C) Figures 13A, 13B, and 13C present propagation loss for the receiver with lowest loss for all events at Site 2 for low frequency, 140 Hz, and 290 Hz, respectively. At 25 Hz for P1 and P3, there are five receiver depths to choose from. At 290 Hz for all events there is only one receiver depth available. For all other cases there are two receiver depths to choose from. All the shot data are for 91 m-shots.

(C) The events which ran over the Indus Fan (A1, S2, and P3) are given line symbols in figures 13A, 13B, and 13C. Those events which run west of the Owen Ridge are given open symbols. Table 8 ranks the events according to increasing propagation loss at each frequency. The most significant feature is the higher losses west of ridge at 140 and 290 Hz. This is evident in figures 13A, 13B, and 13C where there are only three line symbols with larger

Event	Receiver	20 Hz			50 Hz			140 Hz			Frequency
	#	18 m	91 m	243	18 m	91 m	243 m	18 m	91 m	243 m	Shot Depth (m)
S1	3	4.1	4.8	5.5	4.8	9.6	7.0	5.5	3.2	5.5	
S1	7	0	0	0	0	0	0	0	0	0	
A2	3	0.6	2.0		0	0		0	0.1		
A2	7	0	0		1.8	0.8		0.3	0		
A3	3	5.6	5.5		7.3	7.6		4.2	5.0		
A3	7	0	0		0	0		0	0		
S2	3	0	0.2	0	3.3	0	0	0	0		
S2	7	0.4	0	2.9	0	2.1	2.9	5.6	8.9	5.7	
A1	3	0	1.3		0	0		0.5	0		
A1	7	0.2	0		3.9	4.8		0	1.3		

TABLE V7-B. (C) DIFFERENCE BETWEEN BEST AND WORST (BEST SHOWN AS ZERO) OF BMA RECEIVERS 3 AND 7 FOR SEVERAL SHOT EVENTS AT SITE 2. (U)

CONFIDENTIAL

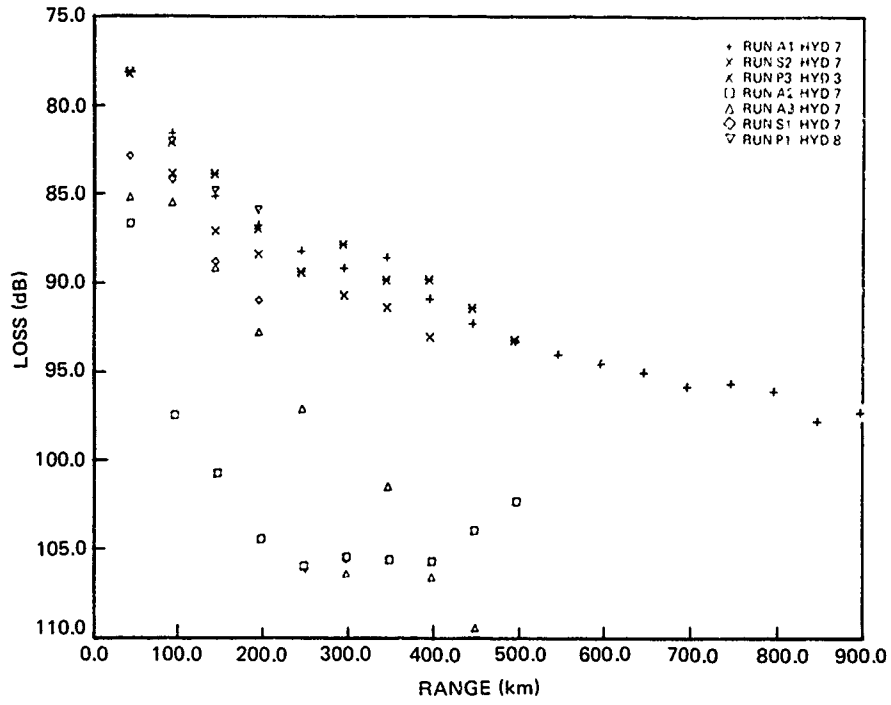

Figure V-13A. (C) Propagation loss versus range for all events at Site 2: low frequency. (C)

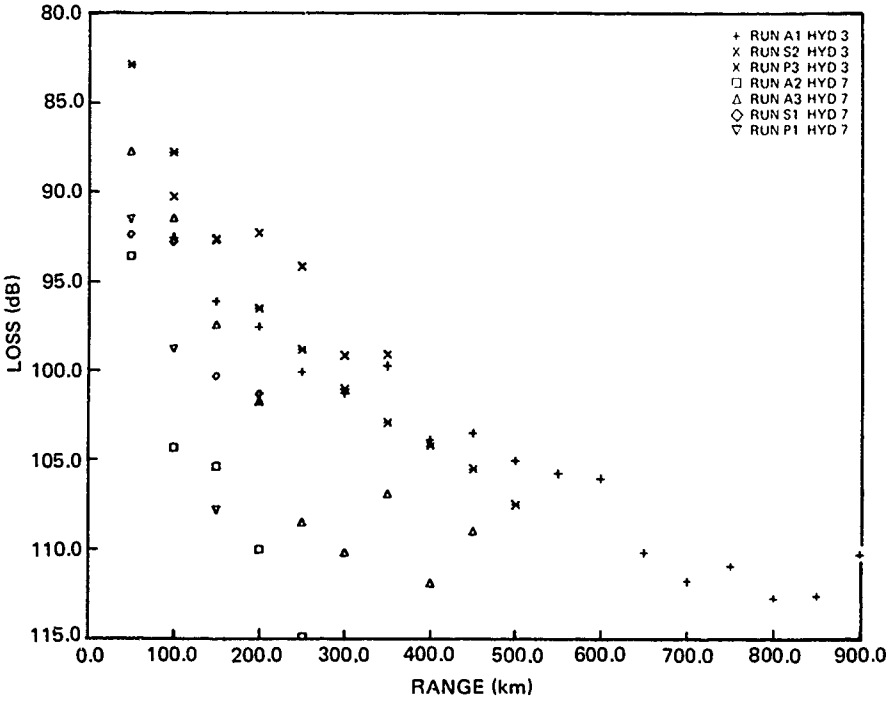

Figure V-13B. (C) Propagation loss versus range for all events at Site 2: 140 Hz. (C)

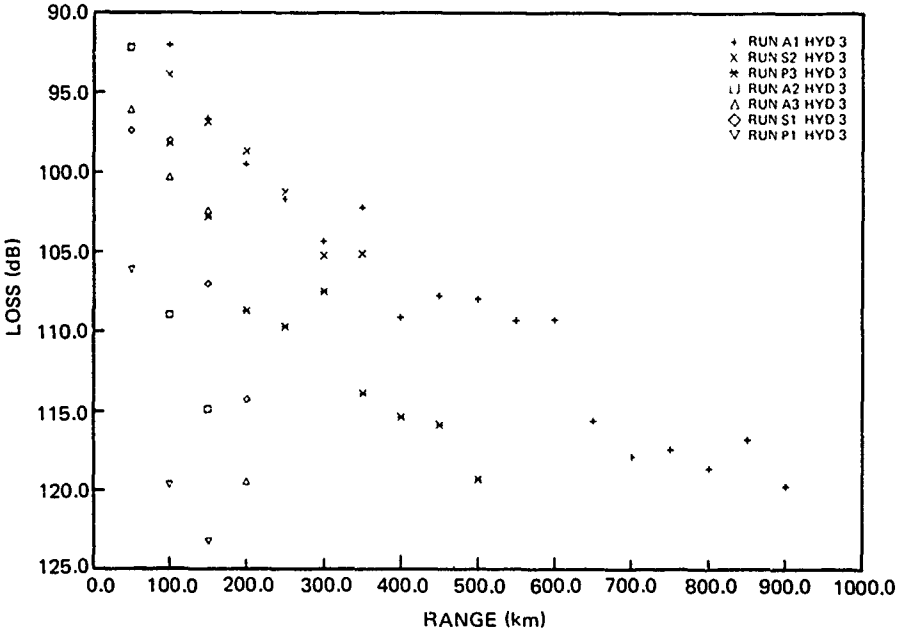

Figure V-13C. (C) Propagation loss versus range for all events at Site 2: 290 Hz. (C)

	Frequency		
RANK	Low Hz	140 Hz	290 Hz
1	A1	S2	A1
2	P1	P3	S2
3	P3	A1	P3
4	S2	A3	S1
5	S1	S1	A3
6	A3	A3	A2
7	A2	P1	P1

TABLE V-8. (C) RANKING OF EVENTS AT SITE 2. (U)

losses than open symbols. At low frequencies event P1 appears to be an exception in that it is a west of ridge event with lower losses than P3 and S2. This result suggests that for low frequency bottom loss west of the ridge may not be a great deal larger than that east of the ridge. Data from event A2 at Site 3 support this idea.

(C) A combination of circumstances at Site 2 makes further analysis exceedingly difficult. In the first place, WECo notes that there were problems with event S1. They did not publish (Osborne, 1978) their results for S1, although NOSC was furnished the data. Our analysis suggests that the S1 data are not seriously in error. In contrast, we believe that the P1 data

at 140 and 290 Hz are seriously in error, as will be discussed later. Our overall assessment of the ranking of events is A1, S2, P3, S1 or P1, A3, and A2. The more detailed analyses of Pedersen and Yee (1979) indicate that the propagation losses for events A2, A3, S1, and P1 are generally larger than those of the highest loss events at any of the other BEARING STAKE sites. This is no doubt due to propagation over regions of high bottom loss. Compared to the CW events at other Sites, event P3 across the Indus Fan has exceptionally high losses at 140 and 290 Hz. The reason for this is not known. The losses for events A1 and S2 appear consistent with those for other sites.

(C) Figure 14 compares the best event at each frequency with the Eleuthera Reference. This is event A1 for 20 and 290 Hz and event S2 at 140 Hz. The slope at 20 and 140 Hz is comparable to that of the reference, whereas the slope at 290 Hz is greater than that of the reference. The propagation loss at 20 Hz is as much as 11 dB less than that of the reference.

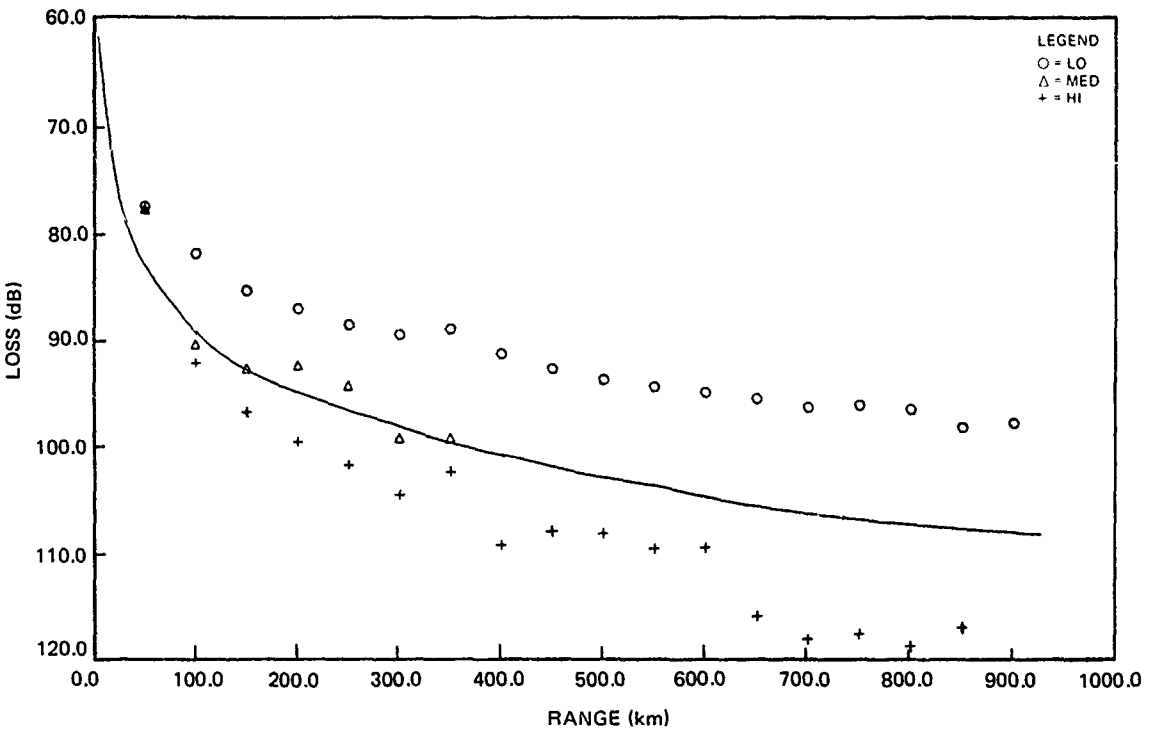

Figure V-14. (C) Comparison of the lowest-propagation-loss events at Site 2 with the Eleuthera reference. (U)

The loss at 140 Hz is slightly less than that of the reference, with values from 4 dB less to 1.5 dB greater than that of the reference. At long range the losses at 290 Hz are as much as 12 dB greater than that of the reference.

V.2.3 (C) Site 3, Indus Fan

(U) The events for Site 3 are shown in figures II-10 and III-1. At Site 3, all the BMA receivers were located on the ocean floor. The ACODAC receivers failed at this site and thus there are no measurements of receiver depth dependence at Site 3. The propagation losses presented here are based on the average for the BMA receivers which were processed.

(C) The propagation loss for the best CW events are presented in figure 15. However, the results for event P4, which was better than P2 at ranges of 250 and 300 km are also presented. The slopes for 25 and 140 Hz appear to be somewhat less than that of the Eleuthera reference, whereas the slope for 290 Hz appears slightly greater. Propagation losses at 25 and 140 Hz are respectively from 5 to 14 and 1 to 4 dB less than that of the reference whereas the corresponding values at 290 Hz are from 0 to 4 dB greater than that of the reference.

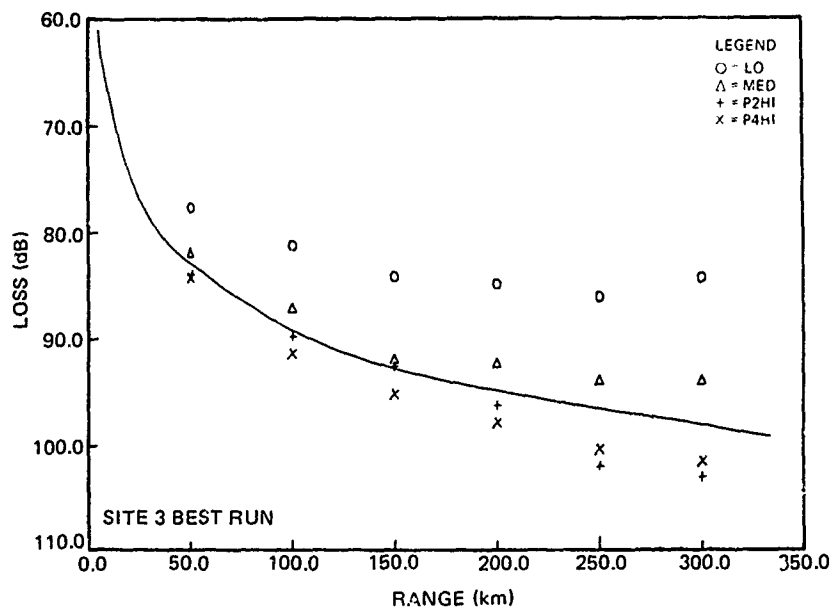

Figure V-15. (C) Comparison of the lowest-propagation-loss events at Site 3 with the Eleuthera reference. (U)

(C) The nine radial events at Site 3 afford a unique opportunity to prepare contours of constant propagation loss. In preparing these contours (figs 16A, 16B, 16C) the 91-m source depth data from the shot events were adjusted to be comparable to the CW events. On the basis of events P4 and S2, which were executed along the same track, it was determined that the propagation loss for the 20-Hz shot data should be increased by 1 dB to be comparable to the CW data at 25 Hz. Similar corrections for 140 and 290 Hz were 1.5- and 0.3-dB increase respectively. A minor adjustment was also made to the 42-Hz data for event P3 to bring them into agreement with the 25-Hz data for the other events.

(C) Figures 16A, 16B, and 16C present propagation loss contours from 85 dB up in 5 dB steps for frequencies of 25, 140 and 290 Hz, respectively.

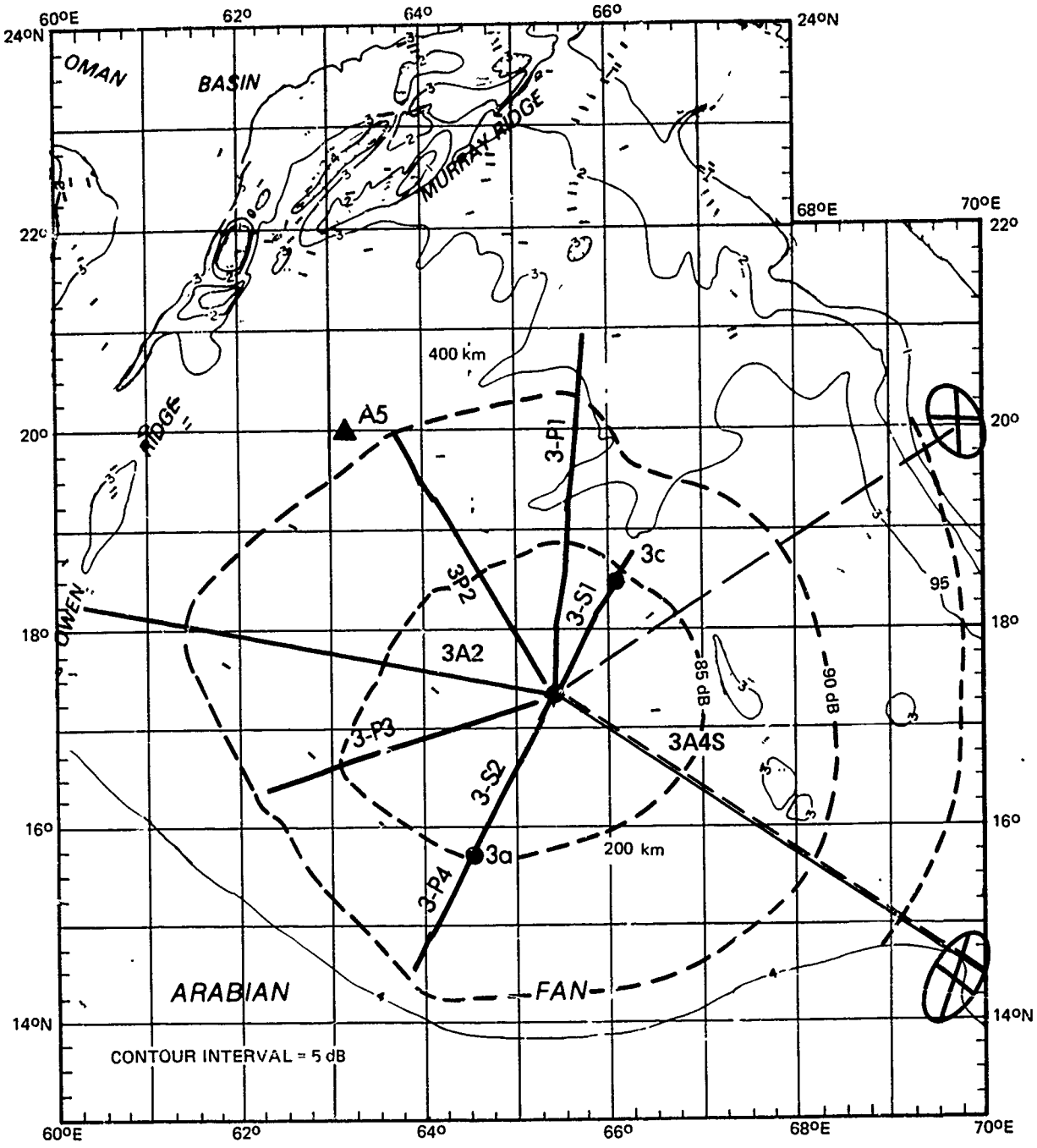

Figure V-16A. (C) Propagation loss contour plot for Site 3: 25 Hz. (C)

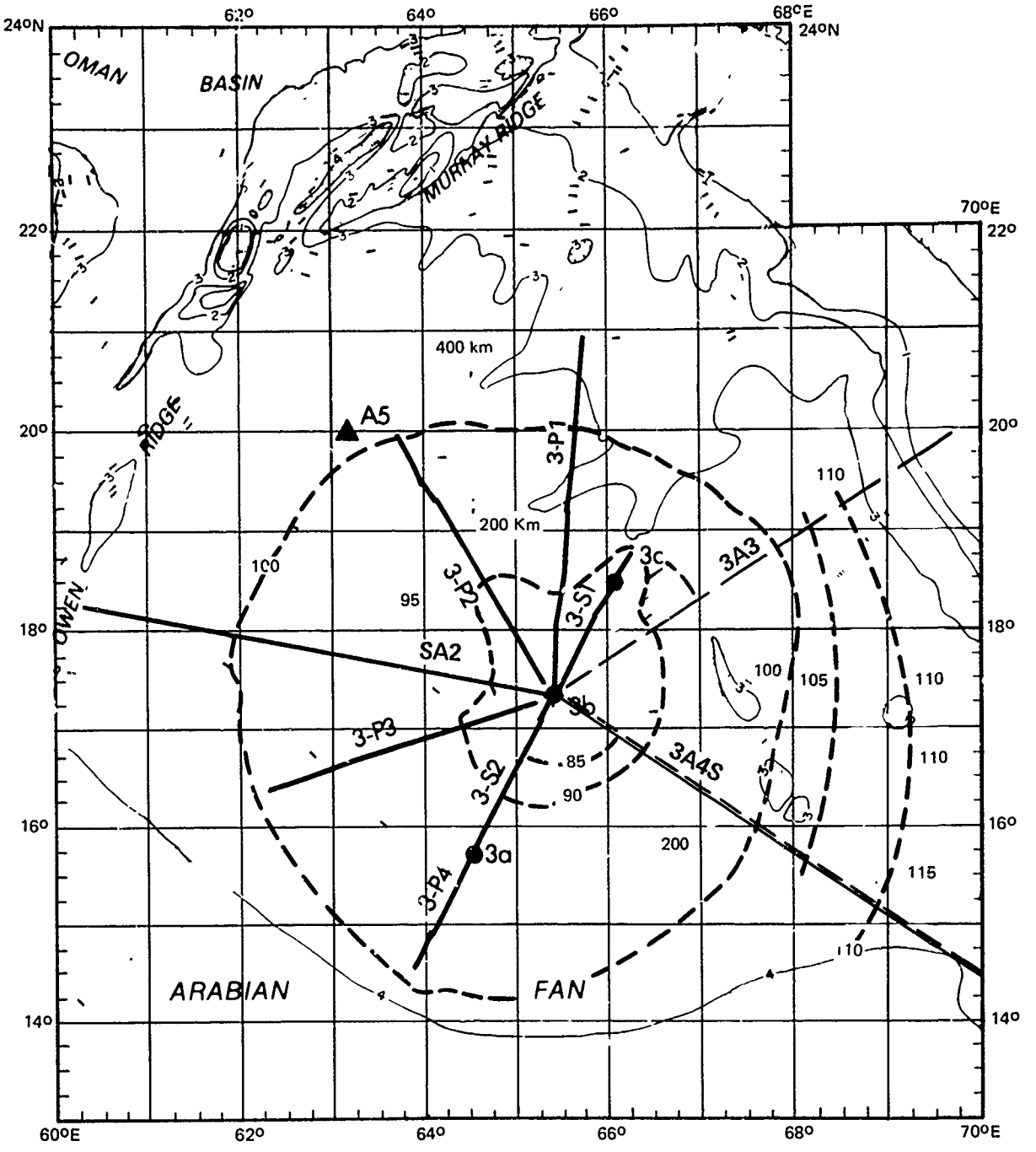

Figure V-16B. (C) Propagation loss contour plot for Site 3: 140 Hz. (C)

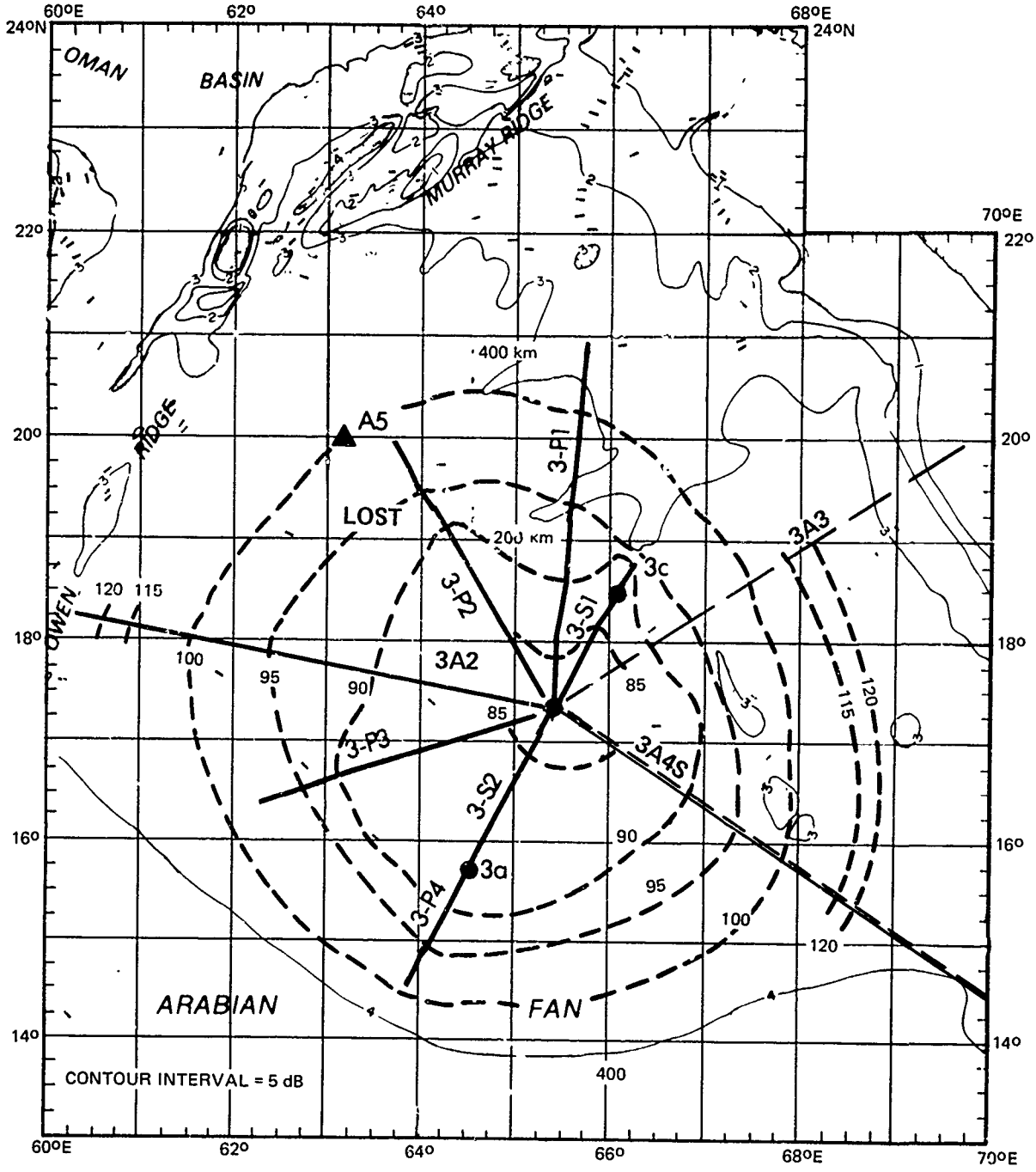

Figure V-16C. (C) Propagation loss contour plot for Site 3: 290 Hz. (C)

Several conclusions are apparent from an examination of these contours. At longer ranges there is consistently better propagation in the directions A2, P3, and P4 as compared to P1, A3, and A4. This is most apparent in the 85- and 90-dB contours at 25 Hz, in the 100-dB contour at 140 Hz, and in the 100–110-dB contours at 290 Hz. Propagation in the direction of event P2 is somewhat ambiguous. No data are available at low frequency because of a source failure. However, at the longest ranges tested, the loss at 140 and 290 Hz falls between that of A2 and P1. For events A1, A3, and A4 the data show some higher propagation losses than those of the closed contours. However, these higher loss data are rather sparse.

(C) The long range results for event 3A2 appear to confirm some of our previous conclusions for Site 2 about propagation west of the Owen Ridge, even though event 3A2 crosses the ridge about 120 nmi north of Site 2. Note that at 25 Hz there appears to be no rapid increase in propagation loss west of the ridge. Thus, at 25 Hz the loss to the west of the ridge is not radically greater than that to the east. In contrast, at 140 Hz there is a very rapid increase in loss to the west of the ridge. Figure 315 of the WECo data report (Osborne, 1978) indicates large losses at 290 Hz to the west of the ridge, with losses exceeding 125 dB and dropping below the noise threshold. This confirms our previous conclusion about propagation to the west of Owen Ridge — a relatively minor increase at 25 Hz and a major increase at 140 and 290 Hz.

V.2.4 (C) Site 4, Somali Basin

(C) The various events for Site 4 in the Somali Basin are given in figures II-15 and III-1. Figure 17 shows the BMA receivers draped up the Chain Ridge with the close range bottom contours appropriate for events P1 and S1. These events continue across the almost flat basin with a bottom depth slightly over 5100 m. The ACODAC receivers were located about 75 km from the foot of the slope along the track of event P1. ACODAC receiver 13 was mounted on the floor of the basin receivers and 2, 5, and 9 were suspended in the water column. Exact depths for the ACODAC and BMA bottom contours vary slightly for other events in that the slope is approached from more oblique angles than for event P1.

(C) Before addressing the acoustic results, we need to place Site 4 in the proper oceanographic context. Table 9 indicates the depth excess for various source depths and events. This table is based on a fixed bottom depth (5106 m) which was the value at ACODAC receiver 13. The maximum bottom depth occurs at the foot of the Chain Ridge and is about 5110 m. The values in table 9 are based on a sound speed which is the average value as measured along the track of the event at critical depths. The 18-m source depth is appropriate for the 140- and 290-Hz CW sources and 91-m source depth for the low-frequency CW source. The entries for 0 source depth are based on the maximum near-surface sound speed. These entries represent the depth excess for the zero angle ray which reaches the ocean surface. For several sound speed profiles along event P5 the near-surface sound speed exceeded that at the bottom (ie, the profiles were bottom limited).

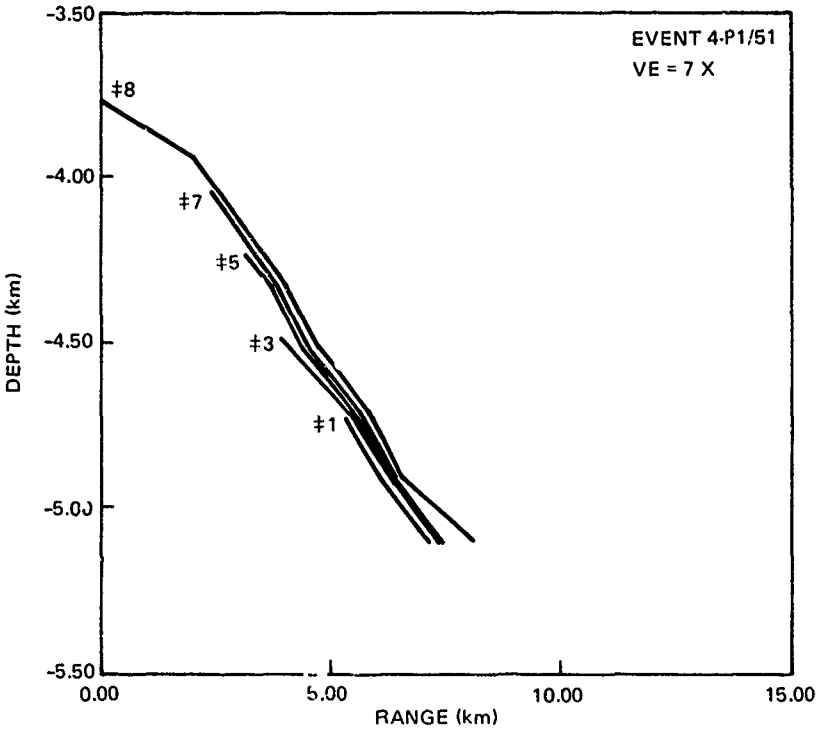

Figure V-17. (C) Short range bathymetry at Site 4 for events 4P1 and 4S1. (U)

	SOURCE DEPTH		
Event	0m	18 m	91 m
P1	121	147	263
S1	96	121	259
P2	51	76	197
P4	35	66	238
P5	0	30	276

TABLE V-9. (C) DEPTH EXCESS (M) AT SITE 4 FOR VARIOUS SOURCE DEPTHS AND EVENTS. (U)

(C) Before discussing the receiver depth dependence, we shall look at some significant data plots from Site 4. Figure 18 presents propagation loss at 290 Hz for event P1, receiver 1, which represents the condition of lowest propagation loss at this frequency. The triangles represent the experimental data averaged in 2-km bins. The solid curve is the corresponding theoretical propagation loss of the RAY WAVE model. The squares are the corresponding result for the ASTRAL model. The convergence zones rise 10 to 20 dB above the bottom-reflected propagation (between the zones). Both RAY WAVE and ASTRAL agree reasonably well with experiment. The crosses represent propagation for

the best receiver for event P5, which had the least depth excess in table 9. It is apparent that the propagation is much poorer in event P5 than event P1.

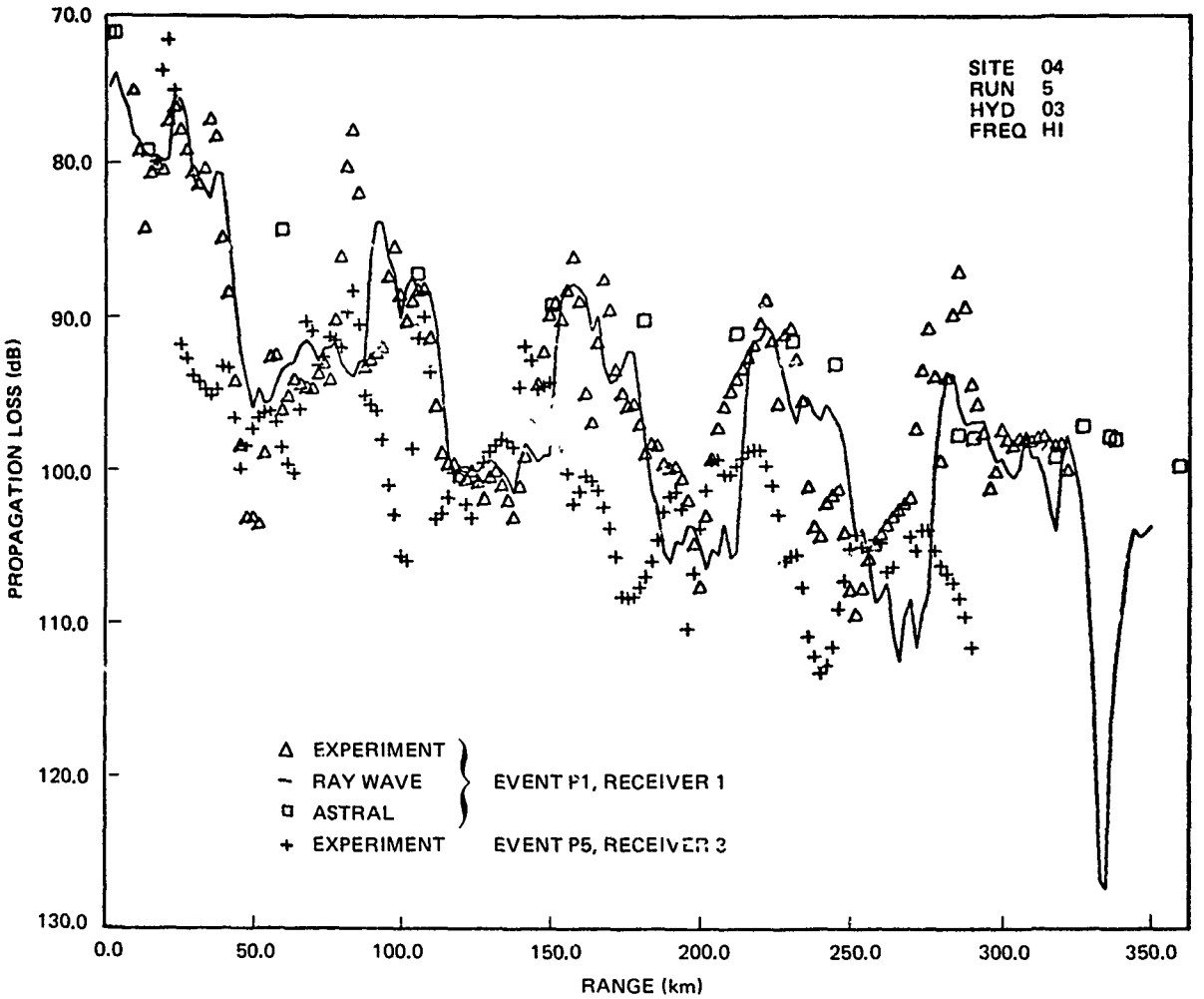

Figure V-18. (C) Propagation loss at Site 4 for 290 Hz, illustrating experimental and theoretical convergence zone structure. (C)

(C) In figure 19 the conditions for the experimental triangle, RAY WAVE, and ASTRAL are the same as those for figure 18 except the frequency is 25 Hz. Again RAY WAVE and ASTRAL agree reasonably well with the data. As can be seen in both experiment and theory, there is little evidence of convergence zones. The low-bottom-loss propagation between zones appears to mask the zones. We call attention to the fact that the source depth at 25 Hz is 91 m as compared to 18 m for 290 Hz. Hence, there are more non-bottom-reflected paths available for 25 than for 290 Hz. Whatever the reason, the behavior of propagation loss at 25 Hz is significantly different from that at 290 Hz. For example, in figure 19 the crosses represent the experimental propagation loss for event P1 for receiver 7, which is the receiver with lowest propagation loss at 25 Hz.

This will be discussed in more detail later. Although not shown here, the results at 140 Hz show a convergence zone structure which is not as pronounced as that at 290 Hz.

(C) Figure 20 compares the experimental data for event P4 having the lowest propagation loss at low frequency with the experimental data for event P5 having the largest propagation loss. The propagation losses at 25 Hz for event P1 (shown in fig 19) and for event P2 fall between those plotted in figure 20. The higher losses for event P5 at 36 Hz as compared to event P1 and P2 at 25 Hz result from higher bottom loss at 36 Hz as well as conditions of smaller depth excess.

(C) The receiver depth dependence for the CW and shot events is given in tables 10A and 10B respectively. The major features of this depth dependence are also illustrated by figures 21A to 21D. All the entries of table 10A and the entries of table 10B for 91-m depth at 20 and 50 Hz and 18-m depth at 140 Hz are plotted in figures 21A to 21D. The receiver numbers are indicated in the vertical scale at their respective depths. There is a scale break between 2000 and 3600 m. The curves on the figures join the average values for each receiver based on all the events available for that receiver. Dashed or missing portions of the curves indicate regions where there are insufficient data to define the curve. In constructing these curves, all the event data were lumped together, although there are events which are significantly different. We will point out the general features of the figures and address significant exceptions.

(C) First, note that the curves have ignored the data for BMA receiver 6. With the possible exception of figure 21B, the data for BMA 6 are clearly out of line with other data. Indeed in all but four cases in tables 10A and 10B (event P4 at 290 Hz and events A1 and A2 at 50 Hz), the losses for BMA receiver 6 are greater than for BMA receivers 3 and 7, which straddle receiver 6. Thus, we regard the BMA receiver 6 results as strongly suspect.

(C) Next, consider data for ACODAC receivers 2 and 5 illustrated in the top section of figures 21A, 21C, and 21D. These receivers have higher losses than the optimum receivers by 3.7 to 8.5 dB. Thus receivers suspended high in the water column are relatively poor for all three tested frequencies.

(C) Consider next the near-bottom section of figures 21C and 21D. Clearly 140 and 290 Hz have a similar receiver depth dependence. Although BMA receiver 1 generally has the lowest loss of the experimental receiver depths, the trends of the data clearly indicate that propagation loss should be even smaller for a receiver between BMA 11 and ACODAC 9. Under convergence zone conditions, we would expect the minimum loss to occur near the critical depth, which, according to table 9, is between 147 and 30 m off the ocean floor for the 18 m-source. In the case of event P5 at 290 Hz the critical depth is 30 m off the ocean floor, and table 10A indicates that indeed ACODAC receiver 9 is the best receiver. The behavior then at 140 and 290 Hz is clear-cut and understood. The maximum loss is for the bottomed receiver 13 since the principal propagation paths must be bottom bounce. As the receiver depth decreases, a minimum loss occurs near the critical depth. As the receiver depth is decreased further, the propagation loss increases again.

CW EVENT		EVENT P1 (Hz)			EVENT P2 (Hz)			EVENT P4 (Hz)			EVENT P5 (Hz)		
RECEIVER #	RECEIVER DEPTH (m)	25	140	290	25	140	290	39	140	290	36	140	290
BMA 1	4726	4.8	0	0	3.3	0	0.1	0	0	0	6.3	3.5	0.6
3	4486	4.5	0.8	0.9	4.8	1.5	0	5.6	2.8	3.3	5.3	0	0
6	4236	12.2	5.5	8.1	5.9	7.0	3.8	6.9	7.4	5.5	8.8	7.8	3.7
7	4048	0	2.4	5.4	0.	5.9	3.0	1.9	6.8	7.9	0	3.7	2.2
8	3778	1.0	3.3	8.5	0.8	5.9	5.0	1.0	6.1	7.6	0.3	3.7	2.3
ACODAC 2	400	4.1	5.1	6.1	4.3	8.3	3.8	5.3	8.5	6.4	4.1	5.2	2.2
5	1916	4.3	4.3	7.5	4.0	8.1	5.5	5.5	8.2	7.5	3.7	5.1	3.6
9	5076	0.5	1.7	8.0	1.4	4.7	6.6	2.0	5.2	9.1	-0.2	1.6	-0.1
13	5106	1.7	10.8	12.0	1.7	14.2	9.7	2.5	13.0	12.4	0.3	11.3	4.7

TABLE V10A. (C) PROPAGATION LOSS DIFFERENCES BETWEEN OTHER RECEIVERS AND THE RECEIVER WITH THE LOWEST PROPAGATION LOSS FOR SITE 4 AND FOR THE CW SOURCE EVENTS. (U)

		20			50			140			Frequency (Hz)
EVENT	BMA Hydrophone	18	91	243	18	91	243	18	91	243	Shot Depth (m)
S1	1	1.	7.7	8.8	.4	.5	1.5	0	0	2.1	
	3	1.0	4.4	6.7	3.0	3.0	3.4	.7	0	1.3	
	6	5.7	10.1	11.7	4.6	4.8	5.6	5.2	5.5	6.8	
	7	0	0	0	.7	0	0.5	1.4	.2	0	
	8				0	.5	0				
A1	1	1.4	1.9		0	0		0	0		
	3	4.3	3.9		5.9	7.2		.4	0		
	6	8.1	8.1		5.7	7.3		6.4	5.5		
	7	0	0		1.4	1.2		3.0	2.3		
					1.0	.2					
A2	1	1.2	0.1		.8	.7		0	0		
	3	7.1	4.3		9.2	8.7		2.7	7.8		
	6	5.5	7.0		4.7	7.3		3.6	3.7		
	7	0	0		1.4	2.7		1.8	1.6		
	8				0	0					

TABLE V-10B. (C) PROPAGATION LOSS DIFFERENCES BETWEEN OTHER RECEIVERS AND THE RECEIVER WITH LOWEST PROPAGATION LOSS FOR SITE 4 AND FOR THE SHOT SOURCE EVENTS. (U)

CONFIDENTIAL

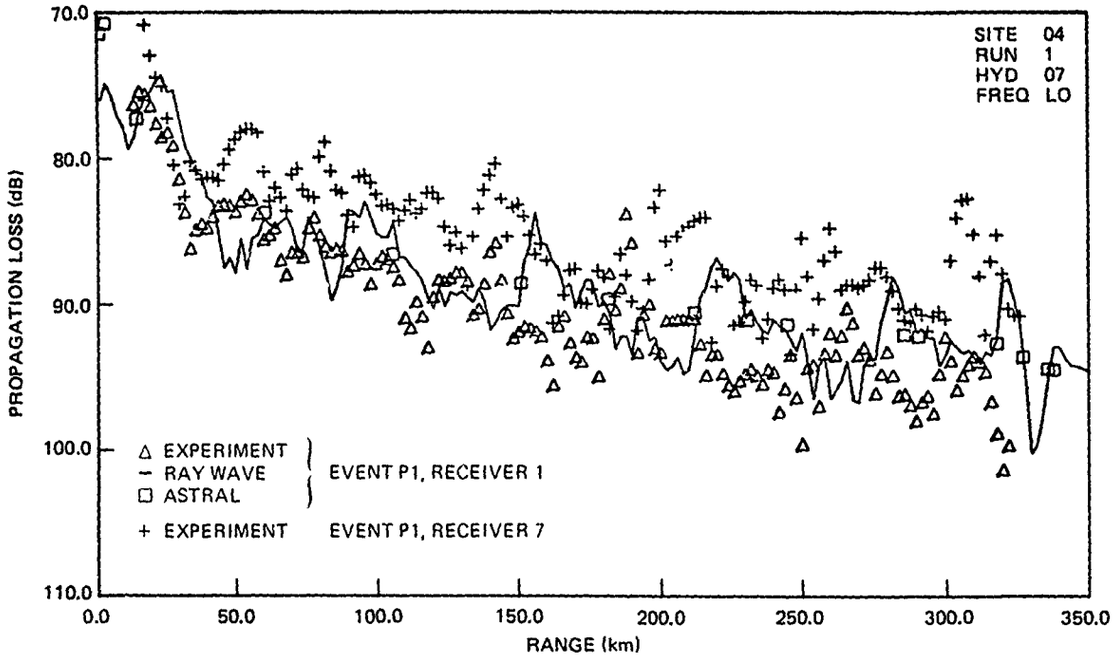

Figure V-19. (C) Propagation loss at Site 4 for 25 Hz, illustrating little convergence zone structure. (C)

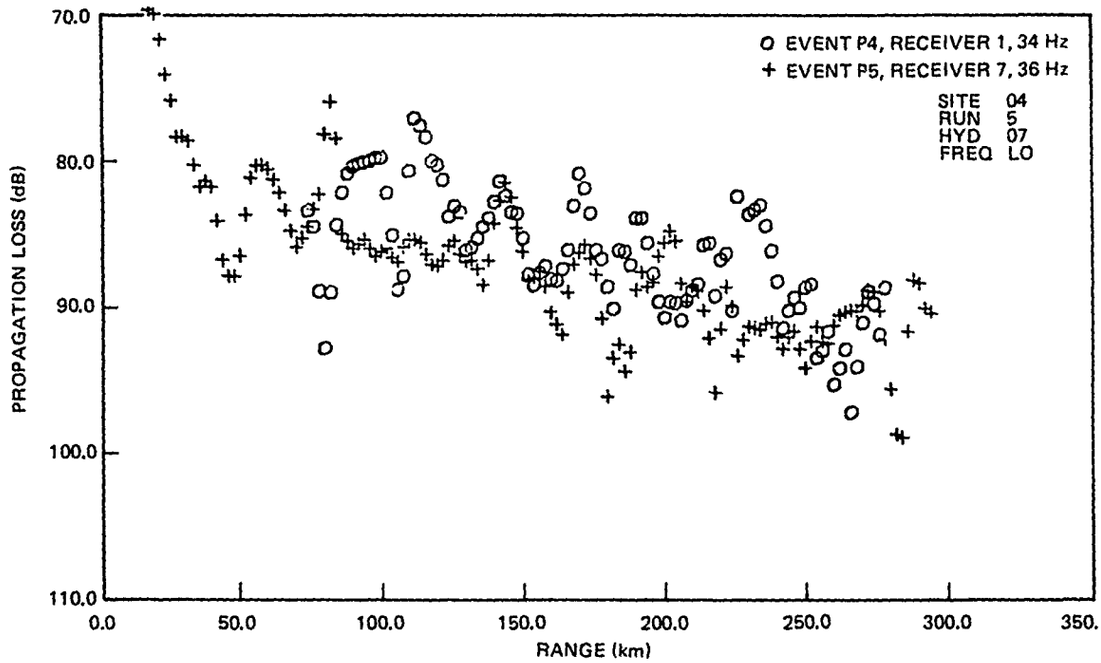

Figure V-20. (C) Comparison of propagation loss at low frequency for events P4 and P5 at Site 4. (U)

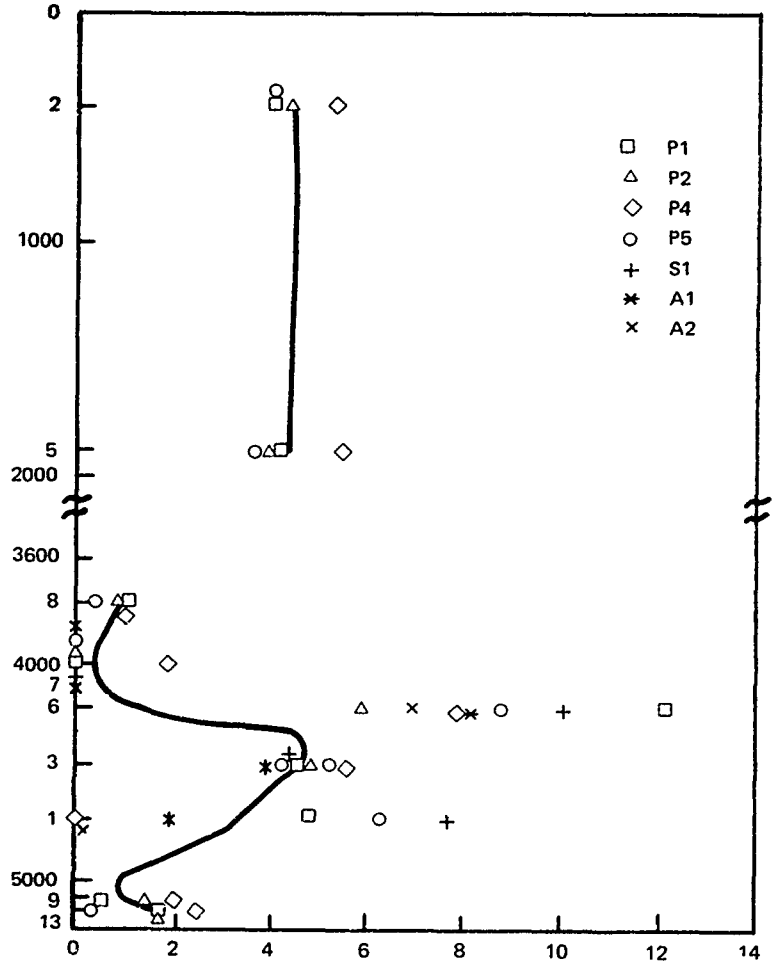

Figure V-21A. (C) Propagation loss differences between other receivers and the receiver with lowest propagation loss for Site 4 events: low frequency. (C)

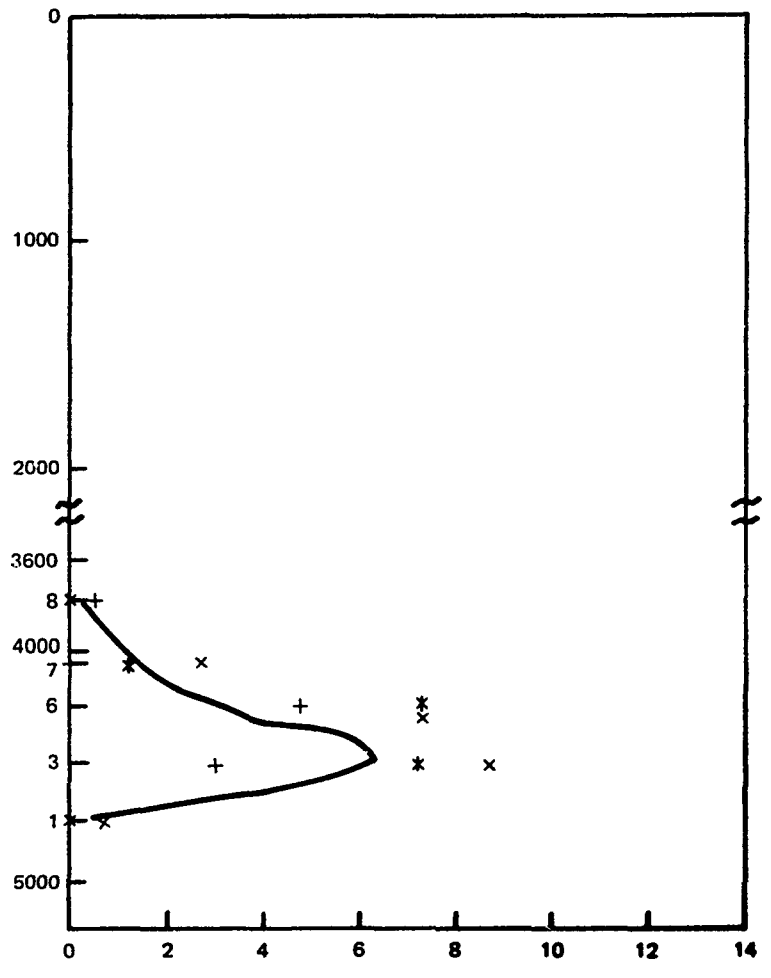

Figure V-21B. (C) Propagation loss differences between other receivers and the receiver with lowest propagation loss for Site 4 events: 50 Hz. (C)

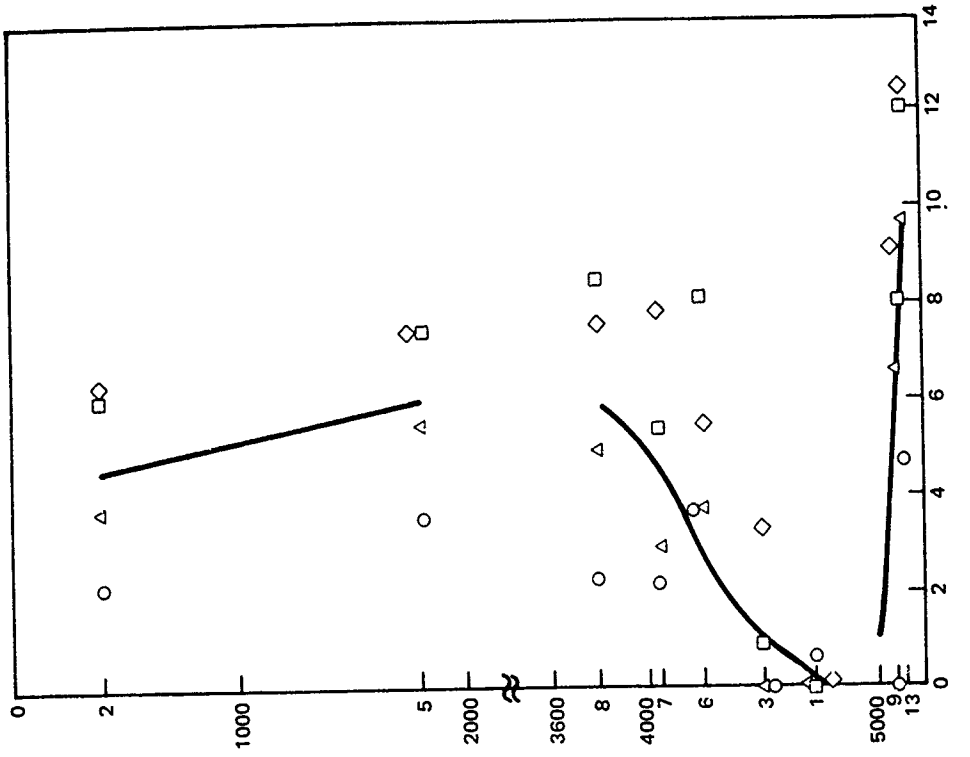

Figure V-21D. (C) Propagation loss differences between other receivers and the receiver with lowest propagation loss for Site 4 events: 290 Hz. (C)

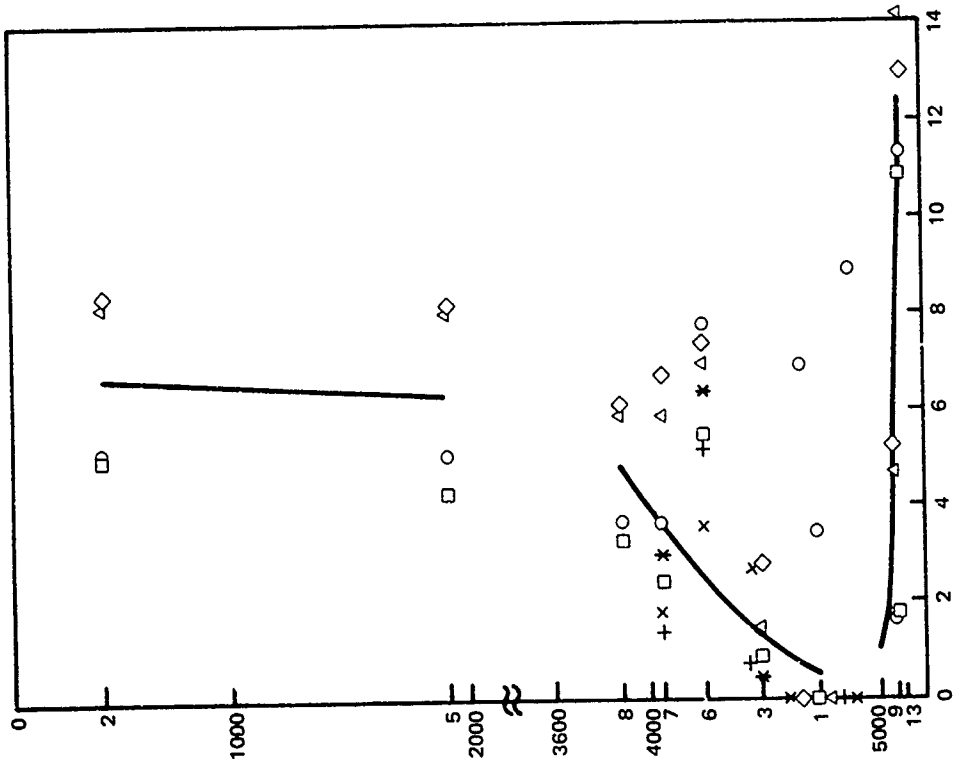

Figure V-21C. (C) Propagation loss differences between other receivers and the receiver with lowest propagation loss for Site 4 events: 140 Hz. (C)

(C) The results at low frequencies in figures 21A and 21B significantly contrast with those at higher frequencies. Under convergence zone conditions we would expect the minimum loss again to occur near the critical depth, which according to table 9 is between 197 and 276 m off the ocean floor for the 91-m source depth of the CW and shot events of figures 21A and 21B. Thus, we would expect that BMA receiver would again be the best receiver, indeed even relatively better than for the 18-m source depth. This is clearly not the case.

(C) In figure 21A, BMA receiver 7 is generally the best receiver, followed by BMA 8, ACODAC 9, ACODAC 13, BMA 1, and BMA 3. The receiver depth behavior is clearly very complicated. The mechanism is not understood and has not been successfully modeled. For example, at 25 Hz for event P1 the ASTRAL model predicts a loss for receiver 7 which is 0.6 dB greater than that for receiver 1 rather than the experiment value, which is 4.8 dB less than that for receiver 1. Despite our inability to explain figure 2A, the data appear to be correct. For example, the paired results of BMA 7 and 8, of BMA 1 and 3, and of ACODAC 13 and 9 are very consistent. Thus, we cannot reject these data as was done with BMA 6.

(C) In figure 21B at 50 Hz the propagation loss is lowest and about the same for receivers 1 and 8. Receiver 11 appears to be better than receiver 7 at 50 Hz. Note in table 10A that event P4 at 39 Hz suggests this. For this event the best receiver is BMA 1 which is 1 to 2 dB better than BMA 8 or 7.

(C) These data indicate that, at frequencies of 50 Hz and below, the receiver depth structure is quite complicated and is strongly dependent on frequency.

(C) It has been recommended by members of the System Assessment Team that the system assessment for Site 4 be conducted for receiver 7. This choice was no doubt based on the smaller propagation loss at 25 Hz. However, as we have seen for event P4, the propagation loss for this receiver is 6.8 and 7.9 dB greater than the propagation loss for receiver 1 at frequencies of 140 and 290 Hz. Moreover, the result at 39 Hz and the mixed results at 50 Hz suggest that a strong case can be made for receiver 1. Furthermore, in other seasons with greater depth excess the dependence on receiver depth may be quite different. Our contention is that the problem of the optimum receiver depth at Site 4 is an open issue. Before we can really select an optimum receiver depth at Site 4, we need a much better understanding of the physical principles involved. This understanding can only be obtained by a rigorous theoretical analysis followed up and verified by additional experimental measurements.

(C) Figures 22A, 22B, and 22C present propagation loss for the receiver with lowest loss for all events at Site 4 for 25 Hz, 140 Hz, and 240 Hz respectively. The CW events are plotted with open symbols while the shot events are given line symbols. Table 11 ranks the events according to increasing propagation loss. With the exception of event A2, the ranking at the low frequency and 140 Hz is the same. There is a general pattern with some exceptions. The ranking at 140 Hz coincides with decreasing bearing.

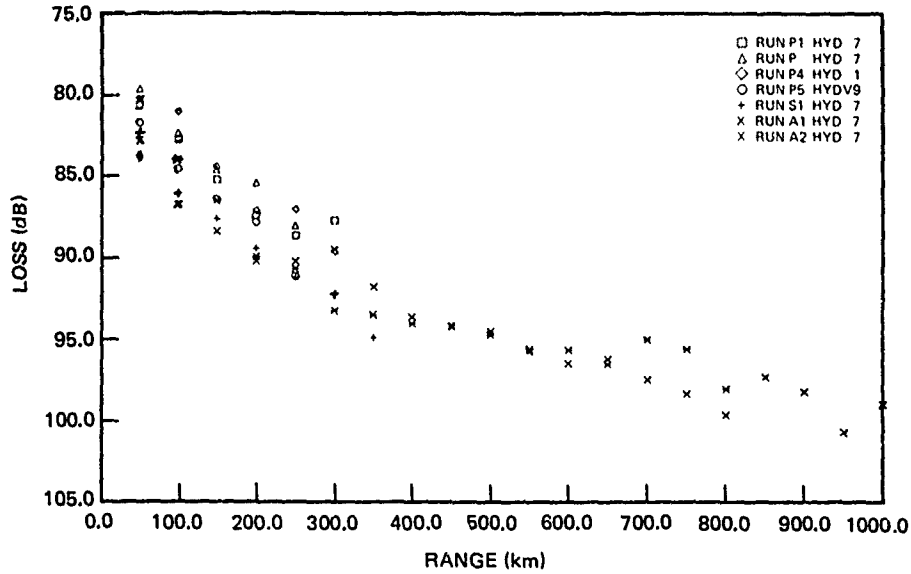

Figure V-22A. (C) Propagation loss versus range for all cvents at Site 4: low frequency. (C)

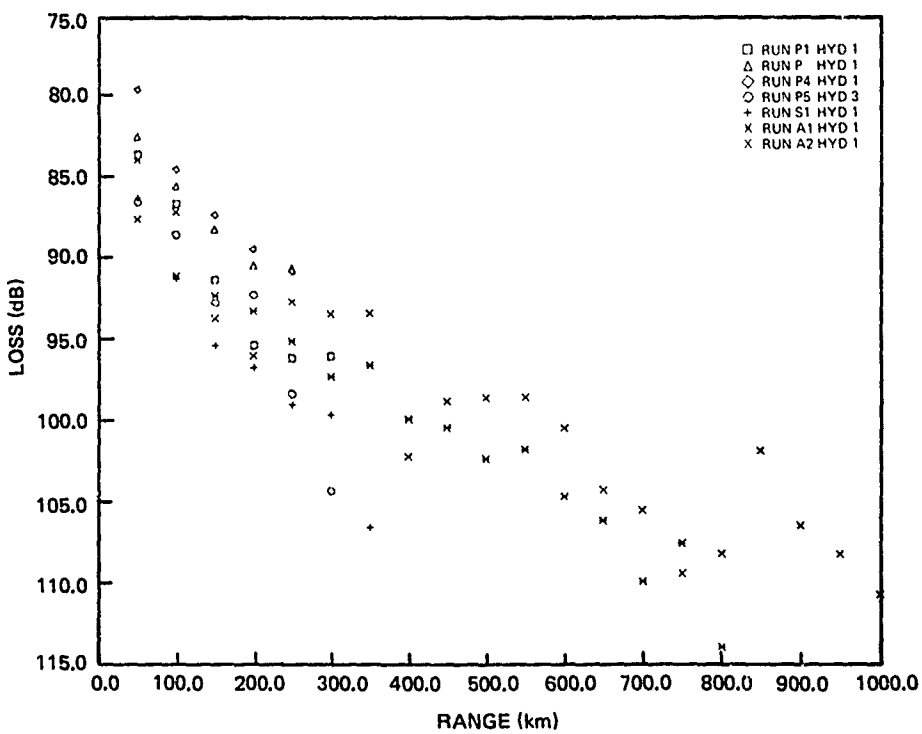

Figure V-22B. (C) Propagation loss versus range for all events at Site 4: 140 Hz. (C)

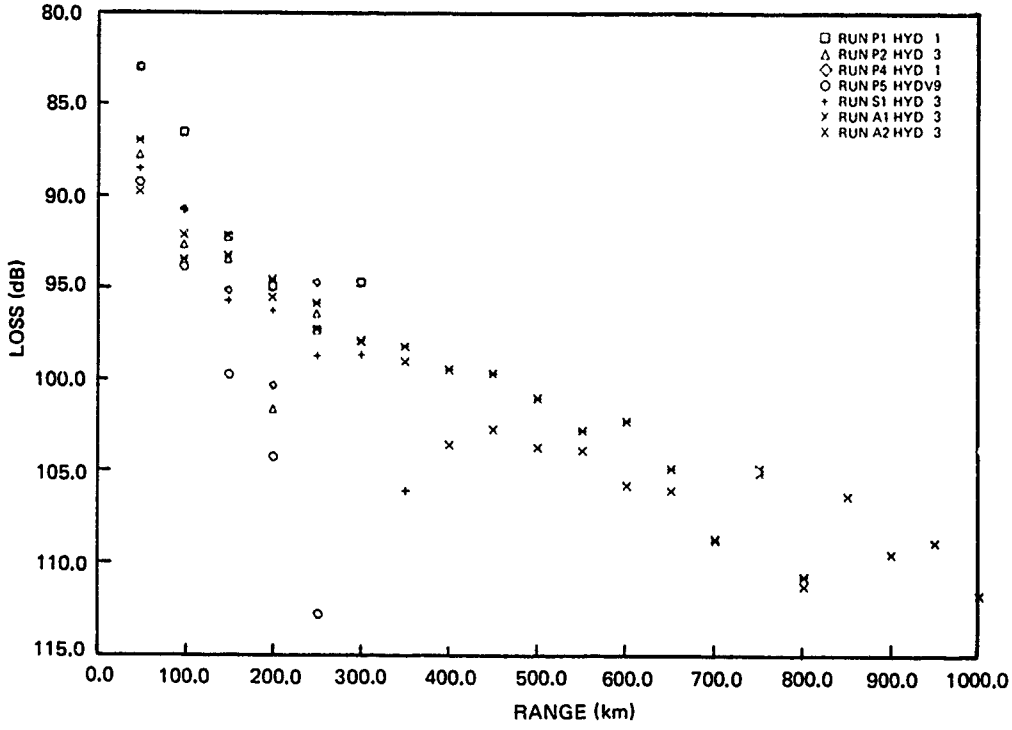

Figure V-22C. (C) Propagation loss versus range for all events at Site 4: 290 Hz. (C)

	FREQUENCY		
RANK	LOW	140	290
1	P4	P4	P1
2	P2	P2	P4
3	P1	P1	A1
4	A1	A2	A2
5	P5	A1	P2
6	S1	P5	S1
7	A2	S1	P5

TABLE V-11. (C) RANKING OF EVENTS AT SITE 4 (U).

(C) As can be seen in figure II-15, the bearing decreases for events P4, P2, P1, and P5 and for events A2, A1 and S1. There is not a great deal of difference in the maximum bottom depth along these events as they cross the Basin — perhaps 2 or 3 m. However, the bottom slope is less in the northerly direction and more in the westerly direction. Small but consistent differences in bottom depth could affect the CW sources at 18-m depths for 140 and 290 Hz. However, it is difficult to see how these differences could affect the 91-m shots since, table 9 indicates relatively large depth excesses for this condition. At 290 Hz the ranking of events P1 and P5 agrees with the depth excesses of table 9. However, this is about the extent of agreement

between tables 11 and 9. As in the use of optimum receiver depths, we need a better understanding of the physical principles of near bottom-limited propagation before we can provide a satisfactory interpretation of the ranking of events at Site 4.

(C) Figure 23 compares the best events for each frequency with the Eleuthera reference. The slopes at 25 and 39 Hz are less than that of the reference, with losses at long range as much as 10 dB less than those of the reference. The slopes at 140 and 290 Hz are similar to that of the reference. At 140 Hz the losses are as much as 6 dB less than those of the reference. At 290 Hz the losses are generally above those of the reference, with values ranging from 3 dB less to 1 dB more.

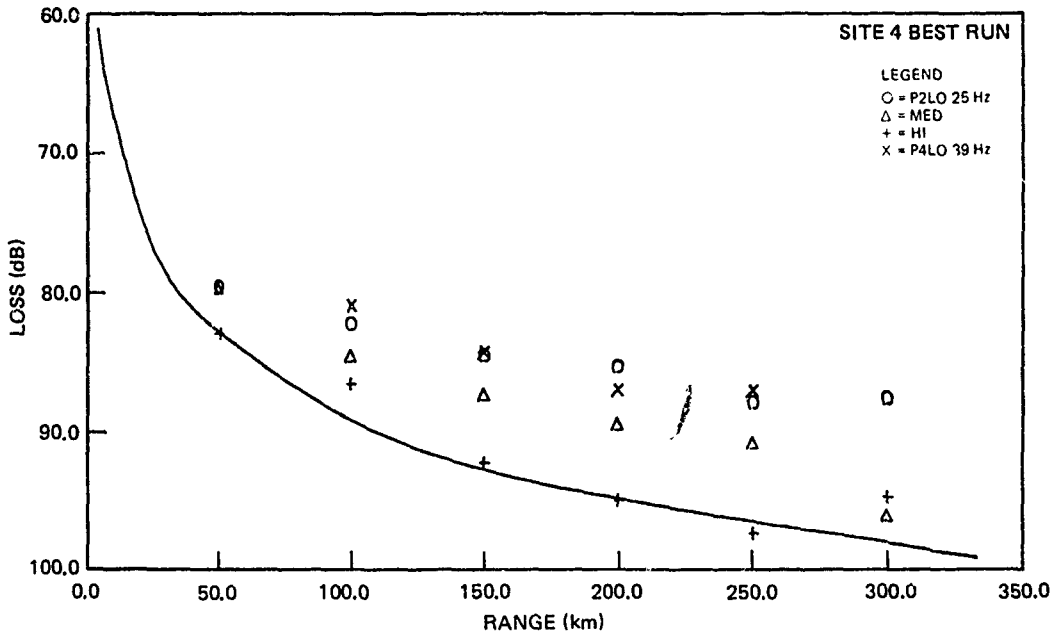

Figure V-23. (C) Comparison of the lowest-propagation-loss events at Site 4 with the Eleuthera reference. (U)

(C) Historical oceanographic data for the Somali Basin indicate maximum surface temperature in April, with higher temperature in May than in March, the month of the BEARING STAKE measurements at Site 4. Thus, propagation at 290 Hz for the months of April and May may be expected to be worse than that encountered in event P5. Propagation for the month of June through February may be better than that encountered on event P1. At low frequency (25 Hz) and perhaps at 140 Hz the propagation conditions for April and May may not be significantly worse than those of event P5. However, propagation at these frequencies could improve significantly during conditions of large depth excess. We anticipate that the propagation conditions at other BEARING STAKE sites will not be strongly dependent on season.

V.2.5 (C) Site 5, Southern Indus Fan

(C) The events for site 5 are shown in figures II-20 and III-1. BMA receivers 3 and 5 were located about 10 m from the top of a small conical hill rising about 700 m above the south end of the Indus Fan. Receiver 2 was buoyed up 380 m above the hill while receiver 1 was buoyed up 600 m above the hill.

(C) Figure 24A presents the close range bathymetry for events P1 and S1. It illustrates the small hill. The bathymetry for the remainder of the event has a very gentle slope as the event proceeds up the Indus Fan. The bathymetry for events A1 and A3 is similar to that of figure 24A, with no obstructions beyond the base of the hill.

(C) Figure 24B presents the close range bathymetry for the propagation paths of event P5, which has a major obstruction centered about 30 km from the receiver. The bathymetry is essentially flat beyond the obstruction. The range limits of event P5 were from 131 to 407 km, so the event itself was over a flat bottom with the propagation paths crossing over the obstruction and into the receiver.

(C) Figure 24C presents the close range bathymetry of event P2, which has a minor obstruction centered about 24 km from the receiver. The close range bathymetry of event A2 was comparable to that of event P2.

(C) The receiver depth dependence of propagation loss is presented in table 12A for the CW events and in table 12B for the shot events. Consider first the low-frequency data. The bottomed receivers (3 and 5) always have less loss than the suspended receivers (1 and 2). There is no significant difference in the propagation loss for receivers 1 and 2 (on the average receiver 1 had 0.1 dB less loss). On the average, receiver 3 had 0.4 dB less loss than receiver 5, whereas receiver 1 had 1.2 dB more loss than receiver 5.

(C) Unfortunately, only two receiver depths were available at 140 and 290 Hz. The results are mixed. If we average over events at 290 Hz, the propagation loss for receiver 1 is only 0.1 dB less than for receiver 5. The corresponding result for 140 Hz is 1.2 dB less than for receiver 5. However, receiver 5 may have been a poor receiver, since it had 1.4 dB less loss than receiver 3 at low frequency. It would be informative to know how receiver 3 would have compared with receiver 1 at 140 and 290 Hz. The differences between receivers 1 and 5 may be a moot subject since, as discussed later, we have strong evidence that a receiver placed on the bottom of the fan will outperform any receiver placed on or suspended above the conical hill.

(C) Figures 25A, 25B, and 25C present propagation loss data for the receiver with lowest loss for all events at Site 5 for 25, 140, and 290 Hz, respectively. All the shot data are for 91-m shots. The events with no obstructing bathymetry (ie, similar to fig 24A) are given by the open symbols, while events with obstructing bathymetry are given by line symbols. The vertical lines with arrows at a range of 131 km span the minimum and maximum propagation loss of ten 30° bearing bins from arc event P3.

CW Source Event

RECEIVER Number	RECEIVER Depth	EVENT P1 (Hz)			EVENT P2 (Hz)			EVENT P5 (Hz)			EVENT A3 (Hz)	
BMA	(m)	22	140	290	36	140	290	36	140	290	36	140	290
1	3243	1.3	0	0	2.7	0	0	0.7	0	0.9	1.3	1.0	0.3
2	3468				2.51			1.7			2.2		
3	3865			0	0			0			1.4		
5	3844	0	2.8	1.0	0.7	2.8	0.6	0.8	0.1	0	0	0	0

TABLE V-12A. (C) PROPAGATION LOSS DIFFERENCES BETWEEN OTHER RECEIVERS AND THE RECEIVER WITH LOWEST PROPAGATION LOSS FOR SITE 5 AND FOR CW SOURCE EVENTS. (U)

RECEIVER Number	EVENT S1			EVENT A1		EVENT A2		EVENT A3	
BMA	18 m	91 m	243 m	18 m	91 m	18 m	91 m	18 m	91 m
1	1.0	2.8	2.4	1.8	3.5	3.4	3.0	5.8	3.3
2	2.7	2.7	2.6	1.5	3.7	3.2	2.8	4.7	3.2
3	0	0	0	0	0	0	0	0	0
5	1.1	2.6	2.8	0.2	2.2	1.6	2.3	2.5	1.8

TABLE V-12B. (C) PROPAGATION LOSS DIFFERENCES BETWEEN OTHER RECEIVERS AND THE RECEIVERS WITH LOWEST PROPAGATION LOSS FOR SHOT EVENTS AT 50 Hz AT SITE 5. (C)

CONFIDENTIAL

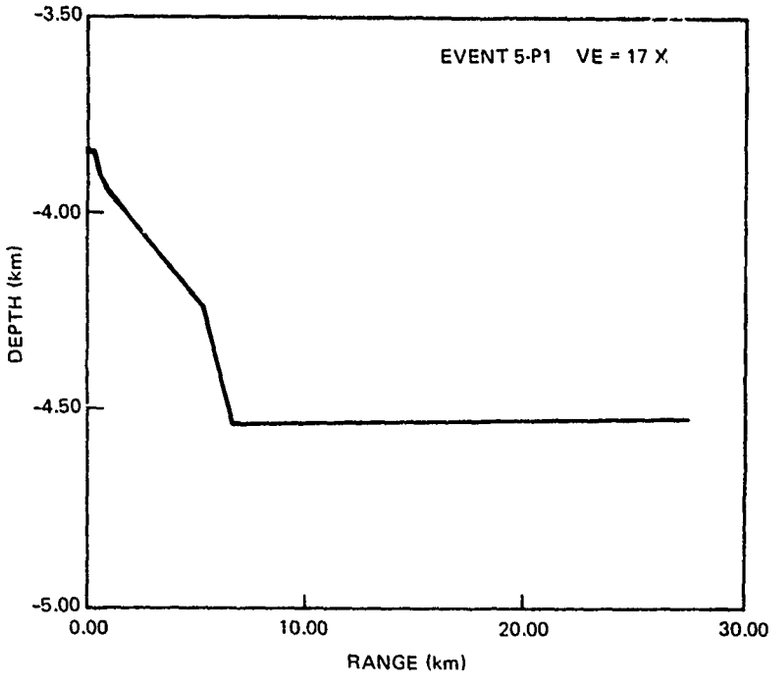

Figure V-24A. (C) Short range bathymetry at Site 5: event P1. (U)

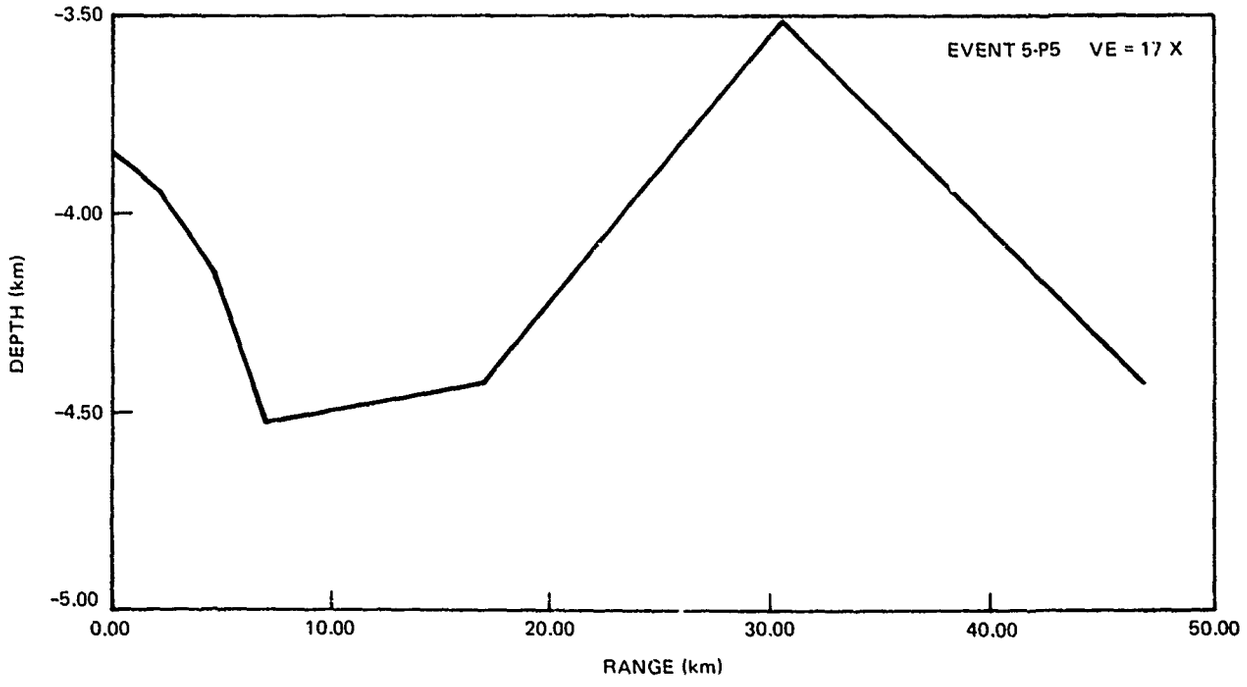

Figure V-24B. (C) Short range bathymetry at Site 5: event P5. (U)

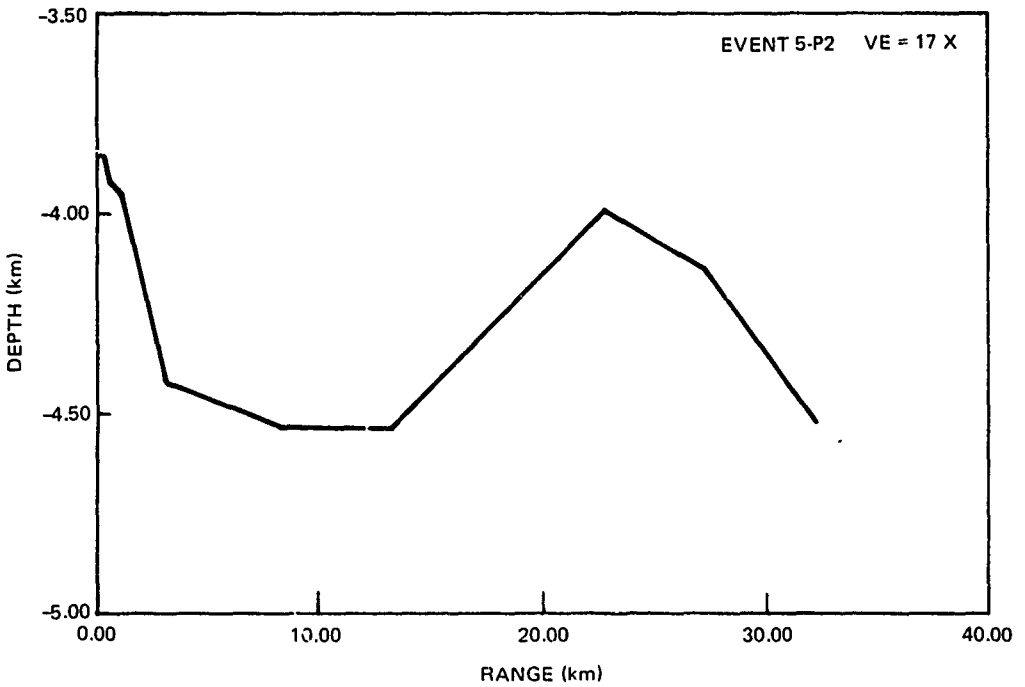

Figure V-24C. (C) Short range bathymetry at Site 5: event P2. (U)

(C) Table 13 ranks the events according to increasing propagation loss at each frequency. The ranking of events is identical for 140 and 290 Hz. The ranking for 25 Hz is slightly different in that events S1 and A1 drop one position and event A3 rises two positions over the ranking at higher frequency. The best event is P1. However, the fact that A3 ranks above S1 suggests that, at low frequency, the track of 5A3 has the lowest loss. With this adjustment, the ranking of S1 is entirely consistent with that of P1.

	Frequency		
RANK	Low Hz	140 Hz	240 Hz
1	P1	P1	P1
2	A3	S1	S1
3	S1	A1	A1
4	A1	A3	A3
5	P2	P2	P2
6	A2	A2	A2
7	P5	P5	P5

TABLE V-13. (C) RANKING OF EVENTS AT SITE 5. (U)

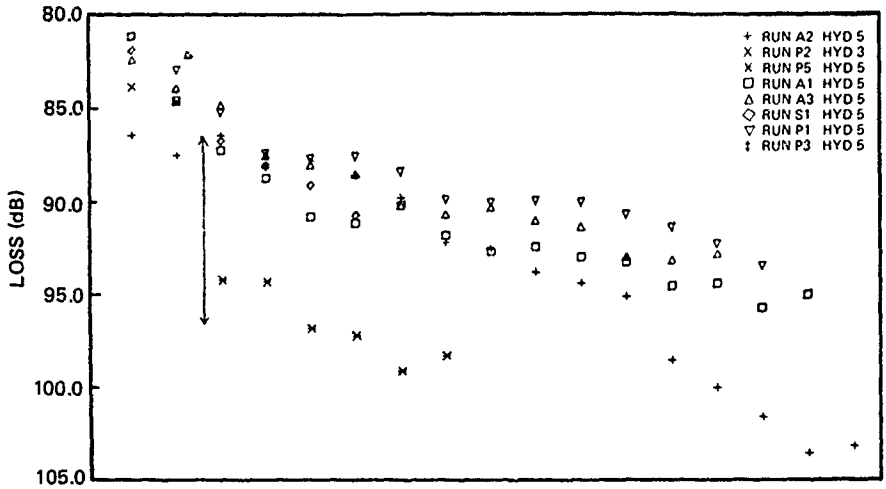

Figure V-25A. (C) Propagation loss versus range for all events at Site 5: low frequency. (C)

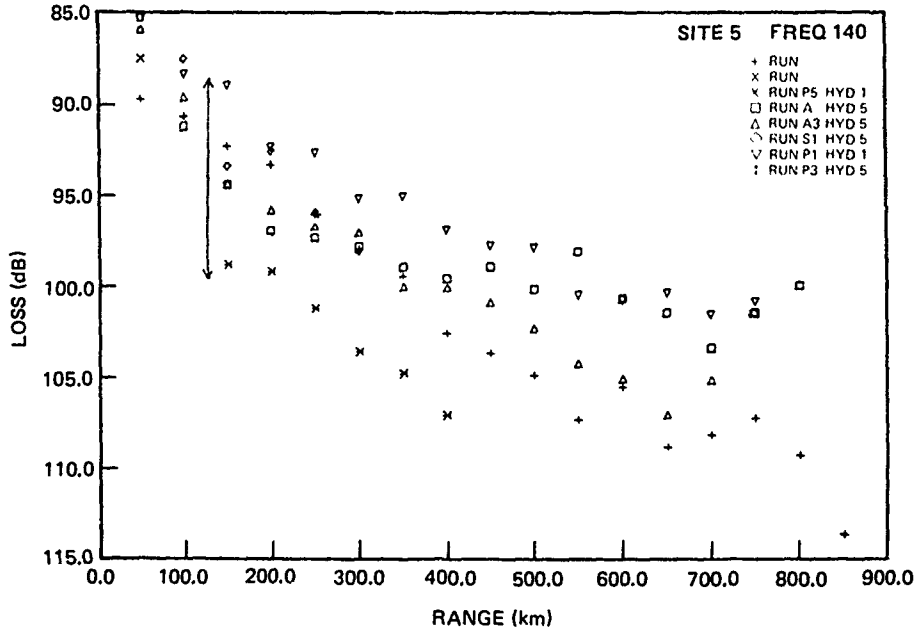

Figure V-25B. (C) Propagation loss versus range for all events at Site 5: 140 Hz. (C)

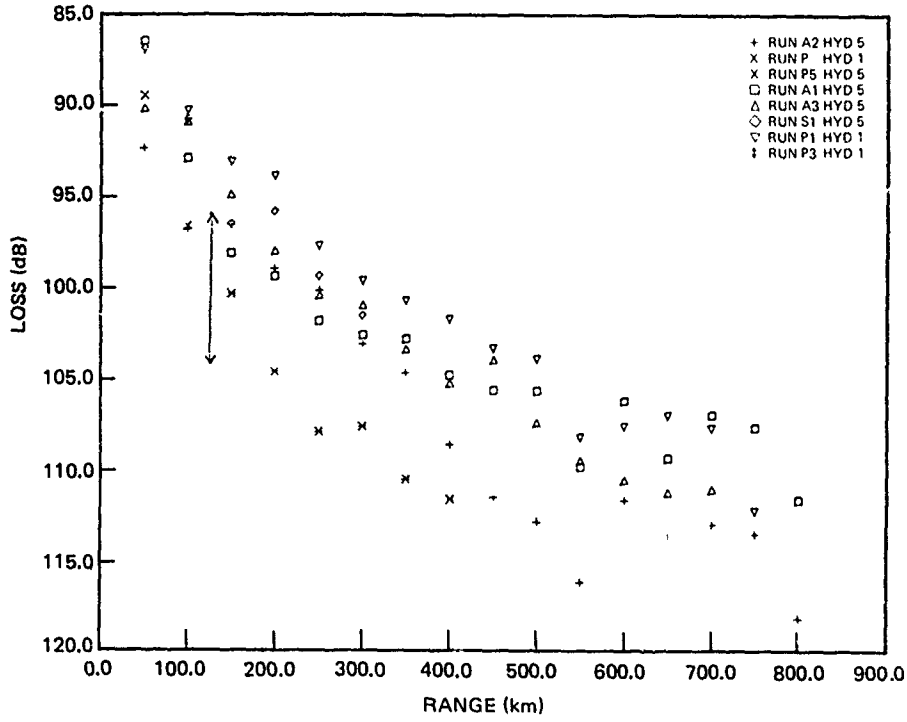

Figure V-25C. (C) Propagation loss versus range for all events at Site 5: 290 Hz. (C)

The ranking of A1 at 140 and 290 Hz is consistent with its being the closest run to P1. It is not clear why A3 ranks below A1 at 140 and 290 Hz whereas it is probably the best track at low frequency. Indeed at shorter ranges (out to 300 A3 ranks above A1. Beyond this range A1 has lower losses. The three lowest ranking events all have a close-range bathymetric obstruction. The behavior of event A2 is somewhat complicated. At intermediate ranges it may rank higher than unobstructed events. For example, at 250 km it appears to outrank events A1 and A3 at all frequencies. However, beyond 400 km it has clearly dropped out of contention. These higher losses at long range appear to be consistent with the high losses for event P3 at Site 2. In figures 25B and 25C there appears to be slope enhancement at 600 km. This range is about 50 km short of the Owen Ridge but may be within the navigational error. The lowest ranking is event P5, which crosses the severe obstruction of figure 24B. The slope of the propagation loss is comparable to that of event P1 or A3. There is an almost constant increase in loss from that of event P1 by an amount of 8.5 dB which appears to be independent of frequency. Propagation appears to undergo an increase in loss of 8.5 dB in passing over the obstruction of figure 24B. The spread in values for the arc event P3 at 131-km range is entirely consistent with other results for events P5, P2, and A2 as expected since the bearing of these events is included in the arc. The high loss extreme in figure 25C at 290 Hz suggests obstructions and losses more severe than those encountered in event P5.

(C) Figure 26 compares the best event (P1) with the Eleuthera reference. The slope at 22 Hz is less than that of the reference, with losses at long range as much as 13 dB less than those of the reference. The slope at 140 Hz is about the same as that of the reference, with losses as much as 6 dB less

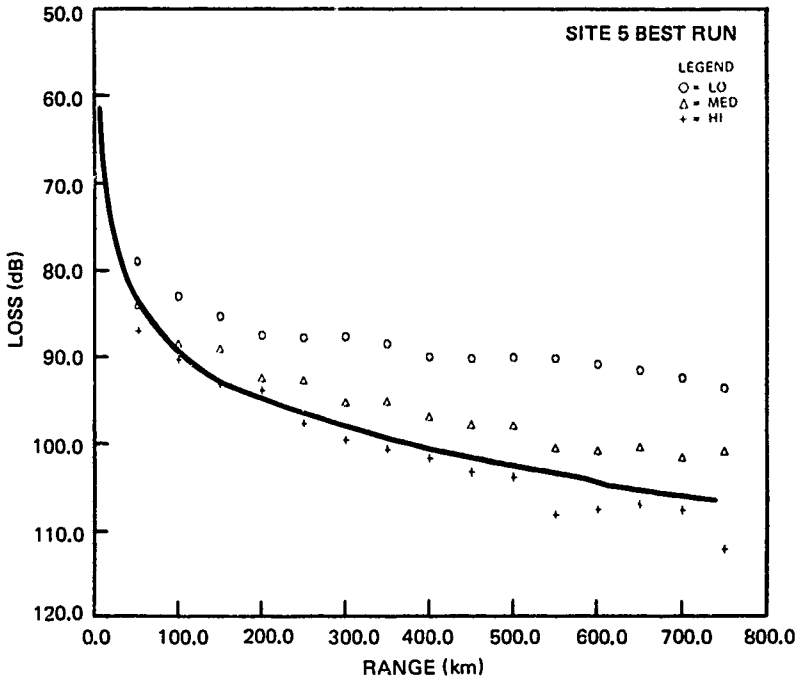

Figure V-26. (C) Comparison of lowest-propagation-loss events at Site 5 with the Eleuthera reference. (U)

than those of the reference. At 290 Hz the slopes are comparable to that of the reference from 100 to 500 km, with losses within 1 dB of those of the reference. Experimental losses from 550 to 750 km are about 3 dB greater than those of the reference.

V.3 (U) SITE INTERCOMPARISONS

(C) This section compares the events with lowest loss at each of the BEARING STAKE sites. Figures 27A, 27B, and 27C present the results at 25, 140, and 290 Hz, respectively. The most surprising feature is the small spread in the data. Indeed, the spread for the various event, at a given site, as presented earlier, is larger than the spread for all sites based on the event with lowest loss.

(C) The results of figures 27A, 27B and 27C are summarized in table 14, which describes the results of arithmetically averaging the propagation loss for the six 50-km range bins (from 50 to 300 km) for each site and each frequency. The numbers in table 14 are a measure of the "average" loss over the range interval from 25 to 325 km, since the values include all the data over this interval. (The values at site 1B are based on the average from 50 to 250 km, with an adjustment by the average increase from this interval to that from 50 to 300 km for the remaining sites.) The losses of table 14 are not as interesting as various difference tables which may be derived.

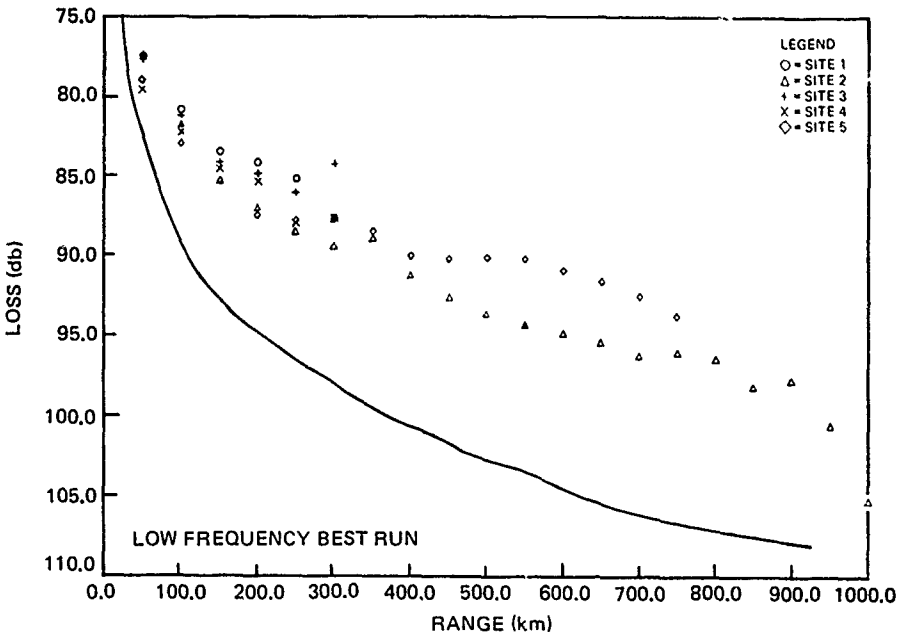

Figure V-27A. (C) Comparison of the lowest-propagation-loss events for each of the BEARING STAKE sites: low frequency. (C)

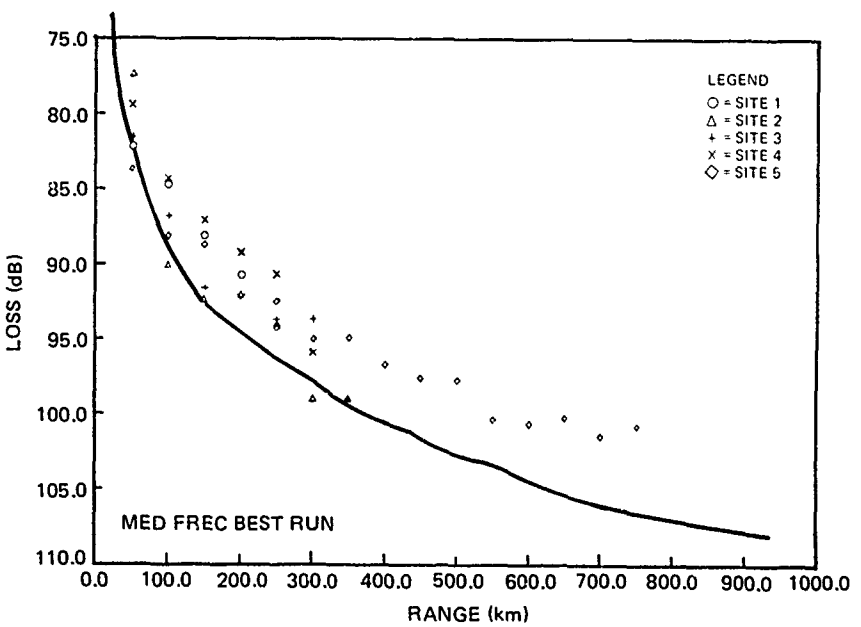

Figure 27B. (C) Comparison of the lowest-propagation-loss events for each of the BEARING STAKE sites: 140 Hz. (C)

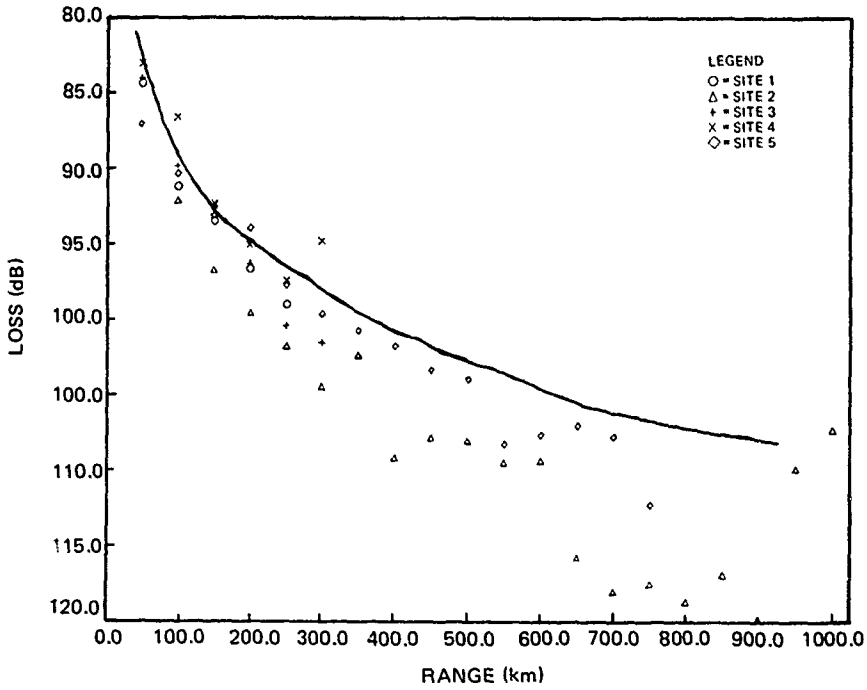

Figure V-27C. (C) Comparison of the lowest-propagation-loss events for each of the BEARING STAKE sites: 290 Hz. (C)

	Frequency		
SITE	Low	140	290
1B	82.9	89.5	94.1
2	85.3	92.3	97.0
3	83.1	90.2	94.1
4	84.6	89.5	91.5
5	85.0	90.3	93.6

TABLE V-14. (C) AVERAGE PROPAGATION LOSS FOR THE BEST EVENT AT EACH SITE FOR THE RANGE 25—325 KM. (U)

(C) Table 15 presents the average propagation loss differences between sites in dB relative to the site with lowest average propagation loss. Table 16 presents the average difference in propagation loss between the two higher frequencies and 25 Hz on a site-by-site basis. This latter table may be regarded as the increase in attenuation due to absorption and higher bottom loss at the higher frequencies for a nominal range of 175 km. Note in table 15 the differences between Sites 1B and 3. The values (for frequencies of 25, 140, and 290 Hz, respectively) are 0.2, 0.7, and 0.0 dB. This result agrees very well with an analysis of the bottom loss and bottom bounce range intervals ("cycle distances"), which indicates that the propagation at Sites 1B and 3 is not significantly different. This result also shows up in table 16, which shows a similar attenuation for Sites 1B and 3. Note also in table 16

that Site 2 has attenuation remarkably similar to that of Sites 1B and 3. This suggests that the attenuation characteristics across the Indus Fan at ranges near Site 2 are comparable to those at Sites 3 and 1B. Note also, in table 16, the significantly smaller attenuation for Site 5 as compared to Sites 1B, 2, and 3. This is in good agreement with the bottom loss measurements at Site 5, which show that the bottom loss at this site is significantly smaller than at Sites 1B or 3. In table 16, Site 4 shows even smaller attenuation. This results because the principal propagation path (at the higher frequencies) is by convergence zones, which do not suffer bottom loss.

	Frequency		
SITE	Low	140	290
1B	0	0	2.6
2	2.4	2.8	5.5
3	0.2	0.7	[illegible]
4	1.7	0	0
5	2.1	0.8	2.1

TABLE V-15. (C) PROPAGATION LOSS DIFFERENCE BETWEEN THE GIVEN SITE AND THE SITE OF SMALLEST PROPAGATION LOSS. (U)

	Frequency		
SITE	Low	140	290
1B	0	6.6	11.2
2	0	7.0	11.7
3	0	7.1	11.2
4	0	4.9	6.9
5	0	5.3	8.6

TABLE V-16. (C) PROPAGATION LOSS DIFFERENCES (IN dB) BETWEEN 140 OR 290 Hz AND 25 Hz. (C)

(C) There remains one crucial question. If the bottom loss is lowest at Site 5, then why does Site 5, in table 15, have higher propagation loss than Sites 1B and 3 at low frequency and at 140 Hz? Moreover, figures 27B to 27C show that Site 5 has the highest propagation loss of all Sites at ranges of 50 and 100 km for 140 Hz and at a range of 50 km for 290 Hz. It is hypothesized that this is because the receivers at Site 5 were mounted on the small conical hill as discussed in the Site 5 analysis (section V.2.5). This hill is part of the Carlsberg Ridge (which has been assigned the highest bottom loss values

in the Northwest Indian Ocean). At least half of the acoustic arrivals at Site 5 must reflect at least once from this hill with high loss. Thus, we estimate that the propagation loss would be increased at this Site B about 3 dB. This hypothesis was tested by two special runs of the ASTRAL model. These runs compared simulations of the propagation loss for a receiver mounted on the hill with those for a receiver mounted north of the hill on the floor of the Indus Fan. The propagation losses, beyond the direct field, for frequencies of 25, 140, and 290 Hz, respectively were about 2, 3, and 3 dB greater for the receiver mounted on the hill. If the propagation losses for Site 5 in table 15 are reduced by these amounts, then Site 5 is comparable to Sites 1B and 3 at 25 Hz and superior to Sites 1B and 3 at the two higher frequencies.

(C) A similar comparison of ASTRAL runs was made at Site 2. Here the receivers are mounted on a scarp which has been assigned to the next to highest bottom loss province. The ASTRAL propagation losses for frequencies of 25, 140, and 290 Hz, respectively, were about 1, 4, and 4 dB greater for the receivers on the scarp than they were for receivers mounted on the Indus Fan at the foot of the scarp. Thus, the larger losses in table 15 for Site 2 as compared to Sites 1B and 3 are no doubt due to receiver placement on the scarp.

(C) Turning now to Site 4 as related to table 15, at 25 Hz the propagation loss is higher than that at Sites 1B and 3 and would also be higher than that at Sites 5 and 2 with the adjustments just discussed. This result is in agreement with other features of Site 4; i.e., at 25 Hz the propagation appears to be by bottom bounce rather than convergence zone and the bottom loss measurements at Site 4 indicate significantly higher bottom loss than at Sites 1B, 3, and 5. At the higher frequencies (140 and 290 Hz) where convergence zones dominate, we believe that the comparability in average propagation loss values of Site 4 to the other sites is fortuitous. We should not draw the conclusion that in general propagation in bottom-limited areas is comparable "on the average" to convergence zone propagation. This appears to be true in the BEARING STAKE areas only because of the low bottom loss for the bottom limited areas and because of marginal convergence zone conditions (small depth excess).

V.4 (U) REMARKS

V.4.1 (U) Evaluation of Receiver System/Processing Errors

(C) At Sites 1A, 1B, and 3, BMA receivers were mounted near each other on an essentially flat bottom. Differences in the propagation loss over range or bearing bins were calculated for these adjacent receivers. The total number of independent evaluations made was eighteen. Of these, 50, 67, 75, and 100 percent differed by no more than 0.3, 0.5, 0.8, and 1.0 dB respectively. These results demonstrate that the manner in which WECo processed their data is remarkably consistent. They also demonstrate that the process of calculating bin averages is very robust.

V.4.2 (U) Standard Deviations of the Data

(C) Throughout this analysis we have presented mean values of propagation loss in 50-km range bins or 30^0 bearing bins. This section discusses the standard deviations of the data about these mean values. This analysis is the first stage in the process of developing statistical distribution models of the variance. These models are a necessary adjunct to the ASTRAL propagation model for the system performance evaluation of bottom-limited regimes.

(U) The standard deviation was calculated as follows: The mean propagation loss was subtracted from the propagation loss for each data point in the bin; these values were squared and summed over all points and averaged; and then the square root was taken to yield a standard deviation.

(C) Analysis of these standard deviations produced some significant results. Consider first the results for CW propagation. The WECO data for Sites 1A, 1B, 2, and 3 were determined to be independent of site and acoustic frequency. A standard error of 5.3 dB is a good characteristic value, which is based on 374 individual determinations of standard error and may be considered a benchmark. The WECo data at Site 5 were independent of frequency, with a value of 4.6 dB, which is significantly lower than that for Sites 1A, 1B, 2, and 3. The WECo data at Site 4 were 5.2, 5.8, and 6.7 dB, respectively, for frequencies of 25, 140, and 290 Hz. We attribute the increase in variance for 140 and 290 Hz to the convergence zones at the site. The values at 25 Hz, for which there was little evidence of convergence zones at Site 4, are comparable to those for Sites 1A, 1B, 2, and 3. Values were obtained for ACODAC data at Sites 1B and 4. These were 5.0, 3.0, and 7.5 dB for frequencies of 25, 140, and 290 Hz at Site 1B. Corresponding values at Site 4 were 4.8, 5.0, and 5.8 dB. These ACODAC values are consistently smaller than the corresponding WECo values but otherwise yield comparable results. The single exception is the 7.5-dB value at 290 Hz at Site 1B. This value differs so much from all the other experimental values that the data are suspect and should be examined before the result is accepted. The variance of normal mode theory was determined in 50-km range bins from data such as those in figure 2. A value of 5.8 dB was determined, based on a limited number of only five bins. Dyer (1977) gives a theoretical value of 5.6 dB, based on a model for random vectors. Both Dyer's value and the normal mode value are larger than the characteristic experimental value of 5.3 dB. This difference is believed to be due to some smoothing, in the data processing techniques, which reduces the variance.

(C) The standard deviation of shot data was also investigated. Here the standard error increased with frequency at all sites. Values for Sites 1A, 1B, 2, and 3 ranged from 0.9 dB at 25 Hz to 2.4 at 290 Hz for 91-m shots. Values for 243-m shots were, in most cases, somewhat larger than for 91-m shots. As was the case for the CW data, the standard error for Sites 5 and 4 was, respectively, lower and higher than for the other sites. As previously mentioned, the convergence zones contribute to the higher values at Site 4. However, the low values for Site 5 remain a subject for further investigation.

V.4.3 (C) Determination of Loss Provinces

(C) For system assessment purposes it is necessary to divide the BEARING STAKE area into various bottom loss provinces. This section indicates how the Indus Fan was divided into provinces 1 and 2. The bottom loss measurements made at Site 5 at the southern end of the fan were significantly lower than those made at Site 3 in a northern portion of the fan. Figure 28 presents a plot of the experimental propagation loss in 2-km bins for event P3 at Site 2 for 290 Hz. The open circles represent results for the ASTRAL model based on Site 3 bottom loss. There is a distinct change in the slope of the experimental data at a range of about 200 km which can be attributed to a change in bottom loss. The slope of the data beyond 175 km is very close to the slope measured in event P1 at Site 5. Other events were investigated for similar slope changes in order to delineate the boundary between Province 1 (low loss) and Province 2 (higher, Site 3 bottom loss).

(C) Figure 29 presents the results of this investigation. The marks labeled B in various events indicate the ranges at which significant changes in slope were determined. The slopes at ranges beyond these marks for events 2P3, 2A1, 2S2, and 3P4 were similar to those measured for event 5P1. No obvious changes in slope were noted for event 5A1, 5P1, 5A3, or 3P3. On the basis of these data, the line dividing Provinces 1 and 2 was estimated. Subsequent analysis has shown four additional slope changes. The change along event 3A2 agrees well with the boundary between Provinces 5 and 2. There is also a distinct slope change along event 5A2, but it is not evident how this ties in with loss provinces. The locations of the rapid increases in propagation loss as previously discussed for events 3A3 and 3A4 are also indicated in figure 29.

V.4.4 (U) Slope Enhancement Effects

(C) Although eight or nine of the BEARING STAKE explosive source runs crossed significant underwater bathymetric features, a corresponding acoustic effect was well-established on only two. This situation arose because the range sampling of the explosives was insufficient to properly define all acoustic changes.

(U) The two runs which gave clear evidence of slope enhancement (4A1 and 1A2) are discussed individually.

V.4.4.1 (U) Run 4A1 (fig 30)

(C) The run was terminated by shoaling between the horn of Africa and the Island of Socotra. The bathymetric profile sketched in the figure has a maximum slope of $2\text{-}1/2^{o}$ at 725-km range.

(C) The corresponding acoustic effect was confined to the lowest two frequencies analyzed (20, 50 Hz) and only with the 18-m source depth. The magnitude of the enhancement was approximately 10 dB at 20 Hz (fig 30A) and 5 dB at 50 Hz (not shown). The higher frequencies (140 and 300 Hz) and deeper source depths produced no enhancement. The 140-Hz case is shown in figure 30B.

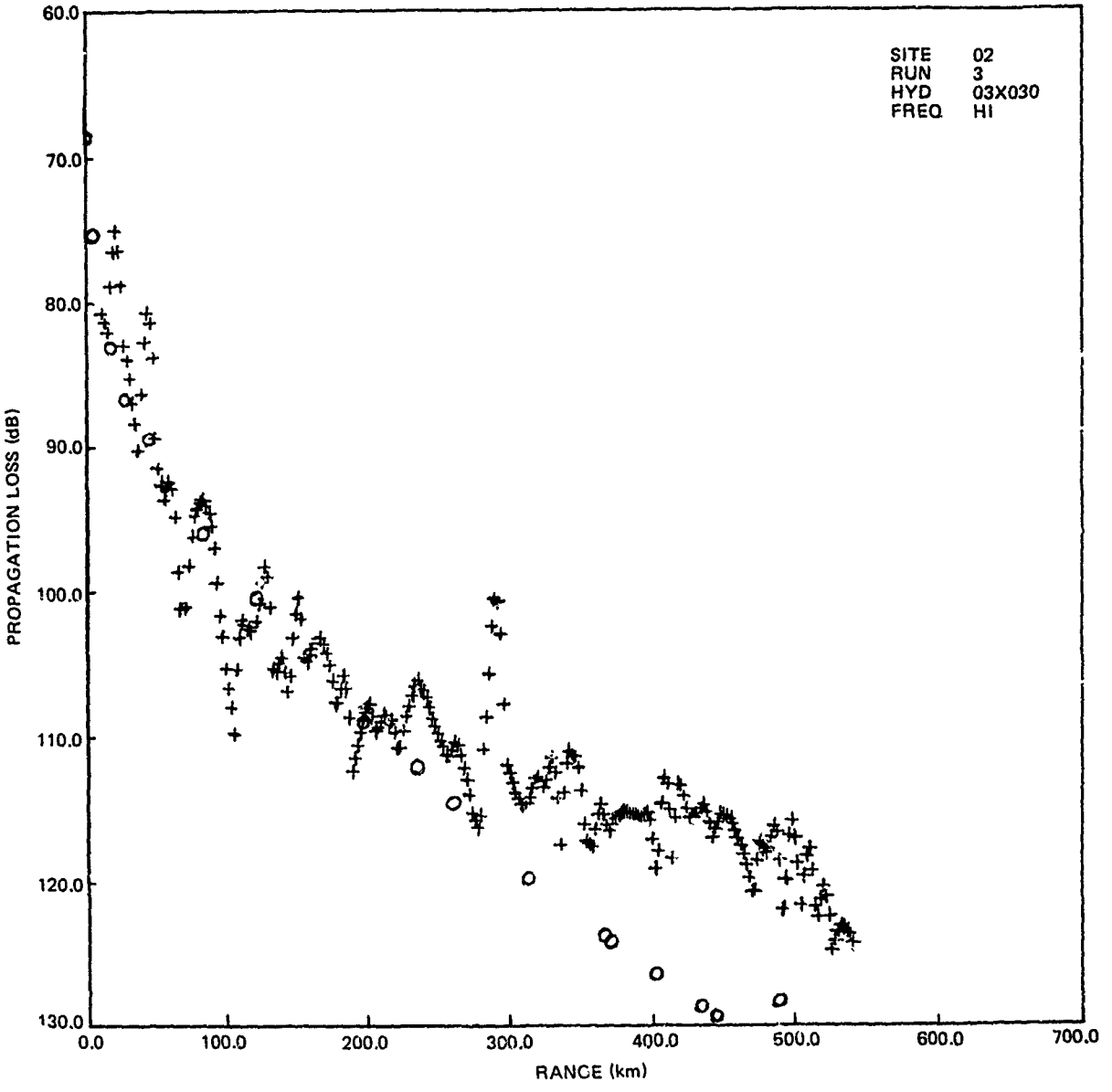

Figure V-28. (C) Comparison of the experimental propagation loss for Site 2, event P3, at 290 Hz with the theoretical results of the ASTRAL model. (C)

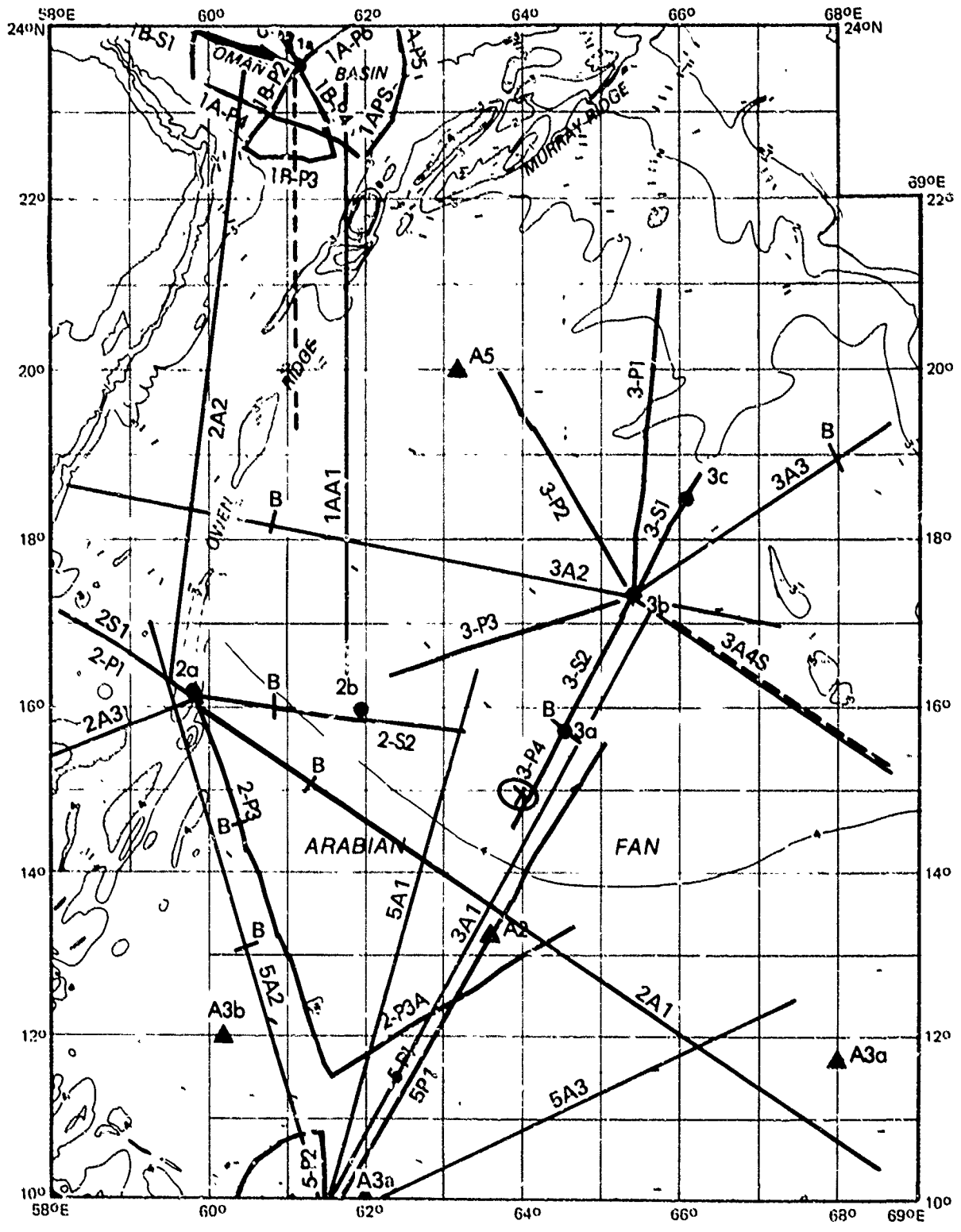

Figure V-29. (C) Tracks for various events on the Indus Fan. The ranges at which changes in propagation loss occur are designated by a B. (C)

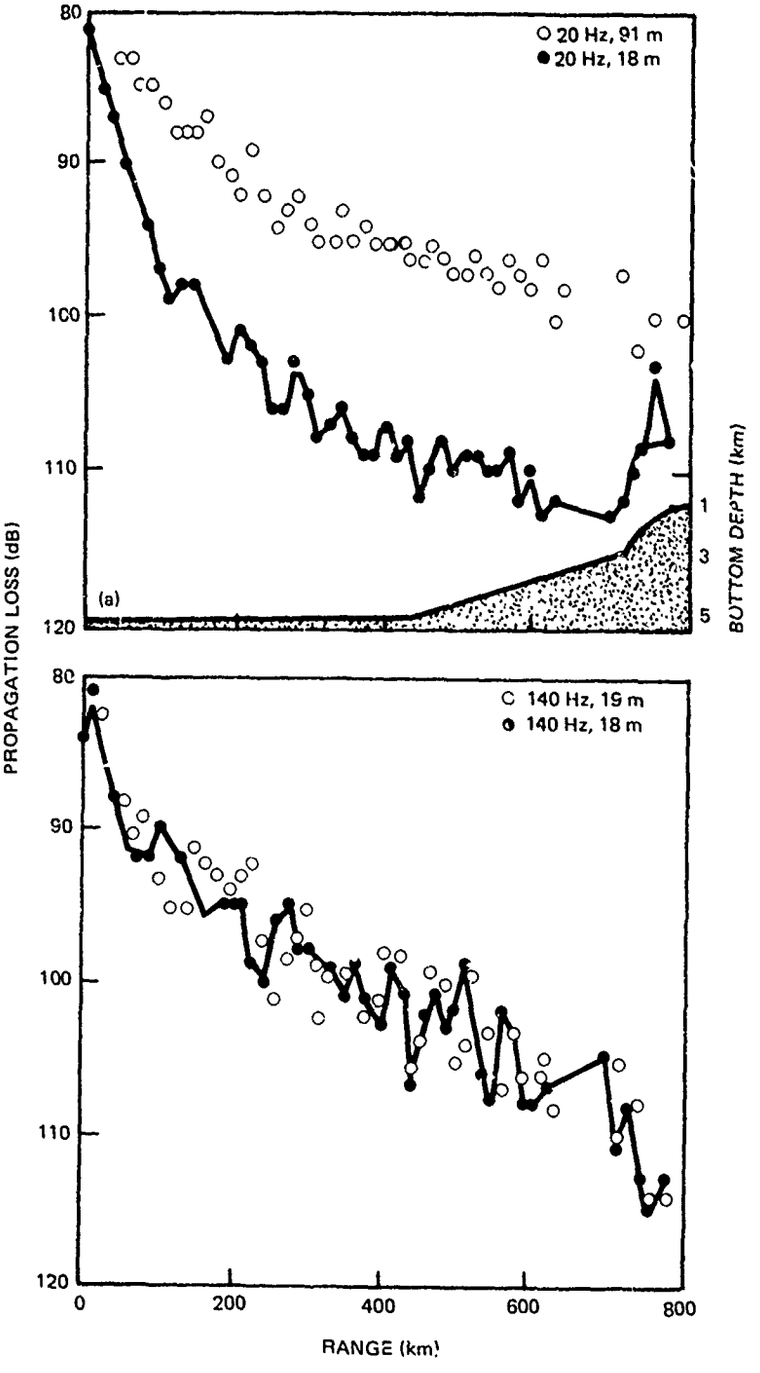

Figure V-30. (C) Comparison of propagation losses for 18- and 91-m shots for Event A1 at Site 4: A, 20 Hz; B, 140 Hz. (C)

V.4.4.2 (U) Run 1A2 (fig 31)

(C) This run traversed a submerged seamount at a range of 275 km from the receiver. It was initially indicated that the run merely crossed a flank of the feature. In view of the major acoustic effect, however, it is assumed that the propagation path intersects near the peak of the seamount (1500 m). The bathymetry in figure 31A is sketched on this basis. Maximum bottom slope was again near 2-1/2°. The acoustic effect is similar to that observed with run 4A1. A level enhancement occurs on the upslope portion of the seamount and is noticeable at 20 Hz (and 50 Hz), only with the 18-m source depth. Higher frequencies and deeper source depths do not show enhancement (fig 31B).

(C) The enhancement character represented by these two runs is qualitatively consistent with a decrease in the surface decoupling loss at the source in the vicinity of the features. For sources over a sloping bottom, steep-angle rays are decreased in angle by repeated bottom reflections. These steep-angle rays give rise to less surface decoupling loss at the source and this causes an increase in received level. The surface decoupling losses are greatest at low frequency and apply only to source depths above the decoupling depth (typically 50-80 m).

(C) Although data from other events are not sufficiently detailed to allow a good description of propagation enhancement, the following trends have been identified. It is clear that enhancement mechanisms other than that described above are responsible in some cases.

Run 1A1 No acoustic effect in spite of major underwater feature.

Run 2A3 Decoupling loss enhancement with character similar to 4A1.

Run 4A2 All frequencies (20 - 300 Hz) only with 18-m source depths.

Run 5A2 All frequencies (20 - 300 Hz) and all source depths (18, 91, 243 m).

V.4.5 (C) Selection of Surveillance Sites on the Indus Fan

(C) The present procedure of selecting surveillance sites mounted up on the ridges bounding a basin does not appear to be the best choice for a bottom-limited basin with low bottom loss. As previously discussed, the experimental data at Sites 2 and 5, as well as the special ASTRAL runs, strongly suggest that surveillance arrays should be placed on the low-loss Indus Fan rather than being mounted above the floor on high-loss hills or scarps. Furthermore, the normal mode model studies and experimental measurements of Site 1B suggest that an improvement of several dB in the signal-to-noise ratio might be achieved with the optimum placement of surveillance arrays about 20 to 30 m off the bottom (depending on the low frequency of primary interest). This improvement can only be achieved in the absence of close range shipping. The placement of surveillance arrays on the periphery of the Indus Fan should be reexamined. Once the hypothesized advantage of mounting receivers on ridges has been eliminated, it is not clear that configurations on the periphery of the basin are superior to other configurations distributed throughout a basin.

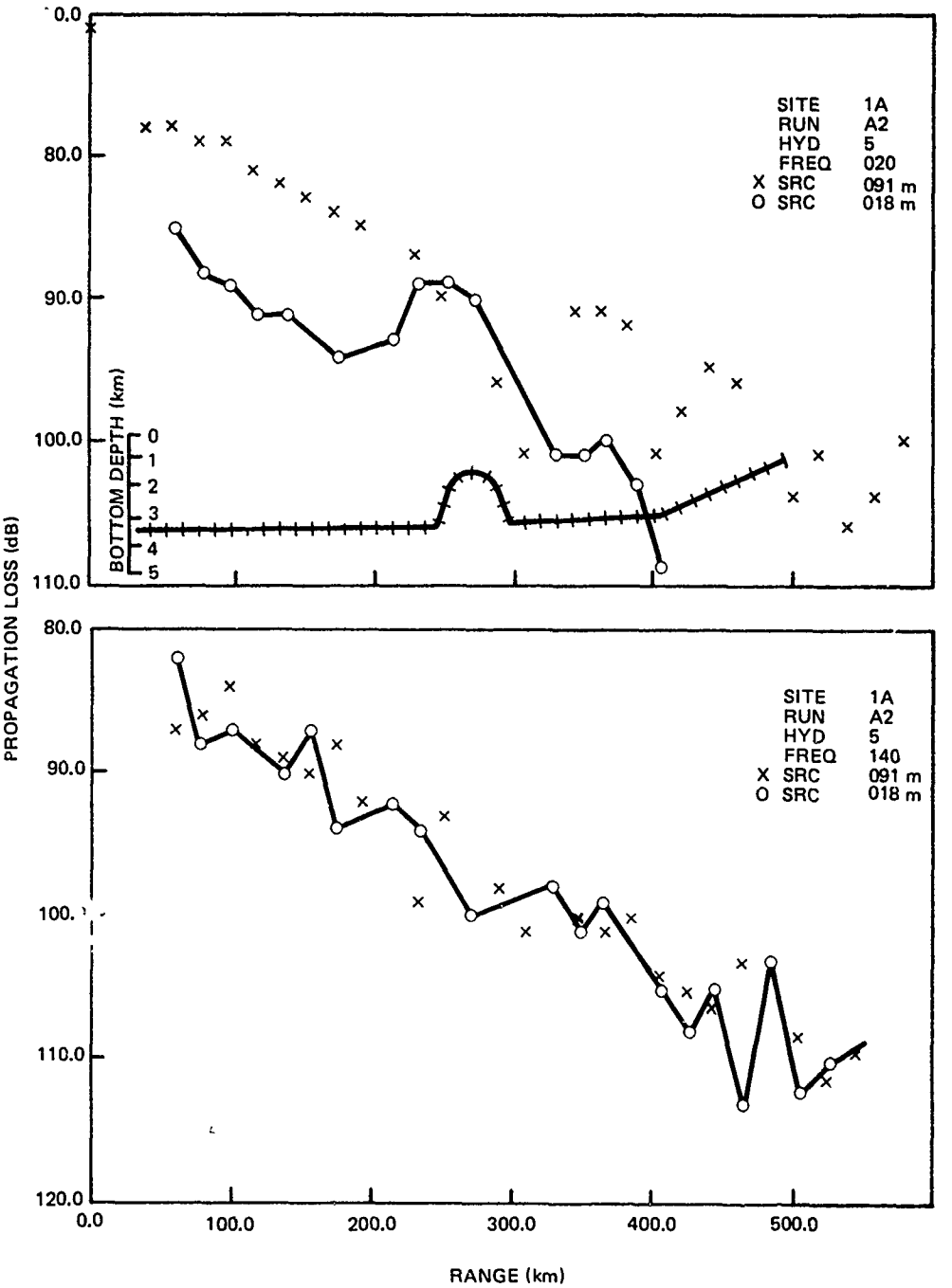

Figure V-31. (C) Comparison of propagation losses for 18- amd 91-m shots for Event A2 at Site 1A: A, 20 Hz; B, 140 Hz. (C)

(C) Figure 32 presents the distribution of cargo ships and tankers in the Western Indian Ocean. On the basis of this distribution, we would recommend a generalized site indicated by the "X" as a potential surveillance site. This was chosen to minimize the noise from close range shipping (by locating it in a region of low shipping density).

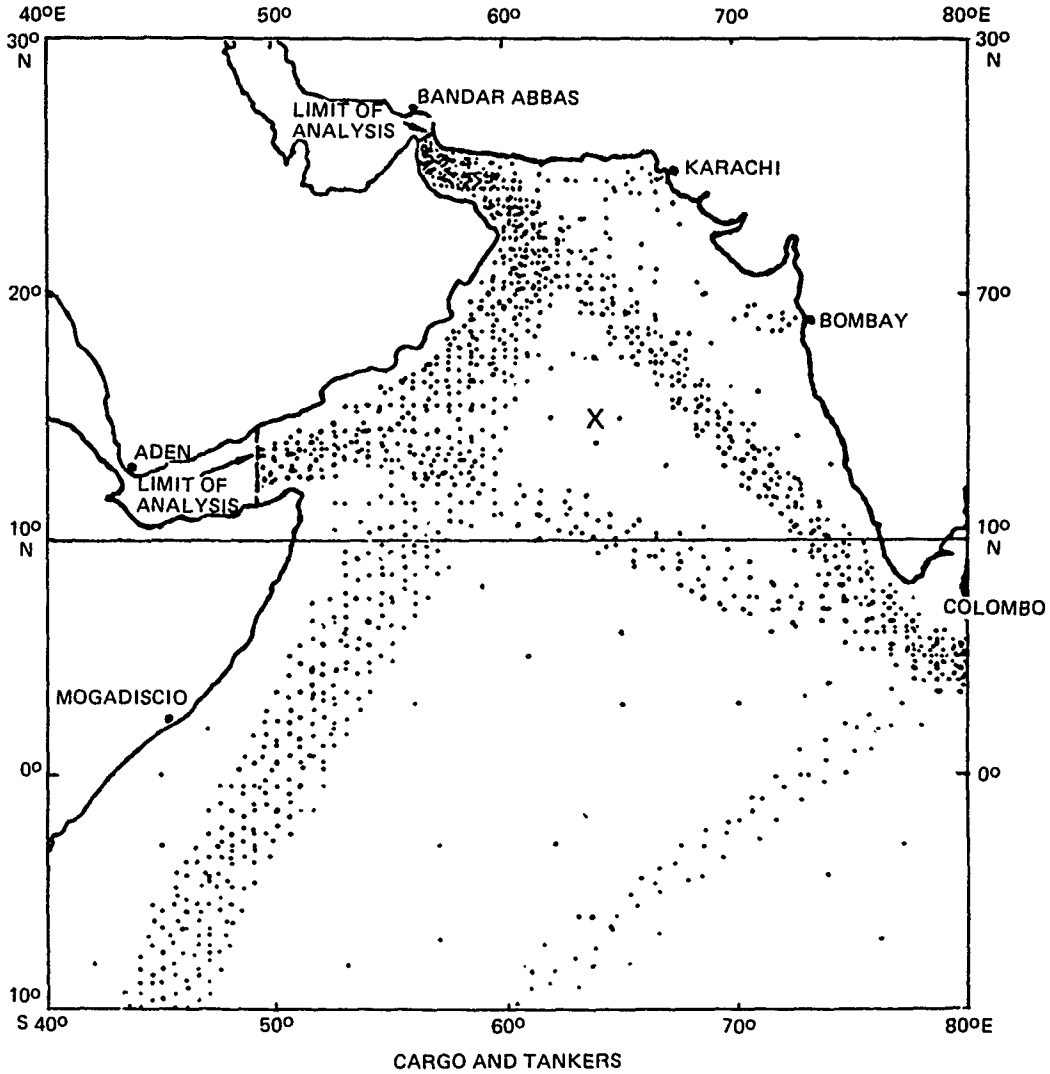

Figure V-32. (C) Selection of surveillance site based on the distribution of cargo and tanker ships. (C)

V.4.6 (U) Recommendations for Additional Measurements

(U) This section consists of a series of recommendations for additional acoustic measurements which should be made in the BEARING STAKE area.

1. (C) Propagation measurements using CW sources should be made across the Chain Ridge, which bounds the Somali Basin to the east; across the Carlsberg Ridge, which bounds the Indus Fan to the south, across the Owen Ridge, which bounds the Indus Fan to the west; and across the Murray Ridge, which separates the Gulf of Oman from the Indus Fan. For a variety of reasons, good quantitative data over these bathymetric features were not obtained in BEARING STAKE. The chief purpose of these recommended measurements is to obtain propagation data which are necessary for the modeling of distant shipping noise which propagates over these bathymetric features.

2. (C) Detailed propagation loss measurements should be made to evaluate the slope enhancement of shipping noise. The shots from aircraft events in BEARING STAKE were too sparse for evaluation of some propagation features. High-density shot runs, with a ship, and/or CW events are recommended. Some events should be conducted with low-frequency CW sources at 6-m depth to properly simulate the source depths of shipping noise.

3. (C) Measurements should be made in several locations on the Indus Fan to verify the existence of the notch of higher propagation loss which theory predicts to be somewhat off the ocean floor. A string of receivers spaced at 10-m intervals above the ocean floor should be utilized. Propagation from simultaneous shallow and deep low-frequency CW sources should be measured. One of the sites tested should be Site X, where measurements of noise should be compared on the various receivers. As previously discussed (section V.4.5), this location was selected as being far from shipping lanes. Other desirable locations would be on the fan near Site 2 and near Site 5. These measurements are needed to verify model results indicating that such receivers will perform better than those deployed on the Owen Ridge at Site 2 or on the conical hill at Site 5.

4. (C) Site 4 should be retested under near-bottom-limiting conditions and should also be evaluated at a time of year when the depth excess is greatest. The experiments should be designed on the basis of a rigorous theoretical analysis of optimum receiver depths for this complicated environment.

5. (C) Any additional experiments on the Indus Fan should be designed to determine whether the fan can be modeled adequately by two bottom loss regimes and if so to locate the boundaries of these regimes.

6. (C) Propagation and bottom loss should be measured at higher frequencies for use in short range surveillance or tactical systems.

REFERENCES (U)

Dyer, Ira (1977). "Fluctuations: An Overview" in the Proceedings of the International Workshop on Low-Frequency Propagation and Noise, Maury Center for Ocean Science, Washington, D.C.

Gordon, D.F. (1977). "Theoretical Propagation of Low-Frequency Sound In the Deep Ocean and Its Interaction with the Bottom (U)," Naval Undersea Center TP 536, January. (CONFIDENTIAL)

Gordon, D.F. (1979a). "Underwater Sound Propagation Loss Program: Computation By Normal Modes For Layered Oceans and Sediments," Naval Ocean Systems Center TR 393.

Gordon, D.F. (1979b). "Multipath Interference Nulls in Long Range, Low-Frequency, Acoustic Propagation by Normal Modes" Jour. Acoust. Soc. Am., In Press.

Gordon, D.F. and E.R. Floyd (1979). "Acoustic Propagation Effects In Beamforming of Long Arrays (U)," JUA(USN) Vol. 29, January. (CONFIDENTIAL)

Mitchell, S.K., et al. (1978). "BEARING STAKE Vertical ACODAC Acoustic Measurements Data Report (U)," Applied Research Laboratories TR-78-8, February. (CONFIDENTIAL)

Osborne, J.T. (1978). "Project BEARING STAKE Transmission Loss and Omnidirectional Ambient Noise From Bottomed Arrays (U)," Western Electric Co. Report, May. (CONFIDENTIAL)

Pedersen, M.A., D.F. Gordon, and D. White (1975). "Low Frequency Propagation Effects for Sources or Receivers Near the Ocean Surface," Naval Undersea Center TP 488, September.

Pedersen, M.A. and G.S. Yee (1979). "BEARING STAKE Propagation Loss Assessment (U)," Naval Ocean Systems Center TR 467. (CONFIDENTIAL)

CHAPTER VI

AMBIENT NOISE (U)

by

R.A. Wagstaff and J.W. Aitkenhead

Systems Concept and Analysis Division, Code 724

Naval Ocean Systems Center

San Diego, California 92152

CHAPTER VI. AMBIENT NOISE (U)

CONTENTS (U)

CHAPTER VI. AMBIENT NOISE. (U)

VI.1 (U) SITE DESCRIPTIONS

(U) The approximate locations of the seven different measurement sites are shown in figure 1 and listed in table 1. The approximate bottom depth, the types of ambient noise measurements for which results are presently available, and the time of year are also included. The proposed scope of the noise data analysis for each site is not limited to that listed in table 1. A more complete description is given by Naval Ocean Systems Center, 1977.

(C) Site 1 is located in the mouth of the Gulf of Oman. The nearby coastlines form a funnel for the high density shipping traffic into and out of the Persian Gulf. The high density shipping, characteristic of the Indian Ocean, is greatly increased in the vicinity of Site 1 as a result. The plus (+) signs in figure 2 mark the positions of ships near Site 1 which were spotted by aerial shipping surveillance on 28 Jan 1977. This figure is illustrative of the extremely high shipping density near Site 1. Even though the acoustic propagation for near-surface sources is severely bottom limited, as illustrated by the sound speed profile for Site 1 in figure 3, the ambient noise at frequencies dominated by such high-density shipping (below approximately 200 Hz) would be expected to be high.

(U) Omnidirectional ambient noise measurements at Site 1 were taken by a bottom-mounted array (BMA), a vertical ACODAC with sensors distributed throughout the water column, and the 925-m nonlinearly spaced 32-element Ocean Acoustic Measurement System (OAMS) towed array. In addition to omnidirectional noise the depth dependence was measured by an ACODAC, and the horizontal directionality of the noise was measured by both the towed array and the bottom-mounted array.

(C) Sites 2 and 3 are in the Arabian Sea. Site 2 is on the side of a seamount which lies to the east of the major shipping lane from the Persian Gulf to the Cape of Good Hope. Site 3 is higher up on the Indus Fan than Site 2 and lies slightly to the west of the Persian Gulf-Straits of Malacca shipping lane. Unfortunately, the shipping surveillance was primarily to the north of these two sites. The minus (-) signs in figure 2 illustrate the positions of ships observed during the surveillance flights in the northern part of the Arabian Sea. The reduction in shipping density away from the Gulf of Oman (and Site 1) is evident in this figure.

(C) As indicated by figure 3, the sound speed profiles at these two sites are quite similar. The most significant difference is that the acoustic propagation is more bottom limited at Site 2 than at Site 3. Only omnidirectional data are available from the BMA for Site 2. Both omnidirectional and horizontal directionality data are available for Site 3 from the BMA and the OAMS array.

(C) Sites L2 and L5 are at the bottom of the Indus Fan and near the great circle path from the southern tip of India to the Gulf of Aden. It is likely that a shipping lane between these two points would possess moderately dense shipping. Unfortunately, shipping surveillance flights were not conducted near these two sites. The density of shipping must be inferred either from historical shipping data or from the noise measurements. Sound speed profiles

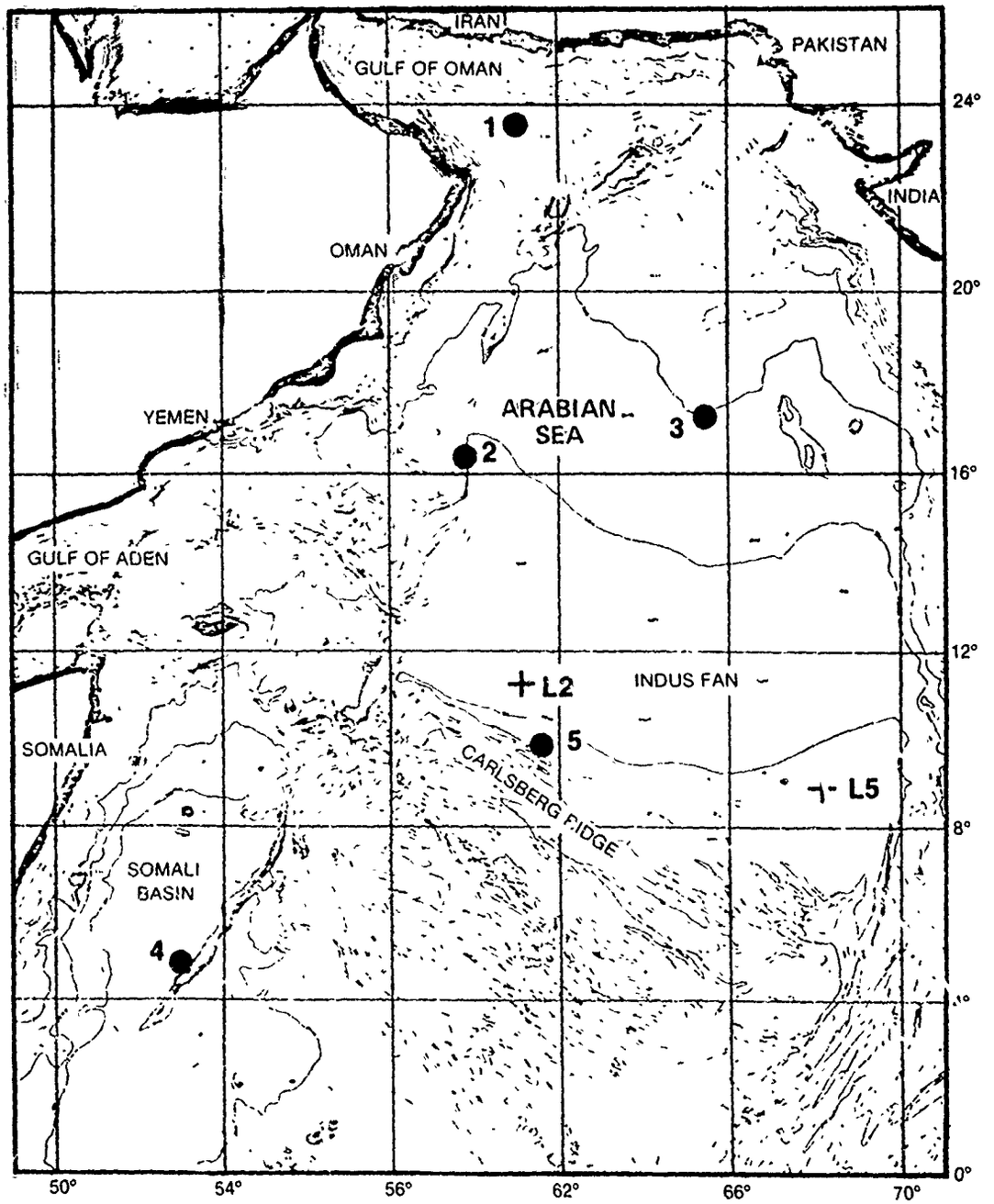

Figure VI-1. (C) Geographic locations of the five principal BEARING STAKE sites (Sites 1 through 5) and two auxiliary sites (L2 and L5). (U)

TABLE VI-1. (C) APPROXIMATE LOCATIONS AND DEPTHS OF MEASUREMENTS AND THE MONTH OF OCCUPATION AT EACH. (U)

SITE NO.	N LAT	E LONG	DEPTH (m)	DATA TYPE*	TIME
1	23°38'	61°09'	3,300	H, D, O	Jan, Feb 1977
2	16°15'	59°45'	3,150	O	Apr, 1977
3	17°18'	65°24'	3,600	H, O	Feb, 1977
4	04°45'	53°09'	5,000	H, D, O	Mar, 1977
5	09°40'	61°00'	4,500	O	Apr, 1977
2L	11°00'	61°00'	4,410	H, O	Apr, 1977
5L	08°45'	68°00'	4,550	H, O	Apr, 1977

*H - Horizontal Directionality
D - Depth Dependence
O - Omnidirectional

for these two sites are similar to the Site 5 profile in figure 3. Omnidirectional and horizontal directionality data are available from the Long Aperture Towed Array (LATA) for both these sites.

(C) Site 3 is located on the northern edge of the Carlsberg Ridge. The BMA at this site was on a flat top of a low rise about 500 m above the basin floor. The predominant shipping is believed to be well to the north of this site. The acoustic propagation is also bottom limited as evidenced by the appropriate sound speed profile in figure 3.

(C) Site 4 is located on the Chain Ridge in the northern Somali Basin. The BMA was on the ridge while the vertical ACODAC and the OAMS and LATA towed arrays were over the deep basin about 10 to 20 miles to the northwest. The shipping surveillance flights near Site 4 confirm the existence of a relatively dense shipping lane along the east coast of Africa. The surveillance results are presented in figure 2 as vertical lines (Naval Ocean Systems Center, 1977). Results for only one of two days are presented in this figure, since the second surveillance flight was only one day later and many of the observed ships must have been the same. The shipping near the coast of Africa at the latitude of Site 4 is believed to be sparse because of the coastline's bending toward the west near Kenya and the economics of traveling the shortest distances possible between two ports. Hence, noise along westerly azimuths at Site 4 would be dominated by nearby ships. Site 4, being to the eastern edge of the shipping lane, would have relatively little noise in southeasterly directions — that is, provided the ships do indeed tend to travel in lanes, leaving vast areas of the oceans sparsely populated. Unfortunately, the shipping surveillance results from the BEARING STAKE exercise were too limited to be used in either support or rejection of this hypothesis.

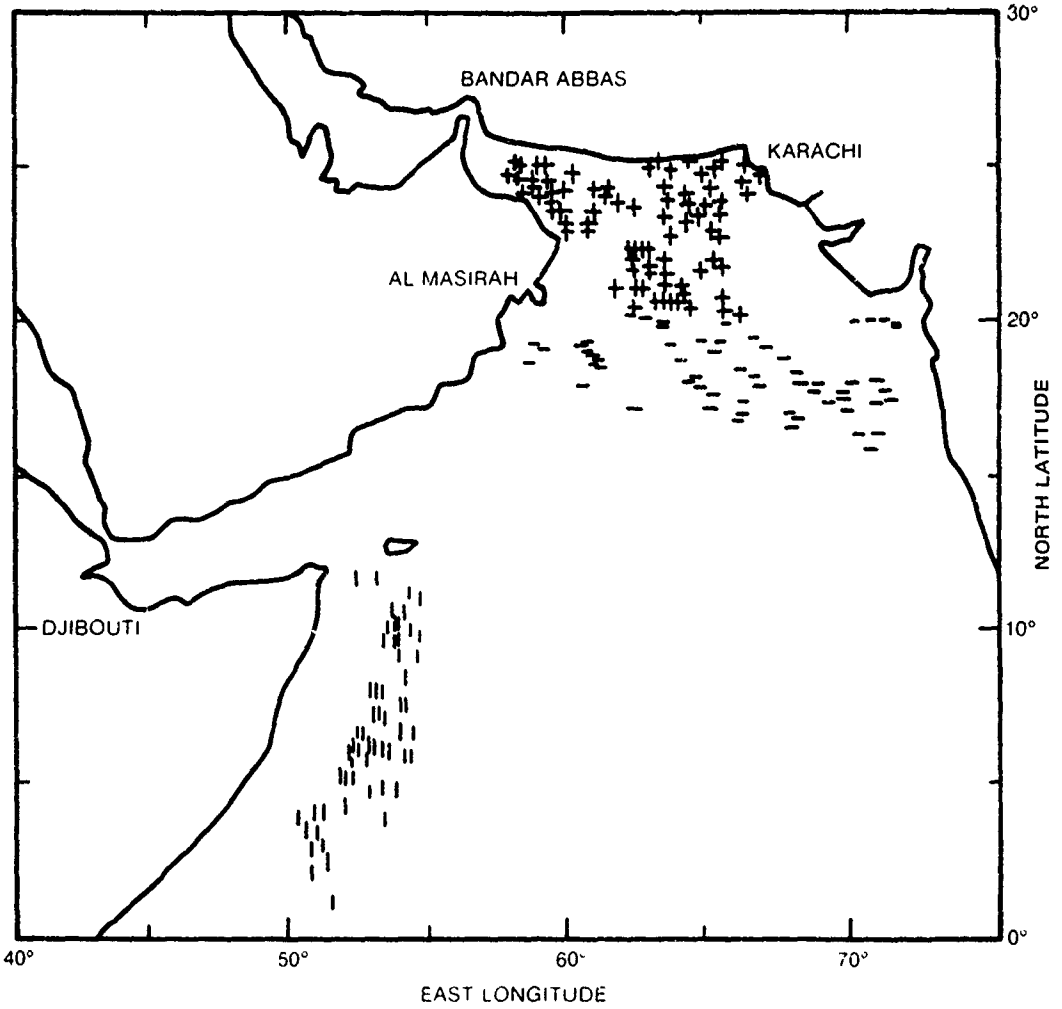

Figure VI-2. (C) Ship positions obtained by aerial shipping surveillance flights on 28 Jan 77 (+), 14 Feb 77 (-), and 21 Mar 77 (I). (U)

VI.2 (U) RESULTS AND DISCUSSION

VI.2.1 (U) Omnidirectional Noise Levels

(C) Figure 4 illustrates median ambient noise spectra obtained from one of the deepest hydrophones of the BMA (Scudder, 1978) at the five principal sites. The low-frequency (less than 200 Hz) noise is greatest at Site 1 and least at Site 5. For example, at 50 Hz it is approximately 14 dB greater at Site 1 than in the Northeast Pacific approximately 700 nmi west of Los Angeles and about 10 dB greater than off Bermuda (Perrone, 1969; Wagstaff et al., 1976). At Site 5 it is about 4 dB greater than in the Northeast Pacific and about equal to that near Bermuda. In light of the aerial surveillance data in figure 2 the Site 1 results appear quite reasonable. With such extremely dense nearby shipping, high noise levels are expected. The corresponding

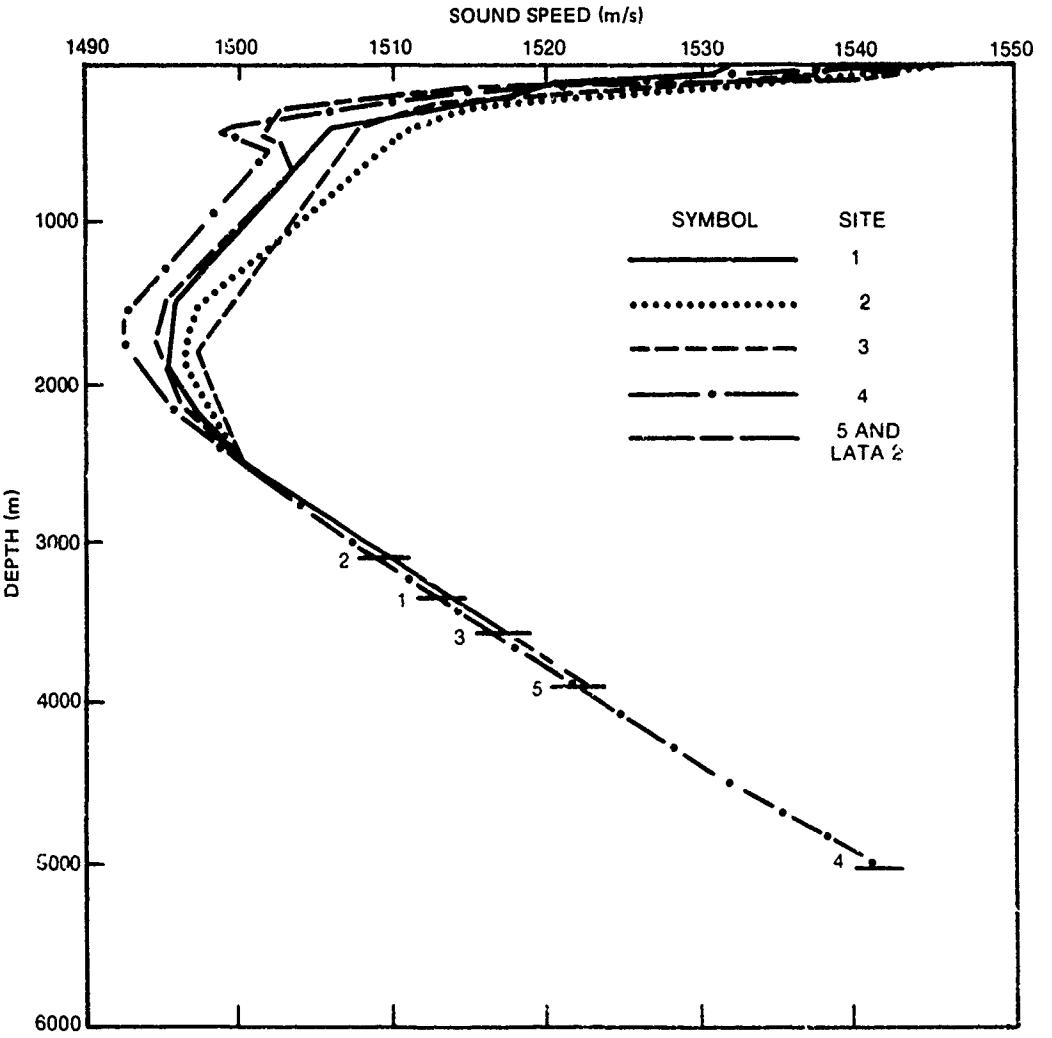

Figure VI-3. (C) Representative sound speed profiles obtained during the occupation of the five principal BEARING STAKE sites. (U)

levels for Sites 2, 3, and 4 are consistent with the moderately high shipping density at those locations as indicated in figure 2. No aerial surveillance shipping data are available for Site 5. Judged by the level of the low-frequency noise, the shipping must be of magnitude similar to that of shipping near Bermuda or the propagation of noise from the distant ships is relatively good. Historical shipping information (Ross et al., 1974; Solomon and Barnes, 1976) suggests the former could be the case. However, cumulative distribution results discussed in a later section support the latter conclusion.

(U) The noise levels above 300 Hz in figure 4 are consistent with wind speeds less than or equal to 10 knots as was generally the case throughout the entire BEARING STAKE exercise (Naval Ocean Research and Development Activity, 1978).

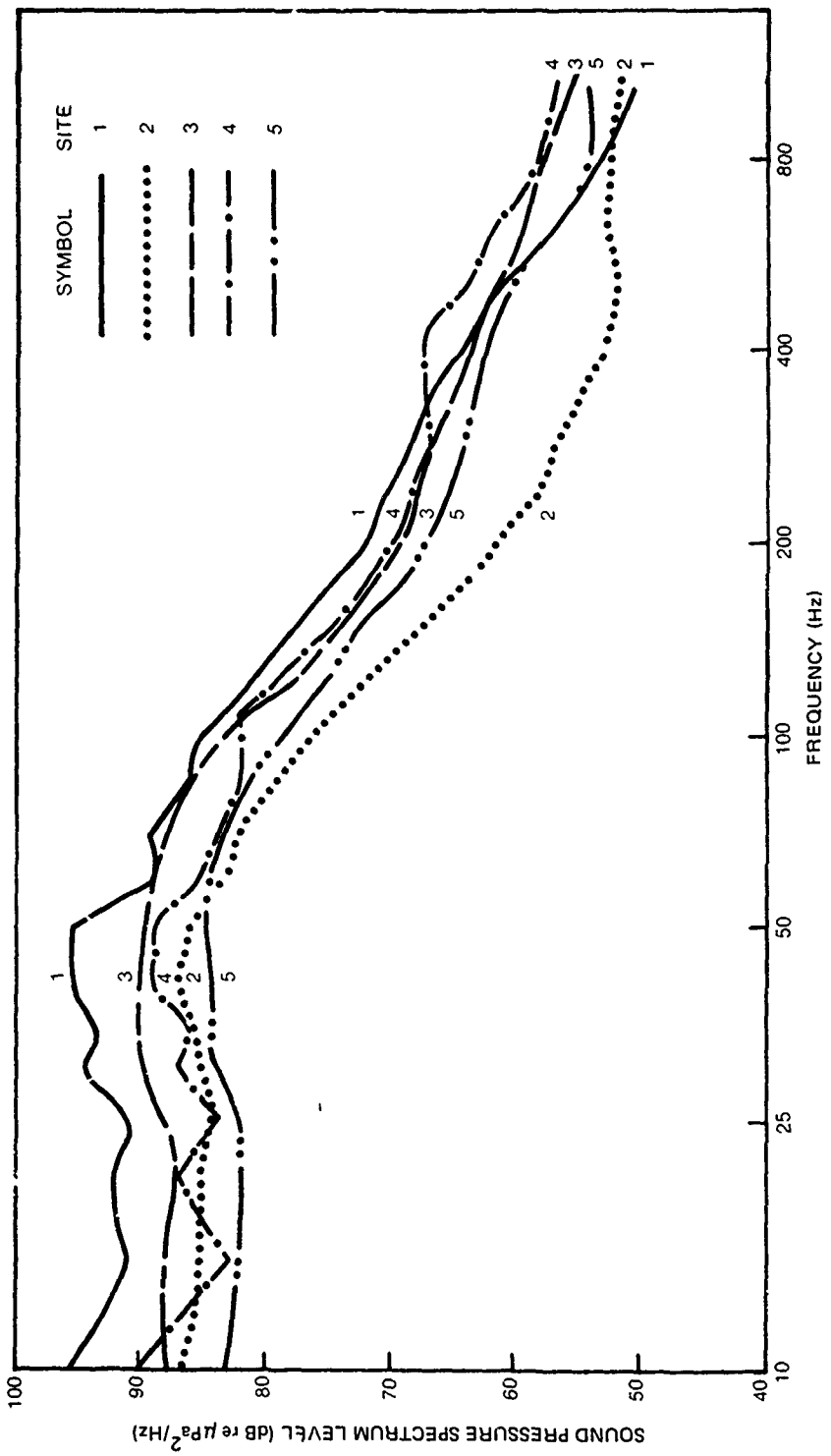

Figure VI-4. (C) Median noise levels for the five principal BEARING STAKE sites obtained from the deepest hydrophone of the bottom-mounted array. (U)

VI.2.2 (U) Ambient Noise Depth Dependence

(U) The depth dependence of the noise was measured by ACOuACs with hydrophones distributed between approximately 400 m and the bottom. Not all sites were occupied by ACODACs, and of those which were only data from Sites 1 and 4 are presently available.

(C) Figures 5 and 6 (Mitchell et al., 1978) illustrate the depth dependence of the median ambient noise spectra for Sites 1 and 4, respectively. The Site 1 results in figure 5 extend from 498 m to the bottom at 3351 m. The high noise levels at 25 Hz are artifacts due to a CW source used to investigate propagation. The Site 4 results extend from near the deep sound channel axis to the bottom. Because of problems in the recording system, no data were obtained from the shallow hydrophones at Site 4. Both figures 5 and 6 show very little depth dependence in the noise. Below 60 Hz at Site 4, for example, the reduction in level with depth is generally less than 1 dB. At Site 1 the change with depth is on the order of 2 dB, with the level increasing with depth. Such small depth dependence is not unexpected in the case of Sites 1 and 4. Whenever the noise is dominated by nearby shipping, as at these two sites, the insonification will be fairly uniform with depth. This may not be the case at the sites less densely populated by shipping, such as Site 5. That the noise levels are relatively low for Site 5 (see fig 4) indicates that the contribution from distant ships is probably a larger percentage of the total noise than it is at either Site 1 or 4. It is this component of distantly generated noise which decreases with depth as a result of bathymetric shielding and boundary interaction over long distances. The amount of depth quieting will depend on how large a fraction of the total noise is due to the distant noise component. Not more than an extra few dB would be expected at Site 5. Similar conditions are expected at Sites 2L and 5L. The low noise levels in figure 4 indicate that Site 2 also has very little nearby shipping. Hence, the depth dependence at this site should be slightly more than for either Site 1 or Site 4. Further discussion of depth dependence is available in Mitchell et al. (1978).

VI.2.3 (U) Horizontal Directionality

(C) Figures 7 and 8 illustrate the ambient noise horizontal directionality results obtained at five sites. The results in figure 7 for Sites 1 and 3 are from OAMS 23-Hz data. The others are for LATA 25-Hz data. In figure 8 the arrays are the same, but the frequencies are 36 and 40-Hz, respectively. The similarities in the directionality patterns in these two figures for a given site suggest the differences between 23 and 25 Hz and 36 and 40 Hz should be negligible.

(C) The noise directionality results for Site 1 indicate high noise levels to the west, southwest, east, and southeast but relatively low noise levels to the north and south. The lowest levels generally correspond closely to the levels anticipated for OAMS sidelobe contributions (about 18 to 22 dB). As a result, levels well below those shown for northerly and southerly directions are quite possible at Site 1. In each of the Site 1 directionality patterns in figures 7 and 8 an east-west bias of 8 dB to 12 dB is clearly evident. The majority of the noise is due to ships within a range of 100-200 nmi (see fig 2). In such a case, acoustic propagation effects have much less influence on the noise directionality than does the clustering of nearby ships (i.e., those

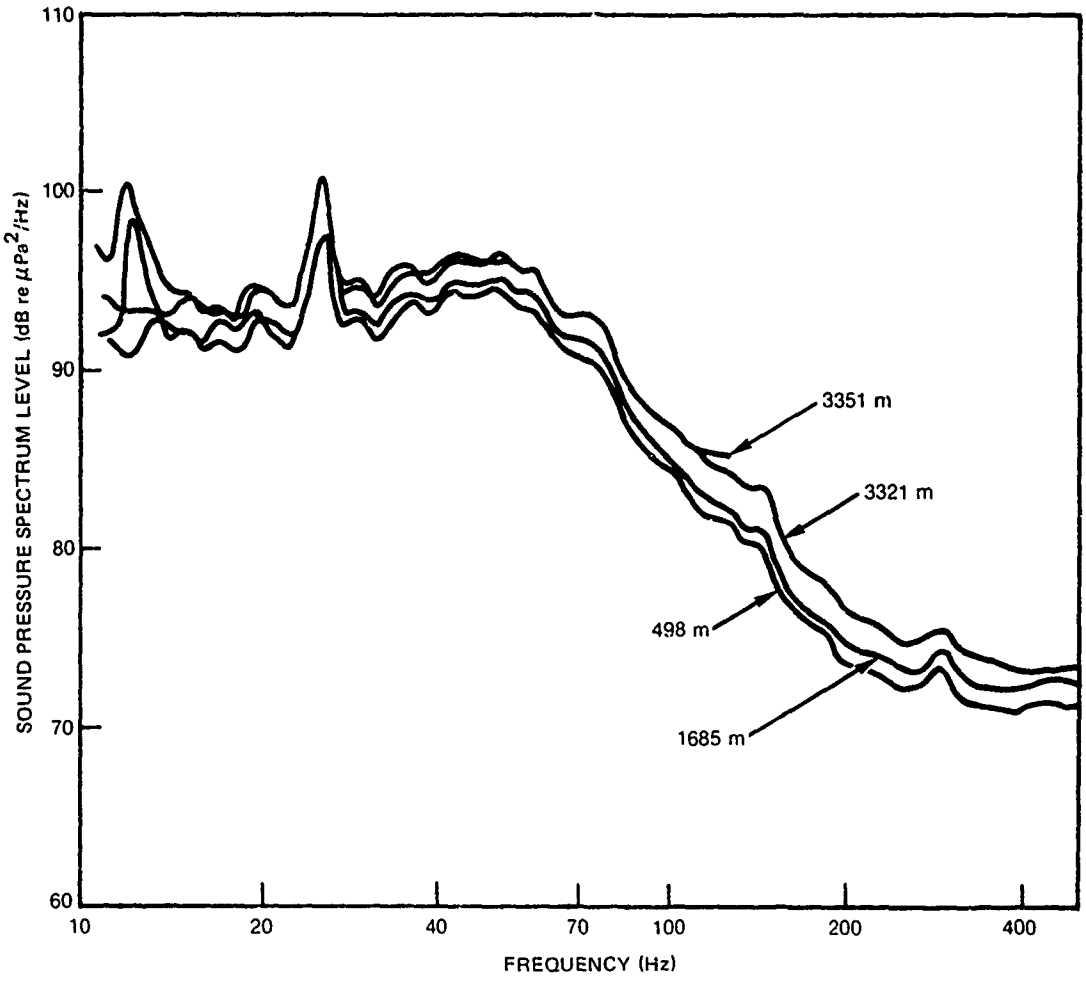

Figure VI-5. (C) Median ambient noise levels as a function of depth at Site 1. (U)

within 100 nmi). Hence, large changes in acoustic propagation will account for only small changes in the noise field at Site 1. Horizontal directionality characteristics should remain time invariant provided that shipping densities and distributions in the general vicinity remain approximately the same. Results suggest that the noise field at Site 1 could be easily modeled or predicted with a high degree of accuracy and confidence (Aitkenhead and Wagstaff, 1978).

(C) The predominant bias in the noise directionality patterns for Site 3 is in the northwest-southeast directions. Level variations in the directionality patterns ranged from 9 to 17 dB and were generally found to be inversely related to frequency (Aitkenhead and Wagstaff, 1978). Bearings toward the northwest tend to be consistently higher than in other directions. The heavy shipping traffic in the Gulf of Oman (see fig 2) could easily account for the observed maxima. Azimuths toward the southeast are also relatively noisy. Northeast and southwest directions are significantly quieter.

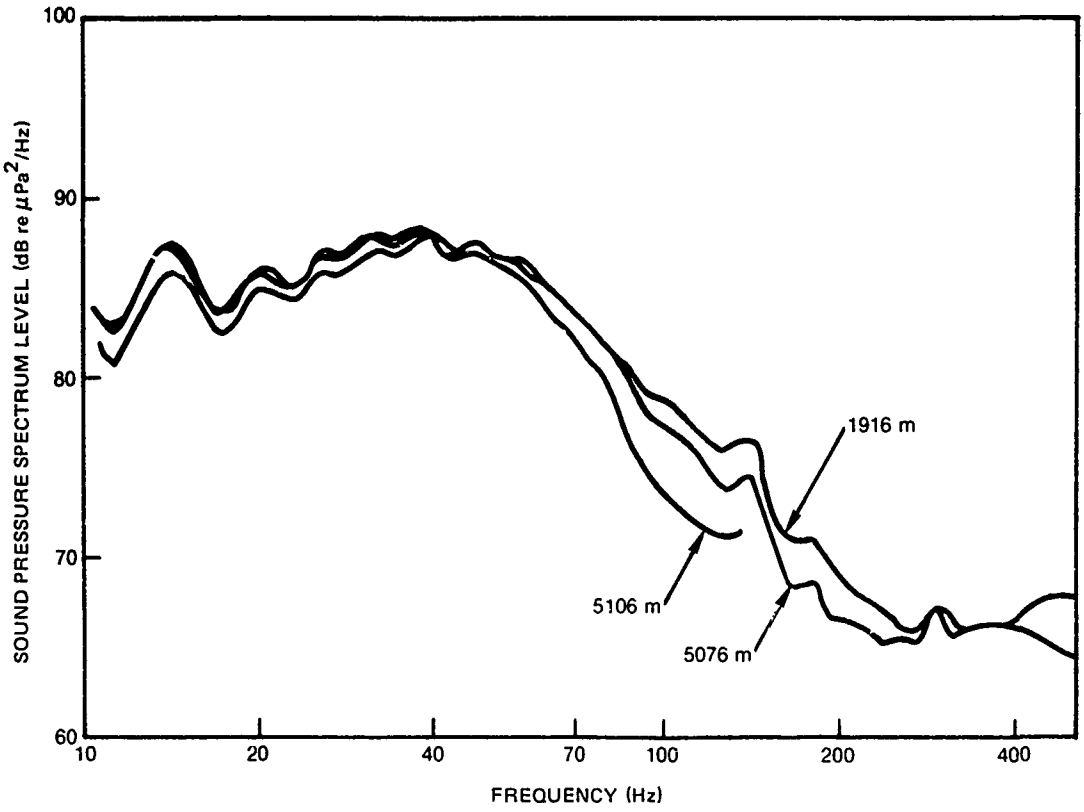

Figure VI-6. (C) Median ambient noise levels as a function of depth at Site 4. (U)

(C) Noise from the northeasterly and southwesterly directions at Site 3 tended to fluctuate from one directional estimate to another but remained fairly low. On the other hand, the northwesterly azimuths always exhibited consistently high levels. Noise toward the southeast tended to fluctuate more but had high levels more often than low levels. These characteristics suggest that a large number of ships are always toward the northwest of Site 3 (i.e., in or near the Gulf of Oman), relatively dense distribution of ships is always to the southeast (Persian Gulf - Straits of Malacca shipping lanes), and a moderately dense distribution of ships is in the immediate vicinity of the measurement site. The first two shipping distributions account for the relatively stable components of the directional noise patterns while the last smooths out the lower levels reducing the azimuthal anisotropy.

(C) A distinct feature of the 25 Hz noise at Sites 2L and 5L (see fig 7) is the relatively low values in a broad sector to the southwest. The levels at 40 Hz in figure 8 along the same azimuths are not correspondingly low. The reason for this is not presently understood. Low levels could be expected as a result of relatively low shipping in that direction (Solomon and Barnes, 1976), but both frequencies should be affected. An additional interesting feature of the noise at these two sites is the nearly uniform character of the noise over large arcs. Noise from a line distribution of sources will produce such an effect when the acoustic propagation increases with 20 times the log

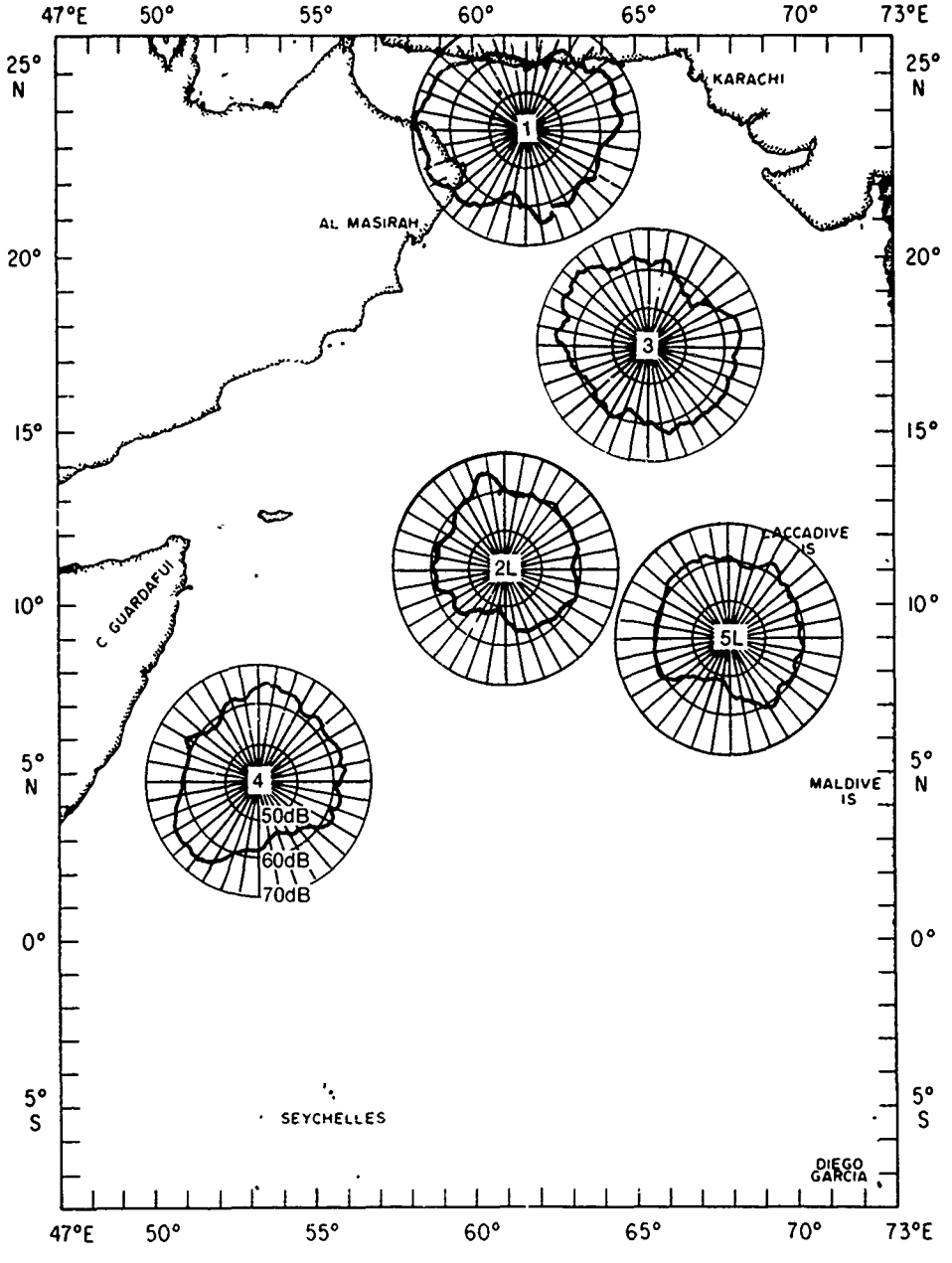

Figure VI-7. (C) Horizontal directionality of 23-Hz (Sites 1 and 3) and 25-Hz (Sites 4, 2L, and 5L) ambient noise in the Northwest Indian Ocean. (U)

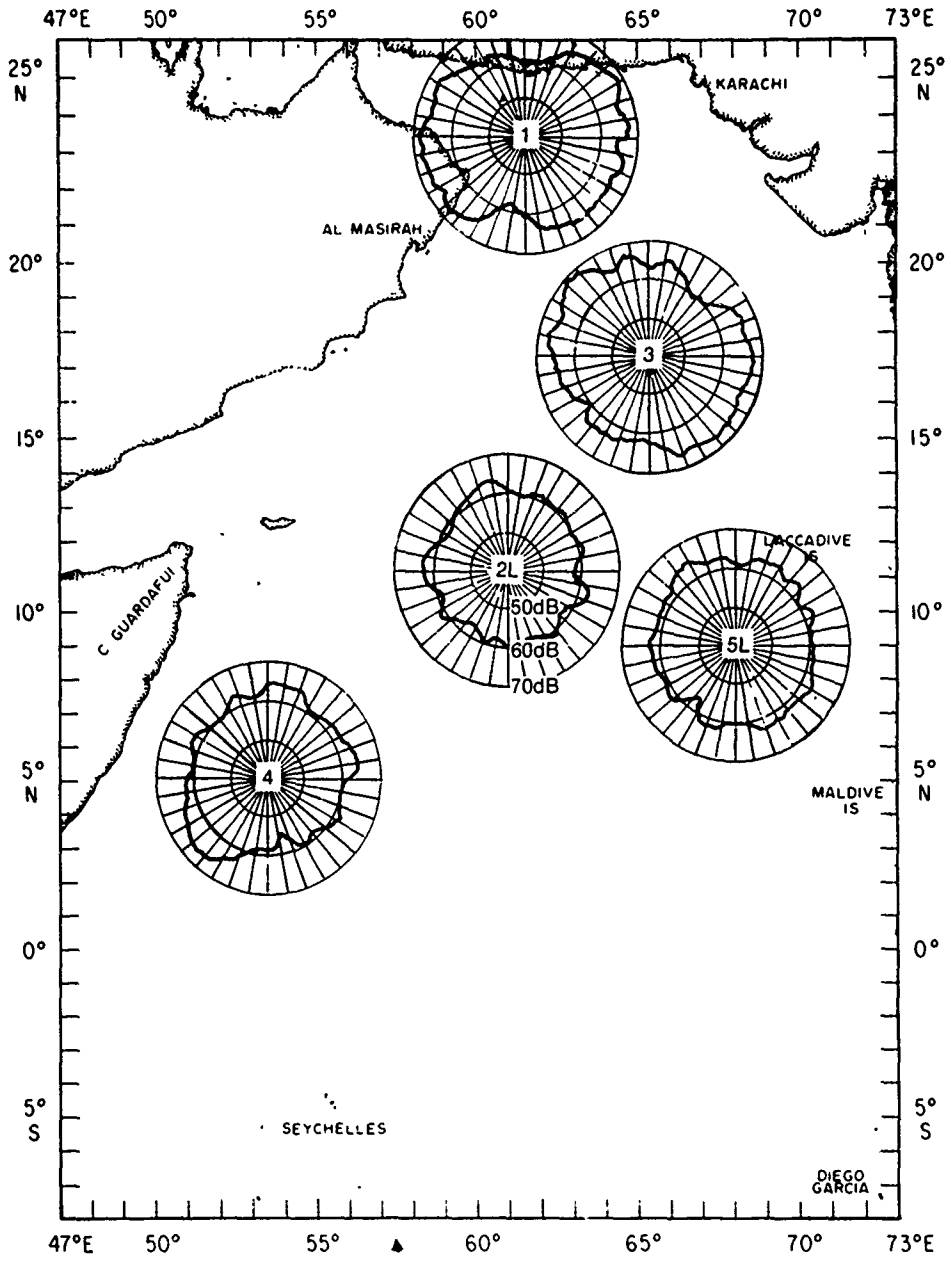

Figure VI-8. (C) Horizontal directionality of 36-Hz (Sites 1 and 3) and 40-Hz (Sites 4, 2L, and 5L) ambient noise in the Northwest Indian Ocean. (U)

of the range. Densely populated shipping lanes appear as line sources from a distance. Propagation loss calculations for near-surface (6-18 m) sources suggest that the character of the propagation is very similar to 20 times the log of the range. Hence, the noise at Sites 2L and 5L appears to be dominated by the shipping lanes along the west coast of India and the east coast of Africa.

(C) The aerial shipping surveillance results in figure 2 indicate that Site 4 is within the Persian Gulf - Cape of Good Hope shipping lane. The width of the lane is uncertain, since the flight path of the surveillance aircraft was generally parallel to the coast. The results at 25 and 40 Hz, however, suggest the lane to be relatively narrow to the southwest of Site 4. The broadening in the noise patterns toward the east and northeast could be a result of shipping lanes from the Cape of Good Hope dividing, part going to the Persian Gulf and the other to Bombay with Site 4 between the two. Traffic from the Gulf of Aden to the southern tip of India would also be contributory to the broadening of the noise pattern to the east and northeast. A more complete discussion of the noise directionality is available in Aitkenhead and Wagstaff, (1978).

(U) A final point should be made in the comparison of the noise patterns of figures 7 and 8. The anisotropy of the patterns decreases with increased frequency. It is doubtful that this effect is real. As the frequency increases, the beamwidth decreases, and the sidelobes become more sensitive to array nonlinearity. Also, the ratio of main beam noise power to the noise introduced by the sidelobes decreases with decreased main beamwidth. Hence, these two factors tend to fill in the lower levels of noise and produce a more uniform pattern.

(C) At this point it would be worthwhile to illustrate the significance and the utility of the noise directionality patterns in figures 7 and 8. The levels plotted in the directionality patterns are absolute sound pressure spectrum levels (relative to 1 micropascal) in a 1^{0} azimuthal sector. For comparable measurement intervals, an ideal unambiguous beam (i.e., uniform response across a 1^{0} sector with infinitely suppressed sidelobes) would have a median noise level equal to the value plotted in these figures for the corresponding steering angle. For wider beams, ambiguous beam pairs, and any other horizontal beam pattern, the estimated noise level is obtained by convolving the patterns shown in figures 7 and 8 with the beam pattern. As an example, suppose the 23-Hz median beam noise levels at Site 3 are needed for a towed array with 4^{0} beamwidths, a steering angle of 45^{0} from forward endfire, and an array heading of 045^{0}. The noise level for an ideal (ambiguous) beam from a horizontal array would be obtained by integrating the 23 Hz noise function shown in figure 7 over the true bearings from 088^{0} to 092^{0} and 358^{0} to 002^{0}. The result would be approximately 77.1 dB. Now suppose the sidelobes are uniformly suppressed by approximately 20 dB. For an omnidirectional level of 88.0 dB, the sidelobe contribution would be approximately 67.8 dB. Combining this, on an intensity basis, with the mainlobe level gives an estimate of the median beam noise level of 77.6 dB.

VI.2.4 (U) Noise Statistics - Temporal

(C) Figure 4 illustrates the noise as a function of frequency measured by the BMA at the five principal sites. Cumulative distribution functions were

also generated at 340, 280, 140, 50, and 25 Hz and are available in the report by Scudder (1978). Figure 9 illustrates the results for 50 Hz. In each case the data are from one of the deepest hydrophones of the array. A normal distribution would be a straight line on the plot. The noise at Site 2 is normally distributed. The curves for Sites 1, 3, and 4 are indicating more of a Rayleigh distribution. The high levels of noise which occur relatively infrequently (less than about 15% of the time) at Site 5 are indicative of a site which occasionally has close sources but is generally dominated by moderately dense distant sources. The lack of high-level noise at Site 2 suggests the shipping lane along the coast of Africa to be relatively distant, perhaps as much as a hundred miles or more. Hence, the shipping must hug the coast of Africa more near Site 2 than at Site 4, where the ships are known to be in the immediate vicinity of the site (see fig 2).

VI.2.5 (U) Noise Statistics - Azimuthal Anisotropy

(C) The results given in figures 7 and 8 indicate that the noise can vary significantly as the array heading is changed. For example, the average broadside beam noise level (at 23 Hz) changes by about 8 dB for selected sets of orthogonal headings at Sites 1 and 3. Although maximum and minimum beam noise levels are of considerable interest, the variation between these extremes is of equal importance. The term "azimuthal anisotropy" identifies one particular method of describing the variability of beam noise levels in a concise yet comprehensive manner. Azimuthal anisotropy characteristics relate the combined effects of spatial and temporal fluctuations in the ambient noise field to beam noise levels and present these relationships as statistical distributions of expected beam noise levels.

(C) Azimuthal anisotropy of the noise field is summarized as a cumulative distribution function of beam noise levels for various ideal beamwidths or ambiguous horizontal sector widths. The 23-Hz noise field observed at Site 1 illustrates the form and content of the azimuthal anisotropy analysis results (see fig 10). Beam noise measurements used for this example were limited to Site 1 data for array headings within $\pm 20^{\circ}$ of north or south. Thus, the OAMS coverage pattern encompasses an azimuthal sector of 200° (i.e., beam bearings within the range of $90^{\circ} \pm 50^{\circ}$ and $270^{\circ} \pm 50^{\circ}$). For an ideal beamwidth of 6°, it is evident from figure 10 that the expected noise level will be less than 75 dB for 47% of the possible beam look directions in this array coverage pattern. Conversely, the expected noise level will be greater than 75 dB on 53% of the look directions.

(C) Azimuthal anisotropy results are presented in figure 11 for beam noise measurements collected on beam bearings of $000^{\circ} \pm 50^{\circ}$ and $180^{\circ} \pm 50^{\circ}$. For this orthogonal array coverage pattern, the expected noise level will be less than 75 dB on approximately 84% of the look directions. Only 16% of the look directions would yield noise levels greater than 75 dB for a 6° beamwidth. In this case, the median noise level for an ideal 5.5° beamwidth is 69.3 dB. Thus, the noise within a fairly large azimuthal sector from the north and south of Site 1 appears to be of relatively low level. However, noise from the east and west of Site 1 appears to be nonuniformly distributed with the loudest sources concentrated in the bearing sectors defined by $070^{\circ} \pm 20^{\circ}$ and $270^{\circ} \pm 20^{\circ}$.

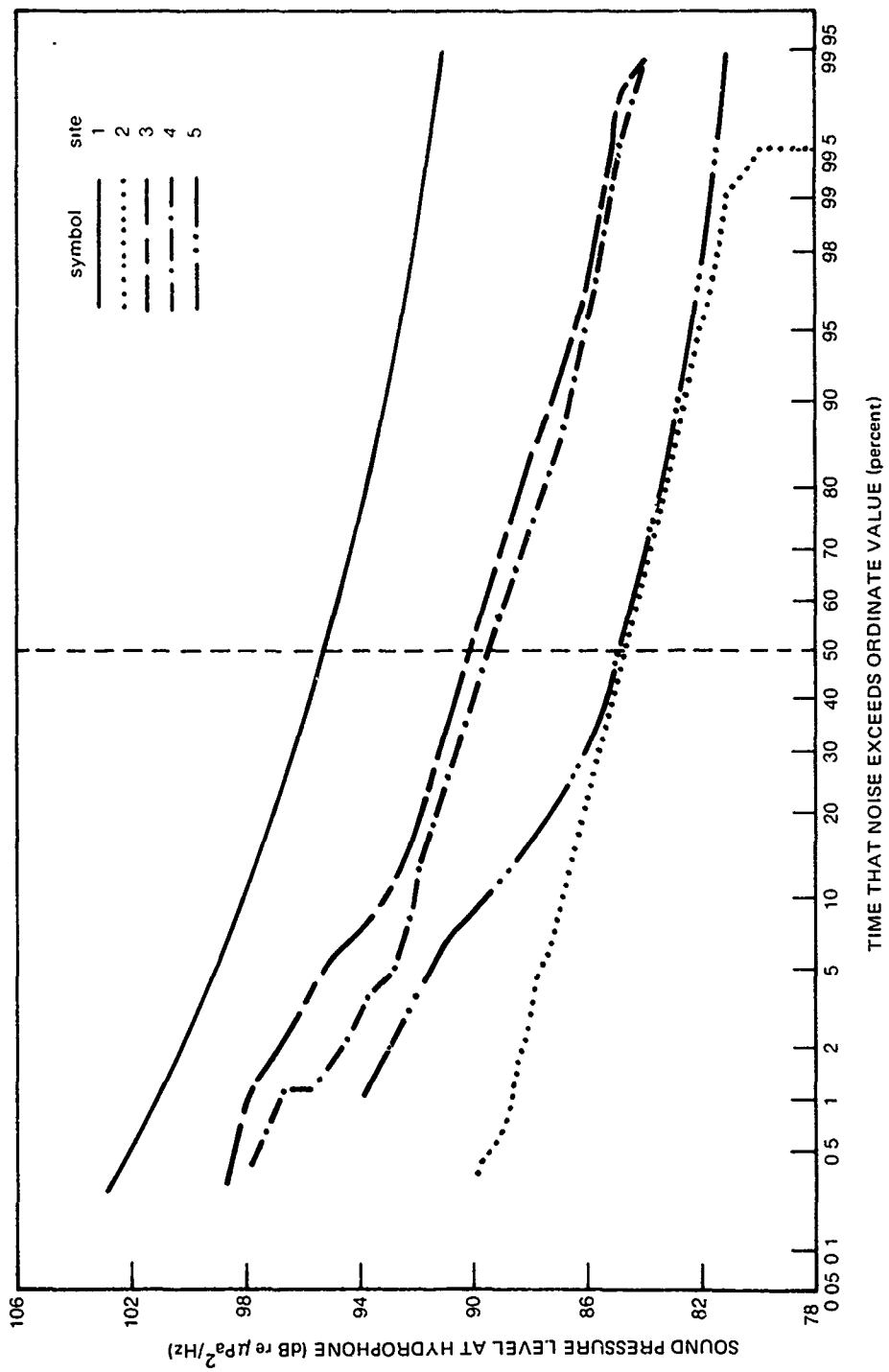

Figure VI-9. (C) Cumulative distribution plots of the 50-Hz noise data obtained at the five principal BEARING STAKE sites by the bottom-mounted array. (U)

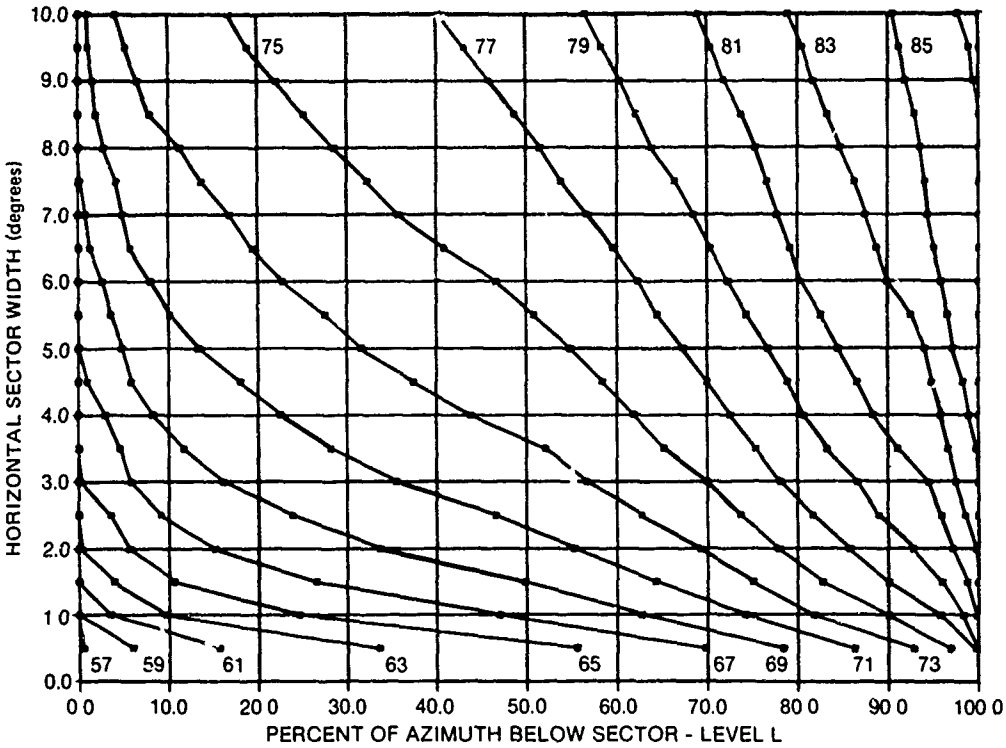

Figure VI-10. (C) Azimuthal anisotropy of beam noise levels for 23 Hz at Site 1--north/south array headings only. (C)

(C) When the direction of a possible target is unknown, as is often the case in performance prediction studies, results for an arbitrary array orientation are preferred. The 23-Hz azimuthal anisotropy results presented in figure 12 were developed from 50 sets of beam noise measurements (25 beams per set) at Site 1 with each set collected on a different array heading. In contrast, only ten sets of beam noise measurements were used in the results shown for the north-south or east-west orientations. Azimuthal anisotropy results such as those shown in figure 12 are suitable for analyses involving arbitrary array orientations while the results presented in figures 10 and 11 apply to more specific array orientations.

(C) Figures 13 and 14 give similar results at 23 Hz for Sites 3 and 4, respectively. At these two sites, however, the directional bias is at an approximate angle of 45° from north. Hence, only beam noise data for headings within 20° of northeast or southwest (fig 13a and 14a) and northwest or southeast (fig 13b and 14b) were utilized. From figures 7 and 8 it is evident that a towed array at Site 3 would have significantly less noise on beams in northeast-southwest directions than in northwest-southeast directions. The azimuthal anisotropy plots in figure 13 show the same results but in greater detail. Figure 13a is for northeast-southwest headings (northwest $\pm 50^{\circ}$ beam directions). Figure 13b is for directions orthogonal to those in figure 13a (northeast-southwest $\pm 50^{\circ}$ beam directions). These results suggest that for an array having a 4° beamwidth the beam noise will be less than 71 dB and 66 dB for 40% of the azimuths covered by the near-broadside beams when the array is

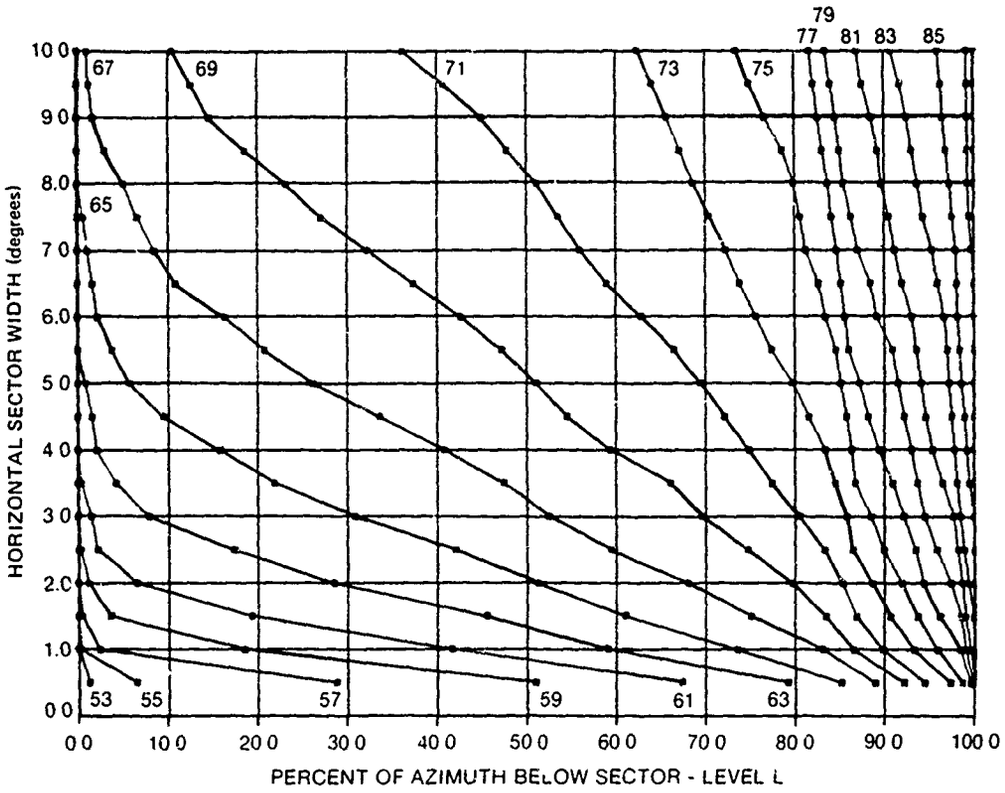

Figure VI-11. (C) Azimuthal anisotropy of beam noise levels for 23 Hz at Site 1 -- east/west array headings only. (C)

on northeast-southwest and northwest-southeast headings, respectively. The analogous results in figure 14 for Site 4 are 64 and 67 dB, respectively. The relative magnitudes of the levels are reversed in this case because Site 4 has a northeast-southwest directional bias whereas Site 3 has a northwest-southeast bias (see fig 7 and 8).

(U) Additional azimuthal anisotropy results for other frequencies are available in the report by Aitkenhead and Wagstaff, 1978.

(U) The azimuthal anisotropy curves are applicable, in the strictest sense, only for linear arrays. No attempt was made to remove ambiguities introduced by the conical beam patterns. The measurement array's finite sidelobe structure also affects azimuthal anisotropy results, especially at the lowest beam levels. Although the deconvolution technique (Wagstaff, 1978) used to produce these results attempts to remove all noise contributions measured via the OAMS sidelobes, this is not entirely possible. Some residual contamination will always be present.

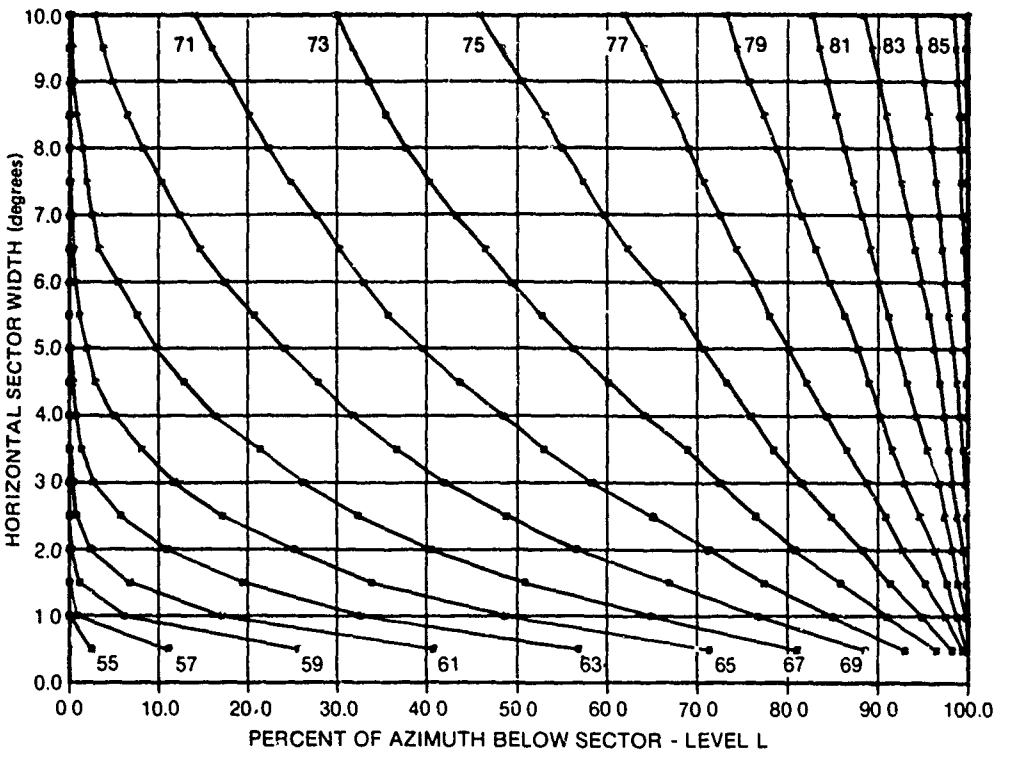

Figure VI-12. (C) Azimuthal anisotropy of beam noise levels for 23 Hz at Site 1 -- all array headings. (C)

VI.3 (U) CONCLUSIONS

(C) In the range from 10 to 100 Hz, omnidirectional noise levels were greatest near the Gulf of Oman (Site 1), being approximately 10 dB greater than the noise near Bermuda. This high level is consistent with the extremely high-density shipping near the Gulf of Oman. The noise levels in the middle of the Arabian Basin (Site 3) were only a few dB less. The levels within the shipping lane in the Somali Basin (Site 4) were approximately 4 to 8 dB less. The noise at Sites 2 and 5 was relatively low, about equal to that at Bermuda and about 3 to 5 dB greater than in the Northeast Pacific. Above approximately 300 Hz the noise at all sites was consistent with that which would be expected from the wind and sea state conditions.

(C) The character of the cumulative distribution function for the 50-Hz noise at Site 5 is indicative of distant noise source domination with infrequent (about 15% of the time) nearby shipping traffic.

(C) The noise at Site 2 was normally distributed and showed no indication of nearby shipping.

(C) The noise at Sites 1, 3, and 4 had definite biases in the horizontal. In the Arabian Basin (Sites 1 and 3) the shipping near the Gulf of Oman was clearly the dominant factor determining the noise directionality bias. In the

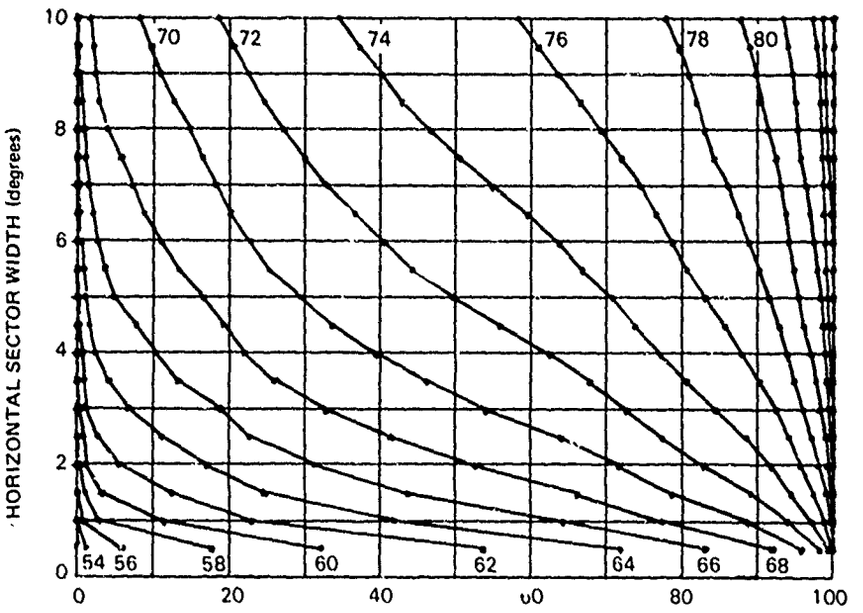

13a

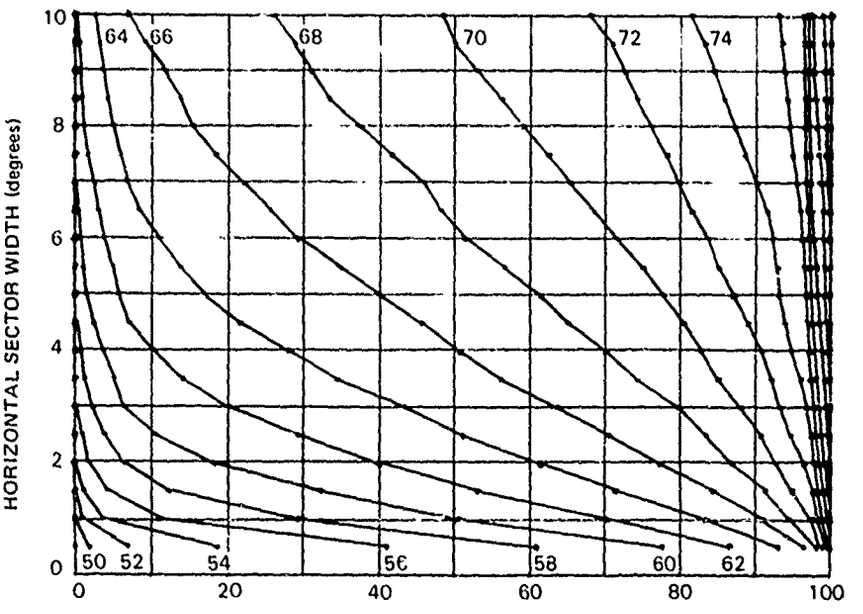

13b

Figure VI-13. (C) Azimuthal anisotropy of beam noise levels for 23 Hz at Site 3 -- northeast/southwest headings only (13a) and northwest/southeast headings only (13b). (C)

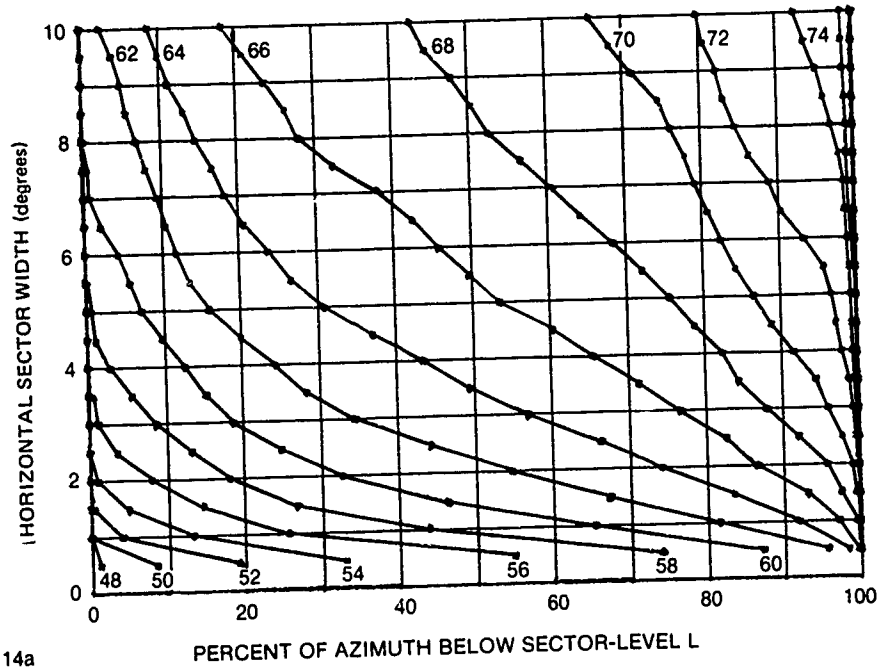

14a

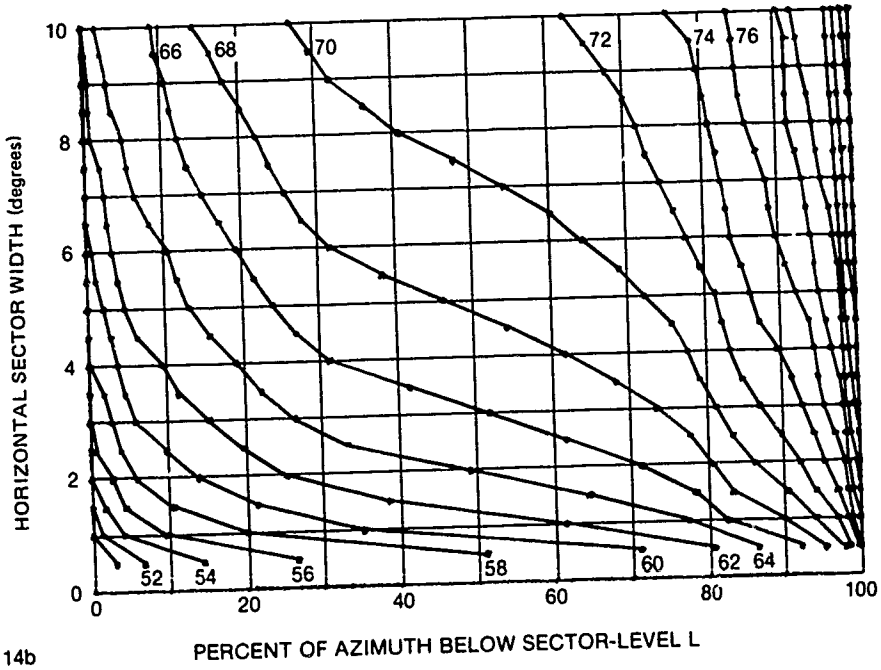

14b

Figure VI-14. (C) Azimuthal anisotropy of beam noise levels for 23 Hz at Site 4 -- northeast/southwest headings only (14a) and northwest/southeast headings only (14b). (C)

Somali Basin (Site 4) the shipping along the coast of Africa was the controlling factor.

(C) Because of the high-density nearby shipping and bottom-limiting conditions, less than 2–3-dB noise depth dependence was measured in the northern part of the Arabian Basin (Site 1) and the Somali Basin (Site 4). Because of less apparent nearby shipping, the depth dependence at Sites 2, 5, 2L, and 5L could be greater, but probably only by a few dB.

REFERENCES (U)

Aikenhead, J.W. and Wagstaff, R.A. (1978), (C) "Horizontal Directionality of Ambient Noise in the Northwest Indian Ocean (U)," Naval Ocean Systems Center, TR 275, June. (CONFIDENTIAL)

Mahler, J. and Solomon, L. (1974), "Interim Shipping Distribution," Planning Systems Incorporated, December.

Mitchell, S.K., (S) "BEARING STAKE Vertical ACODAC Acoustic Measurement (U)," Applied Research Laboratories, University of Texas, TR-78-8, February. (SECRET)

Naval Ocean Research and Development Activity, (1978), (C) "Representative Sound Speed Profiles for the Five Principal Sites (U)," March unpublished. (CONFIDENTIAL)

Naval Ocean Systems Center, (1977), (S) "BEARING STAKE Data Analysis Plan (U)," May (OOS-1055-77). (SECRET)

Perrone, A.J., (1969), "Ambient Noise Specturm Levels as a Function of Water Depth," Naval Underwater Systems Center, NUSC Rpt 1049, November .

Planning Systems Incorporated, (1978), PSI Doc. No. IS-7523, (S) "BEARING STAKE Shipping Surveillance Results (U)," January. (SECRET)

Scudder, R., (1978), (C) "Bottom Mounted Array Results (U)," Western Electric Company, February (unpublished). (CONFIDENTIAL)

Solomon, L.P. and Barnes, A.E. (1974). "Interim Shipping Distribution," Planning Systems Incorporated Systems.

Solomon, L.P. and Barnes, A.E., "Indian Ocean Appendix to the Navy Interim Shipping Distribution," Planning Systems Incorporated, about September.

Wagstaff, R.A., (1978), "Iterative Technique for Ambient Noise Horizontal Directionality Estimation from Towed Line-Array Data," JASA, Vol. 63, No. 3, p. 863-869, March.

Wagstaff, R.A., Pugh, J.D. and J.W. Aitkenhead, (1976), (S) "Horizontal Directionality of Ambient of Ambient Noise in the Northeast Pacific Ocean (U)," Naval Undersea Center TP 419, (SECRET)

CHAPTER VII

COHERENCE AND ARRAY SIGNAL GAIN (U)

by

J. A. Neubert

Environmental Acoustics Division

Naval Oceans Systems Center

San Diego, California 92152

CHAPTER VII. COHERENCE AND ARRAY SIGNAL GAIN (U)

CONTENTS (U)

CHAPTER VII. COHERENCE AND ARRAY SIGNAL GAIN (U)

VII.1 (U) INTRODUCTION

(C) For BEARING STAKE, phase coherence processing was done at six frequencies (22, 25, 36, 42, 140, and 290 Hz) at five sites (Site 3, 1B, 4, 5, and 2) for the OAMS array data, and the results are reported by Neubert (1978a). Phase coherence processing was done at 25 and 36 Hz at Sites 1B and 3 for the BMA, and the results are reported by Neubert (1978b). Phase coherence processing was done at 22 and 25 Hz at Sites 4, 5, and 2 for the LATA, and the results are reported by Fabula and Neubert (1978). Array signal gain processing was done only at 25 Hz for the OAMS array, the BMA, and the LATA, and the results are reported by Neubert (1978c). The purpose of this chapter is to perform an acoustic assessment of phase coherence and array signal gain for these five sites in the Northwest Indian Ocean using the data described above and reported by Neubert (1978a, b, and c) and by Fabula and Neubert (1978).

(U) The information for this phase coherence and array signal gain area assessment report is taken from the four reports referred to above and is treated below in the order: Sites 1B, 3, 4, 5, 2. When referred to but not reproduced in this report, the tables and figures from the four references are prefixed by Na, Nb, Nc, and F for the references: Neubert (1978a, b, c) and Fabula and Neubert (1978), respectively. For example, table 5 from the reference: Neubert (1978a) is denoted herein as table Na-5.

(U) The phase coherence and array signal gain data for all three arrays can be compared directly by using the timing of the data samples and the known positions versus time of the arrays and of the projector tow ship. When the arrays are not collocated (Sites 5 and 2), the possibly different propagation conditions along the different propagation paths from the projector to the receivers should be kept in mind. Even when two arrays are collocated, their different depths have to be considered with regard to possible differences of major propagation paths to each receiver (see Neubert, 1978d).

VII.2 (U) EFFECT OF SOUND PROPAGATION ON AMPLITUDE FLUCTUATION

(C) Before beginning the site-by-site area assessment for BEARING STAKE, it is convenient to appraise the effect of multipath sound propagation on amplitude fluctuation over all the selected sites in the Northwest Indian Ocean. Neubert (1978d) discusses the nature of sound propagation during the BEARING STAKE exercise on a site-by-site basis and shows that the degree of bottom interactions (as indicated by how many of the important rays contact the bottom and at what angles) was highest for Site 1B and lowest for Site 4.

(C) The tables in Neubert (1978a) give C_p [see eq (A-20)], Σ_A [see eq (A-15)], and SNR (the signal plus noise to noise ratio) for the OAMS array; these quantities for the BMA and the LATA are found in the tables of Neubert (1978b) and Fabula and Neubert (1978), respectively. These tables show that generally the degree of amplitude fluctuation, as measured by Σ_A, is largely range independent and does not increase much with frequency at each site and

for each array. This behavior is shown in table 1 on a site-by-site basis for each array (the OAMS array data cover all five sites while the BMA data applies only to Sites 3 and 1B and the LATA data apply only to Sites 4, 5, and 2) and for signal plus noise and for noise.

TABLE 1. (C) THE DEGREE OF AMPLITUDE FLUCTUATION, Σ_A. (U)

	OAMS		BMA(1B,3)/LATA(2,3,5)	
	Signal plus Noise	Noise	Signal plus Noise	Noise
Site 1B	0.3-0.5	0.5-0.6	0.25-0.5	0.5-0.55
Site 3	0.3-0.5	0.5-0.6	0.3-0.5	0.5-0.55
Site 4 (before "crush event")	0.2-0.4	0.5-0.6	0.2-0.5	0.5-0.55
Site 4 (after "crush event")	0.3-0.6	0.6	0.2-0.5	0.5-0.55
Site 2	0.4-0.55	0.55	0.2-0.5	0.55
Site 5	0.3-0.5	0.55	0.2-0.5	0.5-0.5

(C) The SNR levels for the OAMS array were high and comparable for Sites 1B, 3, 4, and 5 and significantly lower for Site 2, where a seamount was present (see Neubert, 1978d). Still table 1 shows that the values of A are comparable for all these sites. However, a closer scrutiny of table 1 does reveal some agreement with three phenomena that occurred during BEARING STAKE. Note that Site 4 is divided into two parts in the table: before and after the "crush event." The crush event occurred at 0400Z on 16 March 1977, when the OAMS approached its nominal crush depth (350 m). See Neubert (1978a) for more details. Note that OAMS signal plus noise amplitude fluctuations were less at Site 4 before the crush event than after it, suggesting that the individual hydrophones are producing more self-noise after having been damaged by the crush event. (This interpretation is supported by noting that the OAMS noise amplitude fluctuation was also increased after the crush event.) This is the first phenomenon that is discernible in table 1. The second is seen by noting that the OAMS signal plus noise amplitude fluctuations are less at the first part of the Site 4 test than at any previous site. This occurs because the propagation conditions were less disturbed by bottom interaction at Site 4 than at the other sites, which were bottom limited. The third phenomenon relates to the OAMS array being towed behind the seamount during the Site 2 exercise (as discussed by Neubert, 1978d). Projector tows 5P1 (Site 5) and 2P3A overlap in the Indus Fan, and it appears that the main difference between these two projector tows is the presence of the seamount between the 2P3A projector tow track and the OAMS array. As observed from tables in Neubert

(1978a), the SNR values are lower for Site 2 than Site 5 by about 5 dB. Table 1 agrees with this by showing higher OAMS signal plus noise amplitude fluctuation at Site 2 than at Site 5.

(C) Note also from table 1 that at both Sites 1B and 3 the BMA and OAMS signal plus noise amplitude fluctuation behavior is essentially the same. The LATA (in contrast to the OAMS) does not detect less signal plus noise amplitude fluctuation at Site 4 (which has little bottom interaction) than at Site 5 (which is bottom limited). In fact, the LATA sensed similar signal plus noise amplitude fluctuation at Sites 2, 4, and 5. This appears to be due to the more complex sound speed profile that occurs at the LATA tow depth; see Neubert, 1978d. Note that Sites 1B and 3 for the BMA and Sites 2, 4, and 5 for the LATA are essentially the same with respect to signal plus noise amplitude fluctuation. Finally note that the noise amplitude fluctuation as measured with all three arrays is quite similar at all five sites.

VII.3 (U) DISCUSSION OF SITE 1B

VII.3.1 (U) OAMS Array Phase Coherence and Array Signal Gain

(C) The OAMS array phase coherence data analysis for Site 1B is summarized by Neubert (1978a) in tables Na-10 through Na-12 and in figures Na-29 through Na-31 for 25, 140 and 290 Hz. The OAMS array signal gain data analysis for Site 1B is summarized by Neubert (1978c) in Table Nc-4 and in Figures Nc-8 and Nc-9 for 25 Hz. The OAMS array phase coherence and array signal gain data were taken on one linear projector tow over the Oman Basin: 1BP1. The relevant figures and tables of Neubert (1978a) show that the phase coherence decreases severely as the frequency increases from 25 to 290 Hz while the SNR values remain comparable and high. This SNR behavior is explained as follows. Although the projector source level was less at higher frequencies and although the propagation loss increases with frequency because of higher bottom reflection losses, the ambient noise level also was less at higher frequencies, and this kept the SNR values high. While there is a decrease in phase coherence with increasing frequency (while SNR remains high), which is relevant to array performance for these higher frequencies (i.e., 140 and 290 Hz), the real significance of this trend must be considered in terms of array length divided by the wavelength. This is important because it has been observed that coherence can decrease as the aperture length (in units of wavelength) increases. Therefore, the best way to compare arrays at different frequencies is in terms of phase coherence for constant aperture length in units of wavelength. This latter procedure is suggested for more detailed studies of phase coherence versus frequency. Figures 1 and 2 show that the phase coherence and the array signal gain are generally range independent up to about 200 km, where they decrease somewhat with range out to about 300 km. This decrease in phase coherence and array signal gain corresponds to the passage of the source over an irregular sloping bottom. There is no significant decrease in SNR values during the tow over the sloping irregular bottom, so the decrease in phase coherence and array signal gain appears to be caused by the irregularity of the bottom contour. Note that the wide variability in C_p and ASG with range due to multipath interference is increased by the irregular bottom slope region. Comparing figures Nc-8 and Nc-9 shows that the values of ASG are somewhat better for the weighted OAMS array than for the unweighted array.

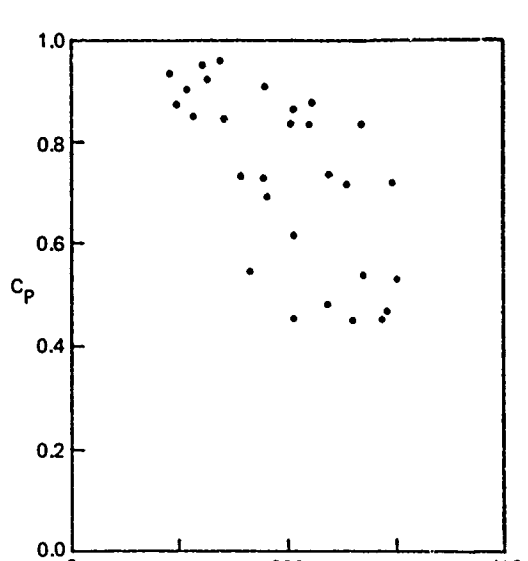

Figure VII-1. (C) Phase coherence as a function of range; OAMS array; Site 1B; track 1BP1; 25 Hz; 19-20 February 1977. (C)

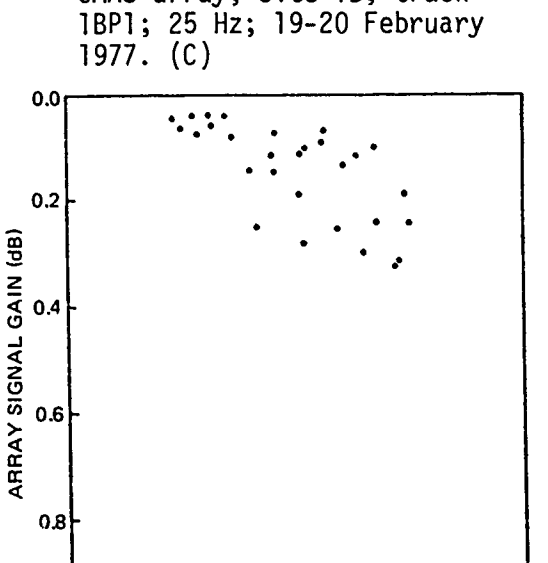

Figure VII-2. (C) Array signal gain vs range, calculations with unity weights, OAMS array; Site 1B; track 1BP1; 19-20 February; 25 Hz. (C)

VII.3.2 (U) BMA Phase Coherence and Array Signal Gain

(C) The BMA phase coherence data analysis for Site 1B is summarized by Neubert (1978b) in tables Nb-3 through Nb-7 and figures Nb-21 through Nb-35 for 25 Hz. The BMA array signal gain data analysis for Site 1B is summarized in tables Nc-16 through Nc-20 and in figures Nc-30 through Nc-34 for 25 Hz. The BMA phase coherence and array signal gain data were taken on five projector tows over the Oman Basin: 1BP1, 1BP4, 1BP3, 1BP2, and 1BP5. Only the results for projector tow 1BP1 are of interest here since the results for the other tows agree with the behavior for tow 1BP1 discussed. Figures 3 and 4 show that the phase coherence and the array signal gain are generally range independent up to about 300 km, and the irregular bottom slope has no apparent effect on ASG beyond 200 km. Note that the wide variability of C_p and ASG with range due to multipath interference is not increased by the irregular bottom slope region.

VII.3.3 (U) Comparison of the BMA and the OAMS Array

(C) Figures 1 through 4 give the relative phase coherence behavior and the relative array signal gain behavior on projector tow 1BP1 for the OAMS array (with the source bearing generally between 75° and 100°) and the BMA (with the source bearing near 160°) as a function of range at 25 Hz. As can be seen from these figures, for the bottom-mounted array the phase coherence and the array signal gain showed no rangewise increase in variability and no rangewise change due to the irregular bottom slope (possibly due to the presence of bottom paths). On the other hand, for the mid-depth towed array, the phase coherence and the array signal gain decreased and became more variable as the projector was towed over the irregular sloping bottom. Observe that the phase coherence behavior and the array signal gain behavior of the bottom-mounted and the mid-depth towed arrays were comparable before the irregular bottom sloping ranges (this is in agreement with the results for projector tow 3P4 in section VII.4.3). Therefore, it appears that for this bottom-limited region (near Site 1B) of the Northwest Indian Ocean the phase coherence and the array signal gain performances are essentially the same for bottom-mounted and mid-depth towed (above 250 m) arrays except for the irregular bottom slope region. Figures 1 through 4 show that performances of the bottom-mounted and middepth-towed arrays are comparable. As shown by Neubert (1978b), the sensor spacing for the BMA at Site 1B was considerably different from that for the OAMS array. To obtain a more nearly accurate comparison of the towed array with the BMA, a subset OAMS array (configured similarly in sensor spacing to the BMA at Site 1B) was studied. Neubert (1978a, b) shows that the behavior of this subset towed array was essentially the same as that of the bottom-mounted array with regard to phase coherence and array signal gain behavior except that the BMA behavior was much less disturbed by the irregular sloping bottom. This latter phenomenon may indicate that the BMA was receiving a significant amount of sound propagated through bottom paths. Incidentally, figures Nc-8, Nc-9, and Nc-36 show that the unweighted and the subset OAMS arrays are similar in ASG rangewise behavior, while the weighted OAMS array slightly outperforms both these cases.

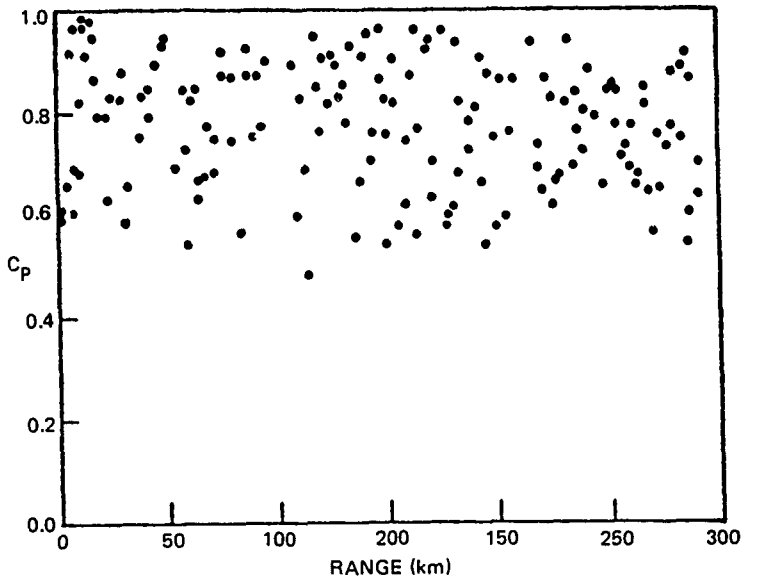

Figure VII-3. (C) Phase coherence as a function of range. BMA; Site 1B; track 1BP1; 19-20 February 1977; 25 Hz. (C)

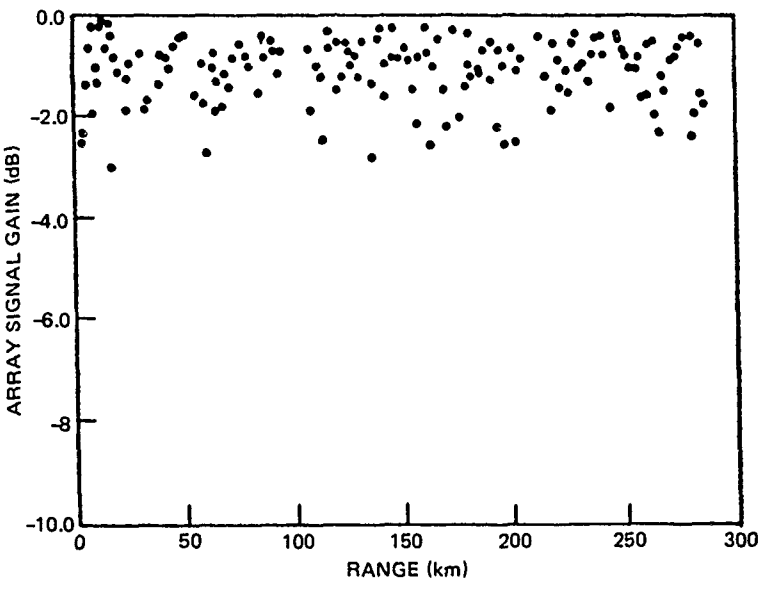

Figure VII-4. (C) Array signal gain vs range, calculations with unity weights. BMA; Site 1B; track 1BP1; 19-20 February 1977; 25 Hz. (C)

VII.4 (U) DISCUSSION OF SITE 3

VII.4.1 (U) OAMS Array Phase Coherence and Array Signal Gain

(C) The OAMS phase coherence data analysis for Site 3 is summarized by Neubert (1978a) in tables Na-1 through Na-9 and in figures Na-2 through Na-28 for 25, 140, and 290 Hz. The OAMS array signal gain data analysis for Site 3 is summarized by Neubert (1978c) in tables Nc-1 through Nc-3 and Figures Nc-2 through Nc-7 for 25 and 42 Hz. The tables give ΔT (the averaging time interval) 20 $\log_{10} A_a$, the source bearing ϕ_k [see eq (A-3)], C_p, Σ_A, C_{TR} [see eq (A-13)], ASG [for weighted and unweighted beamformers; see eq (A-24)], SNR (the signal plus noise to noise ratio in dB), and the range R. Based upon these results some observations can be made about the phase coherence (as measured by C_p) and the array signal gain (as measured by ASG) at Site 3 for the OAMS array.

(C) The OAMS array phase coherence and array signal gain data were taken on three linear projector tows across the center of the Indus Fan: 3P1, 3P3, and 3P4. The relevant figures and tables in Neubert (1978a) show that the phase coherence decreases severely as the frequency increases from 25 to 290 Hz, while the SNR values remain comparable and high. This SNR is similar to the behavior at Site 1B and the explanation given in section VII-3.1. applies here also.

(C) Neubert (1978a), figures Na-2 through Na-10, and (1978c), figures Nc-2 through Nc-7, shows that the phase coherence and the array signal gain, respectively, are generally range independent up to about 310 km. As an example see figures 5 and 6, which correspond to projector tow 3P4 at 25 Hz. (For examples of 140 and 290 Hz results, see figures 7 and 8, respectively.) Note the wide variability of C_p and ASG with range due to multipath interference in this bottom-limited environment with its complex sound speed profile structure (see Neubert, 1978d). Fabula and Neubert (1978) discuss the varying structure of the signal field along the array that causes the high variability of C_p and ASG. The scatter of values that appear in figures 5, 6, etc, is due to undersampling of rangewise continuous functions. Figures Nc-2 through Nc-7 show that the values of ASG are somewhat better for the Hamming-weighted OAMS array than for the unweighted array. This was also observed in section VII.3.1. and is not surprising in a multipath environment since the weighting decreases the contribution to ASG of sensor group pairs at greater separations, i.e., reducing the effective array aperture.

VII.4.2 (U) BMA Phase Coherence and Array Signal Gain

(C) The BMA phase coherence data analysis for Site 3 is summarized by Neubert (1978b) in tables Nb-1 and Nb-2 and in figures Nb-5 and Nb-6 for 25 and 36 Hz. The BMA array signal gain data analysis for Site 3 is summarized by Neubert (1978c) in tables Nc-14 and Nc-15 and in figures Nc-28 and Nc-29 for 25 and 36 Hz. The BMA phase coherence and array signal gain data were taken on two straight projector tows across the center of the Indus Fan: 3P2 and 3P4. Figures Nb-15 and Nb-16 and figures Nc-30 and Nc-31 show that the phase coherence and the array signal gain, respectively, are generally range independent up to 300 km. As an example, see figures 9 and 10, which

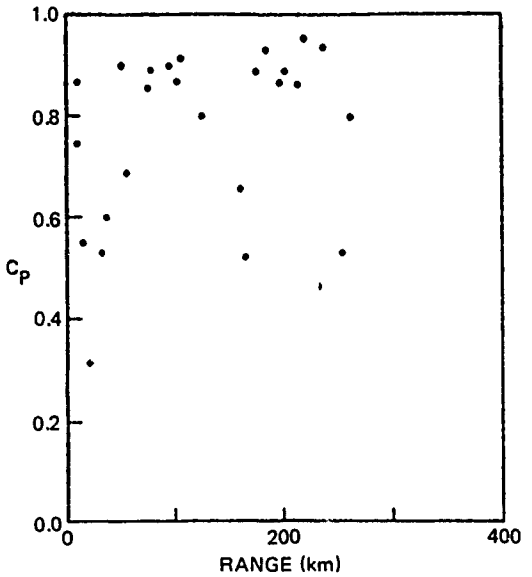

Figure VII-5. (C) Phase coherence as a function of range; OAMS array; Site 3; track 3P4; 25 Hz; 10-11 February 1977. (C)

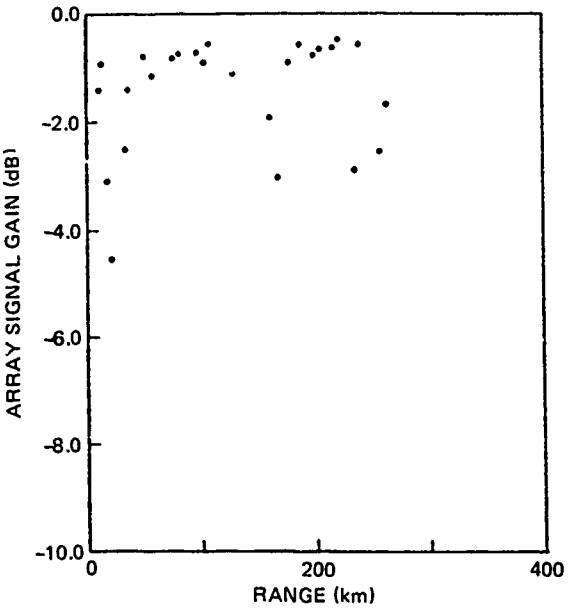

Figure VII-6. (C) Array signal gain vs range, calculations with unity weights. OAMS array; Site 3, track 3P4; 10-11 February 1977; 25 Hz. (C)

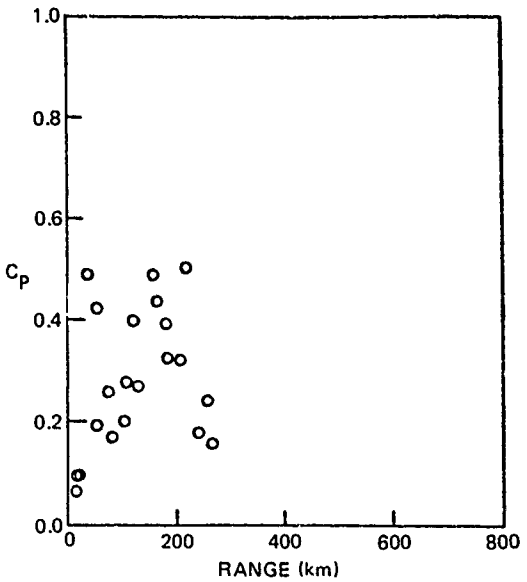

Figure VII-7. (C) Phase coherence as a function of range; OAMS array; Site 3; track 3P4; 140 Hz; 10-11 February 1977.(C)

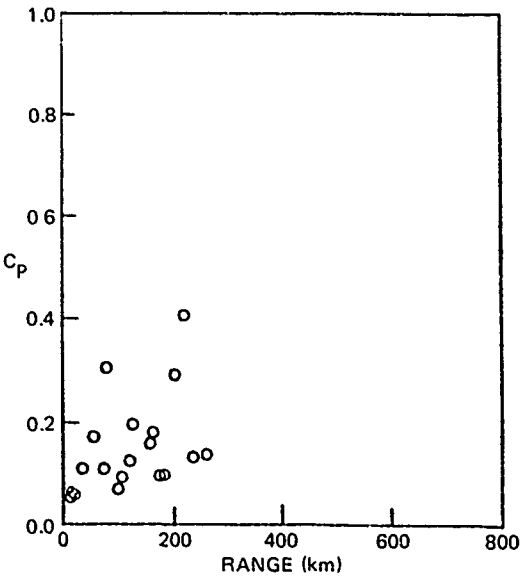

Figure VII-8. (C) Phase coherence as a function of range; OAMS array; Site 3; track 3P4; 290 Hz; 10-11 February 1977. (C)

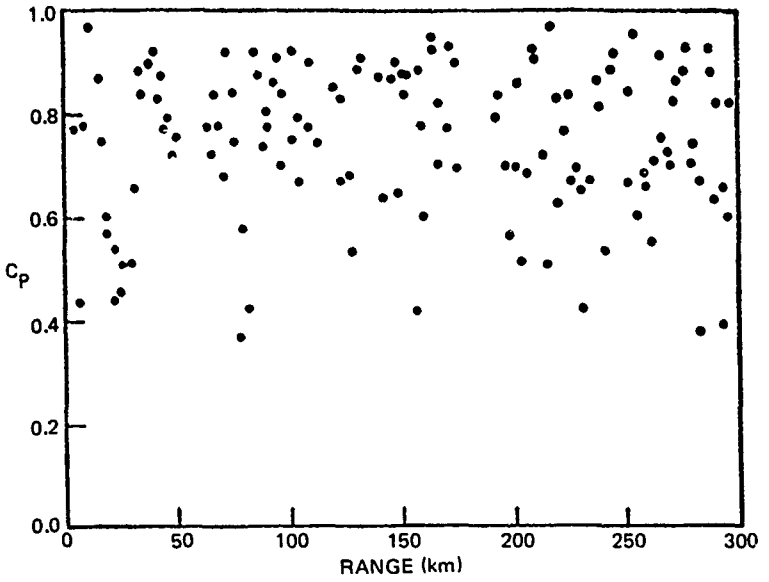

Figure VII-9. (C) Phase coherence as a function of range. BMA; Site 3, track 3P4; 10-11 February 1977; 25 Hz. (C)

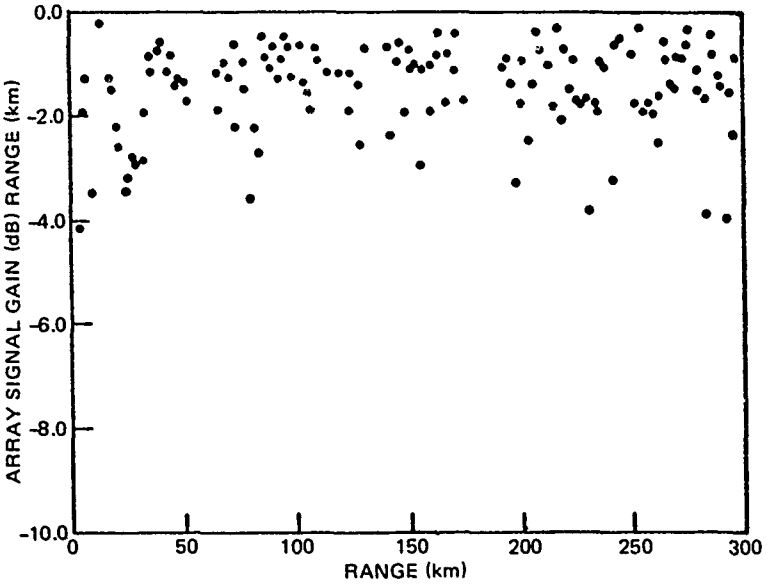

Figure VII-10. (C) Array signal gain vs range, calculations with unity weights. BMA; Site 3; track 3P4; 10-11 February 1977; 25 Hz. (C)

correspond to projector tow 3P4 at 25 Hz. Note the wide variability of C_p and ASG with range that was observed in section VII.4.1.

VII.4.3 (U) Comparison of the BMA and the OAMS Array

(C) Figures 5, 6, 9, and 10 give the relative phase coherence behavior and the relative array signal gain behavior on projector tow 3P4 of the OAMS array (with the source bearing near 90^0, i.e., near broadside) and the BMA (with the source bearing near 16^0) as a function of range at 25 Hz. Figures 1 through 6, 9, and 10 show that the phase coherence behavior and the array signal gain behavior at Site 1B (until the irregular bottom slope region) and at Site 3 are comparable for the BMA and the OAMS array. Therefore, it appears that there is no significant difference in phase coherence and array signal gain behavior between these two sites. This is especially true because of the wide rangewise variability of C_p and ASG caused by the multipath interference in these bottom-limited regions with their complex sound speed profiles. As was shown by Neubert (1978c), the sensor spacing for the BMA at Site 3 was considerably different from that for the OAMS array. To obtain a more nearly accurate comparison of the towed array with the BMA, a subset OAMS array (configured similarly in sensor spacing to the BMA at Site 3) was studied. Neubert (1978b, c) shows that this subset towed array performed essentially the same as the bottom-mounted array with regard to phase coherence and array signal gain behavior. Incidentally, figures Nc-6, Nc-7, and Nc-35 show that the unweighted total and subset OAMS arrays are similar in ASG rangewise performance, while the weighted OAMS array slightly outperforms both these cases.

VII.5 (U) DISCUSSION OF SITE 4

VII.5.1 (U) OAMS Array Phase Coherence and Array Signal Gain

(C) The OAMS phase coherence data analysis for Site 4 is summarized by Neubert (1978a) in tables Na-13 through Na-20 and in figures Na-38 through Na-41 for 25, 36, and 140 Hz. The OAMS array signal gain data analysis for Site 4 is summarized by Neubert (1978c) in tables Nc-5 through Nc-7 and in figures Nc-10 through Nc-15 for 25 and 36 Hz. The OAMS array phase coherence and array signal gain data were taken on three projector tows in the Somali Basin: 4P1, 4P3, and 4P5. The relevant figures and tables of Neubert (1978a) show that the phase coherence decreases severely as the frequency increases from 25 to 140 Hz, while the SNR values remain comparable and high. This is similar to the behavior for Sites 1B and 3 and the explanation is given in section VII.3.1. Figures 11 and 12 show that the phase coherence and the array signal gain are generally range independent up to about 150 km on projector tow 4P1 at 25 Hz. Note the wide variability of C_p and ASG with range due to multipath interference. Comparing figures 5, 6, 11, and 12 shows that the phase coherence and the array signal gain are less variable on projector tow 4P1 than on projector tow 3P4. This behavior reflects the fact that Site 3 is bottom limited while Site 4 is not. Figures 13 and 14 show that the phase coherence and the array signal gain are apparently range independent on projector tow 4P5 at 36 Hz up to about 250 km. This decrease in space coherence and array signal gain corresponds to the passage of the source over an irregular sloping bottom. Because there is no significant decrease in SNR values during the tow over the irregular sloping bottom, the decrease in phase coherence and array signal gain appears to be caused by the irregularity of

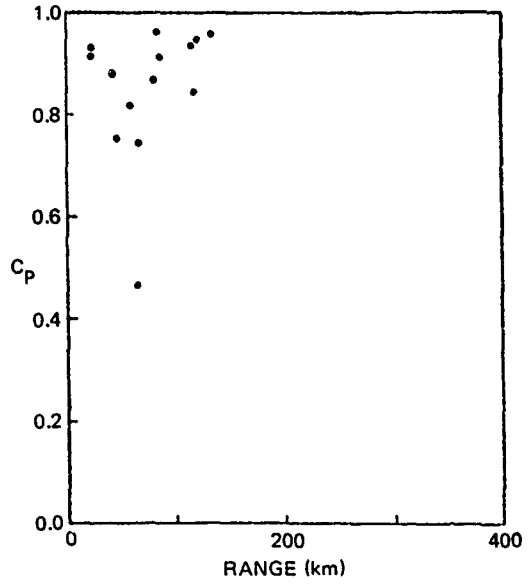

Figure VII-11. (C) Phase coherence as a function of range; OAMS array; Site 4; track 4P1; 13 March 1977; 25 Hz. (C)

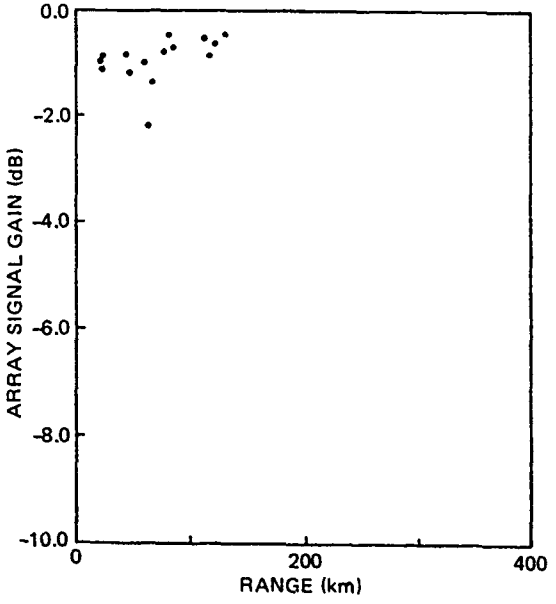

Figure VII-12. (C) Array gain vs range, calculations with unity weights. OAMS array; Site 4; track 4P1; 13 March 1977; 25 Hz. (C)

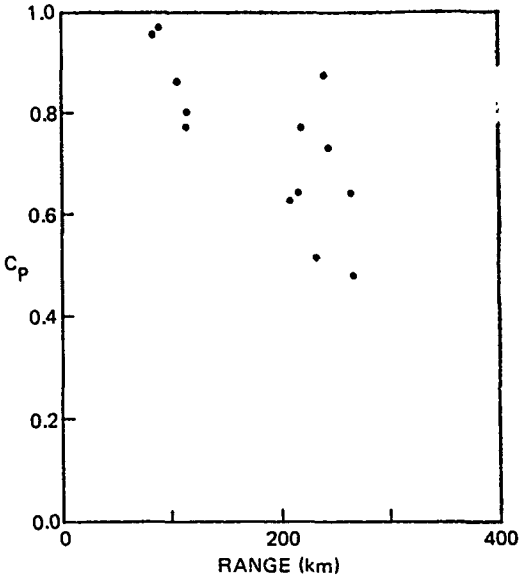

Figure VII-13. (C) Phase coherence as a function of range, OAMS array; Site 4; track 4P5; 18-19 March 1977; 36 Hz. (C)

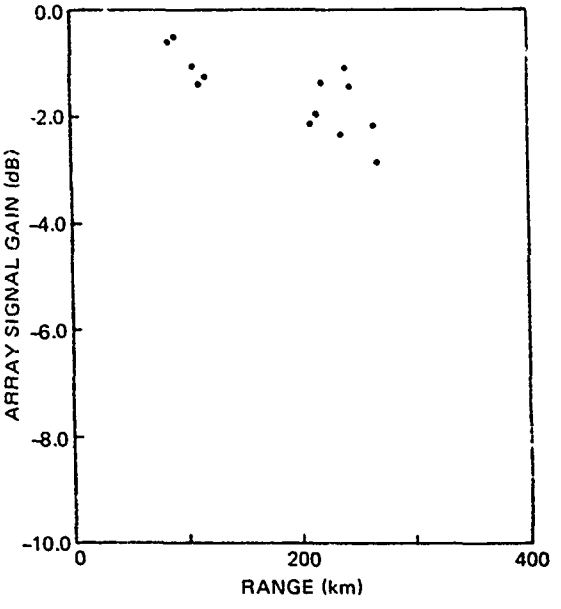

Figure VII-14. (C) Array signal gain vs range, calculations with unity weights. OAMS array; Site 4; track 4P5; 18-19 March 1977; 36 Hz. (C)

the bottom slope region. This behavior also occurred on 1BP1 and is discussed in section VII.3.1. Figures Na-39 and Nc-13 show the C_p and ASG values, respectively, for the arc tow 4P3 at 25 Hz. Here the low values occur at low SNR values and there appears to be no bearing dependence in C_p and ASG. Figures Nc-10 through Nc-14 show that the values of ASG are somewhat better for the weighted OAMS array than for the unweighted arrays. This was also observed in sections VII.3.1 and VII.4.1. Unfortunately, much interesting OAMS coherence data was lost on 17 and 18 March 1977 because the source frequency went to 39 Hz rather than the planned frequency of 36 Hz. (The quadrature detector had not been built to handle 39 Hz.)

VII.5.2 (U) LATA Phase Coherence and Array Signal Gain

(C) The LATA phase coherence data analysis for Site 4 is summarized by Fabula and Neubert (1978) in tables F-2 through F-4 and in figures F-17, F-21, and F-25 for 25 Hz. The LATA array signal gain data analysis for Site 4 is summarized by Neubert in tables Nc-2 through Nc-4 and in figures Nc-17, Nc-21 and Nc-25 for 25 Hz. The LATA array signal gain data analysis for Site 4 was taken on three projector tows in the Somali Basin: 4P1, 4P2, and 4P3. Only the results for projector tows 4P2 and 4P3 are essentially the same. Figures 15 and 16 show that both the phase coherence and the array signal gain are generally range independent up to about 200 km, but both vary greatly because of multipath interference and the sound speed profile small-scale structure discussed by Neubert (1978d).

VII.5.3 (U) Comparison of the LATA and the OAMS Array

(C) Figures 11, 12, 15, and 16 give the relative phase coherence behavior and the relative array signal gain behavior on the projector tow 4P1 of the OAMS array (with the source bearing near 90^0) and of the LATA (with source bearing varying from 30^0 to 180^0) as a function of range at 25 Hz. As can be seen from these figures, the OAMS phase coherence and array signal gain were higher and far less variable than for the LATA. As discussed by Neubert (1978d), this difference in behavior is attributed to the operation of the OAMS array at 200 m, which is above the complex sound speed profile structure that occurs below about 250 m, and of the LATA at 300 m, which is definitely in the more complex profile structure.

VII.6 (U) DISCUSSION OF SITE 5

VII.6.1 (U) OAMS Array Phase Coherence and Array Signal Gain

(C) The OAMS array phase coherence data analysis for Site 5 is summarized by Neubert (1978a) in tables Na-21 through Na-25 and in figures Na-48 through Na-52 for 25, 36, 140, and 290 Hz. The OAMS array signal gain data analysis for Site 5 is summarized by Neubert (1978c) in tables Nc-8 through Nc-10 and in figures Nc-16 through Nc-21 for 25 and 36 Hz. The OAMS array phase coherence and array signal gain data were taken on three projector tows over the Indus Fan and the Carlsberg Ridge: 5P1, 5P3, and 5P5. Only the results for projector tow 5P1 will be considered here since the SNR values on the other projector tows were generally low. The relevant figures and tables of Neubert (1978a) show that the phase coherence decreases severely as the frequency increases from 25 to 140 Hz, while the SNR values remain comparable and high.

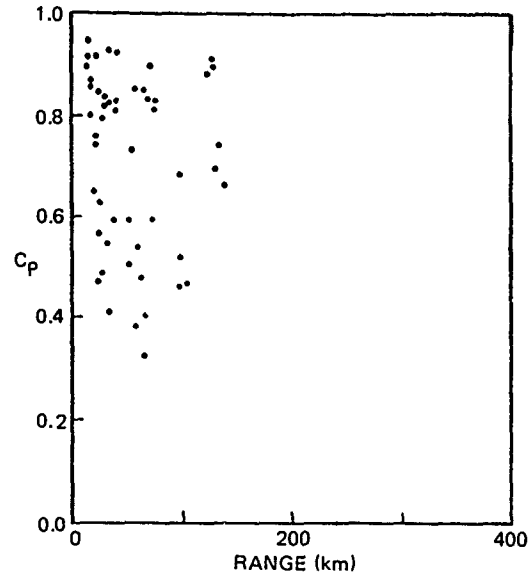

Figure VII-15. (C) Phase coherence vs range; LATA array; Site 4; track 4P1, 13-14 March 1977; 25 Hz. (C)

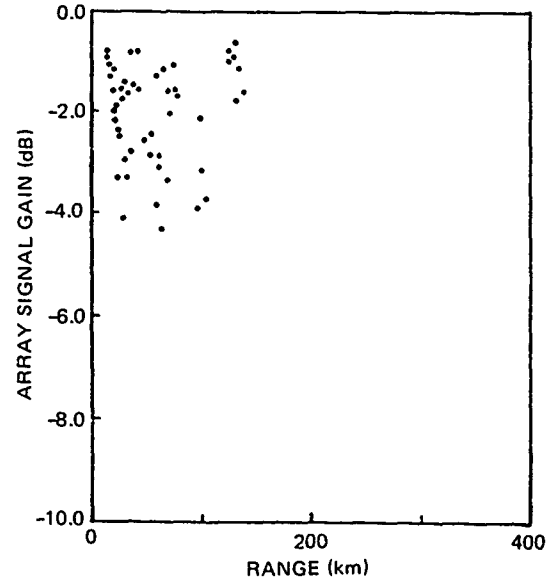

Figure VII-16. (C) Array signal gain vs range calculations with unity weights. LATA array; Site 4; track 4P1; 13-14 March 1977; 25 Hz. (C)

This is similar to the behavior for Sites 1B, 3 and 4, and the explanation is given in section VII.3.1. Figures 17 and 18 show that the phase coherence and the array signal gain are generally range independent up to about 750 km. Note again the wide variability in C_p and ASG with range due to multipath interference. Comparing figures 11, 12, 17, and 18 shows that the phase coherence and the array signal gain are less variable on projector tow 4P1 than on projector tow 5P1. This behavior reflects the fact that the data for the bottom-limited Site 5 are more variable than the data for Site 4, which is not bottom limited. Figures Nc-16 and Nc-17 show that the values of ASG are somewhat better for the weighted OAMS array than for the unweighted array.

VII.6.2 (U) LATA Phase Coherence and Array Signal Gain

(C) The LATA phase coherence data analysis for Site 5 is summarized by Fabula and Neubert (1978) in table F-3 and in figure F-29 for 25 Hz. The LATA array signal gain data analysis for Site 5 is summarized by Neubert (1978c) in table Nc-26 and figure Nc-40 for 25 Hz. Nothing will be said about the LATA results at Site 5 since few LATA data were processed for Site 5 (because of time constraints).

VII.7 (U) DISCUSSION OF SITE 2

VII.7.1 (U) OAMS Array Phase Coherence and Array Signal Gain

(C) The OAMS array phase coherence data analysis for Site 2 is summarized by Neubert (1978a) in tables Na-26 through Na-31 and in figures Na-63 through Na-68 for 25 and 140 Hz. The OAMS array signal gain data analysis for Site 2 is summarized by Neubert (1978c) in tables Nc-11 through Nc-13 and in figures Nc-22 through Nc-27 for 25 Hz. The OAMS array phase coherence and array signal gain data were taken on three projector tows over the Indus Fan: 2P2, 2P3A, and 2P3. Unfortunately, all the OAMS array tows for Site 2 were conducted behind an elongated seamount. Neubert (1978d) discusses the consequences of the presence of a seamount near Site 2. Figures 19 and 20 show that the phase coherence and the array signal gain were generally range independent up to about 1000 km but were somewhat reduced and much more variable on projector tow 2P3A (seamount) than in the comparable case of projector tow 5P1 (no seamount) shown in figures 17 and 18. Tables Na-21 and Na-28A show that the SNR values were about an average of 5 dB higher and less variable at similar ranges for projector tow 5P1 than for projector tow 2P3A. In short, given conditions which are otherwise identical (i.e., same range and source strength), the seamount produces perturbations in the measurements of phase coherence and array signal gain that would otherwise not have appeared. This situation seems to account for the reduced SNR values for Site 2.

VII.7.2 (U) LATA Phase Coherence and Array Signal Gain

(C) The LATA phase coherence data analysis for Site 2 is summarized by Fabula and Neubert (1978) in tables F-6 and F-7 and in figures F-33 and F-34 for 25 Hz. The LATA array signal gain analysis for Site 2 is summarized by Neubert (1978c) in tables Nc-27 and Nc-28 and in figures Nc-41 and Nc-42 for 25 Hz. The LATA phase coherence and array signal gain analysis data were taken on two projector tows over the Indus Fan: 2P3A and 2P3. The results for these two tows were very similar. Figures 21 and 22 show that both the

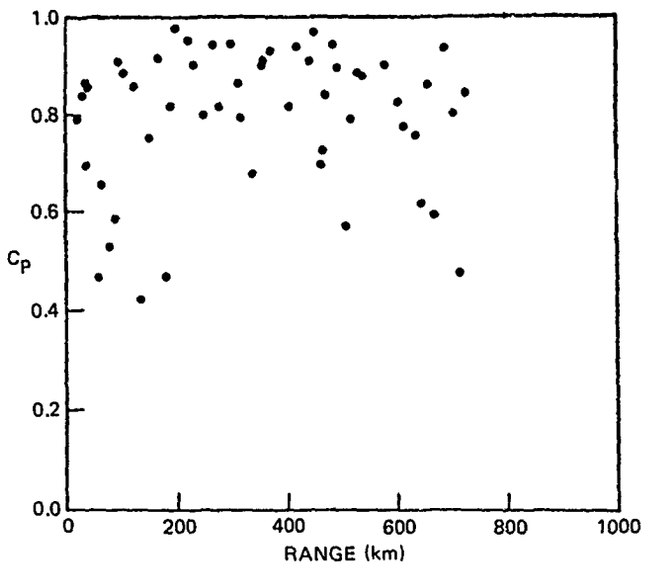

Figure VII-17. (C) Phase coherence as a function of range; OAMS array; Site 5; track 5P1; 12-14 April 1977; 25 Hz. (C)

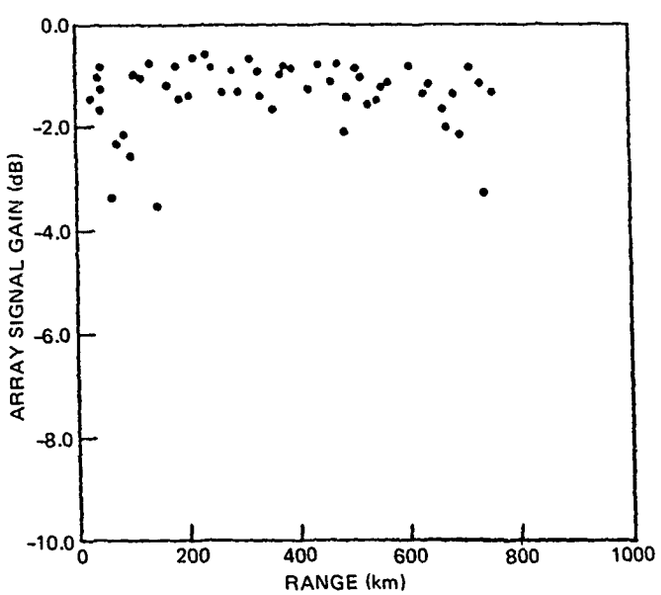

Figure VII-18. (C) Array signal gain vs range, calculations with unity weights. OAMS array; Site 5; track 5P1; 12-14 April 1977. (C)

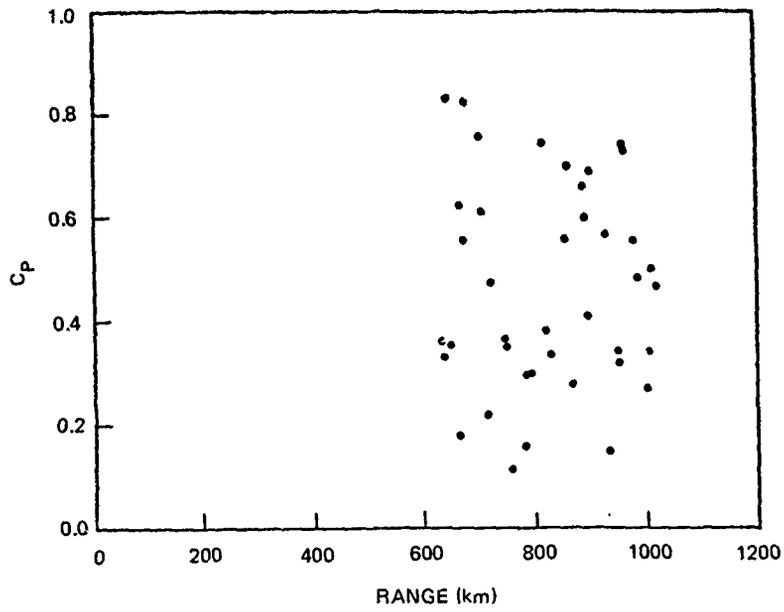

Figure VII-19. (C) Phase coherence as a function of range, OAMS array; Site 2, track 2P3; 27-28 April 1977; 25 Hz. (C)

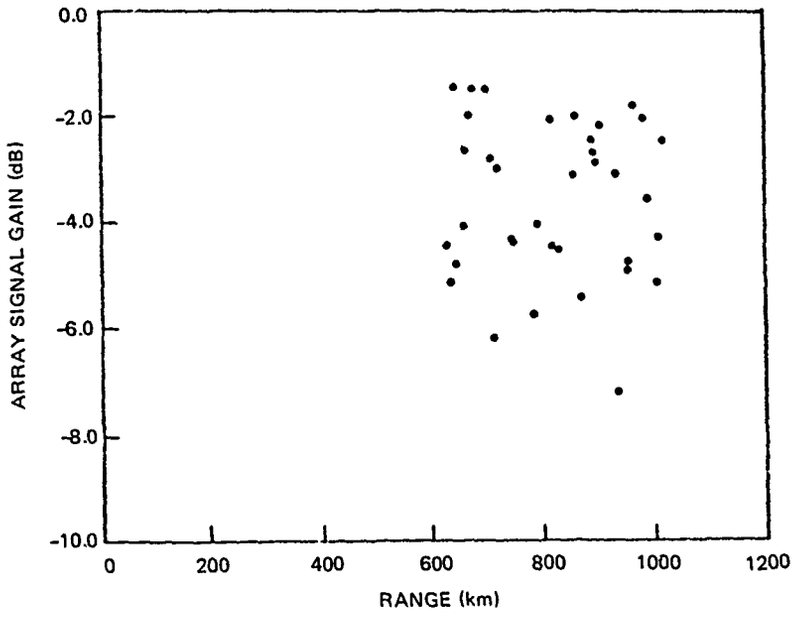

Figure VII-20. (C) Array signal gain vs range, calculations with unity weights. OAMS array, Site 2; track 2P3A; 27-28 April; 25 Hz. (C)

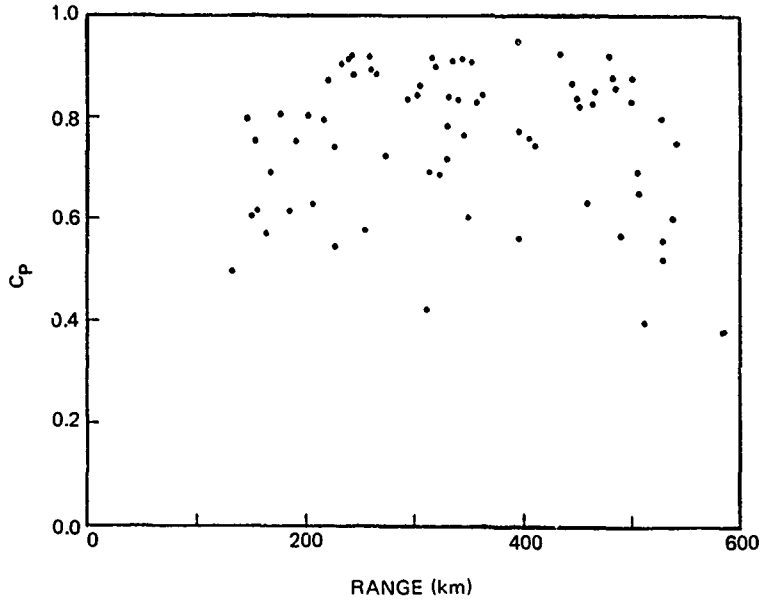

Figure VII-21. (C) Phase coherence vs range; LATA array; Site 2, track 2P3; 28-29 April 1977; 25 Hz. (C)

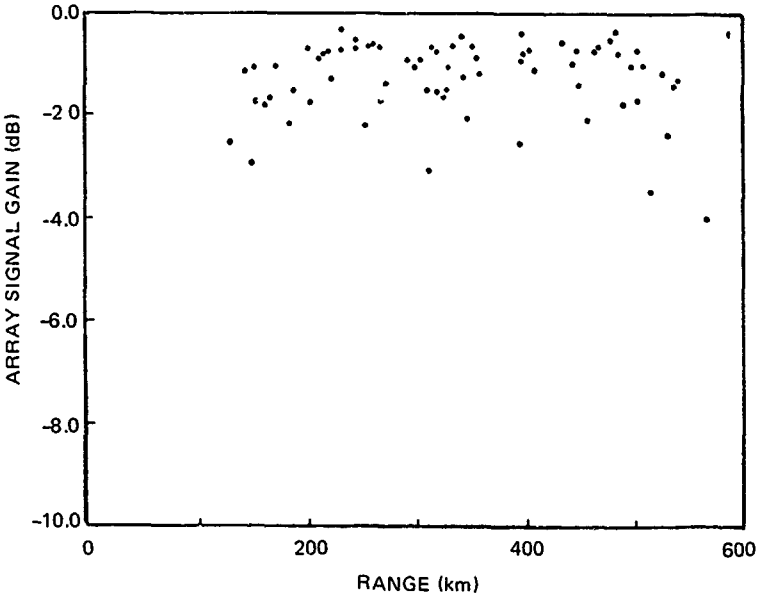

Figure VII-22. (C) Array signal gain vs range, calculations with unity weights. LATA array; Site 2; track 2P3; 28-29 April 1977; 25 Hz. (C)

phase coherence and the array signal gain are generally range independent up to about 550 km, but both vary greatly because of multipath interference and the small-scale sound speed profile structure discussed by Neubert (1978d). The source bearing varied from 10^0 to 150^0. Because of the influence of the seamount on the OAMS data, a useful comparison of the LATA and the OAMS array results at Site 2 cannot be made.

VII.8 (U) CONCLUSIONS

1. (C) Since the Northwest Indian Ocean is usually bottom limited and the sound speed profiles are complex, a considerable rangewise variability exists in the plots of phase coherence and array signal gain for this multipath environment. The variability increases because of the presence of irregular bottom slopes as well as seamounts. This variability is the dominant characteristic of this body of water when the performance of long horizontal acoustic arrays is considered. Thence, a general assessment of signal coherence for the Northwest Indian Ocean, based on the BEARING STAKE data, is as follows. The coherence will be a manageable problem for the performance of long bottom-mounted and mid-depth towed array systems used for surveillance if sufficient rangewise sampling is employed and the towed arrays are not operated in the depth region of complex sound speed profile structure.

2. (C) From the detailed area assessment above several conclusions can be reached about the performance of long horizontal acoustic arrays in the Northwest Indian Ocean.

3. (C) The degree of amplitude fluctuations, as measured by Σ_A, does not change much with frequency and is largely range independent up to about 1000 km even over irregular sloping bottoms.

4. (C) The phase coherence decreases severely with increasing frequency, even when the SNR values remain high enough that noise correlations are negligible. This behavior is discussed in section VII.3.1. Because the phase coherence decreases severely with increasing frequency, the array signal gain should also decrease markedly with frequency increases; see appendix.

5. (C) The phase coherence and the array signal gain are generally range independent up to about 1000 km except when the projector is passing over an irregular sloping bottom. They decrease and become more variable for a mid-depth towed array, but not for a bottom-mounted array, when the projector is passing over an irregular sloping bottom. This behavior may reflect the importance of bottom-propagated sound paths for a bottom-mounted array.

6. (C) The phase coherence and the array signal gain are widely variable with range because of multipath interference and become more variable in an irregular bottom slope region for a mid-depth towed array, but not for a bottom-mounted array. They were less variable at the only site (Site 4) at which propagation was not bottom limited.

7. (C) The relative phase coherence behavior and the relative array signal gain behavior of a mid-depth towed array and of a bottom-mounted array were compared on projector tows 1BP1 (in section VII.3.3) and 3P1 (in section VII.3.4) at 25 Hz. The performances of the bottom-mounted array (at about 20^0

off endfire) and the mid-depth towed array (near broadside) were comparable, and neither array showed a rangewise reduction in phase coherence and in array signal gain (except in the irregular bottom slope region on projector tow 1BP1). Therefore, it appears that for the bottom-limited regions of the Northwest Indian Ocean the phase coherence and the array signal gain behavior of the bottom-mounted and mid-depth (above about 250 m) towed arrays are essentially the same.

8. (C) It was observed that the sensor spacing configuration for the BMA at Sites 1B and 3 was considerably different from the OAMS array sensor group spacing. To obtain a more accurate comparison of the towed array with the BMA, subset OAMS arrays (configured similarly in sensor spacing to the BMA at Sites 1B and 3) were studied. It was found that the bottom-mounted arrays performed essentially the same as the subset towed arrays and that again no array showed any rangewise reduction in phase coherence and array signal gain (except in the irregular bottom slope region on projector tow 1BP1). The subset OAMS arrays performed essentially the same as the total OAMS array for phase coherence and array signal gain.

9. (C) There is no significant difference in phase coherence or in array signal gain behavior between the bottom-limited regions near Sites 1B and 3, while the Site 4 region (which is not bottom limited) evinced less variable behavior.

10. (C) In the Northwest Indian Ocean, the surveillance performance of towed arrays may be significantly dependent on the array tow depths because of the presence of a mid-depth region of sound speed profile complexity.

11. (C) When sound was received by the OAMS array from a source towed behind a seamount for Site 2, the SNR was often too low to allow estimation of phase coherence and array signal gain.

REFERENCES (U)

A. G. Fabula and J. A. Neubert (1978). "BEARING STAKE Data Analysis: LATA (U)," NOSC TN 589, November. (CONFIDENTIAL)

J. A. Neubert (1978a). "BEARING STAKE Coherence Data Analysis: Part I. The OAMS Array (U)," NOSC TN 380, 6 February. (CONFIDENTIAL)

J. A. Neubert (1978b). "BEARING STAKE Coherence Data Analysis: Bottom-Mounted Array (U)," NOSC TN 452, 31 May. (CONFIDENTIAL)

J. A. Neubert (1978c). "BEARING STAKE Array Signal Gain Data Analysis (U)," NOSC TN 624, December. (CONFIDENTIAL)

J. A. Neubert (1978d). "BEARING STAKE Coherence and Array Signal Gain Area Assessment Report (U)" NOSC TR 383, December. (CONFIDENTIAL)

APPENDIX:
METHODOLOGY OF COHERENCE AND ARRAY SIGNAL GAIN (U)

A.1 (U) INTRODUCTION

(C) Coherence measurements were conducted during BEARING STAKE because signal plus noise coherence gives a quantitative measure of array performance under a variety of oceanographic conditions when the SX/R is sufficiently high. This permits the evaluation and direct comparison of passive surveillance systems under varying test conditions. In particular, in comparing the fixed horizontal bottom-mounted array with the towed horizontal mid-depth arrays in the Northwest Indian Ocean environment, the coherence along each array yields performance as a function of frequency and of range from the towed source as it travels over a varying ocean bottom. The array with the largest coherence (normalized to have a maximum of unity) will give the better signal input to the beamformer at the given frequency. A plane wave (i.e., a unidirectional received signal), homogeneous in amplitude along a straight horizontal array, is assumed in the design of conventional beamformers. Therefore, the coherence along the array can be used as a measure of beamformer performance degradation due to nonplanar, nonhomogeneous signals and/or array deformation. The phase coherence and array signal gain measure the degradation in beam directivity as a function of range and frequency while the amplitude nonhomogeneity relates to the degradation in the expected sidelobe suppression. Thus, the measurement of phase coherence and array signal gain gives the relative merits of arrays. Since the array with the largest coherence (when the aperture size is comparable and the frequency is the same) provides the best mean signal plus noise input to a conventional beamformer, it represents the best detection performance capabilities under the prevailing conditions. Likewise, the largest array signal gain yields the best output for a conventional beamformer.

(U) This report is concerned with the study of phase coherence and array signal gain for long, horizontal line arrays receiving multipath signals from long range, narrowband, low-frequency towed CW projectors in the generally bottom-limited Northwest Indian Ocean. Narrowband analysis techniques permit the understanding and quantification of fundamental signal data that significantly affect realizable system performance. Therefore, they provide a valuable method for evaluating and comparing passive surveillance array systems. The phase coherence permits relating the array signal data to the reduction in the actual array performance from that expected for an ideal array in an ideal (vertically variable only) medium. Considering array signal gain directly relates actual performance to that expected for a conventional linear beamformer under ideal conditions.

A.2 (U) PHASE COHERENCE

(U) The narrowband, multipath signal plus noise arriving at the j^{th} sensor group along the long horizontal array at time t can be described by the relation $A_j \cos(\phi_j - \omega t)$, where A_j is the amplitude, ϕ_j is the received phase, and ω is the angular frequency. (The quantities A_j, ϕ_j, and ω are all real.) It is assumed, when using the above signal plus noise form, that the slowly varying functions A_j and ϕ_j can be considered constant for time

periods less than $20\pi/\omega$. The classical definition for the coherence of two complex waveforms F_1 and F_2 is

$$\left(\gamma_{12}^{c}\right)^2 \equiv \frac{|\langle F_1 F_2^* \rangle|^2}{\langle F_1 F_1^* \rangle \langle F_2 F_2^* \rangle} \leq 1 \quad , \tag{A-1}$$

where the operator $\langle \cdot \rangle$ represents the time average (generally over about 4 min for BEARING STAKE data) and the asterisk denotes the complex conjugate. For convenience in narrowband sonar array analysis, the classical coherence approach is modified as follows. The composite (due to multipath arrivals) instantaneous, narrowband response of the j^{th} sensor group can be represented (after basebanding by a quadrature detector) by

$$F_j = A_j e^{i[\phi_j - (\omega - \omega_o)t]} \quad , \tag{A-2}$$

where ω_o is the angular frequency at the center of the frequency bin. To determine the bearing $\bar{\Phi}$ of the source of interest the appropriate peak $B(\Phi)$ of the phase-only linear beamformer output,

$$B(\Phi) \equiv \frac{1}{J^2} \sum_{j=1}^{J} \sum_{\ell=1}^{J} \langle \cos[(\phi_j - \phi_\ell) - k_o(d_j - d_\ell)\cos\Phi] \rangle \leq 1 \tag{A-3}$$

is found, where k_o is the wavenumber, J is the total number of sensor groups in the array, and d_j is the distance from the center of the first sensor group to the center of the j^{th} sensor group ($d_1=0$). $\bar{\Phi}$ is chosen to be zero for a forward endfire arrival. Then the "steered phase"

$$\theta_j \equiv \phi_j - k_o d_j \cos\bar{\Phi} \tag{A-4}$$

is computed. (Note that $\phi_j = \phi_\ell$ for all $j \neq \ell$ with $j,\ell \epsilon [1,J]$ when a plane wave is received by a linear, horizontal array.) The signal plus noise, steered toward $\bar{\Phi}$, is obtained as

$$f_j \equiv A_j e^{i[\theta_j - (\omega - \omega_o)t]} = F_j e^{-ik_o d_j \cos\bar{\Phi} t} \tag{A-5}$$

It is assumed that the instantaneous amplitude can be written as

$$A_j = \langle A_j \rangle + \delta A_j \quad , \tag{A-6}$$

where δA_j is the amplitude fluctuation and $\langle A_j \rangle \neq \langle A_\ell \rangle$ for $j \neq \ell$ represents the amplitude variation nonhomogeneity. The term "fluctuation" denotes the rapid timewise changes that can be averaged out, leaving the slowly changing mean structure that is referred to as the "variation" of the physical parameter of interest.

(U) It is interesting to consider briefly the multipath decomposition of f_j. For M multipaths to sensor group j

$$A_j e^{i\phi_j} \equiv \sum_{m=1}^{M} a_{mj} e^{i\psi_{mj}} \quad , \tag{A-7}$$

where $\psi_{mj} \equiv k_o d_j \cos \Phi_m$, is a linear superposition so a linear beamformer treats each contributing path independently. Then

$$f_j = A_j e^{i[\theta_j - (\omega-\omega_o)t]} \equiv e^{-i(\omega-\omega_o)t} \sum_{m=1}^{M} a_{mj} e^{i\varphi_{mj}} \quad , \tag{A-8}$$

where $\varphi_{mj} \equiv k_o d_j(\cos \Phi_m - \cos \bar{\Phi})$. Define the beamformer output (before averaging and with weights W_j) as

$$\left| \sum_{j=1}^{J} W_j f_j \right|^2$$

$$= \sum_{j=1}^{J} \sum_{\ell=1}^{J} W_j W_\ell f_j f_\ell^*$$

$$= \sum_{j=1}^{J} \sum_{\ell=1}^{J} W_j W_\ell \, A_j A_\ell \cos(\theta_j - \theta_\ell)$$

$$= \sum_{m=1}^{M} \sum_{n=1}^{M} \sum_{j=1}^{J} \sum_{\ell=1}^{J} W_j \, a_{mj} \, W_\ell \, a_{n\ell} \cos(\phi_{mj} - \phi_{n\ell})$$

$$= \sum_{m=1}^{M} \sum_{j=1}^{J} \sum_{\ell=1}^{J} W_j \, a_{mj} \, W_\ell \, a_{m\ell} \cos(\phi_{mj} - \phi_{m\ell})$$

$$+ 2 \sum_{m=1}^{M-1} \sum_{n=m+1}^{M} \sum_{j=1}^{J} \sum_{\ell=1}^{J} W_j \, a_{mj} \, W_\ell \, a_{n\ell} \cos(\phi_{mj} - \phi_{n\ell}) \quad , \tag{A-9}$$

where the operator $|\cdot|^2$ represents the complex product and where the first term in eq (A-9) represents the same path contributions and gives a linear superposition of the formed beams. The second term in eq (A-9) represents the cross-path contributions, and unless the presence of many paths causes this term to average to zero, it will represent a distortion of the sidelobe structure (which becomes apparent when Φ is varied from $\bar{\Phi}$ through all its values).

(U) The classical coherence $(\gamma^c_{j\ell})^2$ between sensor groups j and ℓ could be synopsized by the coherence coefficient

$$C_c \equiv \frac{1}{J^2} \sum_{j=1}^{J} \sum_{\ell=1}^{J} (\gamma^c_{j\ell})^2 \quad . \tag{A-10}$$

However, $(\gamma^c_{j\ell})^2$ mixes the amplitude A_j and phase ϕ_j of the j^{th} sensor group signal plus noise F_j in a manner which is difficult to interpret in terms of the causes of the array performance degradation. Therefore, the phase and amplitude are separated by a quadrature detector and θ_j is found via eq (A-4) and $B(\bar{\Phi})$. Then the array coherence between the j^{th} and ℓ^{th} sensor groups is defined as

$$\gamma_{j\ell} \equiv \text{Re} \left\{ \frac{\langle f_j f^*_\ell \rangle}{\langle | f_j | \rangle \langle | f_\ell | \rangle} \right\} \tag{A-11}$$

$$= \frac{\langle A_j A_\ell \cos(\theta_j - \theta_\ell) \rangle}{\langle A_j \rangle \langle A_\ell \rangle} \tag{A-11a}$$

$$= \frac{\langle A_j A_\ell \rangle}{\langle A_j \rangle \langle A_\ell \rangle} \langle \cos(\theta_j - \theta_\ell) \rangle \tag{A-11b}$$

under the Talpey decorrelation assumption (see ref 17)

$$\langle A_j A_\ell \cos(\theta_j - \theta_\ell) \rangle = \langle A_j A_\ell \rangle \langle \cos(\theta_j - \theta_\ell) \rangle , \tag{A-12}$$

where $\langle A_j A_\ell \rangle$ is an element of the amplitude correlation matrix and $\langle \cos(\theta_j - \theta_\ell) \rangle$ is an element of the phase coherence matrix. Defining $\text{Re} \langle A_j A_\ell e^{i(\theta_j - \theta_\ell)} \rangle$ as the array coherence would have allowed the scatter of $\langle A_j A_\ell \rangle$ (due to $\langle A_j \rangle \neq \langle A_\ell \rangle$) to confuse the good quality of the coherence that is usually present. The Talpey decorrelation assumption that was applied in Eq. (A-11b) is not meant to imply that A_j and θ_j are statistically independent, but only that the quantities $A_j A_\ell$ and $\cos(\theta_j - \theta_\ell)$ are at most weakly correlated, so that eq (A-12) is just a good approximation. The Talpey decorrelation assumption was tested synoptically by the Talpey coefficient

$$C_T \equiv \frac{2}{J(J-1)} \sum_{j=1}^{J-1} \sum_{\ell=j+1}^{J} \frac{\langle A_j A_\ell \cos(\theta_j - \theta_\ell) \rangle}{\langle A_j A_\ell \rangle \langle \cos(\theta_j - \theta_\ell) \rangle} \tag{A-13}$$

and found to be generally justified (i.e., C_T is usually near unity).

(U) The output E of a standard processor (i.e., the beamformed, squared, and time-averaged output) can be written in the useful form (with the Talpey decorrelation assumption):

$$E = \sum_{j=1}^{J} \langle A_j^2 \rangle + 2 \sum_{j=1}^{J-1} \sum_{\ell=j+1}^{J} \langle A_j A_\ell \rangle \langle \cos(\theta_j - \theta_\ell) \rangle \quad . \tag{A-14}$$

The amplitude correlation matrix $[\langle A_j A_\ell \rangle]$ is related to the composite amplitude nonhomogeneity. The phase coherence matrix $[\langle \cos(\theta_j - \theta_\ell) \rangle]$ evinces the relative array distortion due to wavefront corrugation (i.e., nonplanar arrivals) and/or array deformation. The amplitude nonhomogeneity that results, through multipath addition, from a linear superposition of array signal plus noise cannot be decomposed through amplitude correlation techniques and, therefore, these techniques cannot be used to study their effects on the outputs of linear beamformers; they can only treat their effects on the outputs of arrays. (This applies to phase coherence but not to array signal gain; see below.) The components of the linear superposition of array signal plus noise are simply acted on individually by the beamformer as shown in eq (A-9). Therefore, neither the amplitude correlation matrix $[\langle A_j A_\ell \rangle]$ nor the normalized amplitude correlation matrix $[\langle A_j A_\ell \rangle / \langle A_j \rangle \langle A_\ell \rangle]$, nor the phase coherence matrix $[\langle \cos(\theta_j - \theta_\ell) \rangle]$ can predict the results at the output of a linear beamformer from their behavior at the output of the array sensor groups alone. Thus, the array signal gain will be considered later since it gives the results at the beamformer output.

(U) To facilitate treatment of the large coherence data base for BEARING STAKE, five synoptic measures of performance (in addition to C_T) have been devised. The degree of amplitude fluctuation due to correlated amplitude fluctuations can be synopsized by the normalized standard deviation Σ_A, which is defined as

$$\Sigma_A \equiv \sigma_A / \bar{A}_a \geq 0 \quad , \tag{A-15}$$

where

$$\sigma_A^2 \equiv \frac{1}{J} \sum_{j=1}^{J} \langle (A_j - \langle A_j \rangle)^2 \rangle \tag{A-15a}$$

$$= \frac{1}{J} \sum_{J=1}^{J} \langle (\delta A_j)^2 \rangle \tag{A-15b}$$

[when eq (A-6) is assumed] and

$$\bar{A}_a \equiv \frac{1}{J} \sum_{j=1}^{J} \langle A_j \rangle \quad . \tag{A-16}$$

Normalizing by A_a avoids changes in the propagation conditions from biasing the measure Σ_A. The smaller Σ_A is, the smaller the amount of amplitude fluctuation present. The degree of array nonhomogeneity (but not the degree of its sidelobe distorting influence) can be synopsized by the nonhomogeneity coefficient C_n which is defined as

$$C_n \equiv \frac{\sum_{j=1}^{J} \left| \langle A_j \rangle - \bar{A}_a \right|}{J\bar{A}_a} \geqslant 0 \qquad \text{(A-17)}$$

and equals zero for a homogeneous sound field.

(U) It is useful to synopsize an upper bound for the array coherence $\gamma_{j\ell}$ by means of eq (A-11b). First form for any, i.e., [1,J],

$$\frac{1}{J}\sum_{j=1}^{J} \frac{\langle A_i A_j \rangle}{\langle A_i \rangle \langle A_j \rangle} = 1 + \frac{1}{J}\sum_{j=1}^{J} \frac{\langle \delta A_i \delta A_j \rangle}{\langle A_i \rangle \langle A_j \rangle}$$

$$\approx 1 + \frac{\frac{1}{J}\sum_{j=1}^{J} \langle \delta A_i \delta A_j \rangle}{\bar{A}_a^2}$$

$$\lesssim 1 + \frac{\frac{1}{J}\sum_{j=1}^{J} \langle (\delta A_j)^2 \rangle}{\bar{A}_a^2} = 1 + \frac{\sigma_A^2}{\bar{A}_a^2}$$

$$= 1 + \Sigma_A^2 \equiv C_\Sigma \qquad \text{(A-18)}$$

via eq (A-6), A(16), (A-15b), and (A-15) as well as

$$\sum_{j=1}^{J} \langle \delta A_i \delta A_j \rangle \leqslant \sum_{j=1}^{J} \langle (\delta A_j)^2 \rangle \ . \qquad \text{(A-19)}$$

Thus, C_Σ synopsizes the normalized amplitude matrix $[\langle A_i A_j \rangle / \langle A_i \rangle \langle A_j \rangle]$ of the array coherence matrix $[\gamma_{ij}]$. Next define the phase coherence coefficient C_p as

$$C_p \equiv \frac{1}{J^2}\sum_{j=1}^{J} \sum_{\ell=1}^{J} \langle \cos(\theta_j - \theta_\ell) \rangle \leqslant 1 \qquad \text{(A-20)}$$

$$= B(\bar{\Phi}) \tag{A-20a}$$

via eq (A-3) and (A-4). Thus, C_p synopsizes the phase coherence matrix $[\langle\cos(\theta_i-\theta_j)\rangle]$ and the array coherence coefficient C_γ,

$$C_\gamma \equiv C_\Sigma\, C_p \quad , \tag{A-21}$$

synopsizes the array coherence matrix $[\gamma_{ij}]$ in terms of Σ_A and C_p .

A.3 (U) ARRAY SIGNAL GAIN

(U) The array gain, ag, is by definition the ratio of the signal $\langle S^2\rangle$ to noise $\langle N^2\rangle$ power ratio of the array beamformer output to the signal $\langle s^2\rangle$ to noise $\langle n^2\rangle$ power ratio of a single element, i.e.,

$$ag \equiv \frac{\langle S^2\rangle/\langle N^2\rangle}{\langle s^2\rangle\,\langle n^2\rangle} \equiv \frac{asg}{\eta} \quad , \tag{A-22}$$

where

$$\eta \equiv \langle N^2\rangle/\langle n^2\rangle \tag{A-22a}$$

and

$$asg \equiv \langle S^2\rangle/\langle s^2\rangle \tag{A-23}$$

is the array signal gain, or, in decibel units,

$$ASG = 10 \log_{10} asg\,. \tag{A-24}$$

For a weighted (by W_j) array, the asg will be taken to be

$$asg \equiv \frac{\sum_{j=1}^{J}\sum_{\ell=1}^{J} W_j\, W_\ell\, \langle A_j A_\ell \cos(\theta_j-\theta_\ell)\rangle}{\left(\sum_{j=1}^{J} W_j \sum_{\ell=1}^{J} W_\ell\right)\frac{1}{J}\sum_{j=1}^{J}\langle A_j^2\rangle} \tag{A-25}$$

$$\xrightarrow[\substack{W_j,W_\ell \to 1\\ A_j,A_\ell \to \bar{A}_a}]{} C_p \quad . \tag{A-25a}$$

From eq (A-25a) it is seen that C_p can be interpreted as the array signal gain for a phase-only beamformer; see eq (A-3) and (A-20a). Note that the phase incoherence of $\langle\cos(\theta_j-\theta_\ell)\rangle$ and the amplitude nonhomogeneity reduce the ideal array signal gain of 0 dB to the actual array signal gain of eq (A-24). When the array amplitude response is ideal (i.e., $A_j = \bar{A}_a$ for all $j\epsilon[1,J]$), the ideal array signal gain is still directly reduced by the phase incoherence. When the array has perfect phase coherence, the ideal array signal gain is still reduced by the array amplitude nonhomogeneity and amplitude fluctuations. As expected, when the array response is both phase coherent and homogeneous (i.e., $\langle A_j\rangle = \bar{A}_a$), the ideal array signal gain occurs if the amplitude fluctuations are negligible, i.e., $A_j = \bar{A}_a$. The advantage of eq (A-25) (i.e., incorporating both phase coherence and amplitude homogeneity into an array signal gain expression) over giving quantities at the output of just the array (such as phase coherence) is that it gives the performance degradation for a conventional linear beamformer at its output.

CHAPTER VIII

ACOUSTIC REGIONAL ASSESSMENT (U)

by

Aubrey L. Anderson

Numerical Modeling Division, Code 320

Naval Ocean Research and Development Activity

NSTL Station, Mississippi 39529

CHAPTER VIII. ACOUSTIC REGIONAL ASSESSMENT (U)

Contents (U)

CHAPTER VIII. ACOUSTIC REGIONAL ASSESSMENT (U)

VIII.1 (U) INTRODUCTION

(U) This report, and this chapter, are stages in a hierarchy of ever more concise presentations of the results of analysis of environmental and ocean acoustic measurements obtained during the BEARING STAKE exercise. Chapter I includes an outline of the exercise. Chapters II through VII contain condensed statements of the major environmental and ocean acoustic observations which are presented in detail in individual, separate reports by the principal investigators (Fenner and Cronin, 1978; Hamilton and Bachman, 1979; Mitchell et al., 1979; Pedersen and Yee, 1979; Wagstaff and Aitkenhead, 1979; Neubert, 1978a, b,c,d; and Fabula and Neubert, 1978). This chapter represents a final stage of condensation and amalgamation of the material.

(U) The volume of data acquired during BEARING STAKE is prodigious. Fortunately, many generalized observations are possible and these are herein described. Much detail is obviously and necessarily omitted. For a more complete discussion of the results and analysis methods, the interested reader is referred to other chapters of this report, the references above, and their references in turn.

VIII.2 (U) GENERAL DESCRIPTION OF ENVIRONMENT

(C) The Indian Ocean, smallest of the three major subdivisions of the world ocean and bordered on four sides by the continents of Africa, Asia, Australia, and Antarctica, is primarily a southern ocean with over three-fourths of its 28,000,000 square miles of area located south of the equator (fig 1). That portion of the Indian Ocean north of the equator extends only to a north latitude of about 25 degrees and is divided into approximately equal-area eastern and western segments by the subcontinent of India. The Northeast Indian Ocean consists of the Bay of Bengal, which receives drainage from the Ganges River, and the Andaman Sea.

(C) The major portion of the Western Indian Ocean north of the equator, the region which is the subject of this report, is designated the Arabian Sea. This sea receives a major drainage input from India via the Indus River. The Gulf of Oman connects the Persian Gulf with the far northern border of the Arabian Sea while the Gulf of Aden is the water passage from the western boundary of the Arabian Sea to the Mediterranean Sea (via the Red Sea and Suez Canal).

(C) The physiographic features of the floor of the Northwest Indian Ocean (fig 2) invite classification into two general categories: moderately large, comparatively deep basins with essentially featureless floors; and shallower, topographically rugged ridges. The ridges, plus coastal features, bound and separate the basins. Three major basins are the Oman Basin, in the Gulf of Oman; the Arabian Basin (a term used here to denote the basin which is bounded by the four ridges: Carlsberg, Owen, Murray, and Laccadive-Chagos, and which contains the Arabian Fan); and the Somali Basin in the Southwest Arabian Sea. Although the floor of each of these basins is of the Abyssal Plain Province type (see chapter III) and each has a very thick unconsolidated sediment and sedimentary rock section overlying a basalt basement, closer examination

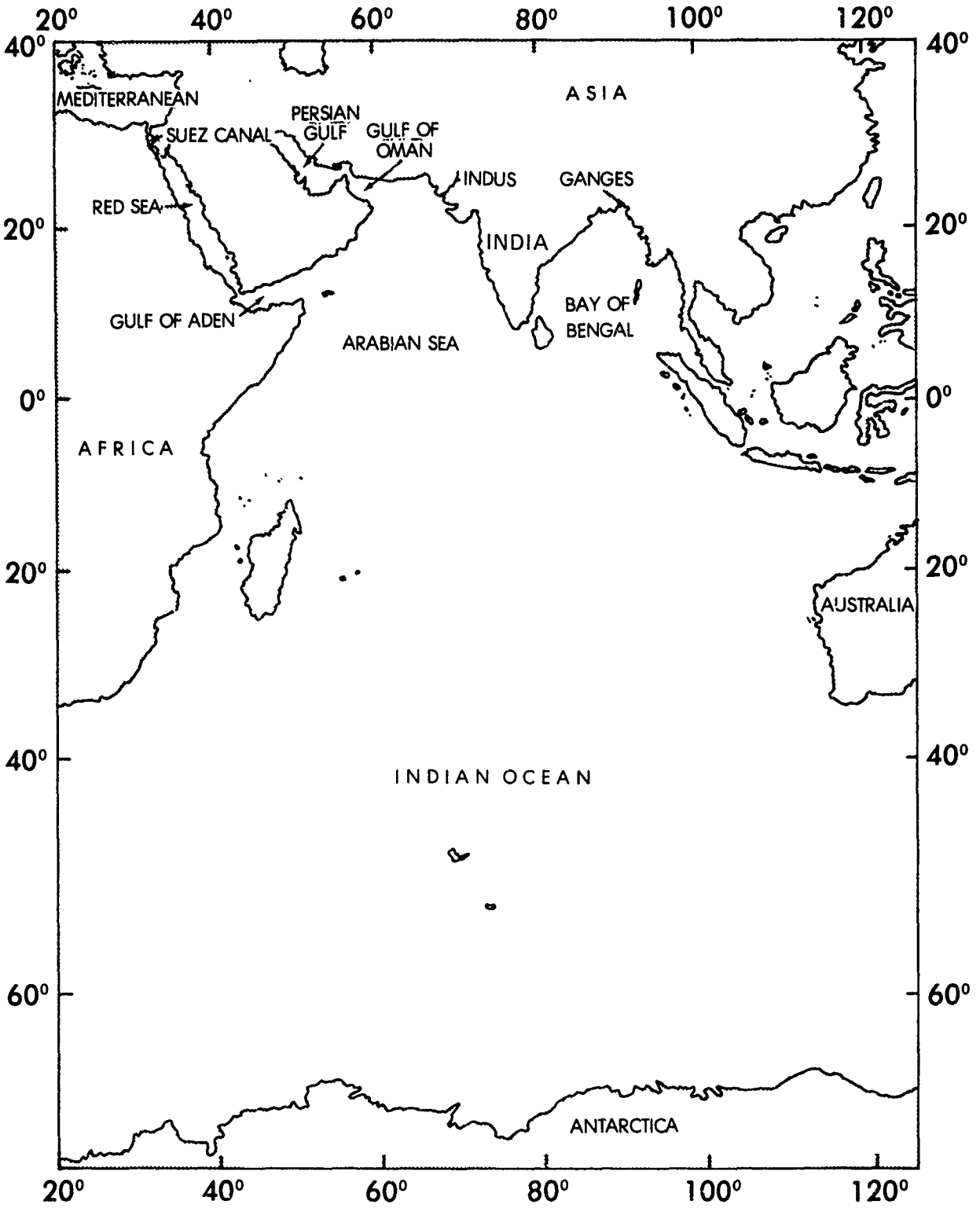

Figure VIII-1. (C) Map of the Indian Ocean. (C)

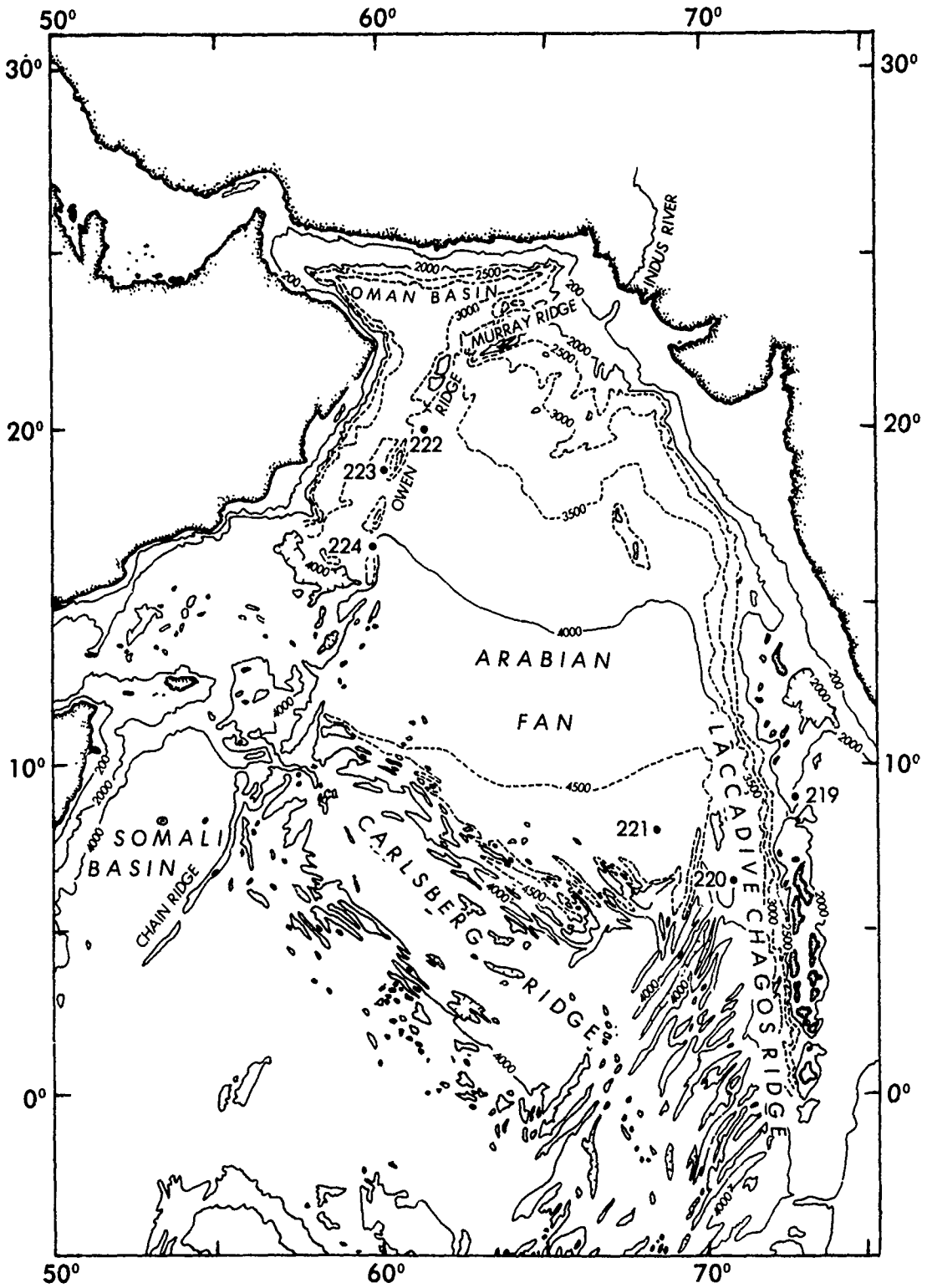

FIGURE VIII-2. (C) Physiographic features of the Northwest Indian Ocean. (C)

reveals unique features (chapter III). These will be discussed in later sections dealing with the individual basins.

(C) The near equatorial latitudes and input from surrounding water masses (chapter II) conspire to produce a unique sound speed versus depth profile type in the Northwest Indian Ocean. Figure 3 (repeated, in part, from chapter II) presents an overplot of representative sound speed profiles for each of the BEARING STAKE measurement sites. Generalities are immediately apparent. The warm surface waters produce high sound speeds at the ocean surface. Steep gradients of sound speed with depth away from the surface, together with a very deep sound channel axis (often on the order of 1800 m in this ocean region), conspire to produce a broad sound channel of very "open" aspect. Seafloor depths at the BEARING STAKE sites (fig 4), indicated on figure 3, together with the profile form, result in significant bottom-limiting (or depth deficiency) at all but Site 4. This is typical of the Northwest Indian Ocean, which at all seasons exhibits significant bottom-limiting throughout except for the northern portion of the Somali Basin, the location of Site 4, wherein small depth excess is present at times.

(C) Also notable from figure 3 is that the profiles from the three northernmost sites (1A/1B, 2, and 3) exhibit smooth sound speed decreases from the near-surface maximum to the sound channel axis while the profiles from the other two sites (4 in the Somali Basin and 5 at the southern end of the Arabian Basin) exhibit distinct subsurface channels in the upper part of the main sound channel (with sound speed minima at about 400-m depth). The Somali Basin profile exhibits more sound speed variability for depths between 400 m and about 1000 m.

VIII.3 (U) BASIN ACOUSTICS

(C) As discussed earlier and indicated in figure 4, the BEARING STAKE measurement sites and source tracks were for the most part in or on the edges of the three basins identified above in section VIII.2 (Oman, Arabian, and Somali). The major acoustic features of these basins, as revealed by the BEARING STAKE results, will be discussed below on a basin-by-basin basis. Material is drawn from chapters II through VII.

VIII.3.1 (C) The Oman Basin

(C) As shown in figure 4, the major portion of the Oman Basin is a plain somewhat exceeding 3 km in depth. The central basin floor is quite flat (fig II-5, II-6, and II-9), with an actual bottom depth of 3350 m. This abyssal plain is composed of a 1250-m layer of flat-lying turbidite sediments unconsolidated to a depth in the bottom on the order of 500 to 700 m (with a transition to sedimentary rock at this depth), underlain by additional sedimentary rock to the basement basalt at about 3340-m depth into the bottom (geoacoustic model 1a in appendix III-A). Figure 4 further shows that the floor of the Oman Basin surrounding the central abyssal plain consists of a gentle slope upward to the north and steeper slopes upward to the southeast and southwest. The geological nature of the sloping regions leading up out of the central Oman Basin is described in chapter III. Only a connected basin south-southwest of the Oman (west of the Owen Ridge) remains deep out to significant horizontal ranges from the central Oman Basin (see bathymetric cross-section in fig II-6).

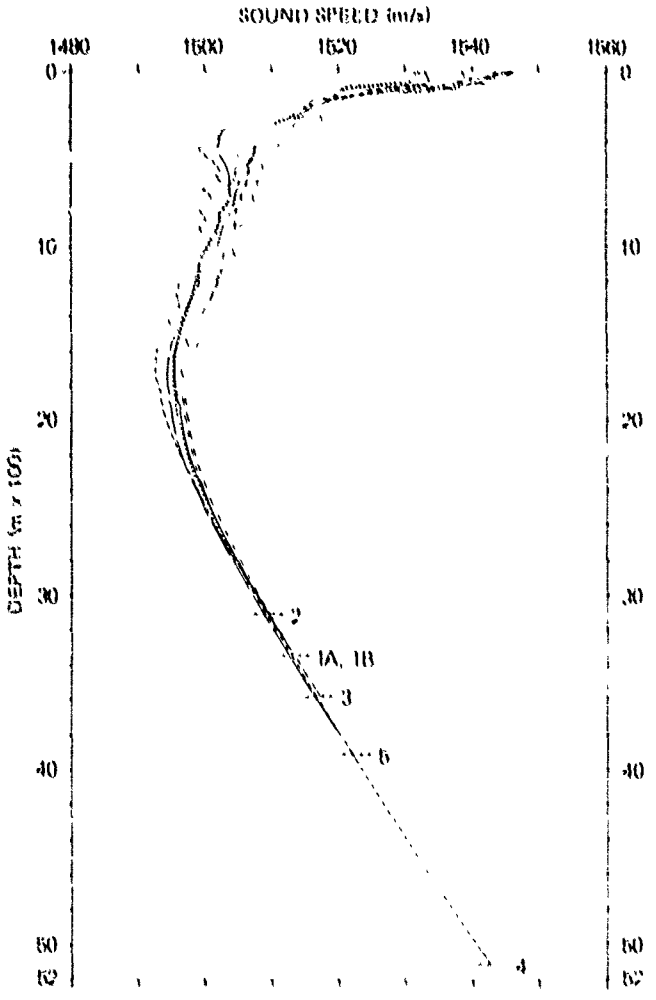

Figure VIII-3. (C) Representative sound speed profiles for each BEARING STAKE site. (U)

(C) The geoacoustic model (tabulation of sediment layer physical properties pertinent to acoustics of the bottom) for the central Oman Basin, developed in chapter III, was presented (as modified by comparison with acoustic measurements) in table IV-3 of chapter IV. Bottom loss data for the central Oman Basin are also presented in chapter IV and will be repeated in section VIII.4 of the present chapter. In this basin, as in all three basins to be described, the bottom loss is low - a result of the return to the water, without significant loss, of most of the acoustic energy which impinges on and penetrates into the seafloor. The strong gradients of sound speed (speed increasing with depth into the sediment) produce strong upward refraction and return the bottom penetrating energy to the water column along short ray arcs in the bottom. These short ray paths together with low absorption in the unconsolidated sediment (chapter IV) remove only a small portion of the energy

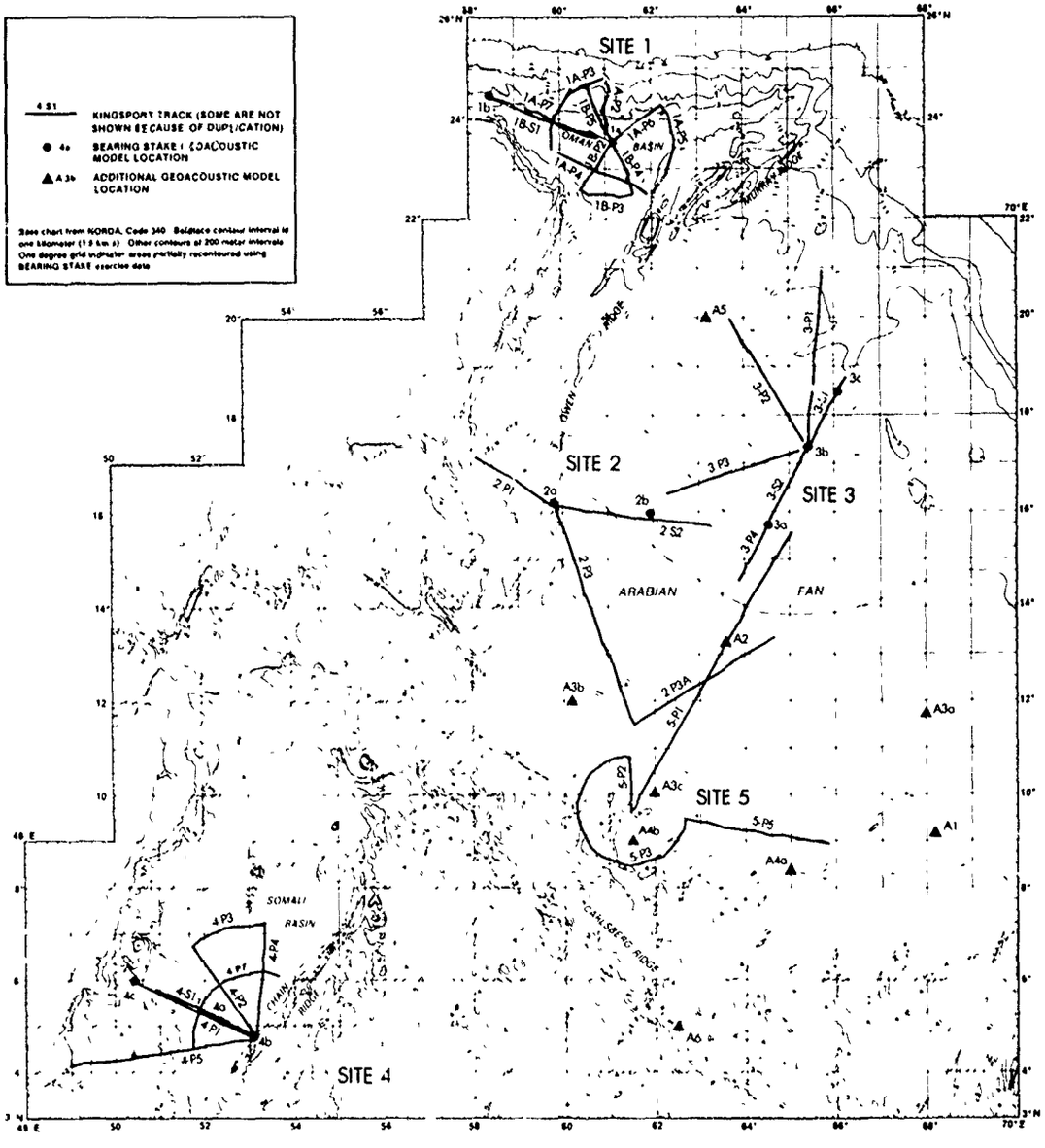

Figure VIII-4. (C) BEARING STAKE sites and source tracks. (U)

for each interaction of the waterborne acoustic wave with the seafloor. Deeper penetration of the ray paths causes increasing bottom loss with increasing bottom grazing angle up to a limit described by the Rayleigh reflection coefficient at steep angles. Bottom loss values in the Oman Basin are intermediate between those for the lower loss Arabian Basin and those for the Somali Basin (section VIII.4).

(C) In the Northwest Indian Ocean, signal propagation, as expressed by propagation loss, exhibits two immediately apparent, distinctive characteristics: large variability over relatively short range intervals with no evidence for the usual convergence zone structure (except for some situations in the Somali Basin - discussed later) and generally low average propagation loss values out to long ranges (figure V-1 of chapter V). These are both consequences of the extremely bottom-limited propagation conditions and low bottom losses — factors which conspire to retain the acoustic energy in the propagating wave to long ranges but to redistribute the energy out of the tightly bound (for shallow sources) and periodically focusing ray bundles of convergence-zone-producing energy into a large number of mutually interfering multipaths.

(C) The range-variable but low-average-loss propagation characteristics described above are characteristic features of the propagation loss data acquired in the Oman Basin during BEARING STAKE in late January (Site 1A) and late February (Site 1B) 1977. Such data are suitable for presentation and comparison in range averaged form and such averaging was done with the propagation data as described in section V.1.2. The two closely spaced, separately occupied fixed receiver sites were surrounded by source tracks (figs II-3 and II-7) to produce a good azimuthal description of propagation loss for the central Oman Basin. In addition to the bottom array (BMA) data, availability of results from the second occupation (Site 1B) for the vertically distributed ACODAC and the horizontal towed OAMS array allows description of receiver depth dependence of propagation loss and ambient noise, horizontal directionality of ambient noise, and a comparison of phase coherence for a bottomed and shallow towed array in the Oman Basin.

(C) As discussed in chapter V, except for depths near either the ocean surface or bottom, the receiver depth dependence of propagation loss in the central Oman Basin is quite small (within an envelope perhaps 2 dB wide). Receivers near the surface (within about two acoustic wavelengths) theoretically would suffer significantly increased loss because of surface decoupling (not demonstrated in the data because no receivers were this shallow). At some frequency- and source-depth-dependent receiver height off the bottom, a similarly phased interference between multipaths would, theoretically, produce a "notch," or maximum of propagation loss. Losses in the notch would be 2 or 3 dB higher than the nearly depth-independent propagation losses for shallower receivers (or indeed for a receiver on the bottom). Presence of such a notch was only partially supported by the BEARING STAKE data. Because the height of the notch off the bottom would be source-depth-dependent, heights could be selected to improve signal-to-noise ratios for sources of interest which were at different depths from the noise sources. The value of this procedure is somewhat reduced by the frequency dependence of notch height off the bottom (see chapter V for a discussion).

(C) Figures V-6A through V-6C illustrate the measured propagation loss for all source events at the three frequencies of 25, 140, and 290 Hz. These demonstrate the low losses observed in this basin as long as the source track is over the abyssal plain and does not pass over a seamount. For example, at 200 km, 50-km averaged propagation loss values range from about 84 to 87 dB at 25 Hz, 85 to 91 dB at 140 Hz, and 82 to 94 dB at 290 Hz. Shortest ranges to sources exhibiting significant increases in propagation loss were observed for tracks to the north from BEARING STAKE Sites 1A and 1B. This is probably because such tracks depart from the abyssal plain and pass over the surrounding sloping region at shortest ranges. The bottom loss on these rough slopes is apparently higher than that on the plain with its thick cover of refracting, low-loss, unconsolidated sediment. Best propagation conditions, and thus best coverage from a propagation loss perspective, for a receiver in the central Oman Basin are for source tracks northwest from the site (into the Gulf of Oman toward the passage to the Persian Gulf). Propagation loss is only slightly higher for tracks to the south from the central Oman Basin. For reference purposes the best (lowest loss) propagation curves for all three frequencies and both occupations of Site 1 (1A and 1B) are shown in figure 5 (repeated from chapter V) in comparison with the familiar Eleuthera reference curve.

(C) Both the low propagation loss and high density of nearby ships (figure VI-2) contribute to high ambient noise levels observed in the Oman Basin. Omnidirectional data measured with the ACODAC at Site 1B, shown in figure VI-5, indicate that the ambient noise varies only 2 dB for depths from 498 m to the ocean floor (3350 m), with noise level increasing with depth. This near independence of depth for the noise level is consistent with both the nearby location of sources (chapter VI) and the lack of depth dependence of the propagation loss (chapter V). The low frequency horizontal directional ambient noise exhibits an 8-to-10 dB anisotropy with maximum noise arriving from the East and West (see fig VI-7 and VI-8).

(C) In Chapter VII, data in figures VII-7 through VII-10 show that both phase coherence and array signal gain exhibit large fluctuation for both the OAMS (towed at 198 m) array and the BMA (bottom) array in the Oman Basin. The fluctuation of these parameters, for these two arrays, was similar at short ranges and remained about the same for the BMA at all ranges. However, the array towed at 198 m experienced significantly increased variations in both phase coherence and array signal gain for source to receiver ranges beyond about 200 km. These data are for the 1BP1 source event, and, for this track, the sources were passing over a sloping bottom region for source-to-OAMS-receiver ranges beyond 200 km (see the bathymetric profile in fig II-9). It is believed that the increased fluctuation of these parameters is due to the movement of the sources off the abyssal plain and over the bordering slope. Note that this reduction in potential array performance occurred only for the towed array and not for the bottom array.

VIII.3.2 (C) The Arabian Basin

(C) As shown in figure 4, the Arabian Basin is the largest basin in the Northwest Indian Ocean, is bounded by the Indian subcontinent and by ridges (Carlsberg to the south, Owen to the west, Murray to the north, and Laccadive-Chagos to the east), and is floored by the approximately flat but tilted

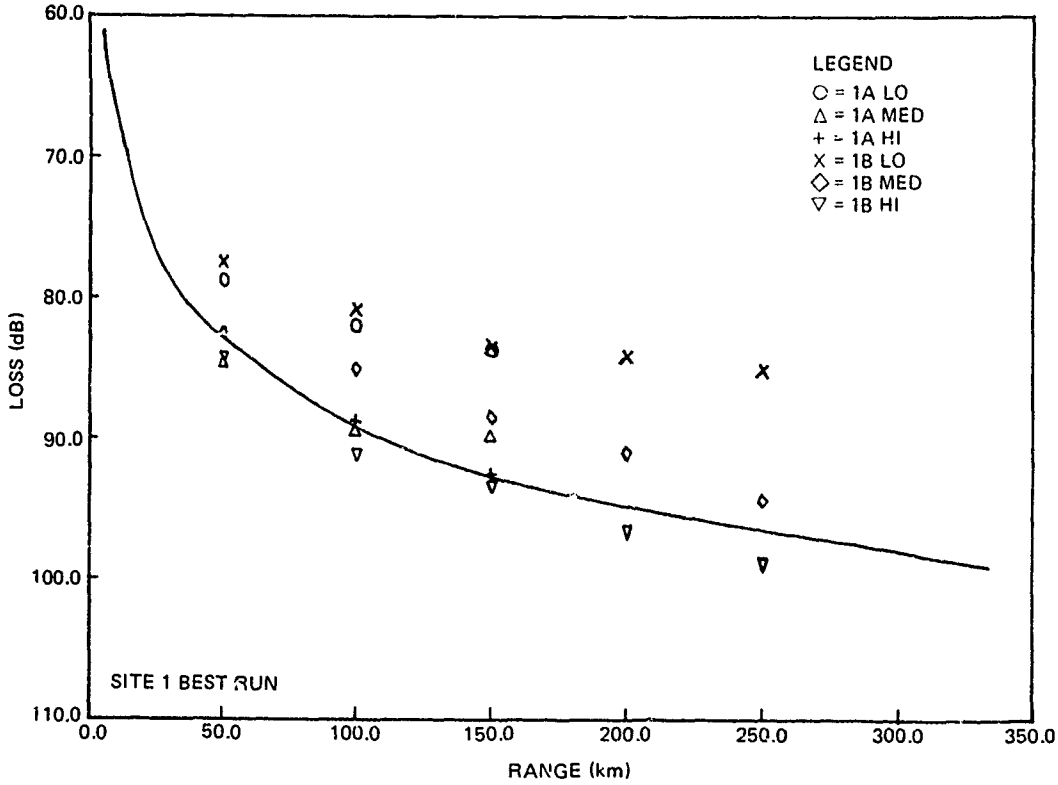

Figure VIII-5. (C) Comparison of the lowest propagation loss events at Sites 1A and 1B with the Eleuthera reference. (U)

(i.e., not horizontal) Arabian Fan. The Arabian Fan is mostly mineral detritus from the Indus River outflow. This sediment material has covered the originally rough basaltic basin floor to great thickness (over 9 km in the northern end of the basin, thinning to 400 to 500 m in the south before pinching out against the Carlsberg Ridge). The top of the sediment (i.e., the basin floor) slopes downward to the south and southwest (fig 4). A sharp escarpment marks the boundary on the eastern edge of the basin between the shallower Owen Ridge and the Arabian Fan. No such sharp boundary marks the southern edge of the Fan, but rather the very rough basaltic flanks of the Carlsberg Ridge, which become increasingly deeper with distance north away from the ridge crest, have been covered with the sediment fill of the fan. Isolated peaks of the ridge material protrude through the surrounding unconsolidated sediment in a band along the southern edge of the fan.

(C) The geoacoustic model for the Central Arabian Fan, developed in chapter III, is presented (as modified by comparison with acoustic measurements) in table IV-5. Bottom loss data for the central Oman Basin are also presented in chapter IV and will be repeated in section VIII.4 of the present chapter. Bottom loss was low in all three basins to be described, but it was lowest (least loss) in the Arabian Basin. Analysis of propagation loss data for the Arabian Fan indicated that two bottom loss versus bottom grazing angle curves should be used for this basin (see section V.4) — one curve (representing the lowest bottom losses observed in the Northwestern Indian Ocean) for the southern end of the fan and another (next to lowest loss) in the northern part

of the fan (see section VIII.4). These low losses are again attributed to strong upward refraction and low absorption in the unconsolidated sediment of the basin floor.

(C) Three BEARING STAKE receiver sites (receivers 2, 3, and 5) were located so that at least some of the source tracks from the site crossed over the Arabian Fan (fig 4). Propagation data from these sites indicate that this severely bottom-limited but low-loss environment provides many multipath contributions to the signal field. This produces a received level (or propagation loss) which is generally low but varies rapidly over short range intervals with no evidence of convergence zones (for discussion see VIII.3.1 and fig V-1, chapter V). The data were averaged over range bins, as described in section V.1.2, to facilitate comparisons.

(C) Receiver depth dependence of propagation loss over the Arabian Fan is difficult to ascertain from the BEARING STAKE data. The ACODAC failed at Site 3, leaving only the flat-lying BMA on the ocean floor, and the propagation to receivers at Sites 2 and 5 was complicated by local bathymetry. Because of many similarities between the Oman and Arabian Basins, it is probably safe to assume that, in the absence of bathymetric effects, the propagation loss, at low frequencies, across the Arabian Fan is independent of receiver depth as long as the receiver is deeper than the surface decoupling depth and is above the near-bottom complexities (e.g., the propagation loss "notch" described in section VIII.3.1). In general, for signals traversing the Arabian Fan, propagation loss is low (figs V-14, V-15, V-16A,B,C, and V-25).

(C) Although data are not available for determining the ambient noise depth dependence, similarity of the propagation conditions indicates the probability of very little depth dependence over the Arabian Fan (as was observed in the Oman Basin, where only about 2-dB difference was observed between near-bottom receivers and a receiver at 498 m depth). Figure 6 compares the median noise levels observed by the deepest BMA hydrophone at Sites 2, 3, and 5. The levels at 50 Hz and below are all at least 5 dB lower than were the levels in the Gulf of Oman. The levels for Sites 2 and 5 are lower than Site 3 levels for all frequencies shown. This is probably because of the increased propagation loss (described in chapter V) experienced by receivers mounted on the Owen Ridge (Site 2) or on one of the prominent features in the southern end of the Arabian Fan (e.g., the conical hill at Site 5). Wind speeds at Site 3 were clearly higher than at either Site 2 or 5 (fig II-11, II-21, and II-25), but not sufficiently higher to account for the difference in noise levels between Sites 3 and 2 for the higher frequencies (in any event, Site 5 noise is also higher than Site 2). The deepest hydrophone at Site 2 is essentially shielded from high-frequency sources west of the site, which may partially explain the very low noise levels at high frequencies.

(C) The phase coherence and array signal gain for arrays towed over or mounted on the Arabian Fan fluctuate rapidly with range but are high, on the average, for low frequencies as long as the signals only reflect from the unconsolidated sediment fill of the the fan (25-Hz data are shown in fig VII-1, VII-2, VII-5, VII-6, VII-17, VII-18, VII-21, VII-22). However, when the signals traverse rough bathymetric features, as was the case for all measurements with the OAMS array at Site 2, the low-frequency coherence and array signal gain are reduced (fig VII-19 and VII-20). This result is consistent with the observations in the Oman Basin. Phase coherence and array

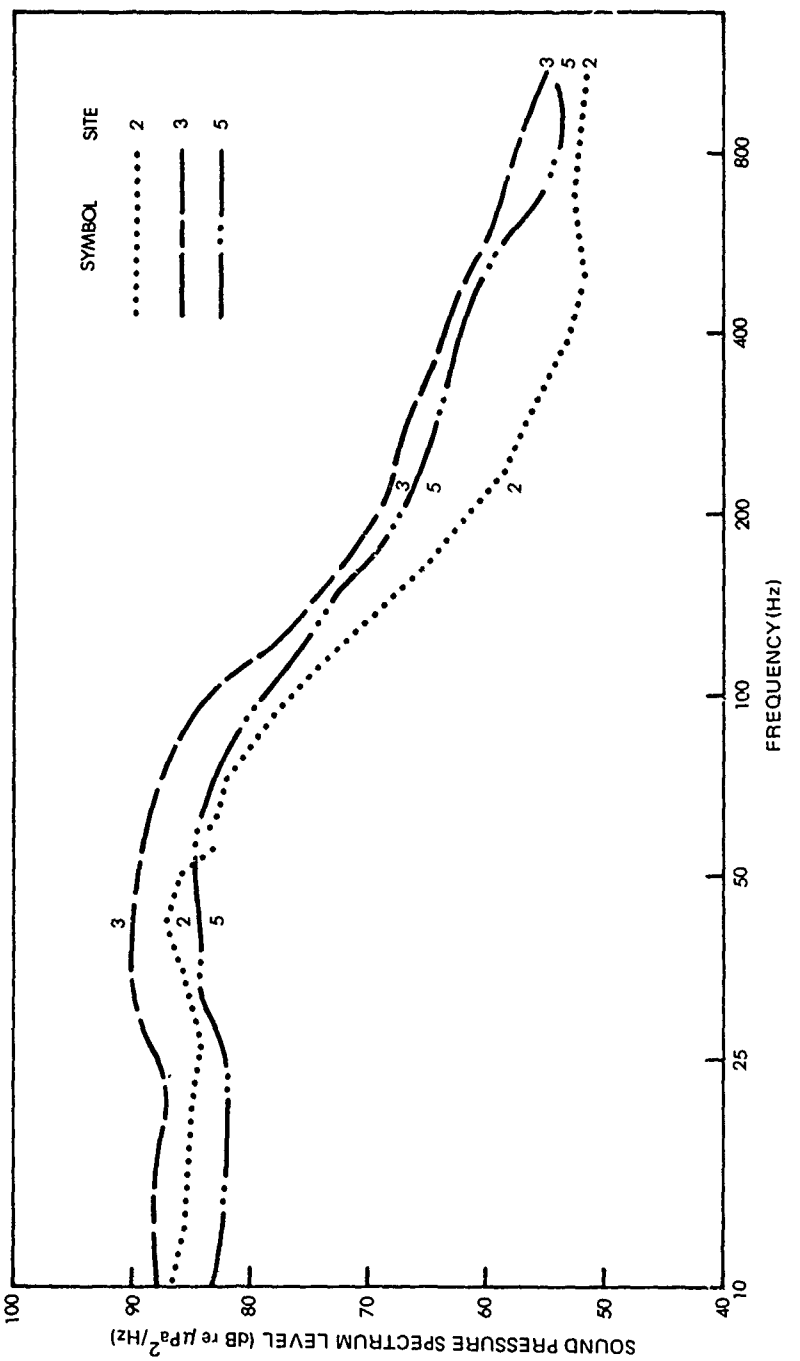

Figure VIII-6. (C) Median noise levels for the three BEARING STAKE sites in the Arabian Basin. Data are from the deepest hydrophone of the bottom-mounted array. (U)

signal gain are also somewhat lower and more variable for a receiver towed at 300 m (VII-21 and V-22) than for a shallower or a bottom array. This is also consistent with observations from the Oman Basin and is probably related to the variability of sound speed at the greater depth. Finally, another result consistent with other observations shows a rapid degradation of phase coherence and array signal gain with increasing frequency (290-Hz data were shown in fig VII-3 and VII-4).

VIII.3.3 (C) The Somali Basin

(C) As shown in figure 4, the Somali Basin is the deepest basin in the Northwest Indian Ocean. The basin is bounded on the north by ridges essentially connecting the African continent to Socotra Island to the Carlsberg Ridge (fig 2). On the west and northwest the basin is bounded by the African continent and on the east by the Chain Ridge. The floor of the Somali Basin is a very flat abyssal plain with a top layer of turbidites almost 1600 m thick. Chain Ridge on the east side of the basin is a continuous basaltic ridge with a series of summit peaks. The base of the ridge is defined by the 5000-m depth contour.

(C) The geoacoustic model for the floor of the Somali Basin, developed in chapter III, is presented (as modified by comparison with acoustic measurements) in table IV-4. Bottom loss data for the central Somali Basin are also presented in chapter IV and will be repeated in section VIII.4 of the present chapter. Somali Basin bottom loss was highest of the bottom loss values obtained during BEARING STAKE in the three basins (Somali, Oman, Arabian).

(C) The Somali Basin is the only region of the Northwest Indian Ocean which is not severely bottom limited (see fig 2). The depth excess in this basin is not large. During BEARING STAKE, depth excess ranged from 0 to 121 m below the critical depth, while it was between 30 and 147 m for the 18-m source depth and between 197 and 276 m for the 91-m source depth (table V-9). An interesting feature of the signal propagation in this basin (during BEARING STAKE) is the presence of convergence zone peaks at 290 Hz of 10–20-dB lower loss than the bottom bounce signals but the total absence of such peaks for 25 Hz.

(C) As discussed in chapter VI, very little depth dependence of median omnidirectional ambient noise was observed during BEARING STAKE. Indeed, for frequencies below 40 Hz, the level changed only about 1 dB from the sound channel axis depth to the floor of the basin (see fig VI-6). For a location in the northeastern end of the basin near the Chain Ridge, horizontal directional ambient noise at about 300-m depth and at low frequency (25 and 40 Hz) clearly shows a bias along the axis of the Somali Basin, with highest noise observed from azimuths to the southwest and to the north. Noise levels from these directions, during BEARING STAKE, were as much as 10 dB higher than levels from the northwest or southeast (fig VI-7, VI-8).

(C) The phase coherence and array signal gain fluctuate significantly with range in this basin (fig VII-11 through VII-16) but do not fluctuate as much as for the two bottom-limited basins. Coherence and array gain are reduced and their variability is increased when sources pass over the irregularly sloping bottom regions which surround the basin. For arrays towed at depths

on the order of 200 m (which is above most of the sound speed profile complexity), phase coherence is higher and less variable than for arrays at depths on the order of 300 m.

VIII.4 (U) REGIONAL ACOUSTICS

(C) The acoustic conditions in the Northwest Indian Ocean are dominated by the nature of the ocean floor. This is true in part because the sound speed profiles for this near-equatorial region exhibit large values for sound speed at the ocean surface (fig 3). Such large sound speeds result in significant bottom limiting of the deep sound channel. This ocean region consists of a series of basins which are divided and bounded by ridges and coastal bathymetric complexity (fig 2 and 4). Some of the thickest known unconsolidated sediment sections form the floor of these basins. Strong increases of sound speed with depth in these sediments produce strong upward refraction of sound energy which penetrates into the bottom from the overlying water. Because of low absorption in the sediments, this upward refracted energy returns to the water column with very little loss (this "bottom loss" does increase with increasing grazing angle on the bottom because of deeper penetration of the impinging energy into the bottom — see chapter IV). The absorption in the sediment filling the floor of the basins increases with frequency; thus, less energy is returned from the bottom and bottom loss increases with frequency. Sediment losses are also different for the different basins; thus, bottom loss values vary among the basins. Lowest bottom losses occur in the southern end of the Arabian Basin (Arabian Fan or Indus Fan) and next lowest occur in the northern end of this same basin. Somewhat higher (but still low) bottom losses are observed in the Oman Basin, with still higher losses in the Somali Basin. Although not directly measured during BEARING STAKE, bottom losses for many of the coastal regions have been inferred to be even higher than those for the floor of the Somali Basin, and bottom losses for many of the bathymetrically rugged ridges have been inferred to be the highest in the Northwest Indian Ocean. Bottom loss values appropriate for model predictions in this region are shown in tables 1 through 6 and the distribution of the loss provinces (on a 1° by 1° square basis) is shown in figure 7.

(C) The low bottom losses exhibited by the seafloor in the shallower basins of this region (Oman and Arabian) moderate the energy loss resulting from the severe bottom limiting of the sound channel. Indeed, most of the energy which would be refracting at great depth to form convergence zones in a non-bottom-limited region is retained in the propagating field in these basins. It is, however, spatially redistributed and "homogenized" to some extent. Strong convergence zones do not occur, but neither do shadow zones. For low-frequency propagation over these basins, many multipaths with significant energy content contribute to a received signal field for all source-to-receiver ranges. This results in a unique propagation loss versus range profile: the average loss is quite low, but levels fluctuate rapidly, with deep fades in the received signal field occurring on the order of three times more often than in either the Pacific or Atlantic. These features have significant impact on the phase coherence and signal gain of arrays.

(C) A peculiarity of the Somali Basin results from its small depth excess. At frequencies on the order of 290 Hz, convergence zones of 10–20-dB less loss than interzone (bottom bounce) levels are formed by energy propagating across the flat basin floor from a shallow source. These convergence zones were not

TABLE VIII-1. (C) SITE 5 BOTTOM LOSS CALCULATIONS — REGIONS NUMBERED "1" IN FIG VIII-7. (U)

FREQUENCY= 25.00 Hz

ANGLE	LOSS	ANGLE	LOSS	ANGLE	LOSS	ANGLE	LOSS	ANGLE	LOSS	ANGLE	LOSS
1	.05	16	.15	31	1.08	46	1.70	61	13.14	76	8.62
2	.07	17	.18	32	1.18	47	1.91	62	13.81	77	8.69
3	.08	18	.22	33	1.18	48	1.90	63	16.18	78	8.13
4	.08	19	.26	34	1.27	49	1.96	64	17.04	79	8.09
5	.08	20	.29	35	1.33	50	2.09	65	13.64	80	8.20
6	.08	21	.33	36	1.35	51	2.20	66	14.34	81	8.48
7	.08	22	.28	37	1.39	52	2.11	67	14.97	82	8.35
8	.09	23	.26	38	1.30	53	1.86	68	14.34	83	8.26
9	.09	24	.28	39	1.49	54	1.89	69	14.95	84	8.32
10	.09	25	.37	40	1.31	55	1.81	70	15.65	85	8.32
11	.10	26	.55	41	1.54	56	1.48	71	13.25	86	8.26
12	.10	27	.71	42	1.41	57	7.92	72	10.14	87	8.06
13	.11	28	.78	43	1.59	58	11.87	73	4.35	88	7.97
14	.12	29	.63	44	1.60	59	12.73	74	6.12	89	7.91
15	.13	30	.76	45	1.64	60	13.66	75	7.52	90	7.24

FREQUENCY= 50.00 Hz

ANGLE	LOSS	ANGLE	LOSS	ANGLE	LOSS	ANGLE	LOSS	ANGLE	LOSS	ANGLE	LOSS
1	.13	16	.38	31	2.10	46	3.51	61	21.35	76	9.14
2	.19	17	.34	32	2.04	47	3.77	62	17.25	77	9.64
3	.19	18	.31	33	2.54	48	3.77	63	12.07	78	9.20
4	.19	19	.34	34	2.47	49	3.99	64	10.06	79	9.76
5	.18	20	.47	35	2.62	50	4.17	65	10.19	80	8.97
6	.17	21	.61	36	2.67	51	4.48	66	10.48	81	8.88
7	.17	22	.58	37	2.79	52	4.39	67	13.81	82	9.55
8	.17	23	.54	38	2.88	53	3.81	68	14.74	83	9.47
9	.18	24	.77	39	2.80	54	3.31	69	14.54	84	9.27
10	.19	25	.94	40	2.83	55	3.26	70	14.82	85	8.84
11	.20	26	.92	41	2.96	56	2.83	71	14.56	86	8.43
12	.23	27	1.17	42	3.08	57	8.97	72	10.99	87	8.45
13	.28	28	1.30	43	3.16	58	13.07	73	5.48	88	8.68
14	.33	29	1.56	44	3.28	59	10.51	74	7.23	89	8.79
15	.38	30	1.63	45	3.56	60	10.67	75	8.64	90	7.52

FREQUENCY= 100.00 Hz

ANGLE	LOSS	ANGLE	LOSS	ANGLE	LOSS	ANGLE	LOSS	ANGLE	LOSS	ANGLE	LOSS
1	.80	16	.78	31	3.86	46	7.28	61	12.66	76	10.74
2	.63	17	.68	32	4.45	47	5.11	62	12.78	77	10.95
3	.50	18	.68	33	4.78	48	6.27	63	18.78	78	11.97
4	.41	19	.92	34	4.80	49	8.67	64	17.43	79	11.14
5	.37	20	.86	35	5.38	50	8.95	65	14.57	80	12.15
6	.34	21	1.01	36	5.30	51	9.58	66	15.37	81	12.56
7	.34	22	1.12	37	5.60	52	9.48	67	15.28	82	11.59
8	.35	23	1.32	38	5.57	53	8.04	68	14.80	83	9.85
9	.39	24	1.49	39	5.65	54	6.65	69	15.42	84	10.22
10	.45	25	1.64	40	5.60	55	6.13	70	15.26	85	11.69
11	.51	26	2.10	41	5.46	56	6.00	71	14.01	86	10.68
12	.51	27	2.31	42	6.28	57	12.24	72	12.87	87	11.22
13	.46	28	2.61	43	5.91	58	15.58	73	7.19	88	11.43
14	.47	29	3.03	44	6.51	59	13.92	74	8.77	89	11.00
15	.61	30	3.39	45	6.72	60	15.03	75	10.22	90	8.17

FREQUENCY= 200.00 Hz

ANGLE	LOSS	ANGLE	LOSS	ANGLE	LOSS	ANGLE	LOSS	ANGLE	LOSS	ANGLE	LOSS
1	.68	16	1.24	31	7.66	46	14.84	61	14.91	76	15.82
2	.69	17	1.41	32	8.64	47	20.34	62	15.19	77	15.52
3	.59	18	1.49	33	9.31	48	14.28	63	13.78	78	13.69
4	.53	19	1.74	34	10.22	49	15.89	64	15.49	79	14.39
5	.51	20	1.88	35	10.85	50	15.89	65	14.66	80	10.59
6	.54	21	2.09	36	11.67	51	14.67	66	14.95	81	9.69
7	.62	22	2.28	37	10.27	52	15.28	67	14.88	82	10.44
8	.71	23	2.66	38	7.29	53	26.23	68	14.71	83	10.49
9	.73	24	2.97	39	12.20	54	14.31	69	14.61	84	13.98
10	.75	25	3.37	40	11.90	55	12.49	70	14.94	85	10.57
11	.92	26	3.97	41	12.34	56	11.75	71	14.69	86	17.05
12	1.06	27	4.57	42	11.75	57	14.40	72	15.08	87	15.75
13	.92	28	5.22	43	11.81	58	14.88	73	11.30	88	11.66
14	1.19	29	5.99	44	13.55	59	14.66	74	14.69	89	12.87
15	1.21	30	7.27	45	14.82	60	14.94	75	14.72	90	9.17

FREQUENCY= 400.00 Hz

ANGLE	LOSS	ANGLE	LOSS	ANGLE	LOSS	ANGLE	LOSS	ANGLE	LOSS	ANGLE	LOSS
1	.18	16	2.60	31	11.35	46	15.16	61	14.99	76	14.78
2	.35	17	2.84	32	10.86	47	13.81	62	15.50	77	14.76
3	.53	18	2.98	33	15.66	48	14.98	63	15.01	78	14.59
4	.81	19	3.40	34	15.68	49	14.98	64	14.77	79	14.54
5	1.22	20	3.66	35	15.21	50	15.02	65	14.79	80	14.82
6	1.37	21	3.94	36	15.42	51	14.93	66	14.81	81	13.58
7	1.30	22	4.56	37	15.34	52	14.92	67	14.84	82	16.32
8	1.42	23	5.36	38	16.51	53	16.56	68	14.99	83	13.78
9	1.46	24	6.30	39	15.80	54	15.02	69	14.84	84	14.47
10	1.70	25	6.01	40	.86	55	14.99	70	14.52	85	15.20
11	1.73	26	7.43	41	14.41	56	15.01	71	14.77	86	14.71
12	1.95	27	9.14	42	14.66	57	16.51	72	14.86	87	14.16
13	2.13	28	10.52	43	16.47	58	14.74	73	15.26	88	15.51
14	2.33	29	11.41	44	14.74	59	14.87	74	14.92	89	14.91
15	2.45	30	10.23	45	15.08	60	14.87	75	14.95	90	10.86

TABLE VIII-2. (C) SITE 1B BOTTOM LOSS CALCULATIONS — REGIONS NUMBERED "2" IN FIG VIII-7. (U)

FREQUENCY= 25.00 Hz

ANGLE	LOSS	ANGLE	LOSS	ANGLE	LOSS	ANGLE	LOSS	ANGLE	LOSS	ANGLE	LOSS
1	0.00	16	.19	31	.73	46	3.46	61	7.39	76	14.07
2	.02	17	.20	32	.95	47	3.32	62	7.30	77	13.96
3	.05	18	.23	33	.94	48	3.58	63	7.76	78	13.98
4	.07	19	.29	34	.91	49	3.95	64	7.43	79	14.26
5	.10	20	.37	35	1.15	50	4.10	65	8.19	80	14.26
6	.12	21	.44	36	1.26	51	4.30	66	7.43	81	14.44
7	.13	22	.45	37	1.47	52	4.58	67	10.52	82	14.07
8	.15	23	.39	38	1.56	53	5.03	68	11.43	83	14.51
9	.16	24	.32	39	1.74	54	5.28	69	15.30	84	14.56
10	.17	25	.30	40	2.10	55	5.98	70	15.06	85	13.63
11	.18	26	.38	41	2.14	56	6.15	71	15.19	86	14.48
12	.18	27	.60	42	2.70	57	6.14	72	13.53	87	14.38
13	.18	28	.76	43	2.81	58	6.21	73	11.60	88	13.97
14	.18	29	.67	44	3.09	59	7.53	74	13.37	89	13.82
15	.19	30	.55	45	3.21	60	7.49	75	14.25	90	13.68

FREQUENCY= 50.00 Hz

ANGLE	LOSS	ANGLE	LOSS	ANGLE	LOSS	ANGLE	LOSS	ANGLE	LOSS	ANGLE	LOSS
1	0.00	16	.68	31	1.44	46	6.41	61	15.36	76	14.13
2	.04	17	.80	32	1.77	47	6.75	62	14.69	77	13.98
3	.10	18	.69	33	1.75	48	7.29	63	14.69	78	14.33
4	.15	19	.50	34	2.04	49	7.38	64	12.32	79	14.27
5	.19	20	.42	35	2.28	50	8.19	65	14.98	80	13.17
6	.23	21	.51	36	2.52	51	8.59	66	13.00	81	12.85
7	.26	22	.80	37	2.80	52	8.88	67	16.21	82	13.49
8	.28	23	.84	38	3.06	53	9.67	68	14.30	83	13.19
9	.30	24	.63	39	3.58	54	11.18	69	14.02	84	12.74
10	.32	25	.83	40	4.14	55	11.19	70	14.07	85	14.47
11	.33	26	1.07	41	4.56	56	12.18	71	14.51	86	14.01
12	.35	27	.97	42	4.91	57	7.83	72	14.12	87	14.17
13	.38	28	1.22	43	5.41	58	11.66	73	13.76	88	14.28
14	.44	29	1.30	44	6.06	59	14.94	74	13.98	89	13.98
15	.54	30	1.45	45	6.29	60	14.61	75	14.20	90	13.96

FREQUENCY= 100.00 Hz

ANGLE	LOSS	ANGLE	LOSS	ANGLE	LOSS	ANGLE	LOSS	ANGLE	LOSS	ANGLE	LOSS
1	0.00	16	.76	31	3.21	46	13.90	61	14.14	76	14.03
2	.08	17	1.06	32	3.45	47	17.48	62	14.10	77	14.01
3	.20	18	1.45	33	3.64	48	22.51	63	14.26	78	13.99
4	.30	19	1.01	34	4.00	49	13.73	64	14.09	79	14.12
5	.38	20	1.14	35	4.59	50	13.85	65	13.99	80	14.08
6	.44	21	1.37	36	5.09	51	14.05	66	14.23	81	14.11
7	.49	22	1.17	37	5.93	52	14.39	67	13.94	82	14.02
8	.53	23	1.44	38	6.09	53	14.23	68	14.09	83	14.17
9	.58	24	1.63	39	7.78	54	14.07	69	14.05	84	14.11
10	.64	25	1.63	40	7.72	55	13.99	70	13.96	85	13.98
11	.77	26	1.85	41	9.01	56	14.36	71	14.56	86	13.92
12	1.04	27	2.27	42	10.68	57	13.05	72	14.00	87	14.05
13	1.48	28	2.43	43	11.91	58	14.41	73	13.98	88	14.01
14	1.49	29	2.66	44	11.15	59	13.94	74	14.12	89	14.14
15	1.00	30	2.94	45	12.26	60	13.87	75	14.04	90	14.06

FREQUENCY= 200.00 Hz

ANGLE	LOSS	ANGLE	LOSS	ANGLE	LOSS	ANGLE	LOSS	ANGLE	LOSS	ANGLE	LOSS
1	0.00	16	2.18	31	6.86	46	13.82	61	14.04	76	14.05
2	.17	17	2.26	32	6.63	47	14.19	62	14.04	77	14.05
3	.40	18	2.34	33	7.41	48	13.82	63	14.06	78	14.05
4	.58	19	2.36	34	7.85	49	14.18	64	14.04	79	14.05
5	.72	20	2.26	35	9.10	50	14.08	65	14.05	80	14.05
6	.83	21	2.31	36	10.06	51	14.14	66	14.05	81	14.06
7	.93	22	2.60	37	12.86	52	13.95	67	14.04	82	14.01
8	1.07	23	2.84	38	9.13	53	13.74	68	14.05	83	14.05
9	1.42	24	3.12	39	9.66	54	14.03	69	14.04	84	14.04
10	2.26	25	3.61	40	13.74	55	14.06	70	14.05	85	14.05
11	2.85	26	3.76	41	14.12	56	14.04	71	14.04	86	14.06
12	1.83	27	4.24	42	13.86	57	14.10	72	14.06	87	14.04
13	1.55	28	4.87	43	14.25	58	14.03	73	14.04	88	14.04
14	2.77	29	5.33	44	14.47	59	14.04	74	14.05	89	14.04
15	2.07	30	5.80	45	14.22	60	14.03	75	14.05	90	14.05

FREQUENCY= 400.00 Hz

ANGLE	LOSS	ANGLE	LOSS	ANGLE	LOSS	ANGLE	LOSS	ANGLE	LOSS	ANGLE	LOSS
1	0.00	16	4.17	31	10.85	46	14.05	61	14.05	76	14.05
2	.34	17	4.26	32	13.08	47	14.03	62	14.05	77	14.05
3	.79	18	4.67	33	14.17	48	14.05	63	14.05	78	14.05
4	1.12	19	4.55	34	14.07	49	14.04	64	14.05	79	14.05
5	1.35	20	5.06	35	13.39	50	14.04	65	14.05	80	14.05
6	1.59	21	4.83	36	14.51	51	14.04	66	14.05	81	14.05
7	2.13	22	5.12	37	14.05	52	14.04	67	14.05	82	14.05
8	3.85	23	5.70	38	14.31	53	14.05	68	14.05	83	14.05
9	4.55	24	6.08	39	15.30	54	14.04	69	14.05	84	14.05
10	2.64	25	7.66	40	14.15	55	14.04	70	14.05	85	14.05
11	4.63	26	8.10	41	14.00	56	14.04	71	14.05	86	14.05
12	3.75	27	8.43	42	14.03	57	14.04	72	14.05	87	14.05
13	4.92	28	9.85	43	14.01	58	14.04	73	14.05	88	14.05
14	4.02	29	10.47	44	14.08	59	14.04	74	14.05	89	14.05
15	4.35	30	11.20	45	14.04	60	14.05	75	14.05	90	14.05

TABLE VIII-3. (C) SITE 3 BOTTOM LOSS CALCULATIONS — REGIONS NUMBERED "3" IN FIG VIII-7. (U)

FREQUENCY= 25.00 Hz

ANGLE	LOSS	ANGLE	LOSS	ANGLE	LOSS	ANGLE	LOSS	ANGLE	LOSS	ANGLE	LOSS
1	.00	16	.26	31	.76	46	5.31	61	13.58	76	13.65
2	.02	17	.29	32	1.19	47	5.55	62	13.64	77	13.67
3	.05	18	.34	33	1.32	48	6.05	63	13.69	78	13.64
4	.07	19	.42	34	1.22	49	6.61	64	13.46	79	13.58
5	.10	20	.53	35	1.51	50	7.65	65	13.81	80	13.60
6	.12	21	.65	36	1.76	51	7.60	66	13.48	81	13.68
7	.14	22	.67	37	2.05	52	7.67	67	13.73	82	13.73
8	.16	23	.58	38	2.29	53	6.67	68	13.62	83	13.72
9	.17	24	.46	39	2.71	54	12.47	69	13.61	84	13.67
10	.19	25	.39	40	3.24	55	13.68	70	13.67	85	13.62
11	.20	26	.43	41	3.69	56	13.70	71	13.64	86	13.58
12	.21	27	.62	42	4.19	57	13.78	72	13.65	87	13.57
13	.22	28	.91	43	4.83	58	13.29	73	13.62	88	13.56
14	.23	29	.93	44	5.00	59	13.64	74	13.65	89	13.56
15	.24	30	.74	45	5.25	60	13.71	75	13.65	90	13.56

FREQUENCY= 50.00 Hz

ANGLE	LOSS	ANGLE	LOSS	ANGLE	LOSS	ANGLE	LOSS	ANGLE	LOSS	ANGLE	LOSS
1	.00	16	.95	31	1.86	46	12.88	61	13.78	76	13.64
2	.04	17	1.20	32	2.27	47	10.35	62	13.63	77	13.65
3	.10	18	1.11	33	2.21	48	15.56	63	13.49	78	13.64
4	.15	19	.81	34	2.88	49	12.42	64	13.46	79	13.63
5	.19	20	.63	35	2.92	50	12.37	65	13.54	80	13.66
6	.23	21	.68	36	3.44	51	13.98	66	13.65	81	13.66
7	.27	22	1.04	37	3.94	52	13.83	67	13.64	82	13.60
8	.30	23	1.24	38	4.51	53	11.85	68	13.56	83	13.63
9	.33	24	.94	39	5.45	54	14.26	69	13.61	84	13.69
10	.35	25	.89	40	6.48	55	13.74	70	13.67	85	13.69
11	.37	26	1.36	41	7.34	56	13.82	71	13.64	86	13.64
12	.40	27	1.32	42	8.19	57	13.63	72	13.64	87	13.60
13	.45	28	1.33	43	9.55	58	13.27	73	13.62	88	13.58
14	.54	29	1.58	44	9.84	59	13.48	74	13.65	89	13.58
15	.69	30	1.70	45	10.19	60	13.47	75	13.64	90	13.58

FREQUENCY= 100.00 Hz

ANGLE	LOSS	ANGLE	LOSS	ANGLE	LOSS	ANGLE	LOSS	ANGLE	LOSS	ANGLE	LOSS
1	.00	16	1.68	31	3.65	46	15.63	61	13.64	76	13.63
2	.08	17	1.36	32	4.03	47	12.29	62	13.65	77	13.64
3	.20	18	2.20	33	4.75	48	13.34	63	13.70	78	13.73
4	.29	19	1.72	34	5.34	49	13.48	64	13.62	79	13.78
5	.38	20	1.46	35	5.60	50	13.46	65	13.60	80	13.53
6	.45	21	2.09	36	7.04	51	13.72	66	13.65	81	13.63
7	.51	22	1.71	37	8.48	52	13.47	67	13.60	82	13.70
8	.56	23	2.01	38	8.27	53	13.39	68	13.64	83	13.60
9	.61	24	2.04	39	13.34	54	13.82	69	13.65	84	13.64
10	.69	25	2.12	40	13.66	55	13.57	70	13.62	85	13.66
11	.84	26	2.63	41	13.49	56	13.23	71	13.65	86	13.66
12	1.16	27	2.49	42	13.25	57	13.52	72	13.66	87	13.63
13	1.75	28	2.65	43	13.54	58	13.66	73	13.67	88	13.60
14	2.02	29	3.10	44	13.56	59	13.70	74	13.65	89	13.59
15	1.46	30	3.31	45	13.44	60	13.63	75	13.65	90	13.58

FREQUENCY= 200.00 Hz

ANGLE	LOSS	ANGLE	LOSS	ANGLE	LOSS	ANGLE	LOSS	ANGLE	LOSS	ANGLE	LOSS
1	.00	16	2.65	31	8.01	46	13.68	61	13.64	76	13.64
2	.17	17	3.57	32	9.64	47	13.59	62	13.65	77	13.65
3	.40	18	3.31	33	9.59	48	13.66	63	13.64	78	13.64
4	.58	19	3.42	34	10.74	49	13.64	64	13.54	79	13.63
5	.73	20	3.41	35	13.65	50	13.64	65	13.64	80	13.64
6	.85	21	3.84	36	10.31	51	13.61	66	13.64	81	13.65
7	.95	22	4.01	37	12.48	52	13.64	67	13.64	82	13.64
8	1.11	23	4.01	38	12.41	53	13.65	68	13.65	83	13.64
9	1.47	24	4.07	39	13.69	54	13.65	69	13.65	84	13.63
10	2.37	25	4.18	40	13.92	55	13.64	70	13.64	85	13.65
11	3.39	26	4.88	41	13.60	56	13.68	71	13.64	86	13.64
12	2.35	27	5.15	42	13.56	57	13.63	72	13.65	87	13.65
13	1.80	28	5.98	43	13.67	58	13.64	73	13.64	88	13.64
14	3.28	29	6.06	44	13.62	59	13.64	74	13.64	89	13.63
15	3.19	30	6.77	45	13.60	60	13.65	75	13.64	90	13.63

FREQUENCY= 400.00 Hz

ANGLE	LOSS	ANGLE	LOSS	ANGLE	LOSS	ANGLE	LOSS	ANGLE	LOSS	ANGLE	LOSS
1	.00	16	5.86	31	11.11	46	13.64	61	13.64	76	13.64
2	.33	17	5.92	32	12.10	47	13.64	62	13.64	77	13.64
3	.78	18	6.20	33	12.89	48	13.64	63	13.64	78	13.65
4	1.11	19	7.12	34	13.65	49	13.64	64	13.65	79	13.65
5	1.36	20	6.79	35	13.81	50	13.64	65	13.64	80	13.64
6	1.61	21	7.54	36	13.84	51	13.64	66	13.64	81	13.64
7	2.14	22	7.25	37	13.66	52	13.64	67	13.64	82	13.64
8	3.86	23	7.95	38	13.73	53	13.64	68	13.64	83	13.64
9	5.34	24	8.20	39	13.60	54	13.64	69	13.64	84	13.64
10	3.01	25	9.76	40	13.65	55	13.64	70	13.64	85	13.64
11	4.64	26	9.93	41	13.64	56	13.64	71	13.64	86	13.64
12	5.08	27	10.16	42	13.64	57	13.64	72	13.64	87	13.64
13	5.67	28	11.12	43	13.64	58	13.64	73	13.64	88	13.64
14	5.02	29	10.99	44	13.64	59	13.64	74	13.64	89	13.64
15	5.87	30	13.25	45	13.64	60	13.64	75	13.64	90	13.64

TABLE VIII-4. (C) SITE 4 BOTTOM LOSS CALCULATIONS — REGIONS NUMBERED "4" IN FIG VIII-7. (U)

FREQUENCY= 25.00 Hz

ANGLE	LOSS	ANGLE	LOSS	ANGLE	LOSS	ANGLE	LOSS	ANGLE	LOSS	ANGLE	LOSS
1	.18	16	.59	31	2.16	46	6.54	61	12.96	76	16.81
2	.20	17	.67	32	2.30	47	6.62	62	11.50	77	16.91
3	.33	18	.79	33	2.22	48	6.98	63	9.40	78	16.51
4	.35	19	.91	34	2.56	49	7.51	64	12.98	79	17.24
5	.35	20	1.01	35	2.85	50	7.80	65	16.22	80	18.04
6	.36	21	1.05	36	3.08	51	8.00	66	16.77	81	18.48
7	.37	22	1.00	37	3.36	52	8.71	67	17.23	82	16.06
8	.37	23	.94	38	3.50	53	9.36	68	17.12	83	13.80
9	.38	24	.94	39	4.22	54	11.07	69	16.50	84	14.97
10	.40	25	1.08	40	4.07	55	10.96	70	17.61	85	10.44
11	.41	26	1.41	41	4.82	56	11.94	71	16.20	86	19.96
12	.43	27	1.70	42	4.91	57	12.82	72	17.79	87	20.59
13	.45	28	1.67	43	5.34	58	12.67	73	16.76	88	26.81
14	.48	29	1.50	44	5.72	59	13.11	74	16.36	89	20.06
15	.53	30	1.66	45	6.28	60	12.44	75	18.19	90	19.85

FREQUENCY= 50.00 Hz

ANGLE	LOSS	ANGLE	LOSS	ANGLE	LOSS	ANGLE	LOSS	ANGLE	LOSS	ANGLE	LOSS
1	.51	16	1.40	31	4.23	46	13.19	61	17.26	76	17.14
2	.75	17	1.33	32	4.10	47	12.16	62	16.95	77	16.91
3	.81	18	1.25	33	4.94	48	13.52	63	13.29	78	17.22
4	.80	19	1.32	34	5.00	49	15.18	64	16.44	79	16.56
5	.78	20	1.66	35	5.61	50	16.58	65	16.82	80	17.56
6	.76	21	2.09	36	6.09	51	16.91	66	17.17	81	16.77
7	.76	22	2.07	37	6.69	52	16.81	67	16.94	82	16.43
8	.76	23	1.86	38	7.52	53	15.65	68	17.16	83	18.18
9	.77	24	2.28	39	8.21	54	16.98	69	17.26	84	16.69
10	.79	25	2.68	40	8.67	55	15.66	70	17.33	85	16.38
11	.84	26	2.57	41	9.17	56	15.70	71	17.01	86	16.72
12	.92	27	2.90	42	9.53	57	16.65	72	17.02	87	17.28
13	1.05	28	3.11	43	10.04	58	17.67	73	17.28	88	17.61
14	1.21	29	3.47	44	11.41	59	18.08	74	17.19	89	17.42
15	1.36	30	3.57	45	12.42	60	16.97	75	16.58	90	17.24

FREQUENCY= 100.00 Hz

ANGLE	LOSS	ANGLE	LOSS	ANGLE	LOSS	ANGLE	LOSS	ANGLE	LOSS	ANGLE	LOSS
1	1.36	16	2.83	31	7.83	46	20.72	61	17.07	76	17.09
2	2.81	17	2.69	32	8.76	47	18.05	62	17.45	77	17.08
3	2.22	18	2.60	33	9.43	48	16.96	63	16.64	78	17.06
4	1.86	19	3.31	34	9.69	49	17.31	64	15.99	79	17.03
5	1.63	20	3.29	35	11.58	50	17.23	65	17.69	80	16.94
6	1.50	21	3.59	36	11.94	51	17.12	66	17.15	81	16.95
7	1.43	22	3.92	37	13.68	52	17.06	67	17.20	82	17.10
8	1.43	23	4.36	38	14.39	53	17.13	68	17.16	83	16.77
9	1.51	24	4.47	39	16.74	54	16.44	69	17.11	84	17.21
10	1.67	25	4.91	40	17.92	55	17.04	70	16.98	85	16.76
11	1.87	26	5.61	41	15.57	56	17.27	71	17.09	86	17.27
12	1.97	27	5.68	42	17.44	57	17.14	72	16.99	87	16.95
13	1.92	28	6.15	43	16.81	58	17.24	73	17.15	88	16.85
14	1.93	29	6.70	44	17.13	59	17.04	74	16.94	89	16.87
15	2.31	30	7.19	45	17.37	60	16.89	75	16.85	90	16.95

FREQUENCY= 200.00 Hz

ANGLE	LOSS	ANGLE	LOSS	ANGLE	LOSS	ANGLE	LOSS	ANGLE	LOSS	ANGLE	LOSS
1	2.47	16	5.03	31	14.03	46	17.25	61	17.08	76	17.01
2	2.70	17	5.34	32	16.94	47	17.20	62	17.12	77	16.99
3	2.39	18	5.71	33	17.71	48	17.25	63	17.11	78	16.97
4	2.12	19	6.50	34	18.07	49	17.24	64	17.18	79	17.00
5	2.00	20	6.63	35	18.02	50	17.22	65	17.10	80	17.04
6	2.05	21	6.99	36	17.73	51	17.17	66	17.05	81	16.99
7	2.29	22	7.82	37	18.09	52	17.19	67	17.05	82	17.00
8	2.71	23	8.80	38	20.15	53	17.17	68	17.04	83	17.03
9	3.05	24	9.51	39	17.40	54	17.16	69	17.05	84	17.02
10	3.17	25	9.89	40	17.34	55	17.15	70	17.04	85	17.00
11	3.55	26	10.91	41	17.47	56	17.13	71	17.02	86	16.96
12	4.01	27	10.98	42	17.41	57	17.14	72	17.01	87	17.03
13	3.81	28	12.48	43	17.49	58	17.19	73	17.01	88	16.96
14	4.45	29	13.32	44	17.29	59	17.14	74	17.08	89	17.00
15	4.72	30	13.58	45	17.28	60	17.12	75	17.15	90	17.00

FREQUENCY= 400.00 Hz

ANGLE	LOSS	ANGLE	LOSS	ANGLE	LOSS	ANGLE	LOSS	ANGLE	LOSS	ANGLE	LOSS
1	.67	16	9.88	31	18.43	46	17.29	61	17.09	76	17.02
2	1.28	17	10.85	32	17.95	47	17.27	62	17.08	77	17.01
3	1.96	18	11.27	33	17.77	48	17.25	63	17.08	78	17.01
4	3.94	19	12.53	34	17.72	49	17.23	64	17.07	79	17.01
5	4.98	20	13.20	35	17.59	50	17.21	65	17.06	80	17.01
6	6.03	21	14.32	36	17.56	51	17.20	66	17.06	81	17.01
7	5.28	22	15.55	37	17.55	52	17.19	67	17.05	82	17.00
8	5.36	23	16.58	38	17.47	53	17.17	68	17.05	83	17.00
9	6.10	24	15.81	39	17.48	54	17.16	69	17.04	84	16.99
10	6.57	25	18.16	40	17.44	55	17.15	70	17.04	85	17.00
11	6.95	26	18.71	41	17.41	56	17.14	71	17.03	86	17.00
12	7.63	27	18.08	42	17.38	57	17.13	72	17.03	87	17.00
13	8.24	28	17.93	43	17.36	58	17.12	73	17.02	88	17.00
14	8.75	29	18.28	44	17.33	59	17.11	74	17.03	89	17.00
15	9.13	30	17.00	45	17.31	60	17.10	75	17.02	90	17.00

TABLE 5. (C) ESTIMATES OF BOTTOM LOSS FOR REGIONS NUMBERED "5" IN FIG VIII-7. (U)

Estimates should be linearly interpolated in angle.

Frequency (Hz)	Loss (dB) 0°	10°	20°	30°	≥50°
25	0.0	2.5	3.0	5.0	15.0
50	0.0	5.0	5.5	8.0	15.0
100	0.0	6.0	8.0	9.0	15.0
200	0.0	6.0	10.0	12.0	15.0
400	0.0	8.0	10.0	15.0	15.0

TABLE 6. (C) ESTIMATES OF BOTTOM LOSS FOR REGIONS NUMBERED "6" IN FIG VIII-7. (U)

Estimates should be linearly interpolated in angle.

Frequency (Hz)	Loss (dB) 0°	10°	20°	30°	≥50°
25	0.0	3.0	5.0	8.0	15.0
50	0.0	6.0	9.0	10.0	15.0
100	0.0	8.0	9.0	10.0	15.0
200	0.0	8.0	9.0	10.0	15.0
400	0.0	9.0	11.0	11.0	15.0

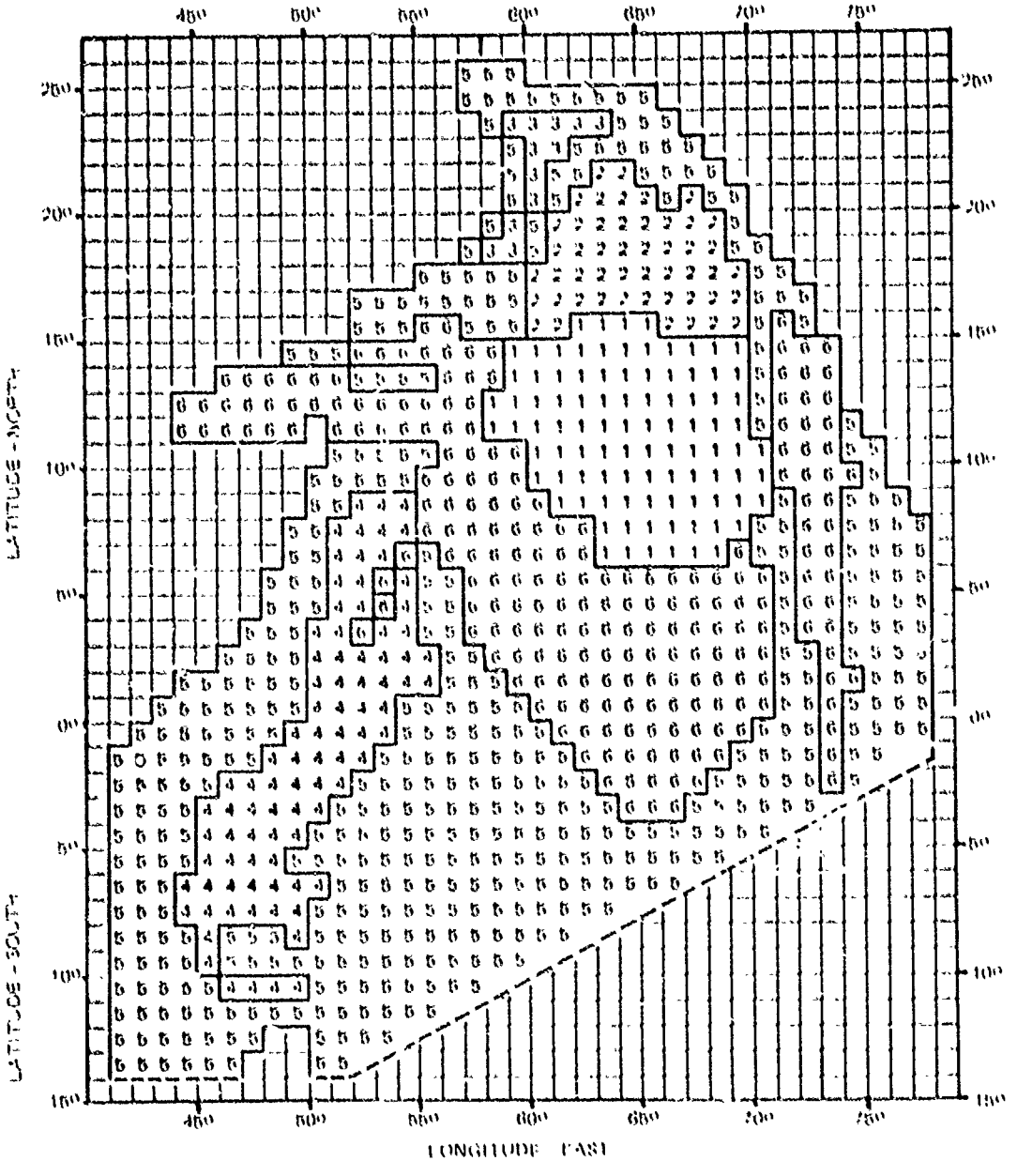

Figure VIII-7. (C) Bottom loss provinces for the Northwest Indian Ocean. (C)

formed at 25 Hz during BEARING STAKE and were weaker at 140 Hz. Cooler surface waters would result in more depth excess and probable increase of convergence zone strength (perhaps even forming zones at 25 Hz) while warmer surface waters would reduce or eliminate the depth excess and reduce the convergence zone strength. Thus, details of the form of propagation loss versus range in the Somali Basin are strongly dependent on the sound speed profile (thus time of year), acoustic frequency, and source depth.

(C) The low propagation losses for signals propagating across the basins of the Northwest Indian Ocean are illustrated by the range averaged data, plotted in figures 8, 9, and 10. These are the best (lowest loss) events observed at the five sites of BEARING STAKE. For reference purposes, the Eleuthera reference curve is also plotted in the three figures. To illustrate the total variation of range dependence of propagation loss in this ocean region, propagation loss observations for worst (highest loss) events at the BEARING STAKE sites are plotted in Figs. 11, 12 and 13. Higher losses were observed for sources mounted on ridges (specifically Chain Ridge) or on one of the features protruding up through the sediment in the southern Arabian Fan. This is probably because of higher bottom loss for these features (i.e., the low bottom loss is only clearly exhibited by the unconsolidated sediment floors of the basins). Higher losses were also observed (except at 25 Hz) for signals propagating across some of the topographically rugged features (seamounts and ridges). Receiver depth dependence of propagation loss appears to be low in the Oman and Arabian Basins with two exceptions (neither of which was strongly verified by BEARING STAKE data): surface decoupling would significantly increase loss for receivers near the ocean surface and coherent interaction of multipaths would vary the loss (by 2 or 3 dB from the water column average) observed by receivers near the bottom. This near-bottom propagation loss maximum (or "notch") could be used to gain signal-to-noise ratio advantage for near-bottom receivers because its height off the bottom is source depth dependent (for sources below the surface decoupling depth). Thus, for sources of depth greater than the surface decoupling depth, the propagation loss notch would occur at a different depth from the notch associated with shallower depth noise sources. (See chapter V for a further discussion.) It should be noted that this is at present a hypothesized effect, only partially supported by data, which should be examined further with additional measurements.

(C) As observed during BEARING STAKE, omnidirectional ambient noise at frequencies between 10 and 400 Hz is virtually independent of depth in the Oman and Somali Basins. Total noise level variation from shallow or midwater depth to bottom receivers is on the order of 2 dB (fig VI-5 and VI-6). Similarity of conditions in the Oman and Arabian Basins indicates a probable similar order of magnitude for noise depth dependence in the Arabian Basin. Noise levels observed by the deepest hydrophone of the BMA at each of the five BEARING STAKE sites are shown in figure 14. Highest noise levels at low frequencies clearly were observed at Site 1 in the Oman Basin. It is conjectured that this is a result of the very high density of surface shipping in the Oman Basin (fig VI-2). Noise directionality in these basins (fig VI-7 and VI-8) exhibits anisotropy consistent with the shipping patterns, and anisotropy of about 10 dB for 25 to 40 Hz occurs for the Oman Basin with more noise arriving at the center of the Basin from the east and west than from the north and south. In the northern Somali Basin, noise at these frequencies is on the order of 6 dB higher from the southwest and north than from other directions.

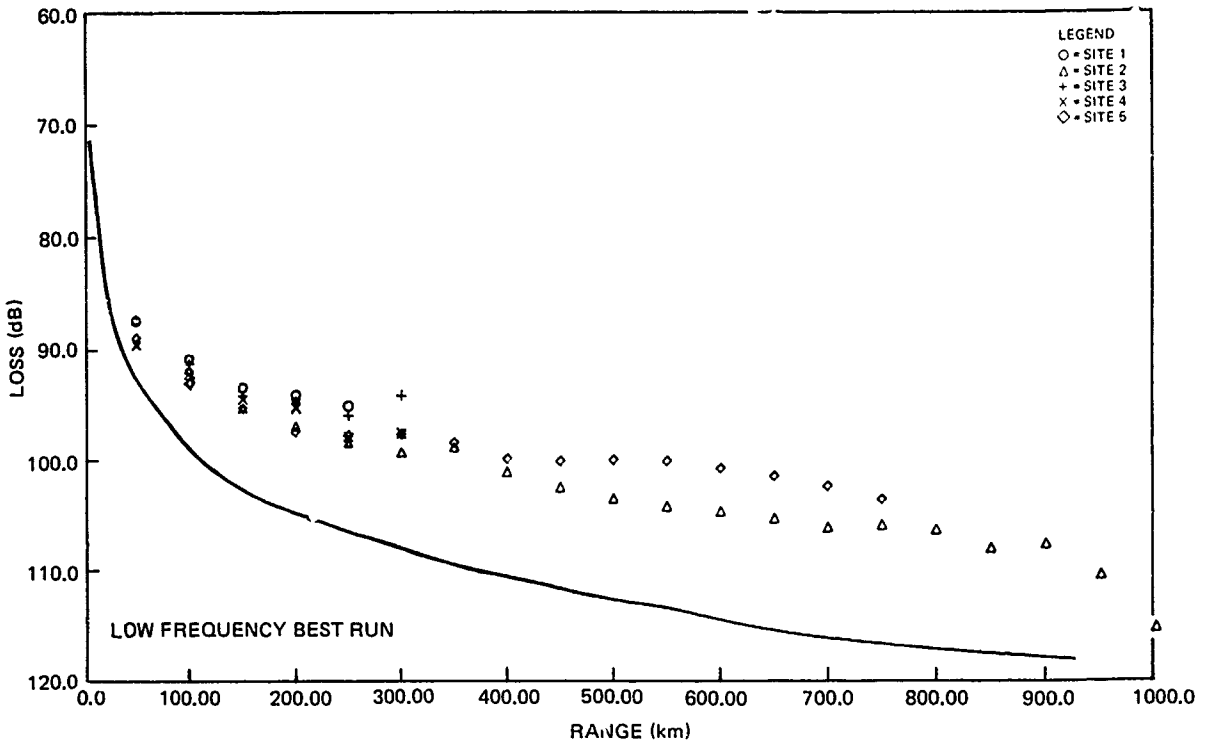

Figure VIII-8. (C) Comparisons of the lowest-propagation-loss events for each of the BEARING STAKE sites: 25 Hz. (C)

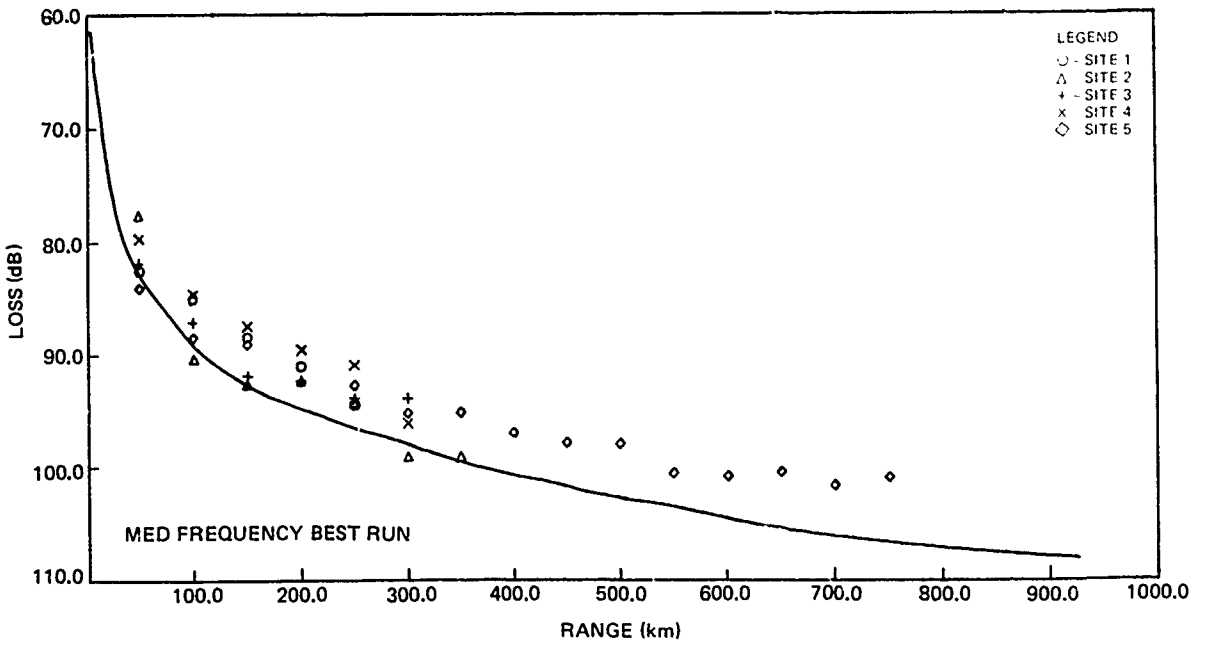

Figure VIII-9. (C) Comparisons of the lowest-propagation-loss events for each of the BEARING STAKE sites: 140 Hz. (C)

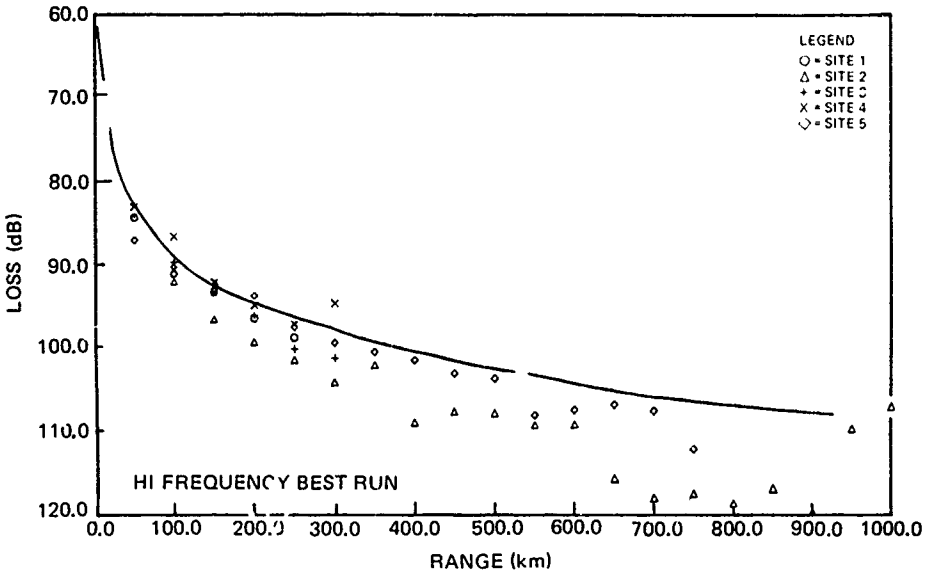

Figure VIII-10. (C) Comparisons of the lowest propagation-loss events for each of the BEARING STAKE sites: 290 Hz. (C)

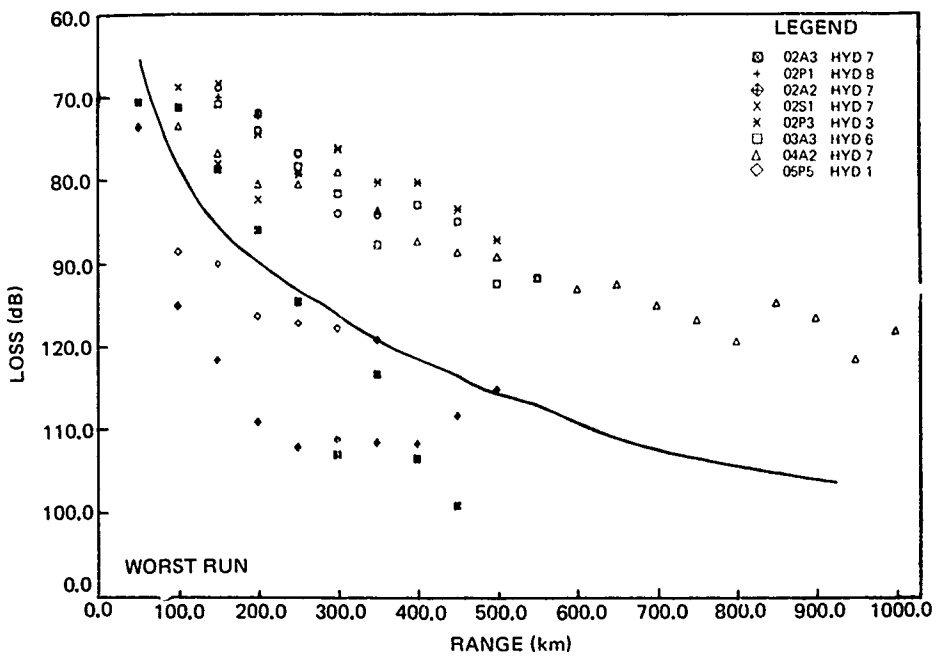

Figure VIII-11. (C) Propagation loss data for worst cases (highest loss) at each BEARING STAKE site except Site 2, for which all data are shown: 20 Hz. (C)

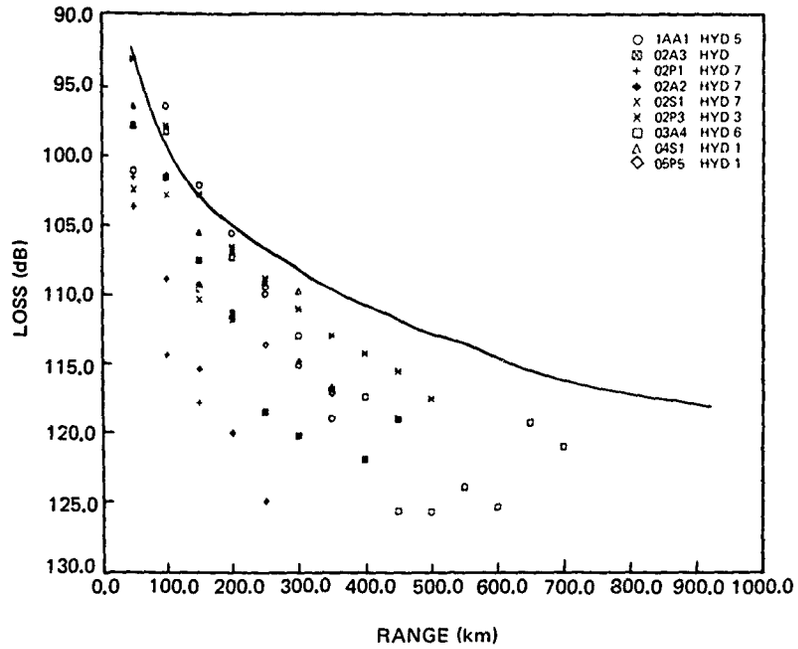

Figure VIII-12. (C) Propagation loss data for worst case (highest loss) at each BEARING STAKE site except Site 2, for which all data are shown: 140 Hz. (C)

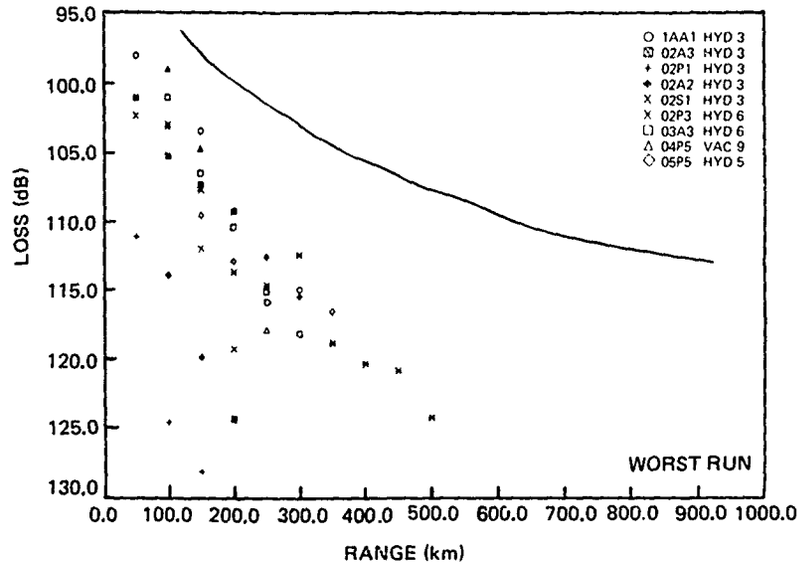

Figure VIII-13. (C) Propagation loss data for worst case (highest loss) at each BEARING STAKE site except Site 2, for which all data are shown: 290 Hz. (C)

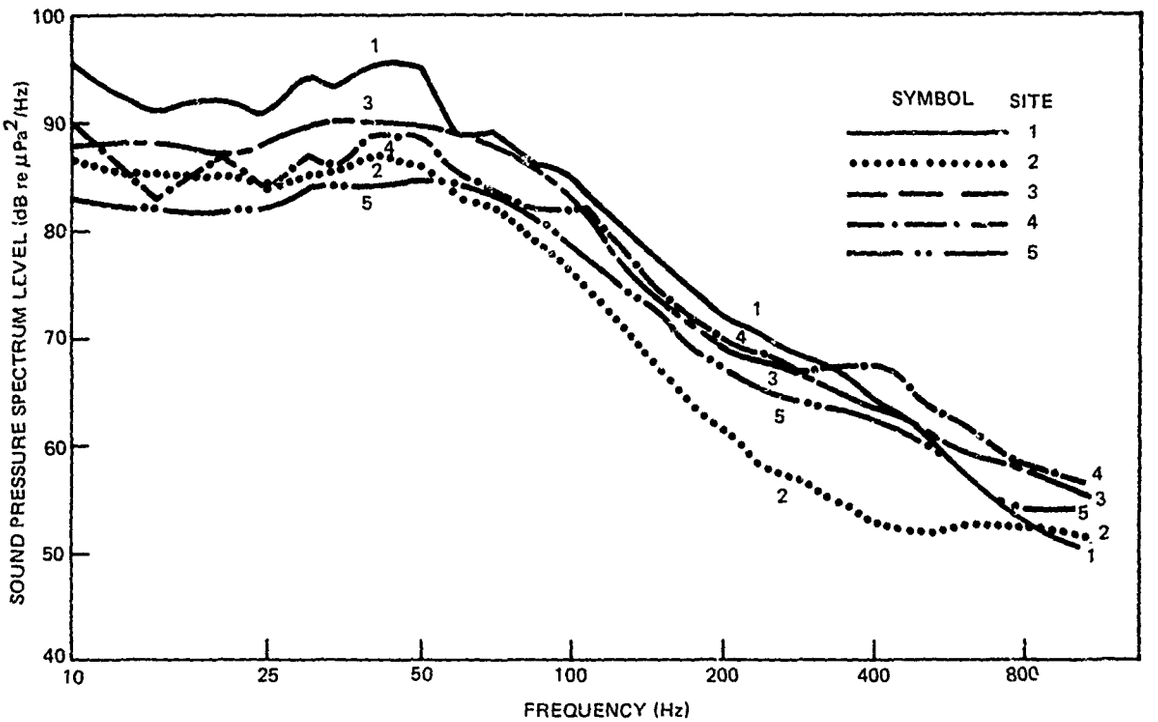

Figure VIII-14. (C) Median noise levels for the five principal BEARING STAKE sites obtained from the deepest hydrophone of the bottom-mounted array. (U)

Also, for these same frequencies in the northern Arabian Basin, higher noise levels, by about 6 to 10 dB, occur for northwest and southeast directions than for other directions. Noise levels at these frequencies in the central to southeastern Arabian Basin (Sites 2L and 5L, fig VI-7 and VI-8) are lower than at the other sites and the noise field is more nearly isotropic.

REFERENCES (U)

Fabula, A.G. and J.A. Neubert (1978). "BEARING STAKE Data and Analysis: LATA (U)," Naval Oceans Systems Center, San Diego, California, NOSC TN 589, November (CONFIDENTIAL)

Fenner, D.F. and W.J. Cronin, Jr. (1978). "BEARING STAKE Exercise: Sound Speed and Other Environmental Variability (U)," Naval Ocean Research and Development Activity, NSTL Station, Mississippi, NORDA Report 18, September (CONFIDENTIAL)

Hamilton, E.H. and R.T. Bachman (1979). "Geoacoustic Models of the Sea Floor: Gulf of Oman, Arabian Sea, and Somali Basin (U)," Naval Ocean Systems Center, San Diego, California (CONFIDENTIAL)

Mitchell, S.K., K.C. Focke, J.J. Lemmon and M.M. McSwain (1979). "Analysis of Acoustic Bottom Interaction in BEARING STAKE (U)," Applied Research Laboratories, The University of Texas at Austin, Texas, ARL-TR-79-24, February (CONFIDENTIAL)

Neubert, J.A. (1978a). "BEARING STAKE Coherence Data Analysis: Part I. The OAMS Array (U)," Naval Ocean Systems Center, San Diego, California, NOSC TN 380, February (CONFIDENTIAL)

Neubert, J.A. (1978b). "BEARING STAKE Coherence Data Analysis: Bottom-Mounted Array (U)," Naval Ocean Systems Center, San Diego, California, NOSC TN 452, May (CONFIDENTIAL)

Neubert, J.A. (1978c). "BEARING STAKE Array Signal Gain Data Analysis (U)," Naval Ocean Systems Center, San Diego, California, NOSC TN 624, December (CONFIDENTIAL)

Neubert, J.A. (1978d). "BEARING STAKE Coherence and Array Gain Area Assessment Report (U)," Naval Ocean Systems Center, San Diego, California, NOSC TR 383, December (CONFIDENTIAL)

Pedersen, M.A. and G.S. Yee (1979). "Propagation Loss Assessment of the BEARING STAKE Exercise (U)," Naval Ocean Systems Center, San Diego, California NOSC TR 467, September (CONFIDENTIAL)

Wagstaff, R.A. and J.W. Aitkenhead (1979). "BEARING STAKE Ambient Noise (U)" (Approximate Title; Report in Preparation), Naval Ocean Systems Center, San Diego, California (CONFIDENTIAL)

CHAPTER IX

CONCLUSIONS (U)

by

Aubrey L. Anderson

Numerical Modeling Division, Code 320

Naval Ocean Research and Development Activity

NSTL Station, Mississippi 39529

CHAPTER IX. CONCLUSIONS (U)

CONTENTS (U)

CHAPTER IX. CONCLUSIONS (U)

IX.1 (U) GENERAL

(C) Although the primary intention of this report has been a discussion of the low frequency ocean acoustic nature of the Northwest Indian Ocean based on results of the BEARING STAKE exercise, as pointed out in earlier chapters such a discussion cannot be totally separated from discussion of the measurement and data analysis programs or from theoretical studies performed during the analysis. Thus, this conclusions section, which is not another stage of summarization of the acoustic results (this is contained in the SUMMARY section at the front of the report), will contain remarks about the exercise and analysis in addition to those about the regional acoustics.

IX.2 (U) REGIONAL ACOUSTICS

(C) Throughout the Northwestern Indian Ocean, low frequency propagation and noise are dominated by bottom interaction effects. This is not surprising and indeed was foreseen prior to the BEARING STAKE exercise. Thus, great emphasis was placed on measurement and interpretation of bottom interaction during BEARING STAKE, and the best available procedures were used . As a result, it is known that the low average propagation loss and high ambient noise over the sediment filled basins are primarily caused by generally low bottom losses in the basins. These low bottom losses are caused in turn by low absorption in the unconsolidated sediment floor of the basins (thus, refractive return to the water column of most bottom-penetrating acoustic energy). Bottom losses are so low over the basins that a propagation loss disadvantage results from placement of receiver sites on ridges or rugged topographic highs (hills) at the edges of the basins. Apparently, this is because energy propagating to receivers mounted on these ridges or hills suffers significantly increased loss upon reflection from the higher-loss flanks of the ridge or hill.

(C) The virtual independence of transmission loss with depth (for receivers removed from either the surface or bottom by more than a few acoustic wavelengths) is clearly related to the low bottom loss up to high grazing angles on the bottom. That is, many multipaths, containing most of the energy from a source, contribute to the received signal at any depth in the water column. This richness of high-energy multipaths contributes to high received levels (low propagation losses) but also results in a high rate of variability (fluctuation) of level with range. Near depth independence of omnidirectional ambient noise is closely related to the depth independence of propagation loss and to high shipping densities.

(C) The anisotropy of the low-frequency horizontal directional noise field in this area correlates well with the distribution of surface ships and should be predictable with high confidence when surface ship distribution is accurately known. The confidence is somewhat reduced when significant components of the noise field must traverse the lower confidence bottom type 5 or 6 regions.

(C) Generally high but range-variable (fluctuating) phase coherence for low-frequency signals propagating over the basins indicates that the interaction of signal energy with the unconsolidated sediment floor in the basins

preserves the signal coherence of the individual multipaths. This further supports the emerging picture of bottom interaction in the basins as primarily a refraction phenomenon within the basin floor sediments. Reduction of coherence when the signals reflect from slopes or other topographic features in or around the basins also supports this concept of basin bottom interaction and indicates a transition to more of a scattering phenomenon for bottom interaction outside the basins.

IX.3 (U) BEARING STAKE EXERCISE

(C) This exercise sampled a significant portion of the third largest of the worlds's oceans. The region studied represents one of the largest bottom-limited ocean regions. It was recognized prior to the exercise that bottom interaction would dominate the underwater acoustics in the area and that entirely new types of behavior of the acoustic fied could emerge as compared to the two other heavily sampled, largely non-bottom-limited oceans (Atlantic and Pacific). This foresight, which caused a significant amount of planning effort for bottom interaction measurement and which devoted much of the measurement time and resources to acquiring data allowing proper interpretation of bottom interaction, has proven to be the key to understanding the regional acoustics as shown by the BEARING STAKE acoustic data. Significant interaction between the acoustic measurements and the geoacoustic model has allowed not only a high-confidence interpretation of the bottom interaction phenomenon but also high-confidence extrapolation of this phenomenon outside the bounds of the actual measurements. A cohesive picture of the signal propagation and coherence and of the ambient noise field can be drawn — even though several new phenomena (not previously observed in data sets from other oceans) occur.

IX.4 (U) IMPLICATIONS

(C) High received signal levels and high signal coherence should allow low-frequency surveillance of significant portions of the Northwest Indian Ocean from a few sites (either fixed or mobile). These positive aspects of the signal propagation are partially weakened by the also high ambient noise levels. Placement of sites away from concentrations of ships and taking advantage of the noise field horizontal anisotropy should reduce the negative impact of the noise field. Actual estimates of system performance for various regional scenarios are being made by a separate system performance assessment which is also based on the BEARING STAKE results and is utilizing inputs and model evaluations from the acoustic assessment. These will be reported separately.

(C) The acoustic assessment results suggest certain system placements which should perhaps be avoided (these would of course require further verification from actual system performance estimates). The high signal losses (and potentially reduced coherence) for receivers not over the unconsolidated sediment of the basin floor indicate that receivers would probably perform better (in terms of basin surveillance) if placed on or over the flat floors of the basins rather than on surrounding ridges or localized topographic highs. Towed arrays would experience less fluctuation of coherence if operated at depths outside those exhibiting significant sound speed fluctuation (shallower than 300 m or deeper than 1000 m).

(C) Designers of systems placed near the bottom on the basins should consider several unique aspects of the regional acoustics. First, the near-bottom signal and noise fields exhibit depth-dependent features, including localized notches (or minima of levels), which result from coherent interaction of bottom-reflected and non-bottom-reflected (upgoing and downgoing) multipaths near this bottom interface. Whether or not optimization of system performance is attempted by taking advantage of these notches (as suggested elsewhere), accurate estimation of system performance will require including the phenomena in the acoustic field estimates. Furthermore, penetration of most of the bottom interacting energy into the bottom with subsequent refractive return to the water column will produce a different spatial distribution of the near-bottom energy fields from that predicted by theoretical techniques treating the bottom interaction as a reflection occurring at the water-sediment interface. Specifically, vertical arrival structure of the signal and noise fields near the seafloor will be controlled by bottom penetration of the energy and will require treatment of the water and sediment system as coupled propagation domains for accurate prediction.

IX.5 (U) LIMITATIONS

(C) Bottom loss, which was very well defined for the sediment filled basins, can only be inferred for the ridges and coastal areas. Thus, predictions of transmission loss over BEARING STAKE types 5 and 6 bottom loss regions should be used with greater caution than those over bottom types 1 through 4.

(C) The near-bottom notch (maximum) of propagation loss on the basin floors is primarily a theoretical result and is only partially supported by BEARING STAKE data. Because of the potential signal-to-noise ratio gain, such a phenomenon could be important in the design of near-bottom systems and should be further tested. Note that the height of the notch off the bottom is both frequency and source depth dependent. Also, the ambient noise notch is predicted only for distant sources and may be absent for nearby noise sources.

GLOSSARY (U)

(C)	Arabian Basin	the large central basin in the Arabian Sea containing the Arabian Fan and bounded by the subcontinent of India and the following ridges: Murray, Owen, Carlsberg, and Laccadive-Chagos.
(C)	Arabian Cone	synonymous (in this report) with Arabian Fan.
(C)	Arabian Fan	deep sea fan, in the Arabian Sea, formed by detrital material from the Indus River.
(C)	ASTRAL	ASEPS TRAnsmission Loss Model, a high speed transmission model.
(U)	BMA	Bottom Mounted Array, described on page 14.
(C)	Carlsberg Ridge	rugged, mostly bare basalt ridge at the southern edge of the Arabian Sea.
(C)	Chain Ridge	continuous basalt ridge with peaks; forms the eastern boundary of the northern Somali Basin.
(U)	CW	Continuous Wave.
(C)	DIAMANTINA	Australian ship which operated the LATA array and collected oceanographic data.
(U)	DSC	Deep Sound Channel.
(U)	Events	term used in Chapter V when referring to CW source tows or aircraft or ship explosive source deployments.
(C)	Indus Basin	synonymous (in this report) with Arabian Basin.
(C)	Indus Cone	synonymous (in the report) with Arabian Fan or Arabian Cone.
(C)	KINGSPORT	U.S. Naval ship which towed CW sources, deployed explosive sources (SUS), and collected environmental data.
(U)	LATA	Long Acoustic Towed Array, described on page 15.
(C)	MIZAR	U.S. naval ship which launched and retrieved the VAC systems and operated the OAMS array.
(C)	MYER	U.S. naval ship which was responsible for all BMA operations.
(C)	Murray Ridge	basaltic ridge separating the Oman Basin and Arabian Basin.

(U)	NAVOCEANO	Naval Oceanographic Office.
(U)	NORDA	Naval Ocean Research and Development Activity.
(U)	NOSC	Naval Ocean Systems Center.
(U)	OAMS	Ocean Acoustic Measurement System - towed array described on page 15.
(C)	Oman Basin	small ocean basin on the northern edge of the Arabian Sea. Connects with the Persian Gulf.
(C)	Owen Ridge	sediment and rock ridge on the western edge of the Arabian Basin. Bounds the western edge of the Arabian Fan with a steep fault scarp.
(U)	Somali Basin	deep ocean basin off the coast of Somalia in the Northwest Indian Ocean.
(U)	SUS	Signal, Underwater Sound, an explosive source with a preset pressure (depth) activated fuse.
(U)	SV/STD	Sound Velocity/Salinity-Temperature Depth measuring instrument or data obtained with such an instrument.
(U)	VAC	Vertical ACODAC, vertical array of hydrophones with self-contained power and data recording capability. Used to obtain data for bottom interaction analysis.
(U)	WECO (or WECo)	Western Electric Company.
(U)	WHOI	Woods Hole Oceanographic Institution.
(C)	WILKES	U.S. naval ship that collected environmental data (see page 16).
(U)	WRE	Weapons Research Establishment, Australia.
(U)	XBT	Expendable Bathythermograph.

(U) INITIAL DISTRIBUTION (U)

DEPUTY UNDER SECRETARY OF DEFENSE R&E
(TACT, WARFARE PROGRAMS)
DIR NAVAL WARFARE

ARPA RESEARCH CENTER
UNIT 1
T KOOIJ

ASSISTANT SECRETARY OF THE NAVY (RE&S)
DEP ASST SECRETARY (SYSTEMS)
G CANN

CHIEF OF NAVAL OPERATIONS
NOP-095
NOP-098
NOP-951 (2)
NOP-951F (2)
NOP-952 (2)
NOP-9520

CHIEF OF NAVAL MATERIAL
NMT-08T24 (GR SPALDING)

NAVAL ELECTRONIC SYSTEMS COMMAND
CODE 320 (J SINSKY)
PME-124-20 (R KNUDSEN)
PME-124-30
PME-124-60 (4)

NAVAL SYSTEMS COMMAND
NSEA-06R (CD SMITH)

NAVAL AIR SYSTEMS COMMAND
NAIR-370

OFFICE OF NAVAL RESEARCH
ONR-102B

NAVAL RESEARCH LABORATORY
CODE 8108
CODE 8160 (BB ADAMS)

NAVAL INTELLIGENCE SUPPORT CENTER
CODE 222

NAVAL POSTGRADUATE SCHOOL
LIBRARY

NAVAL AIR DEVELOPMENT CENTER
CODE 303 (J HOWARD) (2)

NAVAL OCEANOGRAPHY COMMAND

NAVAL OCEAN RESEARCH AND DEVELOPMENT
ACTIVITY
CODE 110 (TECH DIRECTOR) (2)
CODE 320 (2)
CODE 500
CODE 520 (RR GARDNER)
CODE 115
CODE 340 (DR S MARSHALL)
CODE 360 (T HOLCOMB)

NAVAL UNDERWATER SYSTEMS CENTER
NEW LONDON LABORATORY
CODE 312 (ROY DEAVENPORT)

NAVAL OCEANOGRAPHIC OFFICE
CODE 3410 (J CARROLL)
CODE 3400 (WH GEDDES)

NAVAL OCEAN RESEARCH AND DEVELOPMENT
ACTIVITY LIAISON OFFICE

COMMANDER IN CHIEF U.S.
ATLANTIC FLEET
PACIFIC FLEET
COMMANDER
CODE 352

COMMANDER THIRD FLEET
N-32

COMMANDER SEVENTH FLEET
N34

THE UNIVERSITY OF TEXAS
APPLIED RESEARCH LABORATORY
S MITCHELL (2)

WOODS HOLE OCEANOGRAPHIC INSTITUTE
E HAYES

BELL TELEPHONE LABORATORIES
WHIPPANY, NJ 07981
R LAUVER
PENNOTTI

WESTERN ELECTRIC COMPANY
PO BOX 20046
GELFORD CENTER
GREENSBORO, NC 27420
R SCUDDER (3)

PLANNING SYSTEMS, INC.
7900 WESTPARK DRIVE
MC LEAN, VA 22101
DR L SOLOMON

TRW, INC.
7600 COLSHIRE DR
MC LEAN, VA 22101
R MURAWSKI

APPLIED HYDROACOUSTICS, INC.
656 QUINCE ORCHARD RD
GAITHERSBERG, MD 20760
F RYDER

COMPUTER SCIENCES CORP.
2251 SAN DIEGO AVENUE
SAN DIEGO, CA 92110

DEFENSE DOCUMENTATION CENTER (2)

DEPARTMENT OF THE NAVY
OFFICE OF NAVAL RESEARCH
875 NORTH RANDOLPH STREET
SUITE 1425
ARLINGTON VA 22203-1995

IN REPLY REFER TO:

5510/1
Ser 321OA/011/06
31 Jan 06

MEMORANDUM FOR DISTRIBUTION LIST

Subj: DECLASSIFICATION OF LONG RANGE ACOUSTIC PROPAGATION PROJECT (LRAPP) DOCUMENTS

Ref: (a) SECNAVINST 5510.36

Encl: (1) List of DECLASSIFIED LRAPP Documents

1. In accordance with reference (a), a declassification review has been conducted on a number of classified LRAPP documents.

2. The LRAPP documents listed in enclosure (1) have been downgraded to UNCLASSIFIED and have been approved for public release. These documents should be remarked as follows:

   Classification changed to UNCLASSIFIED by authority of the Chief of Naval Operations (N772) letter N772A/6U875630, 20 January 2006.

   DISTRIBUTION STATEMENT A: Approved for Public Release; Distribution is unlimited.

3. Questions may be directed to the undersigned on (703) 696-4619, DSN 426-4619.

BRIAN LINK
By direction

Subj: DECLASSIFICATION OF LONG RANGE ACOUSTIC PROPAGATION PROJECT (LRAPP) DOCUMENTS

DISTRIBUTION LIST:

NAVOCEANO (Code N121LC – Jaime Ratliff)
NRL Washington (Code 5596.3 – Mary Templeman)
PEO LMW Det San Diego (PMS 181)
DTIC-OCQ (Larry Downing)
ARL, U of Texas
Blue Sea Corporation (Dr.Roy Gaul)
ONR 32B (CAPT Paul Stewart)
ONR 321OA (Dr. Ellen Livingston)
APL, U of Washington
APL, Johns Hopkins University
ARL, Penn State University
MPL of Scripps Institution of Oceanography
WHOI
NAVSEA
NAVAIR
NUWC
SAIC

Declassified LRAPP Documents

Report Number	Personal Author	Title	Publication Source (Originator)	Pub. Date	Current Availability	Class.
Unavailable	Penrod, C. S., et al.	MOORED SURVEILLANCE SYSTEM FIELD VALIDATION TEST SENSOR PERFORMANCE ANALYSIS. VOLUME I. DATA COLLECTION AND MESUREMENT SYSTEM DESCRIPTION	University of Texas, Applied Research Laboratories	781231	ADC018009	C
Unavailable	Watkins, S. L., et al.	MOORED SURVEILLANCE SYSTEM FIELD VALIDATION TEST SENSOR PERFORMANCE ANALYSIS. VOLUME III. VERNIER RESOLUTION DATA PRODUCTS	University of Texas, Applied Research Laboratories	781231	ADC018373	C
Unavailable	Watkins, S. L., et al.	MOORED SURVEILLANCE SYSTEM FIELD VALIDATION TEST SENSOR PERFORMANCE ANALYSIS. VOLUME II. STANDARD RESOLUTION DATA PRODUCTS	University of Texas, Applied Research Laboratories	781231	ADC018374	C
NORDATN44	Bucca, P. J.	ENVIRONMENTAL VARIABILITY DURING THE CHURCH STROKE II CRUISE FIVE EXERCISE (U)	Naval Ocean R&D Activity	790201	ADC020353; NS; AU; ND	C
NADC7820830	Balonis, R. M.	TEST STEERED VERTICAL LINE ARRAY (TSVLA) MEASUREMENTS FOR BEARING STAKE SURVEYS (U)	Naval Air Systems Command	790301	ADC018003; NS; ND	C
USIControl674779	Williams, W., et al.	REPORT OF THE LRAPP EXERCISE PLANNING WORKSHOP TRACOR INC ROCKVILLE MD 16 - 17 OCTOBER 1978 (U)	Underwater Systems, Inc.	790302	NS; ND	C
NOSCTR357	Hamilton, E. L., et al.	GEOACOUSTIC MODELS OF THE SEAFLOOR: GULF OF OMAN, ARABIAN SEA, AND SOMALI BASIN (U)	Naval Ocean Systems Center	790615	ND	C
Unavailable	Unavailable	RAPIDLY DEPLOYABLE SURVEILLANCE SYST (RDSS) ACOUSTIC VALIDATION TEST (AVT) EXERCISE PLAN (U)	Naval Electronic Systems Command	790625	AU	C
LRAPPRC79027	Brunson, B. A., et al.	GULF OF MEXICO AND CARIBBEAN SEA DATA AND MODEL BASE REPORT (U)	Tracor, Inc.	790701	ADC019153; NS; ND	C
Unavailable	Unavailable	BEARING STAKE BMS DATA QUALITY ASSESSMENT REPORT (U)	University of Texas, Applied Research Laboratories	790705	AU	C
PME12430	Unavailable	RAPIDLY DEPLOYABLE SURVEILLANCE SYSTEM (RDSS) ACOUSTIC VALIDATION TEST (AVT) DATA REDUCTION AND ANALYSIS PLAN (U)	Naval Electronic Systems Command	790815	NS; AU	C
Unavailable	Unavailable	RAPIDLY DEPLOYABLE SURVEILLANCE SYSTEM (RDSS) ACOUSTIC VALIDATION TEST (AVT) EXERCISE PLAN (U)	Naval Electronic Systems Command	790917	AU	C
NOSCTR467	Pedersen, M. A., et al.	PROPAGATION LOSS ASSESSMENT OF THE BEARING STAKE EXERCISE (U)	Naval Ocean Systems Center	790928	ADC020845; NS; AU; ND	C
NOSCTR466	Anderson, A. L., et al.	BEARING STAKE ACOUSTIC ASSESSMENT (U)	Naval Ocean Systems Center	790928	ADC020797; NS; AU; ND	C